Large pit thermal energy storage for solar district heating plant

Xiang, Yutong

Publication date:
2023

Document Version
Publisher's PDF, also known as Version of record

DTU Civil and Mechanical Engineering
PhD Thesis

Large pit thermal energy storage for solar district heating plant

Yutong Xiang

Preface

This thesis has been submitted as partial fulfillment of the requirements for the degree of Doctor of Philosophy (PhD) from the Technical University of Denmark (DTU). The work presented was carried out between January 2020 and June 2023 at the Section of Energy and Services at the Department of Civil and Mechanical Engineering, DTU. The study has been supervised by associate professors Jianhua Fan and Simon Furbo.

This work has been financially supported by the Danish Energy Agency EUDP project for participation of the IEA ECES Annex 39: “Large Thermal Energy Storges for District Heating” under the grant number 64020-2036, and the Chinese Scholarship Council (CSC) under the grant number 201909110075.

Abstract

In recent years, there has been an increased interest in constructing large-scale seasonal thermal energy storage to balance the heat supply and demand. Among various types of seasonal thermal energy storage, pit thermal energy storage (PTES) stands out due to several advantages. These advantages include its large energy capacity, flexible geometry size, independence to construction site, easy operation characteristics, and low construction costs. Notably, PTES exhibits the lowest investment costs per m^3 water equivalent when the storage volume exceeds 60,000 m^3, making it an attractive option that deserves more attention. However, despite its potential, only 15 out of 530 large-scale solar thermal systems (>350 kWth, 500 m^2), are currently integrated with PTES. This indicates that there are certain barriers hindering the global development of PTES.

In this thesis, the development of PTES is comprehensively reviewed. From the perspective of actual project operation, the planning, design, and operation strategies of PTES have a significant impact on system efficiency of solar district heating (SDH) plants. An optimum cover design plays a crucial role in reducing heat loss and improving storage efficiency. Additionally, the selection of suitable insulation and liner materials, as well as their proper installation, not only extends the service life of PTES but also ensures the stable operation of the SDH system. Moreover, implementing a well-defined operating strategy for PTES system can contribute to achieving high system efficiency. Therefore, it is of utmost importance to consider and incorporate a proper PTES design during the planning stage.

According to the PTES technology review, there is limited research available on the topic, as integrating PTES into the SDH plant has mainly been driven by commercial actors. In this context, most research is concentrated on simulation studies due to the impracticalness of conducting experiments on such a large scale. To reduce computational complexity, simplified one-dimensional (1D) models are widely used. However, they pose challenges in accurately representing experimental results. To this end, a full-scale three-dimensional (3D) model of PTES, including the surrounding soil, is developed. The developed 3D model is validated using Dronninglund PTES measurements, allowing for accurate short-term and long-term calculations.

One of the major challenges faced by the multi-node 1D models used in PTES simulation is numerical diffusion. The numerical diffusion arises from the assumption that each node within the storage is fully mixed. To improve the heat transfer calculation accuracy in multi-node models, a criterion for determining the grid size distribution is proposed in this study. The thermocline temperature gradient is identified as the suitable indicator for selecting the optimum grid size distribution along the PTES height. This method is verified by conducting a three-year calculation using a multi-node model (TRNSYS Type 343). The results of this calculation highlight that the optimal grid size distribution strikes a balance between computational efficiency and accuracy.

Additionally, considering the mixing effect in modeling can significantly improve the accuracy of PTES temperature prediction. However, incorporating the 3D characteristics of inlet mixing

into a 1D model presents a challenge. This study introduces two performance indexes to characterize the inlet flow mixing region inside the PTES. Notably, correlations are developed to establish relationships between these two indexes, dimensionless height, and dimensionless time. This method opens possibilities to improve the calculation accuracy of existing 1D models by including inlet mixing.

Furthermore, the large uninsulated interface between the water body and the surrounding soil can lead to significant thermal losses. Consequently, the soil's thermal properties can strongly influence the PTES performance and result in inefficient PTES operation. However, the heat loss may be overestimated when a constant heat transfer coefficient is used along the sidewalls in 1D models. This study conducts long-term simulation to assess three main aspects: transient natural convection, soil temperature distribution, and the influence of different geometries on a 3D scale. The results contribute to a better understanding of the interaction between the water and the soil regions and provide insight into methods for improving the calculation of 1D models by considering the overall heat transfer coefficient along the PTES sidewalls.

Resumé

I de seneste år har der været en øget interesse for at opføre store termiske sæsonlagre for at balancere varmeforsyningen og -efterspørgslen. Blandt de forskellige typer af sæsonlagre skiller damvarmelagre, også kendt som PTES, sig ud på grund af flere fordele. Disse fordele inkluderer deres store energikapacitet, fleksible geometri, simple styring og lave bygningsomkostninger. De laveste investeringsomkostninger pr. m^3 vandækvivalent opnås ved brug af damvarmelagre for volumener over 60.000 m^3. Dette gør damvarmelagre til et attraktivt valg, der fortjener mere opmærksomhed. Dog er kun 15 ud af de 530 store solvarmeanlæg (>350 kWth, 500 m^2) integreret med PTES. Dette indikerer, at der er visse barrierer, der hindrer den globale anvendelse af PTES.

I denne afhandling præsenteres den historiske udvikling af PTES teknologien. Set ud fra et drifts perspektiv har planlægning, design og driftsstrategier for PTES en betydelig indflydelse på effektiviteten af solvarmecentraler. Et optimalt låg design spiller en afgørende rolle for at reducere varmetab og forbedre lagerets effektivitet. Derudover har valget af isolerings- og liner-materialer samt deres korrekte installation ikke kun betydning for damvarmelagerets levetid, men sikrer også en stabil drift af solvarme-systemet. Implementering af en veldefineret driftsstrategi for PTES-systemer kan desuden bidrage til at opnå høj systemeffektivitet. Det er derfor yderst vigtigt at dimensionere og designe damvarmelagre korrekt i planlægningsfasen.

Baseret på et omfattende litteraturstudie er der begrænset forskning tilgængelig om damvarmelagre, da integrationen af damvarmelagre i solvarmeanlæg primært har været drevet af kommercielle aktører. Størstedelen af den eksisterende forskning omhandler simuleringsstudier på grund af praktiske udfordringer ved at udføre eksperimenter i så stor skala. For at reducere beregningskompleksiteten er det udbredt at anvende forenklede éndimensionelle (1D) modeller. Sammenligninger med eksperimentielle resultater har dog vist at disse modeller ikke er tilstrækkeligt nøjagtige. I dette studie er der derfor udviklet en fuldskala tredimensionel (3D) model af et damvarmelager, herunder den omkringliggende jord. Den udviklede 3D-model er valideret ved sammenligning med målinger fra damvarmelageret i Dronninglund.

En af de største udfordringer ved en-dimensionelle modeller af damvarmelagre er numerisk diffusion. Numerisk diffusion opstår som følge af antagelsen om, at hvert enkelt lag er fuldstændig blandet. For at forbedre nøjagtigheden af 1-D modeller, er der i denne afhandling foreslået en metode til bestemmelse af netstørrelsen. Temperaturgradienten i lageret er identificeret som en passende indikator til at vælge den optimale netstørrelse. Denne metode er valideret ved at simulere tre år med en multi-node model (TRNSYS Type 343). Resultaterne fremhæver, at den optimale netstørrelse er en balance mellem beregningstid og nøjagtighed.

Derudover kan nøjagtigheden af temperaturfordelingen væsentligt forbedres ved at tage hensyn til opblanding i lageret. Dog udgør det en udfordring at inkorporere de tredimensionelle egenskaber ved indløbs-diffusoren i en én-dimensionel model. Denne undersøgelse introducerer to performance indekser til at karakterisere damvarmelagerets indløb. Til dette formål blev der udviklet korrelationer for at etablere sammenhænge mellem disse to indekser,

dimensionsløs højde og dimensionsløs tid. Denne metode åbner muligheder for at forbedre beregningsnøjagtigheden af eksisterende én-dimensionelle modeller ved at inkludere opblanding ved indløbet.

Desuden kan grænsefladen mellem vandet og den omkringliggende jord medføre betydelige varmetab. Derfor kan jordens termiske egenskaber have stor indflydelse på lagerets ydeevne og resultere i ineffektiv drift. Varmetabet kan blive overestimeret, når en konstant varmeoverførselskoefficient anvendes langs sidevæggene i en-dimensionelle modeller. I ddette studie blev der gennemført langtids simulering for at vurdere tre hovedaspekter: transient naturlig konvektion, jordtemperaturfordeling og indflydelsen af forskellige geometrier. Resultaterne bidrager til en bedre forståelse af interaktionen mellem vand- og jorddomainet og giver indsigt i metoder til at forbedre beregningen af 1D-modeller ved at tage højde for den samlede varmeoverføringskoefficient langs lagerets sidevægge.

List of papers

The PhD thesis is based on the following papers, which constitute the second part of this thesis:

1. **Yutong Xiang**, Zichan Xie, Simon Furbo, Dengjia Wang, Meng Gao, Jianhua Fan. (2022). A comprehensive review on pit thermal energy storage: Technical elements, numerical approaches and recent applications, *Journal of Energy Storage, 55, 105716.* https://doi.org/10.1016/j.est.2022.105716

2. **Yutong Xiang**, Meng Gao, Simon Furbo, Dengjia Wang, Zhiyong Tian, Jianhua Fan. (2022). Heat transfer of a large-scale water pit heat storage under transient operations, *Journal of Energy Storage, 55, 105455.* https://doi.org/10.1016/j.est.2022.105455

3. **Yutong Xiang**, Meng Gao, Simon Furbo, Jianhua Fan, Gang Wang, Zhiyong Tian, Dengjia Wang. (2023). Assessment of inlet mixing during charge and discharge of a large-scale water pit heat storage, *[Submitted to Renewable Energy, under review]*

4. **Yutong Xiang**. (2023). Assessment of interaction between underground pit thermal energy storage and surrounding soil under transient conditions, *[Done preparation]*

Publications that are part of the PhD study but not included in the thesis are the following:

1. **Yutong Xiang.** (2023) Muti-year analysis and validation of a dynamic model for solar collector field in a large-scale district heating plant, *[Done preparation]*

2. Zichan Xie, **Yutong Xiang**, Dengjia Wang, Oleg Kusyy, Weiqiang Kong, Simon Furbo, Jianhua Fan. (2021). Numerical investigations of long-term thermal performance of a large water pit heat storage, *Solar Energy, 224, 808-822.* https://doi.org/10.1016/j.solener.2021.06.027

3. Xinyu Pan, **Yutong Xiang**, Meng Gao, Jianhua Fan, Simon Furbo, Dengjia Wang, Chao Xu (2022). Long-term thermal performance analysis of a large-scale water pit thermal energy storage, *Journal of Energy Storage, 52, 105001.* https://doi.org/10.1016/j.est.2022.105001

4. Meng Gao, Jianhua Fan, Simon Furbo, **Yutong Xiang** (2022). Energy and exergy analysis of a glazed solar preheating collector wall with non-uniform perforated corrugated plate, *Renewable Energy, 196, 1048-1063.* https://doi.org/10.1016/j.renene.2022.07.026

Acknowledgements

Transitioning back to academia from the workforce can indeed be a challenge, but I am glad that I managed to complete it. It is important to acknowledge the assistance and encouragement I received from various individuals throughout this journey. Here I would like to express my sincere appreciation.

I would like to extend my gratitude to my supervisors Prof. Dr. Jianhua Fan and Prof. Dr. Simon Furbo, for their unwavering patience and support throughout my study. Their availability for discussion and insightful comments have been invaluable to my academic progress. I am truly grateful for their guidance and mentorship.

Thanks to the whole Solar Group, and colleagues in Section of Energy and Services at the Technical University of Denmark. Their collective support has been instrumental in my academic journey. In particular, I would like to express my gratitude to Adam Rasmus Jensen for assisting in revising the Danish version of the abstract.

Thanks to my previous supervisors Prof. Dr. Guobing Zhou and Prof. Dr. Baoping Xu. Your pertinent guidance and encouragement have given me the confidence to pursue academic success.

Thanks to the external stay institutions, specifically acknowledging Yonghong Wang and Wei Feng. Their guidance and support during my internship in China were invaluable to my professional growth. I am thankful for their expertise, mentorship, and the opportunities they provided me to learn and apply my skills in a real-world setting.

Thanks to all my lovely friends in Denmark, especially those who resided in the same apartment as me, the exchange students, and the students from the Technical University of Denmark. Your delicious meals, shared travels, and daily interactions have made my time in Denmark truly memorable and enjoyable.

Thanks to my best friends in China and other counties. Despite the distance, you have always been there for me, offering guidance and standing by my side.

Last but not least, I would like to express my deepest gratitude to my parents, Mr. Aidong Xiang and Ms. Hua Zhang, as well as my entire family. Their daily non-stop greetings, unwavering support, and constant encouragement have been the foundation of my success. Their presence in my life has been a source of strength and motivation.

Table of Contents

List of akronyms

1D	One-dimensional
3D	Three-dimensional
CFD	Computational fluid dynamics
DH	Distric heating
ECG	Expanded clay granules
EGG	Expanded glass granules
EPS	Expanded polystyrene
FGG	Foam glass gravel
GFG	Glass foam gravel
HDPE	High-density polyethylene
LDPE	Low-density polyethylene
PE	Polyethylene
PIR	Polyisocyanurate
RMSD	Root mean square deviation
PP	Polypropylene
PTES	Pit thermal energy storage
PVC	Polyvinyl chloride
TTES	Tank thermal energy storage
SDH	Solar district heating

List of symbols

$C_{1\varepsilon}$	Turbulence constant, [-]
C_2	Turbulence constant, [-]
$C_{p.jm}$	Specific heat of mixed water in layer j, [J/kg·K]
$C_{p.s}$	Specific capacities of soil, [J/kg·K]
$C_{p.w}$	Specific capacities of water, [J/kg·K]
D_d	Diameter of diffuser disc, [m]
$E_{ch,meas}$	Measured charge energy, [MWh]
$E_{ch,calc}$	Calculated charge energy, [MWh]
$E_{disch,meas}$	Measured discharge energy, [MWh]
$E_{disch,calc}$	Calculated discharge energy, [MWh]
F	Buoyancy flux, [m^4/s^3]
Fr	Froude number, [-]
F_{sol}	Solar fraction, [-]
g	Gravitational acceleration, [m/s^2]
H_d	Distance between diffuser discs, [m]
k	Turbulent kinetic energy, [kg m^2/s^2]
M	Momentum of inlet flow, [J/m]
N	Total number of values obtained for the simulation period, [-]
N_{cyc}	Storage cycle, [-]
$P_{calc,i}$	Calculated parameters, [-]
$P_{meas,i}$	Measured parameters, [-]
Q_{aux}	Heat supplied from auxiliary system, [MWh]
Q_{charge}	Heat charged into the PTES, [MWh]
$Q_{discharge}$	Heat discharged from the PTES, [MWh]
Q_{max}	Maximum heat capacity, [MWh]
Q_{load}	Heat demand, [MWh]
dQ_{PTES}	Internal energy change, [MWh]
Re	Reynolds number, [-]
$R_{\Delta T/\delta}$	Thermocline gradient, [K/m]
t	Time, [s]

T	Temperature, [°C]
T_0	Initial PTES temperature, [°C]
T_{in}	Inflow temperature, [°C]
ΔT	Temperature difference between inflow and water inside PTES, [K]
u	Water velocity within PTES, [m/s]
V_{in}	Inlet flow rate at the inlet pipe scale, [m/s]
Z	Penetration height, [m]
ε	Turbulent energy dissipation rate, [m^2/s^3]
η_j	Energy distribution ratio, [-]
η_{PTES}	Storage efficiency, [-]
ϑ_{ch}	Relative deviation ratio for charge energy, [-]
λ_w	Thermal conductivity of water, [W/m·K]
λ_s	Thermal conductivity of soil, [W/m·K]
μ_w	Dynamic viscosity of water, [kg/m·s]
ρ_0	Initial average water density within PTES, [kg/m^3]
ρ_{in}	Inflow water density, [kg/m^3]
ρ_s	Soil density, [kg/m^3]
ρ_w	Water density, [kg/m^3]
σ_k	Turbulence constant, [-]
σ_ε	Turbulence constant, [-]
τ_w	Stress tensor of water, [$kg/m^2 \cdot s^2$]

Part I Summary

1

Introduction

The availability of energy has had a transformative impact on humanity over the past few centuries. It has revolutionized various aspects of our lives [1]. The discovery and utilization of fossil fuels, starting from the industrial revolution, marked a significant milestone in energy generation. As a result, many countries around the world have heavily relied on fossil fuels in their energy mix [1].

However, the heavy reliance on fossil fuels has had significant implications for global climate change and human health. The combustion of fossil fuels for energy generation is responsible for approximately three-quarters of global greenhouse gas emissions [2]. Additionally, it results in local air pollution and other forms of environmental pollution. Furthermore, as depicted in Figure 1.1, the consumption of primary energy from renewable energy resources has experienced an upward trend starting 1950, particularly in recent years. This surge can be attributed to the efforts aimed at addressing the energy crisis and advancing the carbon neutrality goal. Despite this growth, it is important to note that renewable technologies accounted for only around 17% of global primary energy consumption as of 2021 [1,3].

Therefore, there is still a considerable gap between the current share of renewable energy and the overall energy demand. To address this gap, it is critical to continue investing in research, development, and innovation in the renewable energy sector.

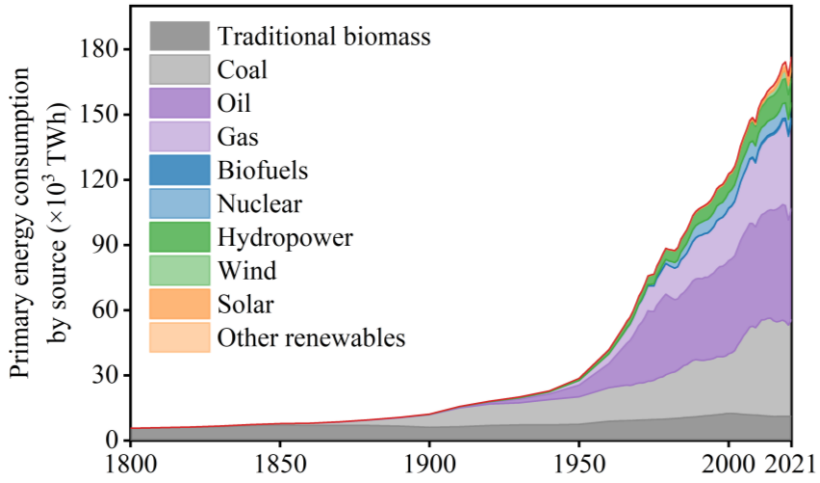

Figure 1.1 Evolution of primary energy consumption by source worldwide [1].

Among the energy demand, buildings account for one-third of the total final energy consumption, with 77% attributed to thermal energy consumption (shown in Figure 1.2) [4]. Consequently, promoting low-carbon heating is crucial for leveraging renewable energy

resources. According to The Net Zero Emissions Scenario, the potential for decarbonization in existing district heating (DH) networks far exceeds current projections. By 2026, the share of renewables in worldwide district heating supplies is expected to surpass twice its current level [5]. Under this prediction, the consumption of renewable energy in district heating needs to grow at a rate six times faster than our current outlook. This growth will be driven not only by bioenergy but also by the utilization of solar thermal energy and large-scale heat pumps.

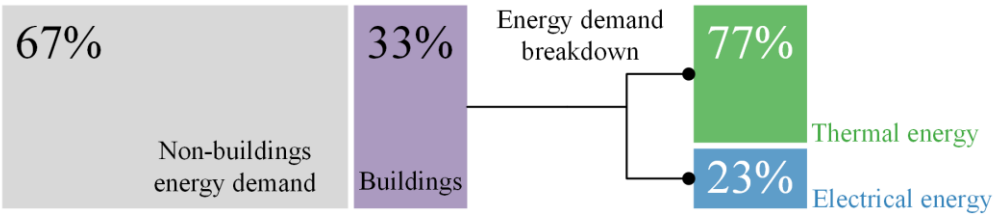

Figure 1.2 Proportion of global energy demand [4].

1.1 Solar district heating with seasonal thermal energy storage

With the increased interest in 4th and 5th generation DH systems, which operate at lower working fluid temperatures compared to the previous generations, solar district heating (SDH) systems have gained significant attention from both the research community and real-world applications [6]. Figure 1.3 depicts the development of large-scale solar thermal systems worldwide, in terms of the number of systems added and cumulative collector area in operation. By the end of 2021, there were 530 large-scale solar thermal systems (>350 kWth, 500 m^2) were in operation. The total installed capacity of these systems corresponds to 2.8 million m^2 collector area. Notably, until 2016, large-scale solar thermal systems were primarily concentrated in Europe [7]. Yet, since 2016, a growing number of countries outside of Europe have shown interest in this technology, recognizing its potential to decarbonize the heat sector in neighborhoods and cities.

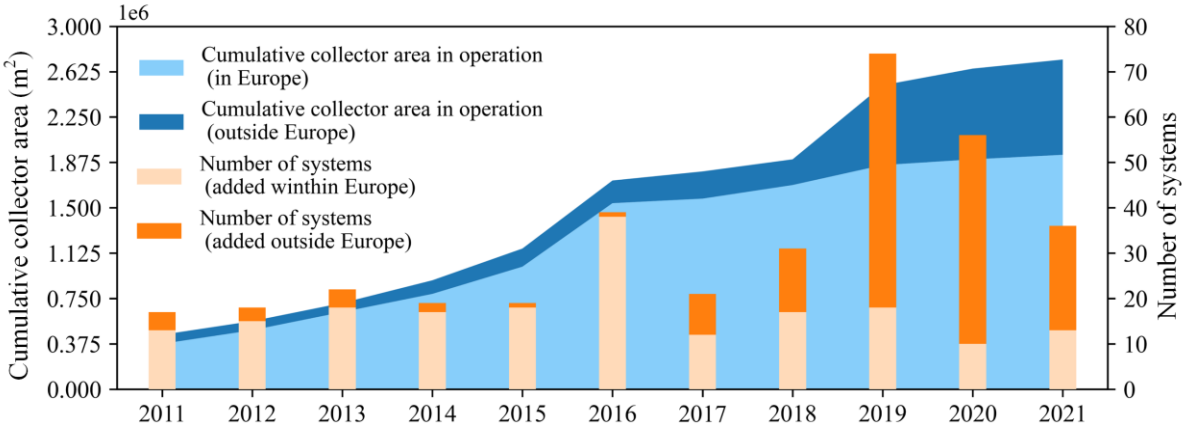

Figure 1.3 Annual additions of large-scale solar thermal systems and cumulative collector area in operation worldwide [4].

However, solar thermal energy faces challenges in terms of stability and reliability due to its intermittent nature. In this scenario, the usage of thermal energy storage (TES) is a promising solution. TES can be classified into diurnal thermal energy storage (DTES) and seasonal

thermal energy storage (STES) [8–10] based on the duration of energy storage. In particular, STES has emerged as a viable choice for district heating systems [11]. The significance of STES lies in its ability to enhance flexibility in the generation, transmission, and demand sides of SDH systems. By enabling the seasonal balancing of heat supply and demand, STES contributes to the resilience of SDH systems. Therefore, the incorporation of STES can lead to a decrease in total energy costs and promote a more efficient and sustainable energy system [12].

The different types of STES commonly used in SDH systems can be broadly categorized into four categories [13–17]: tank thermal energy storage (TTES), pit thermal energy storage (PTES), borehole thermal energy storage (BTES), and aquifer thermal energy storage (ATES). , Among these, PTES systems are generally considered superior to other STES systems in terms of energy density, geometry size, construction site independence, operation characteristics, and construction costs. Particularly, the investment costs per m^3 water equivalent of PTES have proven to be the lowest when the storage volume exceeds 60,000 m^3 [18,19]. Therefore, PTES has gained recognition as a promising technology for TES in recent years, primarily due to its ability to meet the requirements for large storage capacities.

However, when it comes to research, PTES has been the least studied among these four types of STES systems. This can be attributed to a couple of reasons. Firstly, there is a limited number of actual projects, with most of them concentrated in Europe, as shown in Figure 1.4. This scarcity of real-world projects results in a lack of available experimental data. Secondly, there are still technical barriers that need to be overcome in the planning, design, and practical application of PTES systems.

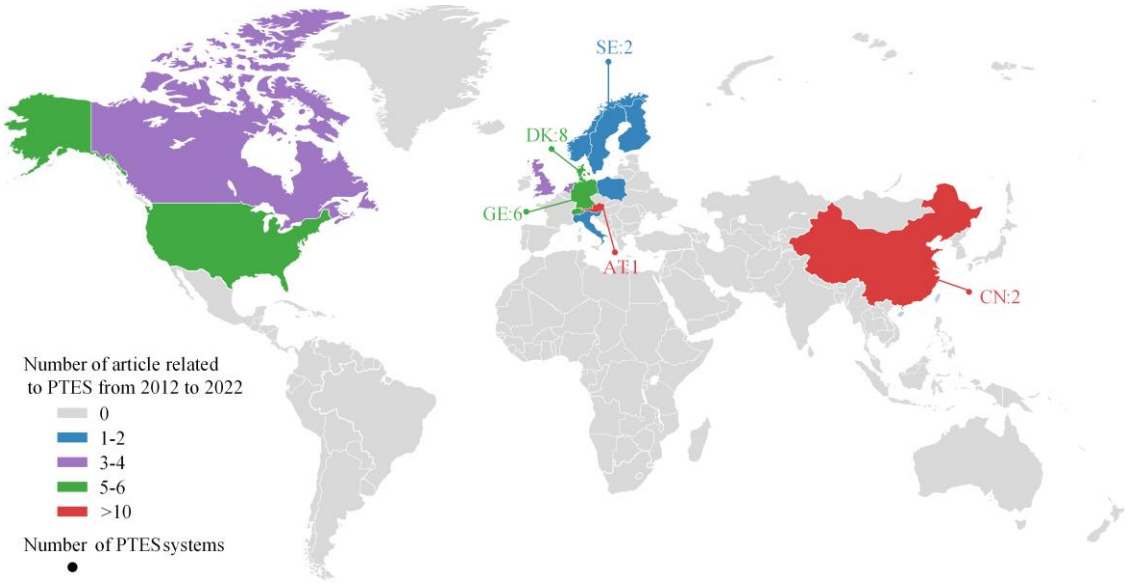

Figure 1.4 Global scientific publications on solar district heating plants with PTES **[Paper 1]**.

1.2 Research questions

Integrating PTES into the SDH plant has primarily been driven by commercial actors, leaving limited research available on the topic. Moreover, the utilization of a one-dimensional (1D)

simplified model poses challenges in accurately representing the complex three-dimensional (3D) features, leading to insufficient calculation accuracy. Therefore, this Ph.D. study aims to address this by comprehensively evaluating the performance of PTES. Especially, this study seeks to answer the following research questions:

(1) *What are the key challenges and problems that need to be solved in the development of PTES?*

(2) *What grid size can achieve improved calculation accuracy without a significant increase in computation time?' and 'Whether a criterion that can be used for the guidance of selecting appropriate grid sizes*?'

(3) *What are the specific characteristics of inlet mixing that occur inside PTES during actual operation?' and 'Can the characteristics of the inlet mixing be quantified?*

(4) *How is the interaction between buried PTES and surrounding soil?*

1.3 Organization of the thesis

The research questions presented in Section 1.2 give rise to research topics and scientific challenges that form the structure of this thesis. This thesis primarily focuses on theoretical groundwork and exploratory research to enhance the understanding of PTES performance during transient operation in a 3D scale. The specific contributions of each chapter are outlined as follows:

Chapter 2 provides an overview and discussion of the global development of PTES. The implemented PTES systems worldwide are summarized, with particular attention to their distribution across different regions and their real-world operation status. A summary of the key technical elements involved in PTES design is provided. This includes discussing the PTES structure and the material commonly used for PTES construction. The state-of-the-art numerical methods for PTES investigation are examined.

Chapter 3 introduces the Dronninglund PTES in detail, including its design, operational conditions, and measurements. A full-scale 3D model is developed to represent the physical characteristics and behavior of the Dronninglund PTES. The model is validated for both short-term and long-term application scenarios.

Chapter 4 explores the heat transfer characteristic inside PTES during dynamic operation. Various representative cases are selected to understand the influence of heat transfer under different grid size distributions. Based on the findings, a criterion determining the grid size distribution within the PTES is proposed. A three-year analysis of the thermal performance of Dronninglund PTES is conducted to determine the optimum size distribution. Furthermore, the result is applied to a 1D model to demonstrate its capability.

Chapter 5 assesses the inlet mixing phenomena within the PTES system. The characteristics of both positive and negative buoyancy jets are analyzed through the examination of various parameters. Two specific parameters are proposed to effectively represent the inlet mixing effect. Furthermore, a methodology for quantifying these two parameters is developed. The developed method can be used to improve existing 1D PTES models.

Chapter 6 analyzes the interaction between the water and soil region around the PTES. Based on long-term calculation results, the overall heat transfer coefficients along the PTES sidewall over the year are presented. This finding offers a valuable reference for developing and enhancing one-dimensional models. Long-term changes in soil temperature distribution are profiled to determine the effects on the subsurface environment under specific geological conditions. Moreover, the heat transfer effect between the water and soil regions is compared based on different PTES geometries and soil temperature distributions.

Chapter 7 discusses the significance of this study and its implications for future PTES development.

Chapter 8 summarizes the main results of this Ph.D. thesis and proposes the limitations of this investigation.

Chapter 9 provides an outlook for future research.

Chapter 2, 4, 5 have been published in peer-reviewed journal as papers I, II, III respectively. Chapter 6 is done preparation as paper IV.

2

Review on PTES technology

Pit thermal energy storage (PTES) has been developed since 1985. From the operational point of view, PTES is frequently considered similar to the tank thermal energy storage (TTES) as they both utilize the stratification concept to store energy. In contrast, PTES is typically constructed with a sloped geometry such as pyramid stump with a rectangular cross-section placed upside-down, or a truncated cone with a circular cross-section [20]. The excavated soil can create raised banks along the sides of PTES, increasing the overall storage volume [12].

PTES is primarily designed for large-scale applications to achieve long-term storage while minimizing thermal losses. In this case, it enables more flexible and smoother integration of solar energy into district heating systems, resulting in various benefits such as reduced reliance on fossil fuel, higher primary energy savings, and lower emissions [21]. However, only 15 of the 530 large-scale solar district heating (SDH) systems have successfully implemented PTES, indicating that certain shortcomings need to be addressed [22].

Key challenges in the PTES application include limited space availability, complex planning layouts, identification of reliable materials for stability, and addressing groundwater table considerations, among others. Additionally, the lack of supportive legalization presents challenges during the planning and construction approval phases [23]. However, based on an extensive literature review, there is currently no consistent comprehensive overview contrasting PTES technologies and summarizing the major findings from implemented storage facilities.

To address the question '*What are the key challenges and problems that need to be solved in the development of PTES?*', this chapter presents a comprehensive review of the PTES development from three perspectives: application, technical elements, and numerical method. Section 2.1 summarizes the implemented PTES system worldwide, with particular emphasis on their operational status metrics. Next, Section 2.2 focuses on the key technical elements of PTES design. Finally, Section 2.3 analyzes the latest numerical methods employed in PTES research.

2.1 Application of PTES

2.1.1 Worldwide distribution

To date, the primary information on 14 identified large-scale SDH plants with PTES (PTES volume > 500m^3) is presented in Table 2.1 [22]. Denmark has emerged as a leader in PTES

implementation, driven by the popularity of district heating. However, countries were actively researching PTES in the early years, such as Sweden and Germany, has fallen behind. On the other hand, the promotion of district heating and energy storage policies to establish a fossil fuel-free energy market has sparked significant interest in PTES system in China and Austria.

Table 2.1 Primary information on global PTES systems **[Paper 1]**.

Position	Country	Year	Solar collector field area (m^2)	PTES volume (m^3)	Heat pump (type/capacity (kW))
Lambohov	Sweden	1980	2700	10000	Compression/--
Stuttgart	Germany	1985	211	1050	Compression/66
Julich	Germany	1996	1200	2500	--
Augsburg	Germany	1996	2000	6000	--
Steinfurt	Germany	1999	510	1500	--
Chemnitz	Germany	2000	2000	8000	--
Eggenstein	Germany	2008	1600	4500	Compression/60
Ottrupgård	Denmark	1995	560	1500	--
Marstal	Denmark	2012	33300	75000	Compression/1500
Dronninglund	Denmark	2014	37573	60000	Absorption/4700
Gram	Denmark	2015	44000	122000	Compression/900
Vojens	Denmark	2015	70000	200000	Absorption/5100
Toftlund	Denmark	2017	27000	70000	Absorption/5100
Langkazi Tibet	China	2018	22275	15000	--

To provide a clear quantification of changes in PTES construction, Figure 2.1 illustrates the evolution of installed PTES number and volumes. The evolution reveals a moderate development in the early years until 2011. This is primarily driven by the construction of small systems within pilot projects. However, starting from 2012, a notable shift occurs both in the total installed volume and the system numbers. Regarding the PTES volume, the increase is not solely attributed to the rise in PTES numbers. Instead, it emphasizes the trend towards larger PTES installations during this period.

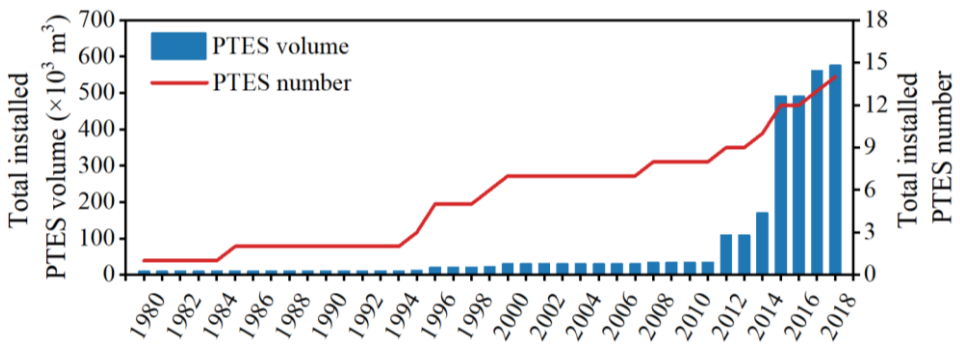

Figure 2.1 Evolution of the number and volume of PTES.

2.1.2 Operation status

For the comparison of PTES performance, a collection of characteristic numbers can be used. As different indicators supply different information, it is often not sufficient to report a single metric. In this case, the indicators commonly used and reported in the literature are as follows [23–26]:

Solar fraction: $$F_{sol} = \frac{Q_{load} - Q_{aux}}{Q_{load}} \quad (2.1)$$

Storage efficiency: $$\eta_{PTES} = \frac{Q_{discharge} + dQ_{PTES}}{Q_{charge}} \quad (2.2)$$

Number of storage cycles: $$N_{cyc} = \frac{Q_{discharge}}{Q_{max}} \quad (2.3)$$

Where Q_{load} refers to the heat demand, while Q_{aux} is the heat provided by the auxiliary system. Q_{charge} and $Q_{discharge}$ represent the heat charge into the PTES and discharge from the PTES, respectively. dQ_{PTES} is the internal energy change within the year and Q_{max} is the maximum heat capacity of the PTES during the year.

Figure 2.2 depicts these metrics along with the PTES's maximum and minimum temperatures. In terms of solar fraction (F_{sol}), most projects have F_{sol} between 30% and 50%. However, the Lambohov and Langkazi Tibet projects stand out with solar fraction exceeding 60%. It is important to note that these two projects only provide heating without domestic hot water. In addition, F_{sol} of the Marstal project experienced a decrease F_{sol} below 30% in 2017 due to rainwater entering the cover through the leakage.

In terms of storage efficiency (η_{PTES}), the Stuttgart and Dronninglund projects have η_{PTES} above 80%, outperforming other projects. Particularly, the Dronninglund project stand out, reaching a maximum η_{PTES} of 96% in 2017. This exceptional performance can be partly attributable to a higher storage cycle (N_{cyc}) compared to other projects. Moreover, the Dronninglund project employs a proper operation strategy that effectively lowers the minimum PTES temperature to approximately 10°C. This strategy helps to reduce the heat losses from the side and bottom walls.

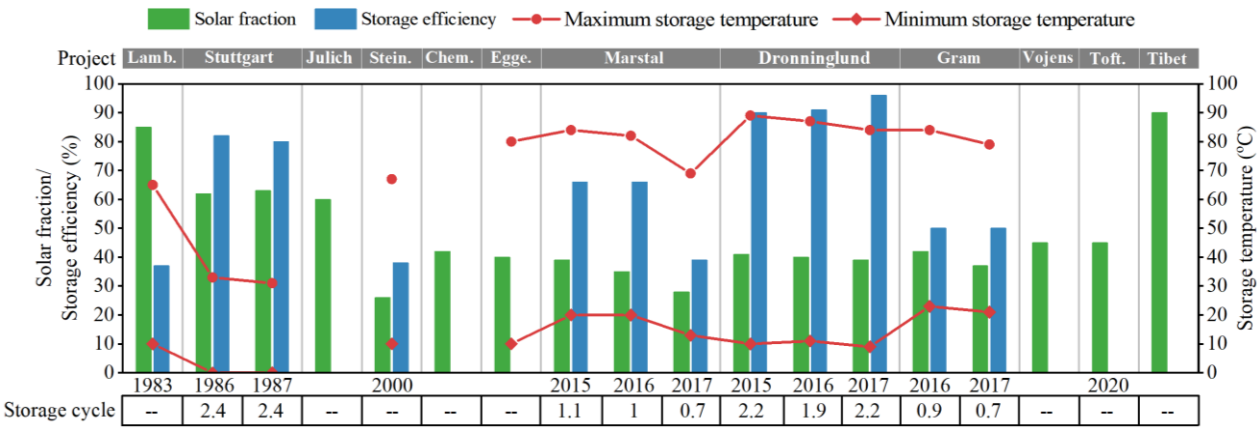

Figure 2.2 Comparison of performance metrics **[Paper 1]**.

2.2 Technical design of PTES

The technical design of PTES plays a crucial role in determining the investment cost. Additionally, it will significantly affect the storage efficiency and stability over its lifetime. The key technical elements that must be considered during the design process are highlighted with a red background in Figure 2.3.

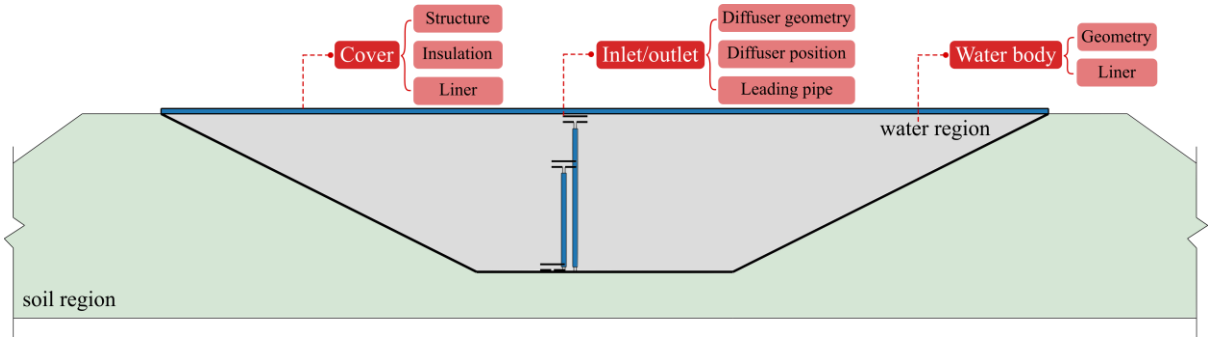

Figure 2.3 Scheme of PTES and its primary technical elements.

2.2.1 The PTES structure

Water Body

Typically, for PTES larger than 10,000 m^3, a slope angle of around 30 is utilized to prevent sidewall collapse [27–30]. However, it is worth noting that the specific slope angle may vary depending on the site conditions, engineering design, and geotechnical factors. Considering the practical challenges related to construction and structural stability, it is suggested that the slope angle should be as high as possible.

To meet the increased PTES volume requirements while avoiding groundwater, more irregular-shaped PTES may be developed, as seen in the case of Toftlund and Vojens PTES systems. However, it is important to note that most current research still focuses on regular water body shapes. One challenge that arises with different PTES geometries is ensuring effective insulation for the side and bottom walls. This presents difficulties in maintaining optimal thermal performance and economic feasibility. As a result, there is a need for more research on irregular body shapes.

Inlet/outlet design

Water entering PTES may cause mixing, which spoils the thermal stratification. To reduce such mixing, inlets/outlets must be carefully designed [31]. Radial diffusers are frequently used as a solution in existing PTES systems since they have benefits such as a simple structure, convenient installation, low cost, and good thermal stratification [32]. However, the diffuser design relies heavily on the experience from small-scale TTES without considering the scaling-up impact. Moreover, the effect of inlet/outlet position and operating parameters on PTES performance has not been fully understood. Therefore, it is necessary to try performing a full-

scale simulation of PTES systems to identify the optimal inlet/outlet designs under real-world conditions.

Cover design

The cover usually consists of three main layers, with an insulation layer in the middle and two liner layers on both sides of the insulation. There are three main technical challenges that need to be addressed in the cover design: insulation and liner materials, moisture removal, and rainwater removal. To maintain the thermal insulation effect of the cover during the long-term application while reducing investment costs, proper structural design, material selection, and installation must be considered.

2.2.2 The materials used for PTES

The envelope of the buried PTES serves vital functions, including minimizing heat losses and maintaining service life. Therefore, the selection of materials for PTES enclosure is essential.

As a summary and comparison of materials investigated for recent PTES systems, Figure 2.4 illustrates the relationship between thermal conductivity and density for insulation materials. It is observed that the insulations have a thermal conductivity within 0.1 W/(m·K) under dry conditions. However, it is difficult to avoid water absorption during actual utilization. Unfortunately, limited information is available regarding the effect of moisture on the thermal conductivity of these insulations, with only four of them showing recorded changes. Notably, the thermal conductivity change after water absorption by expanded glass granules (EGG) appears to be unacceptable high, revealing its infeasibility for practical applications.

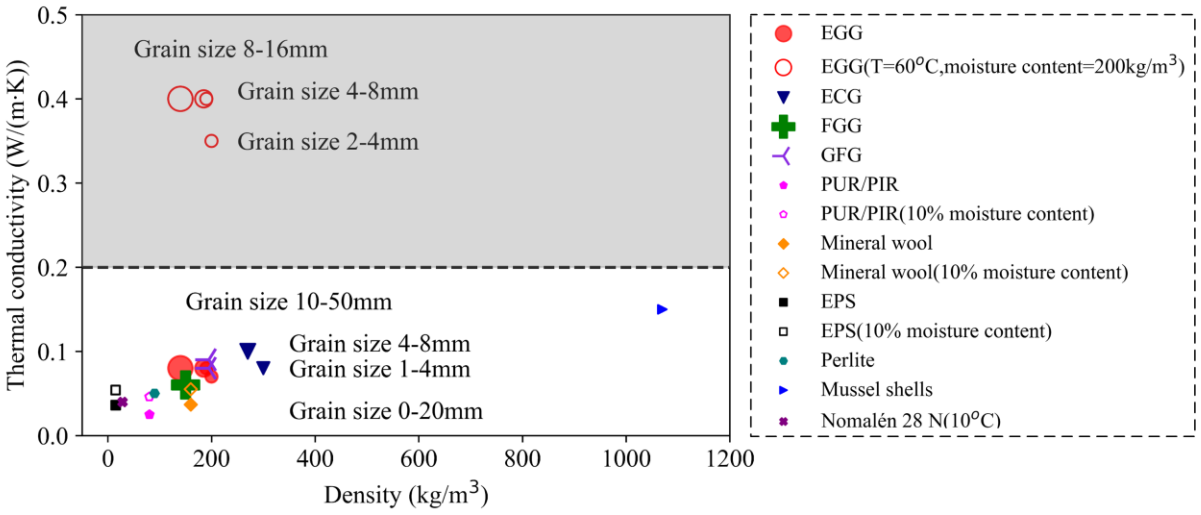

Figure 2.4 Thermal properties of insulation materials mentioned in the literature research **[Paper 1]**.

No specific waterproofing membranes have been developed for buried PTES, so liners used in other areas must be utilized. However, liners produced for other purposes frequently do not meet the high-temperature resistance requirements of PTES systems. Polymeric liners are

widely utilized at present. Figure 2.5 demonstrates that the recorded thermal conductivity of polymeric liners is below 0.6 W/(m·K) and is currently limited to 20°C to 30°C test temperature. Moreover, only three liners' lifetimes at various test temperatures can be collected. The service life of high-density polyethylene (HDPE) and polypropylene (PP) liners appears to decrease with rising temperatures, but research findings are inconsistent, which may be due to differences in experimental parameters and methods.

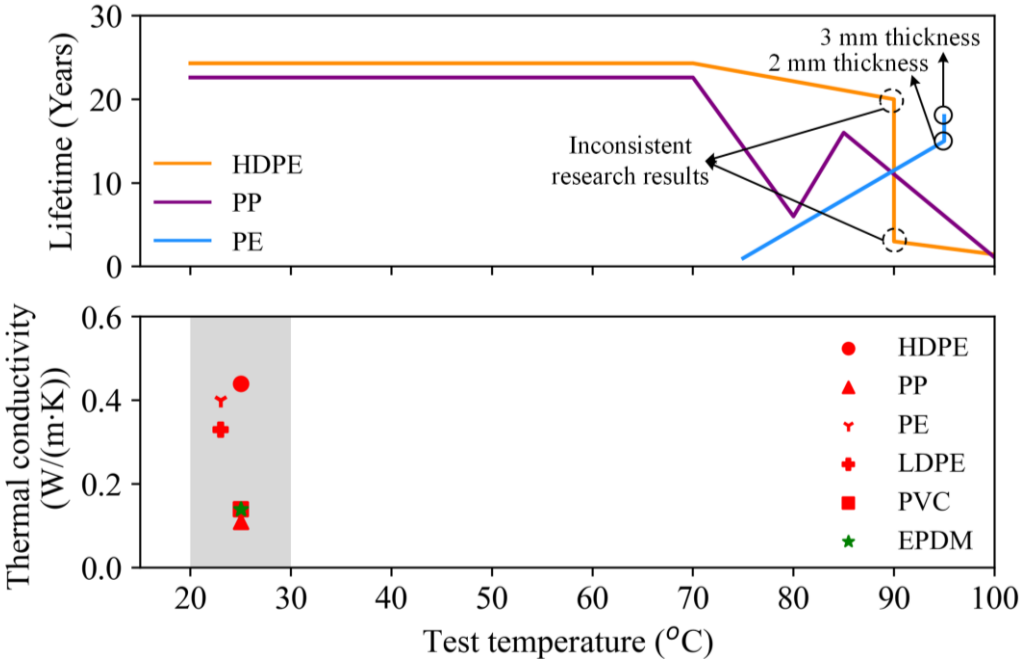

Figure 2.5 Thermal properties and lifetime of liner materials mentioned in the literature research **[Paper 1]**.

In conclusion, developing new insulation materials with low thermal conductivity is essential for minimizing heat losses in PTES systems. It is also desirable to compare various thermal insulation materials in terms of thermal conductivity, durability, water resistance, and installation costs [33]. Future research should focus on exploring novel liner materials (e.g., bentonite, bitumen, geo-membranes, and high-performance concrete [34]), with an emphasis on assessing their long-term durability under temperatures exceeding 90°C. Furthermore, it is vital to consider both the temperature and pH of water when researching liner materials.

2.3 Numerical study of PTES

2.3.1 Component-level modeling

Computational fluid dynamics (CFD) models, such as Fluent, can consider all transport processes that occur in PTES systems. However, finding published three-dimensional (3D) CFD models that are valid for large-scale PTES is challenging. The computational requirements for investigating large-scale PTES are substantial, despite the detailed outcomes provided by CFD models. In this context, there has been an extensive effort to develop coarse models to reduce computational efforts [35].

TRNSYS is widely preferred for modeling PTES because of the validated coarse models, which can be easily integrated at the system level. These simplified models are based on certain assumptions related to geometry, material properties, and boundary conditions. While the TRNSYS models are discretized similarly, they do exhibit some differences. The main differences between the models are summarized in Table 2.2 [36–40]. The stars in Table 2.2 indicate the features that the models can achieve.

For model simplification, most of the current models are simplified to axial symmetry such as cylindrical and truncated cone geometries. Among these models, only Type 1536 can consider actual PTES geometries, such as pyramid stumps. However, it is important to note that there is currently no corresponding soil model that can be combined with Type 1536. This limitation arises from the requirement of setting the soil region to a 3D domain, which greatly increases the challenges of model building.

Moreover, newly developed models, such as Type 1534 + Type 1302 and Type 1535 + Type 1301, incorporate several key features to enhance the calculation accuracy of PTES and soil performance. These features include, but are not limited to the followings:
1) Non-uniform initial temperature distribution in the water and soil regions.
2) Time-varying soil properties.
3) Variable heat transfer coefficients along the PTES sidewall between water and soil regions.
4) Introduction of energy distribution to different nodes through inflow mixing.
However, obtaining data for the third and fourth items through actual measurements is not possible. In this context, it is necessary to determine these parameters using full-scale 3D models simulations.

2.3.2 System-level modeling

There are relatively few studies available. This can be attributed to a couple of reasons. Firstly, the calculation accuracy of PTES models is still insufficient, which often leads to larger deviation when conducting system simulations. Additionally, the high dynamic and computational complex of SDH system integrated PTES presents significant challenges in system-level modeling.

In conclusion, the current stage of numerical studies for PTES has not yet reached a mature level. Therefore, there are several potential directions for future research in the numerical analysis of PTES, especially in developing sophisticated models that consider geometrical suitability and geological conditions. Additionally, it would be more meaningful to assess the performance and applicability of recent models by employing the same settings and boundary conditions. Moreover, making full use of the characteristics and capabilities offered by different simulation platforms could help improve the accuracy of existing models. Furthermore, there is a strong need for system-level investigation to determine the optimum system design and operation strategies for PTES systems [41].

Table 2.2 Comparison of the TRNSYS models.

Model characteristics		Type 342	Type 343	Type UGSTS	Type 1534 +Type 1302	Type 1535 +Type 1301	Type 1536
PTES geometry	Cylinder	★	★	★	★	★	
	Truncated cones		★	★		★	
	Pyramid stumps						★
Nodes size	Equal size	★	★	★	★	★	★
	Unequal size		★				
Inlet modes	Max. ports number	6	6	2	5	10	10
	Specified nodes position	★	★	★	★	★	★
	Closed temperature nodes				★	★	★
	Inflow fractioned nodes				★	★	★
Initial water temperature	Uniform	★	★	★	★	★	★
	Stratification			★	★	★	★
Water - soil collaboration	Separated				★	★	
	Combined	★	★	★			
	Constant heat transfer coefficient	★	★	★	★	★	
	Various heat transfer coefficients				★	★	
Initial soil temperature	Uniform				★	★	
	Stratification				★	★	
Soil thermal properties	Uniform	★	★	★	★	★	
	Various				★	★	
	Groundwater flow						
Energy balance	Thermal conductivity of adjacent nodes	★	★	★	★	★	★
	Fully mix temperature inversions	★	★	★	★	★	★
	Mixing rate for inversion of adjacent layers				★	★	★
Numerical solution scheme		DIFFEQ	DIFFEQ	DIFFEQ	DIFFEQ	DIFFEQ	DIFFEQ

3

Model description and validation

For designing and planning solar district heating (SDH) plants with pit thermal energy storage (PTES), integrated dynamic system simulation is crucial. The accuracy of the PTES model used in such simulations can have a significant impact on the calculated results and consequently influence design decisions [42]. In this context, an accurate and fast computing PTES model is required.

However, it should be noted that recent simplified one-dimensional (1D) PTES models often fail to consider certain important factors, such as inflow buoyancy, inflow mixing, enhanced natural convection along the PTES sidewalls. As a result, these models may not provide a high level of accuracy in representing the actual PTES system behavior.

Considering the limitations of the 1D models in capturing the three-dimensional (3D) features of a PTES system, a full-scale 3D PTES mode has been developed based on the Dronninglund PTES. The purpose of this 3D model is to gain deeper insights into the PTES behavior under transient conditions and provide valid correlations that can help enhance the accuracy of low-order models.

The chapter is structured as follows: Section 3.1 briefly introduces the Dronninglund project and emphasis the actual operation during a typical year. Section 3.2 provides a detailed description of the Dronninglund PTES. Subsequently, the developed 3D PTES model utilized throughout this thesis is presented in Section 3.3. Finally, Section 3.4 shows the model validation for different investigation scenarios.

3.1 The Dronninglund SDH plant

The Dronninglund project has been demonstrated as the most successful large-scale solar district heating (SDH) plant with PTES. Figure 3.1 shows a schematic diagram of the Dronninglund SDH. The system comprises several key components, including two solar collector fields with a total aperture area of 35,573 m^2, a 60,000 m^3 (PTES), and an absorption heat pump [43].

When the heat supply exceeds the heat demand, heat from the solar collector fields is charged into the PTES. When the heat supply is lower than the heat demand, the PTES is discharged. If the PTES temperature is high enough, water is extracted from the PTES top and directly utilized for the district heating grid. However, if the PTES temperature is too low for direct use, the heat pump extracts heat from the PTES, thereby achieving high storage efficiency [26].

Moreover, the system is equipped with a combined heat and power plant fed by four gas engines, a bio-oil boiler, and a natural gas boiler to supply the remaining heat requirements [28]

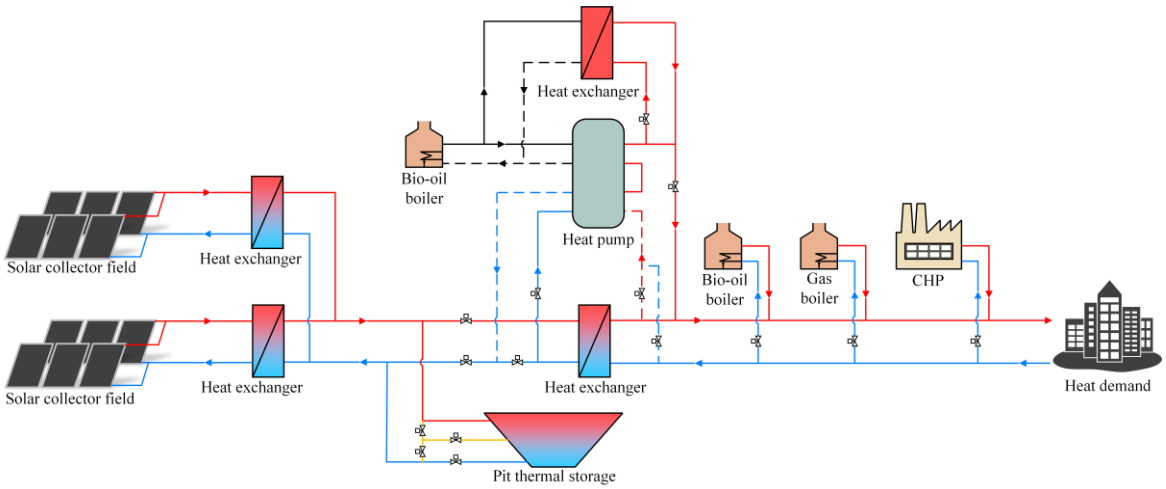

Figure 3.1 A simplified schematic of the Dronninglund solar district heating plant **[Paper 3]**.

To further demonstrate the actual operation status of the Dronninglund SDH system, a Sankey diagram is presented in Figure 3.2. This diagram summarizes the energy flow based on measurements during a typical operating year (2017). It is indicated that the overall system can meet around 70% of the heat demand using renewable energy sources [26]. Approximately 27% of the heat from the solar collector is directly supplied to the district heating grid, satisfying immediate heating requirements. The remaining heat is stored in the PTES for later use. Notably, a solar fraction of 40% is reached by integrating the PTES into the system.

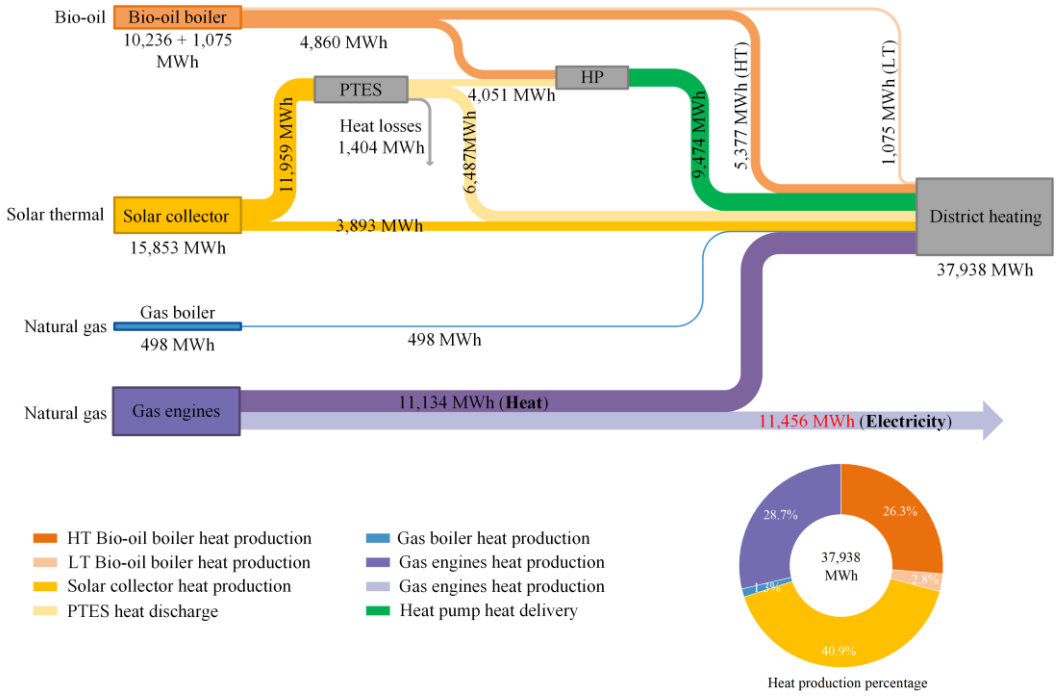

Figure 3.2 Sankey diagram of the major energy flows in the Dronninglund SDH plant in 2017 (the heat losses of the transmission are not shown due to the lack of measurements).

3.2 The Dronninglund PTES

3.2.1 The PTES description

The PTES is partly constructed as a truncated pyramid stump above the ground level. The total depth of the PTES is 16 m, 4.3 m above the ground level as indicated in Figure 3.3. The top surface has outer dimensions of 90 m × 90 m, and the bottom surface measures 26 m × 26 m [44,45]. To prevent sidewall collapse, the sidewalls have a slope of 26.6º.

On the top of the PTES, there is a floating lid that consists of five layers, arranged from top to bottom: a 1.5 mm HDPE Geomembrane, a 3 mm Hypernet CN-E, a 240 mm Nomalén insulation, a 3 mm Hypernet HF-E, and a 2 mm HDPE Geomembrane. For the side and the bottom wall, a 2.5 mm HDPE Geomembrane layer and a fabric layer are used to enclose the water [20].

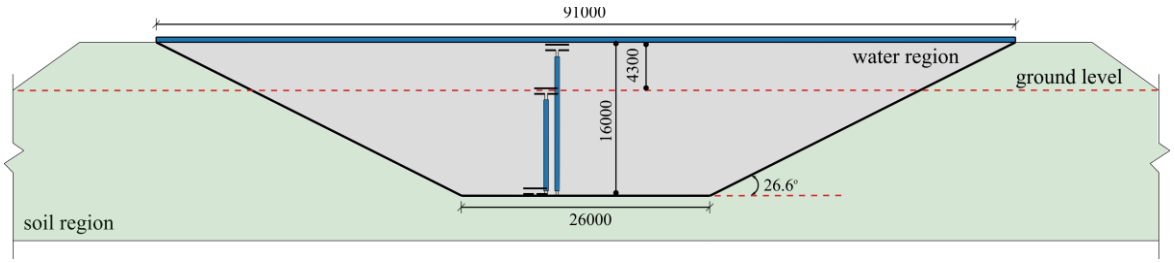

Figure 3.3 Schematic of Dronninglund PTES **[Paper 4]**.

PTES is typically designed large enough to accommodate long-term storage needs. To maintain thermal stratification inside PTES, the uniform introduction of water at different temperatures is crucial [46,47]. In this end, three diffusers are installed at different levels within the PTES: the top, middle, and bottom. Figure 3.4 illustrates the position of these diffusers. The top diffuser is located near the PTES top, while the bottom diffuser is near the PTES bottom. Each diffuser is equipped with two radial discs with a diameter of 2.5 m [48,49].

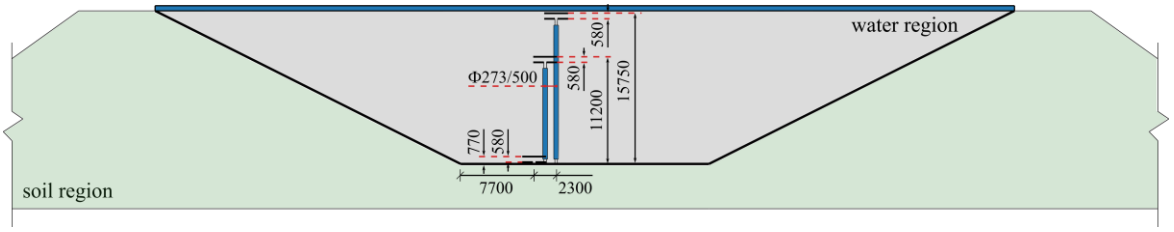

Figure 3.4 Illustration of the inlet/outlet pipes arrangement inside the PTES.

3.2.2 Measurement and uncertainty

To effectively monitor the PTES's behavior, several sensors have been mounted inside and around the PTES [26,50]. Figure 3.5 depicts the arrangement of the temperature sensors. A total of 32 temperature sensors are installed inside the PTES, one is located 0.1 m below the insulating cover, and the other 31 are evenly spaced at 0.5 m intervals from the bottom to the

top. Additionally, two temperature sensors are placed on the top and bottom surfaces of the insulating cover, respectively.

To assess the thermal behavior of the surrounding environment, four temperature sensors are placed in the soil at a depth of 10 m, 15 m, 20 m, and 25 m on the north side of the PTES. Furthermore, three temperature sensors and three flow meters are installed in the pipes (sections in the technical building) connected to the three diffusers. It is worth mentioning that the flow meters measure both direction and flow rate.

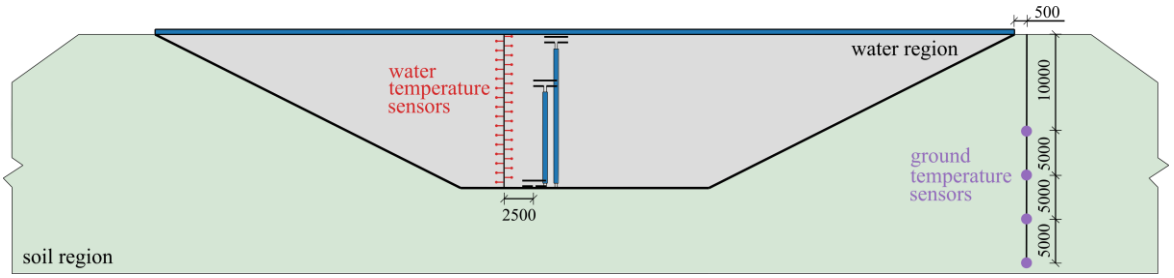

Figure 3.5 Scheme diagram of monitoring sensor positions **[Paper 4]**.

The temperature sensors are Class A PT100, with an accuracy of ±0.15 K [51]. Electromagnetic flow meters are employed to measure the volume flow rate, and their accuracy is ±0.4% [52]. All the measurements are recorded at 10-minute intervals.

3.3 The three-dimensional CFD model

A 3D model of the experimental geometry presented in Section 3.2 was developed in ANSYS 2019 R2. As illustrated in Figure 3.6 (a), the model includes the water and soil regions. It is important to highlight that the soil region was created sufficiently large to minimize the impact of soil boundaries on soil temperature variation near the water body. The soil region was divided into two parts at the height of 17 m. In this case, different soil properties according to the geological investigation can be considered.

The structured mesh was adopted in the model with a maximum mesh skewness of 0.82. Notably, a boundary layer was added along the sidewalls of the water body to enhance the accurate representation of heat transfer between the water and soil regions. Given that the grid distribution within the PTES plays a crucial role in the PTES temperature calculation, a grid refinement analysis was performed.

Chapter 4 presents a comprehensive analysis of the grid distribution. Finally, a mesh density of 1.6 million cells, with a good compromise between accuracy and calculation time was selected for the detail investigations in this thesis.

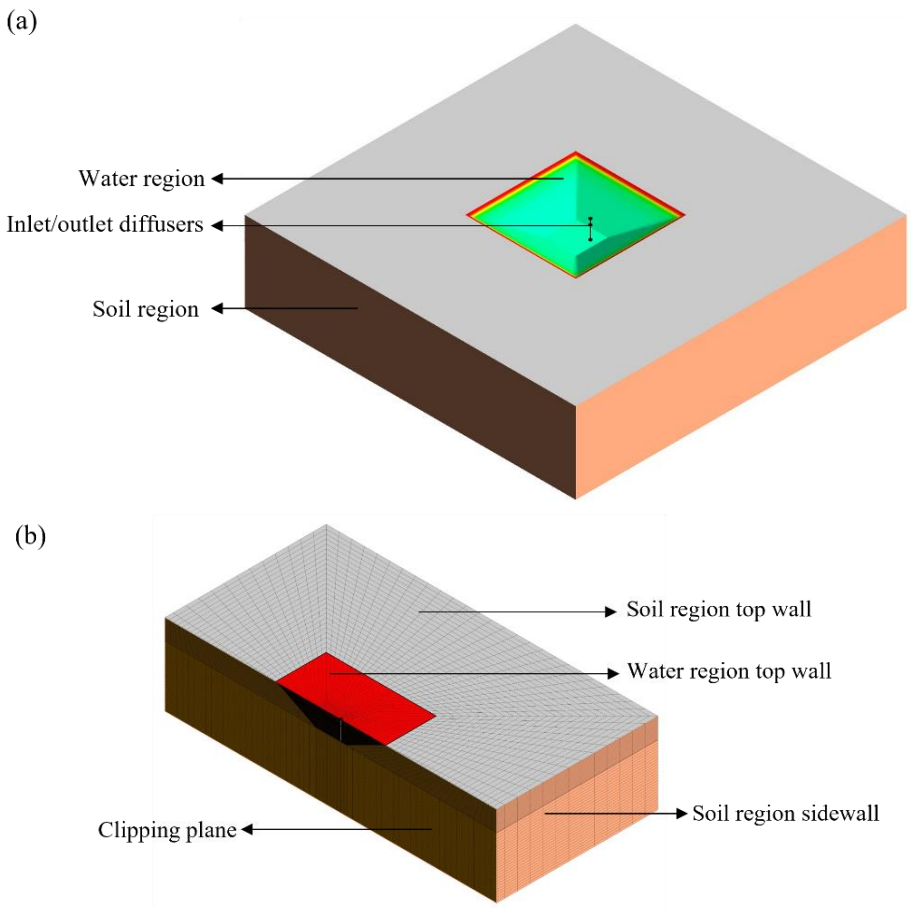

Figure 3.6 3D CFD model: (a) Model diagram; (b) Grid scheme (the clipping plane is positioned through the center of the diffusers to show the mesh inside the model) **[Paper 3]**.

3.3.1 Mathematic model

In the model, the water region was considered an incompressible fluid with temperature-dependent thermophysical properties. The upper and lower soil regions were assumed to have constant thermal properties. To reduce computational efforts, the model did not consider groundwater flow.

The 3D conservations of the flow and heat transfer in the water and soil region are defined as follows [53]:

$$\nabla \cdot (\rho_w \vec{u}) = 0 \tag{3.1}$$

$$\frac{\partial(\rho_w \vec{u})}{\partial t} + \nabla \cdot (\rho_w \vec{u}\vec{u}) = -\nabla p + \nabla \cdot \tau_w - \rho_w g \tag{3.2}$$

The enthalpy equation of the water region and soil are shown in Eq. (3.3) and (3.4).

$$\frac{\partial(\rho_w C_{p.w} T)}{\partial t} + \nabla \cdot (\rho_w C_{p.w} \vec{u} T) = \nabla \cdot (\lambda_w \cdot \nabla T) \tag{3.3}$$

$$\rho_s C_{p.s} \frac{\partial T}{\partial t} = \lambda_s \nabla^2 T \tag{3.4}$$

Where ρ_w and ρ_s indicate the density of water and soil; u is the velocity of water; $C_{p.w}$ and $C_{p.s}$ represent the specific capacities of water and soil; λ_w and λ_s are the thermal conductivity of water and soil; τ_w presents the stress tensor of water.

The realizable k-ε model was selected due to its ability to more accurately predict the spreading rate of round jets [53,54]. The transport equations in the model for the kinetic energy k and the dissipation rate ε are given as Eq. (3.5) and (3.6).

$$\frac{\partial(\rho_w k)}{\partial t} + \nabla \cdot (\rho_w k U) = \nabla \cdot \left[\left(\mu_w + \frac{\mu_t}{\sigma_k}\right) \cdot \nabla(k)\right] + G_k + G_b - \rho\varepsilon \quad (3.5)$$

$$\frac{\partial(\rho_w \varepsilon)}{\partial t} + \nabla \cdot (\rho_w \varepsilon U) = \nabla \cdot \left[\left(\mu_w + \frac{\mu_t}{\sigma_\varepsilon}\right) \cdot \nabla(\varepsilon)\right] + C_{1\varepsilon}\frac{\varepsilon}{k}C_{3\varepsilon}G_b - C_2\rho_w \frac{\varepsilon^2}{k+\sqrt{\frac{\mu_w}{\rho_w}\varepsilon}} \quad (3.6)$$

The turbulence constants $C_{1\varepsilon} = 1.44$, $C_2 = 1.9$, $\sigma_k = 1.0$, and $\sigma_\varepsilon = 1.2$ are established [53].

The governing equations were solved within each cell using a SIMPLE pressure-velocity coupling scheme. The spatial discretization settings were applied as follows: PRESTO for pressure, second-order upwind for momentum, and second-order upwind for energy. The respective relaxation factor values were set to 0.3 for pressure, 0.8 for density, 0.7 for momentum, and 0.95 for energy. In terms of convergence criteria, a tolerance level of 10^{-6} was set for energy calculation, while for velocity, continuity, and other variables, it was kept at 10^{-3}.

3.3.2 Thermal properties and boundary conditions

Water was used as the heat storage media inside PTES. The following correlations provide the temperature dependence of the density, dynamic viscosity, thermal conductivity, thermal expansion coefficient, and specific heat capacity of water, respectively [55,56], where T is temperature in Kelvin.

Density, [kg/m^3] $$\rho_w = 863 + 1.21 * T - 2.57 * 10^{-3} * T^2 \quad (3.7)$$

Dynamic viscosity, [kg/m·s]

$$\mu_w = 9.67 * 10^{-2} - 8.207 * 10^{-4} * T + 2.344 * 10^{-6} * T^2 - 2.244 * 10^{-9} * T^3 \quad (3.8)$$

Thermal conductivity, [W/m·K] $$\lambda_w = 3.75 * 10^{-1} + 8.84 * 10^{-4} * T \quad (3.9)$$

Specific heat, [J/kg·K] $$C_{p.w} = 4432.6 - 1.819 * T + 3.3 * 10^{-3} * T^2 \quad (3.10)$$

In addition, Table 3.1 presents the soil properties and other solid material properties utilized in this study based on geological surveys and model parameter debugging.

Table 3.1 Physical properties of solid materials used in the numerical model [57–64] **[Paper 2].**

Material	Density [kg/m^3]	Thermal conductivity	Specific heat

		[W/m·K]	[J/kg·K]
Soil (upper part)	1840	1.8	900
Soil (lower part)	2200	2.3	1800
Nomalén 28N	28	0.06	2857
HDPE	940	0.4	1900
HF-E	940	0.4	1900
Stainless Steel	7600	15	490

For each detailed study, the temperature distribution during the actual operation was adopted as the initial condition for the simulation period. Measured operating conditions, including inlet/outlet temperature, flow rate, and ambient temperature, were considered the boundary conditions. More details can be given to the relevant investigation documented in this thesis.

3.4 Investigation scenarios and validation

Figure 3.7 shows the models used in different research scenarios and highlights the corresponding research objectives. It is crucial to employ a full-scale model when investigating the heat transfer characteristics and assessing the inlet mixing to accurately capture the 3D phenomenon. However, when studying the interaction between the water and soil regions, conducting long-term calculations becomes necessary. Considering the computational efficiency, two simplifications were made in this study. Firstly, the turbulent model was replaced by the laminar model. Secondly, the inlet/outlet was moved to the center within the PTES, allowing for the transfer of the full-scale model to a one-quarter model.

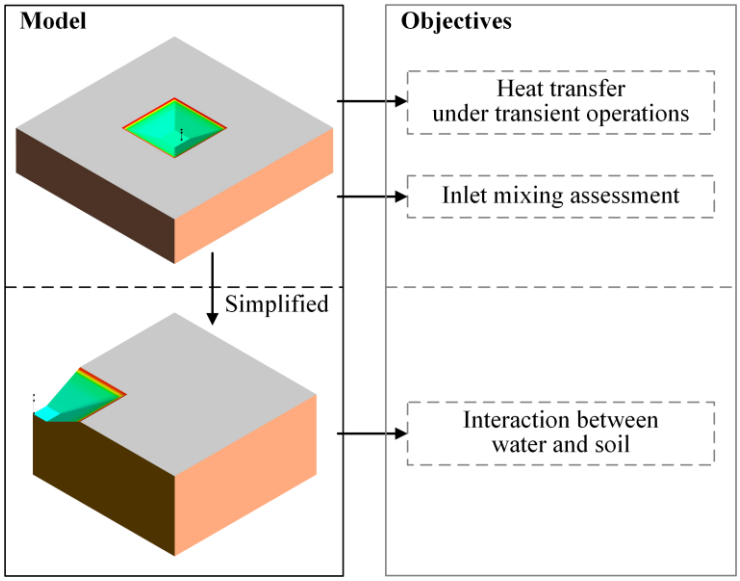

Figure 3.7 Investigation scenarios and their corresponding research objectives.

Given the computational complexity of such a large-scale model, validation was performed using different timescales for various research aspects. It is important to emphasize that uncertainties may arise from both the measurements and the modeling approach.

3.4.1 Short-term validation

Four representative cases in 2017 were selected to evaluate the accuracy of the full-scale 3D model to study the heat transfer and flow characteristics inside the PTES. These cases, namely January 5th, March 15th, June 2nd, and September 1st, exhibit different PTES temperature distributions and charging/discharging characteristics.

Figure 3.8 displays the calculated and measured temperature development inside PTES every six-hour each day. Notably, there is a remarkable agreement between the calculated and measured PTES temperature for January 5th and September 1st. On January 5th, the maximum temperature difference along the PTES height is within 0.5 K, while on September 1st, it is 1 K.

However, there is a noticeable temperature difference above 14 m on March 15th and June 2nd. Specifically, the temperature difference from 18:00 on March 15th is less than 2 K, while the temperature difference throughout the day on June 2nd is less than 5 K. Two reasons explain the larger temperature difference observed on March 15th and June 2nd. First, in the CFD calculation, the monitored temperature points inside PTES are assumed to be fixed. However, the temperature sensors' position may have an uncertainty of ±0.3 m. Second, there is a considerable temperature difference within a smaller thickness above 14 m. In this situation, having only two measurement points cannot accurately reflect the actual temperature distribution over such a small thickness.

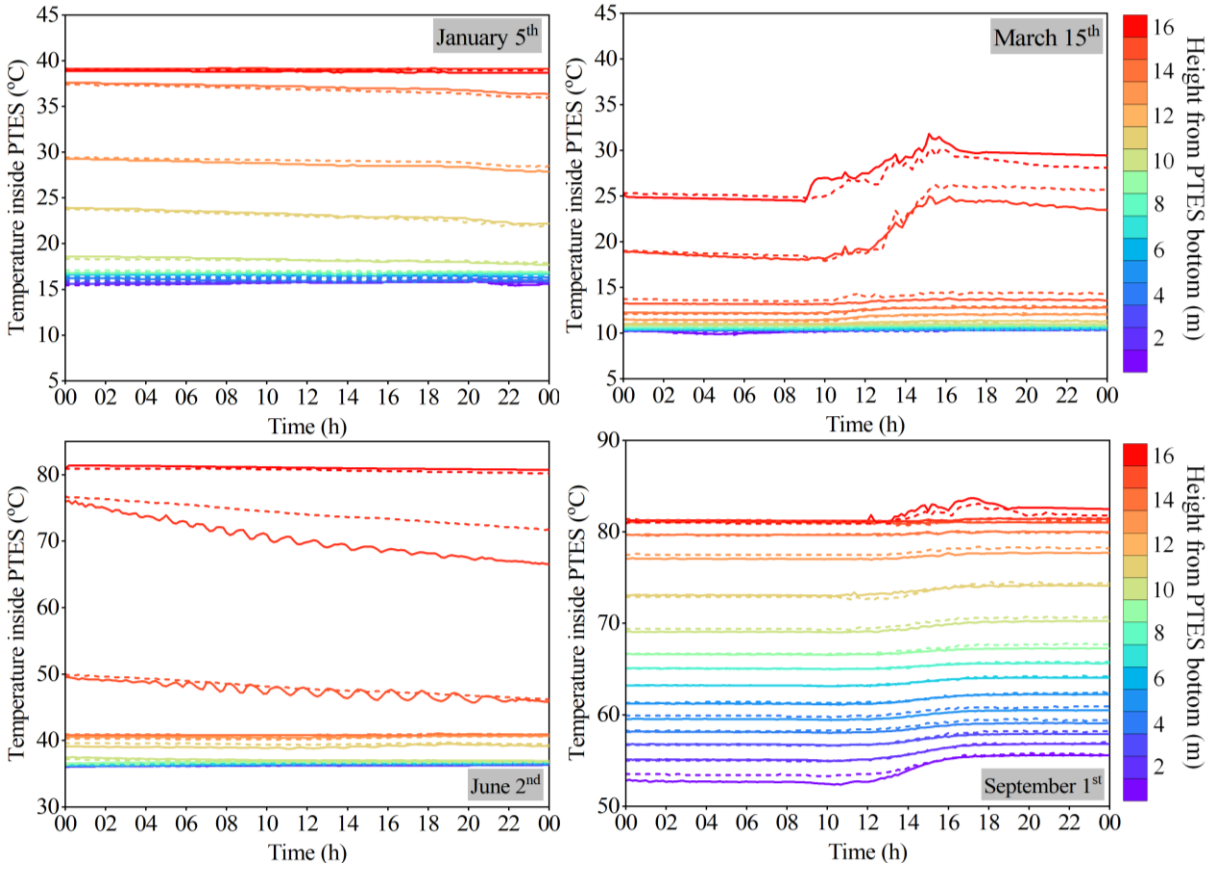

Figure 3.8 Comparison of calculated and measured PTES temperatures for representative days **[Paper 2]**.

Figure 3.9 compares the operation conditions regarding inlet/outlet temperature and inlet/outlet mass flow rate. The results demonstrate a high level of agreement between the calculated and measured values. Only slight differences in the inlet/outlet temperature can be observed, which can be attributed to uncertainties in the operation measurements.

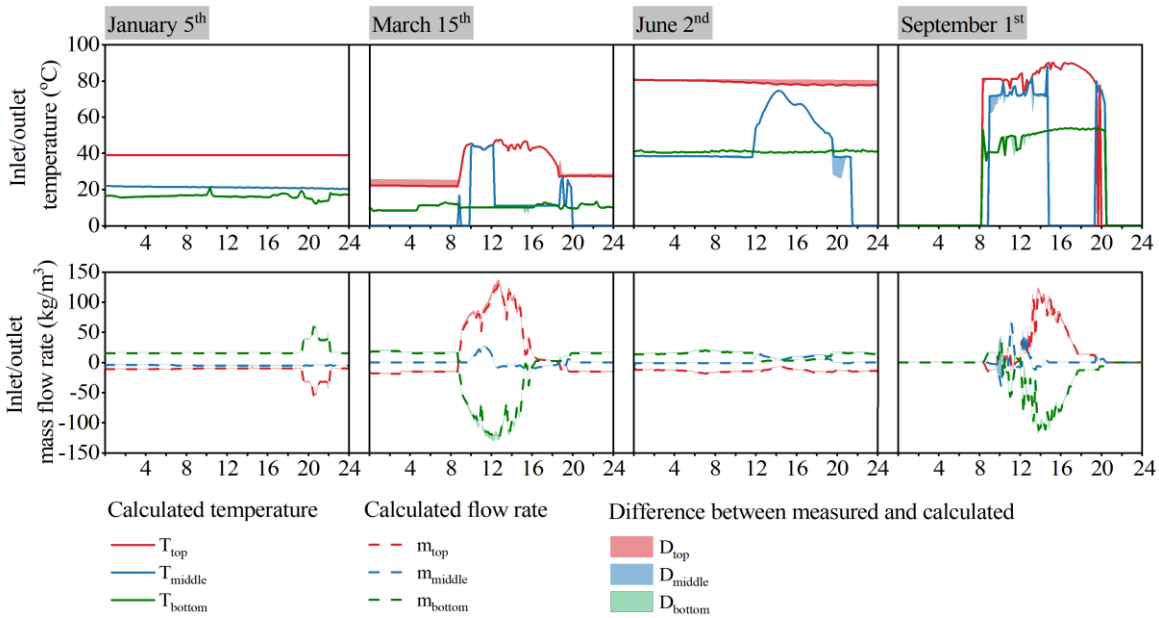

Figure 3.9 Comparison of charging/discharging conditions with 10 min resolution **[Paper 2]**.

3.4.2 Long-term validation

The long-term validation is based on the simplified one-quarter model to save computational resources. It is worth mentioning that the grid distribution of the one-quarter model is consistent with the full-scale model.

Figure 3.10 compares PTES temperature distribution and soil temperature variation throughout the year. The calculated PTES temperature agreed well with the measurements for the entire year, except for a significant temperature difference observed at the position above 14 m from February to June. This discrepancy aligns with the findings from the short-term validation.

For the soil temperature, the discontinuity in the measurement results is due to a hardware failure of the SCADA system [26]. The maximum differences between the measured and calculated soil temperatures at 10 m, 15 m, 20 m, and 25 m are 2 K, 1.8 K, 1.6 K, and 0.8 K, respectively. These differences can be explained by the variations in soil thermal properties caused by changes in soil moisture content over time.

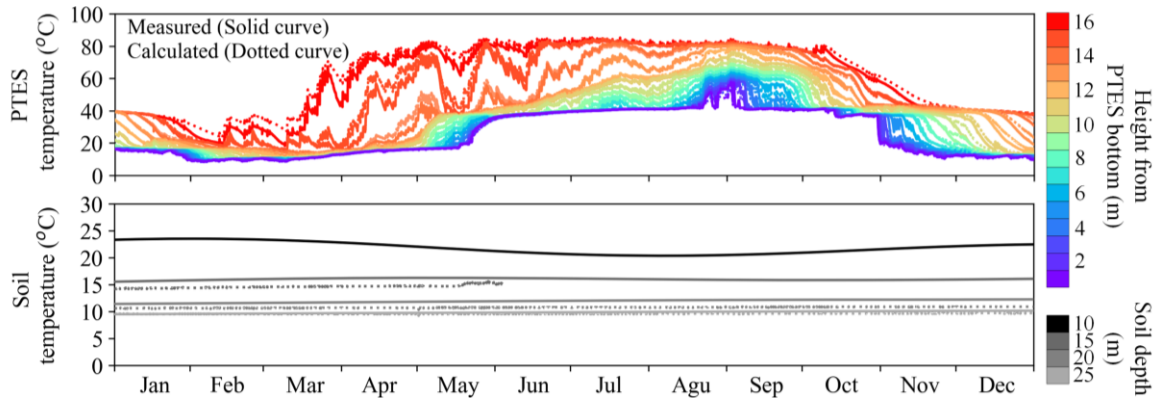

Figure 3.10 Comparison of PTES temperature and soil temperature with 10min resolution **[Paper 4]**.

Overall, the full-scale 3D model proves sufficient in predicting the thermal performance of a large-scale PTES. Additionally, the one-quarter model demonstrates its capability to perform dynamic simulations for the entire year within a reasonable calculation time. Therefore, these models can contribute to a comprehensive understanding of the dynamic characteristics of PTES.

4

Heat transfer inside the PTES

Pit thermal energy storage (PTES) mainly utilizes water as the storage material. Similar to other water-based heat storage systems, PTES achieves stratification through temperature-driven density differences. A high level of thermal stratification is beneficial for improving PTES efficiency. The study of stratification gained popularity in the 1970s and remains an active research topic today [65]. This research has led to the development of various models and techniques for better predicting and understanding the behavior of stratified storages.

To reduce computational complexity, simplified models are often employed. These models typically assume one-dimensional temperature profiles within the storage, neglecting radial variations in temperature. However, a significant issue with this approach is numerical diffusion resulting from the assumption that each node within the storage is fully mixed. In Section 2.3, it was discussed that recent models built in TRNSYS for PTES adopt a multi-node method. By introducing artificial mixing at different time steps, significant numerical diffusion can be observed when a small number of nodes are used. In this regard, it is recommended to specify a large number of nodes for the thermocline region to observe the changes in the level of stratification with time [66].

Although increasing the nodes' number can help minimize numerical diffusion, it often leads to longer computational times, which is not desired. As a result, there is a trade-off between achieving accurate results and computational efficiency in the PTES modeling. It is worth noting that most investigations on numerical diffusion minimization have been conducted on small-scale water storage tanks with two inlets/outlets [67]. The thermal stratification observed in such systems may differ from that in large-scale PTES. Thus, determining the optimal number of nodes to achieve satisfactory results without significantly increasing computational efforts for PTES investigation remains uncertain.

Therefore, the research presented in this chapter aims to address the question '*What grid size can achieve improved calculation accuracy without a significant increase in computation time?'* and *'Whether a criterion that can be used for the guidance of selecting appropriate grid sizes?'*. Through this research, valuable insights can be gained regarding the impact of grid size on calculation accuracy and computation time in PTES modeling. Ultimately, it will contribute to facilitating the selection of appropriate grid sizes for future PTES investigations.

4.1 Investigation method and cases

The full-scale 3D CFD model described in Section 3.3 was utilized to analyze the heat transfer characteristics within the PTES. To capture a comprehensive understanding of the system's performance, four representative days were carefully selected. The characteristics of these days, including the initial PTES temperature distribution and operation conditions over the entire day are illustrated in Figure 4.1.

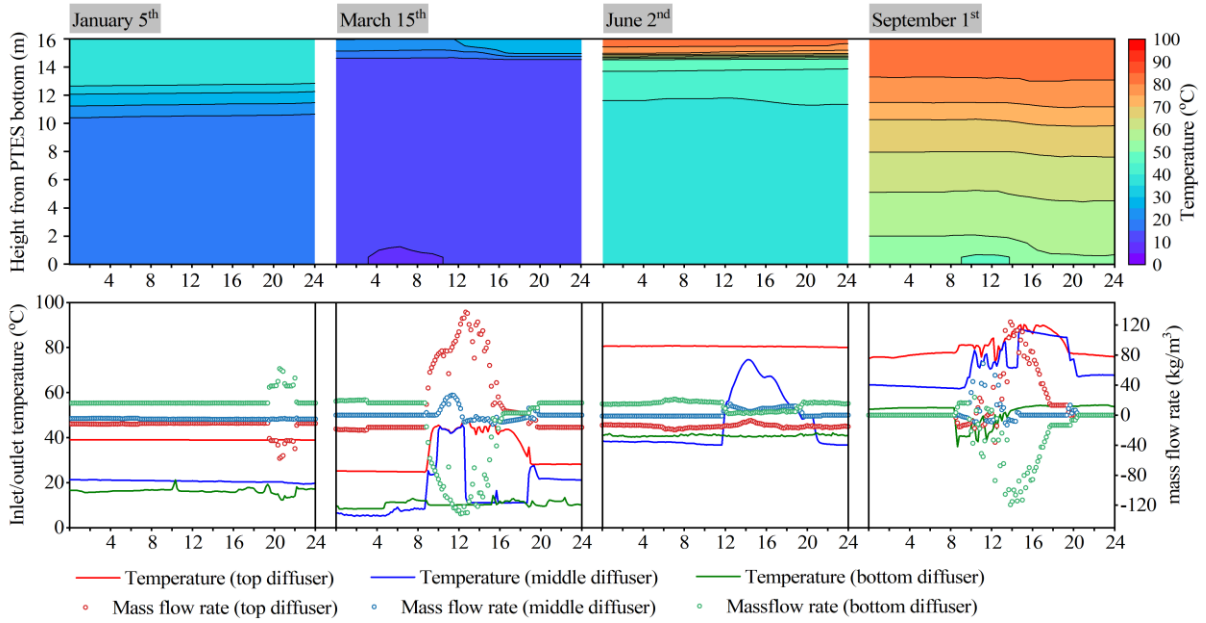

Figure 4.1 The characteristics of four representative days for investigating heat transfer inside the PTES **[Paper 2]**.

To compare the calculated and the measured values during the simulation period, the root mean square deviation (RMSD) is used. RMSD is defined by Eq. (4.1).

$$\mathrm{RMSD} = \sqrt{\frac{1}{N}\sum_{i=1}^{N}\left(P_{calc,i} - P_{meas,i}\right)^2} \tag{4.1}$$

Where $P_{calc,i}$ and $P_{meas,i}$ are the calculated and the measured parameters logged every 10 min, respectively. N denotes the total number of values obtained for the simulation period.

4.2 Grid size sensitive analysis

A grid size sensitive analysis was conducted to emphasize the primary heat transfer phenomena occurring within PTES under transient conditions. It was found that the grid density in the x/y direction had a negligible effect on the temperature calculation accuracy, whereas the grid size in the z-direction (vertical direction) had a significant impact on the PTES temperature calculation accuracy.

Figure 4.2 illustrates the PTES temperature distribution calculation accuracy under various grid sizes using root mean square deviation (RMSD). Notably, the thermocline region is

distinguished by a grey background. Additionally, an arrow indicates the maximum change in RMSD as the grid density increases. It is evident that the grid size has a negligible effect on temperature calculation accuracy in non-thermocline regions. The RMSD for non-thermocline heights remains below 0.5 K over a 24-hour simulation period. However, within the thermocline region, the grid size has a noticeable impact on the temperature calculation accuracy, and the effect varies for different cases.

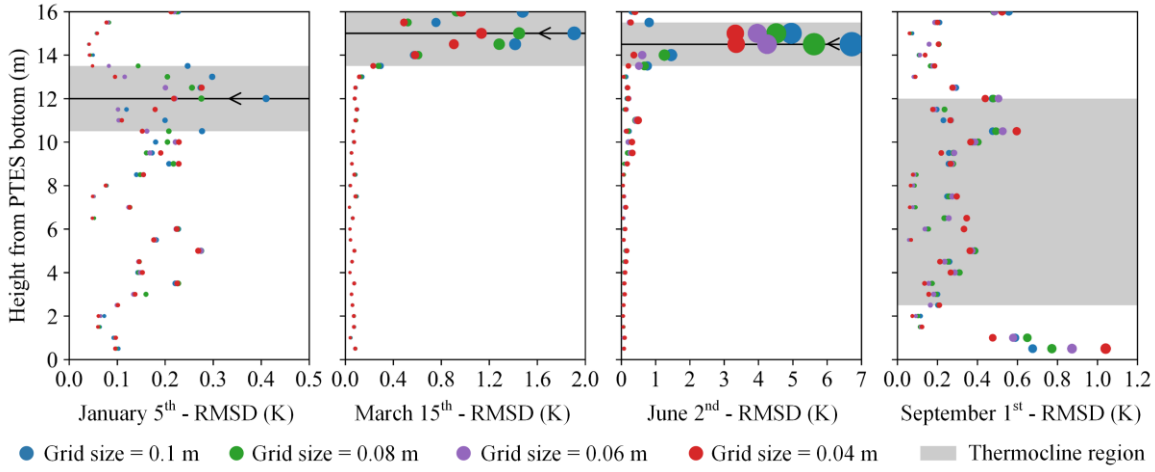

Figure 4.2 Impact of grid size on the PTES temperature calculation accuracy (the dot size corresponds to the value of RMSD, meaning that larger dots represent higher RMSD values, while smaller dots indicate lower RMSD values) **[Paper 2]**.

Together with Table 4.1, it can be concluded that the primary factor affecting the accuracy of PTES temperature calculation is the thermocline's temperature rather than its position. This finding is particularly relevant when comparing the cases of March 15th and June 2nd. Despite both dates having a similar thermocline position ranging from 13.5 m and 16 m, the RMSD for June 2nd is around three times that of March 15th. This discrepancy can be attributed to more significant temperature differences within the thermocline region.

Table 4.1 Thermocline characteristics for the representative cases **[Paper 2]**.

Case	Time	Thermocline characteristics		
		Thermocline thickness (m)	Thermocline temperature difference (K)	Thermocline temperature gradient (K/m)
January 5th	0:00 – 24: 00	3.5	18.8	5.4
March 15th	0:00 – 16: 00	2.5	10.5	4.2
	16:00 – 24: 00	1.8	13.8	7.7
June 2nd	0:00 – 24: 00	2	31.4	15.7
September 1st	0:00 – 24: 00	9.5	21	2.2

4.3 Grid size determination criteria

Based on the analysis conducted in Section 4.1, the temperature gradient ($R_{\Delta T/\delta}$) is proposed as a metric to guide the selection of appropriate grid sizes for 1D models. The recommended grid sizes can be summarized in Table 4.2 to achieve a higher calculation accuracy, depending on $R_{\Delta T/\delta}$.

Table 4.2 Recommended grid size depending on $R_{\Delta T/\delta}$ **[Paper 2]**.

Recommended grid size (m)	Applicable temperature gradient range (K/m)
0.1	$R_{\Delta T/\delta} \leq 5$
0.06	$5 < R_{\Delta T/\delta} < 7$
0.04	$R_{\Delta T/\delta} \geq 7$

The grid size determination criteria reveal that a higher temperature gradient of the thermocline requires a smaller grid size, in other words, a higher number of grid points in the 1D models. However, it is vital to strike a balance with the grid size, as it should neither be too coarse nor too fine. The recommended grid sizes balance these factors, optimizing accuracy while keeping computational expenses within reasonable limits.

4.4 Application of the grid size determination criteria

4.4.1 Yearly thermocline characteristics of Dronninglund PTES

Based on the proposed grid size determination criteria in this study, three-year thermocline characteristics of the Dronninglund PTES were studied. The primary object was to obtain the optimal grid size distribution for effectively investigating the Dronninglund PTES using 1D models.

Figure 4.3 provides an overview of the yearly development of thermocline characteristics in terms of thermocline position, thickness, and temperature gradient for the Dronninglund PTES from 2015 to 2017. It can be observed that when $R_{\Delta T/\delta} \geq 7$ K/m, the thermocline position is above 13 m most of the time. When 5 K/m $< R_{\Delta T/\delta} < 7$ K/m, the thermocline position is generally between 9 m to 13 m.

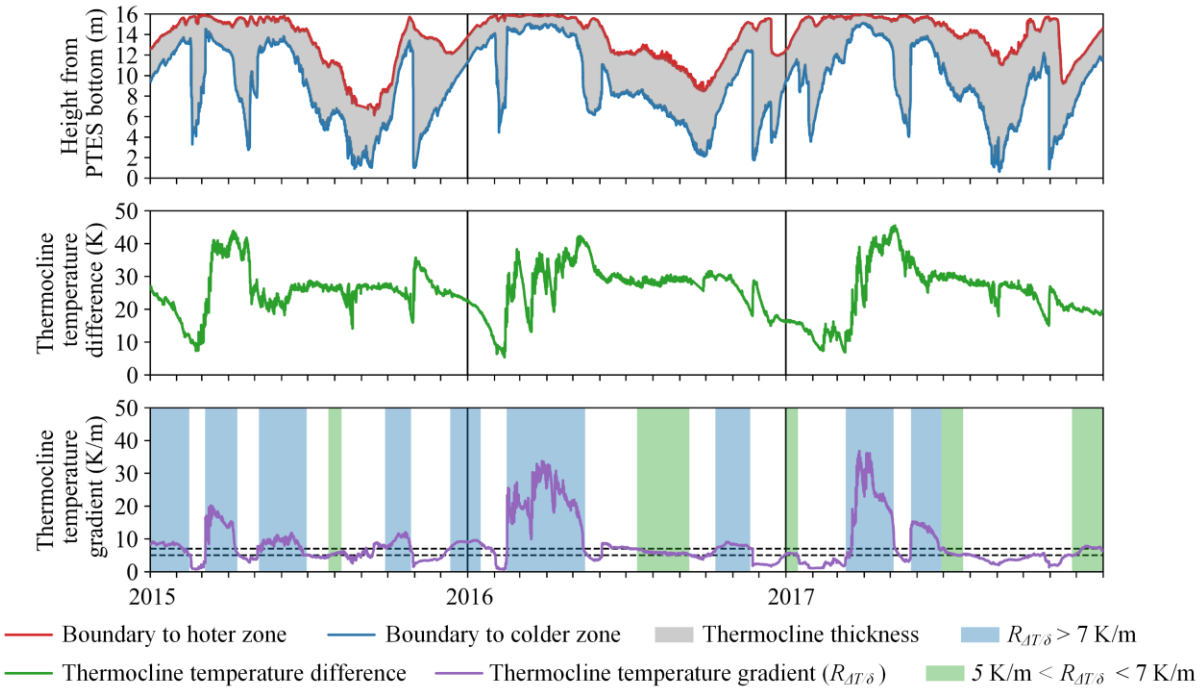

Figure 4.3 Variation of thermocline position, thermocline temperature differences, and thermocline temperature gradient.

Therefore, the suggested grid sizes for various heights in the 1D model used for the Dronninglund PTES investigation are shown in Figure 4.4. A grid size of 0.04 m should be used above a height of 13 m, a grid size of 0.06 m between 9 m and 13 m height, and below 9 m, the grid size should be 0.1 m.

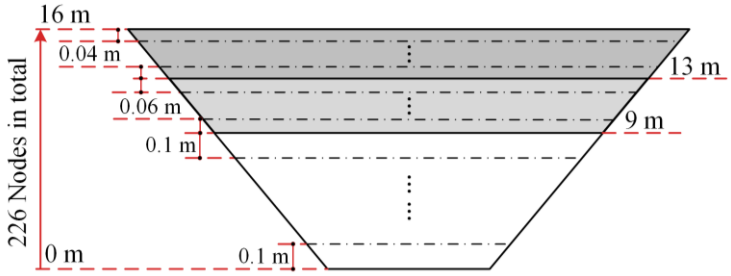

Figure 4.4 The recommended grid size distribution for Dronninglund PTES investigation.

4.4.2 Analysis scenarios regarding grid size distribution

To verify the grid size determination criterion proposed in this study, a TRNSYS model Type 343 developed for PTES was employed [38]. Three additional grid size distributions, shown in Figure 4.5, were implemented to demonstrate the advantages of the criterion.

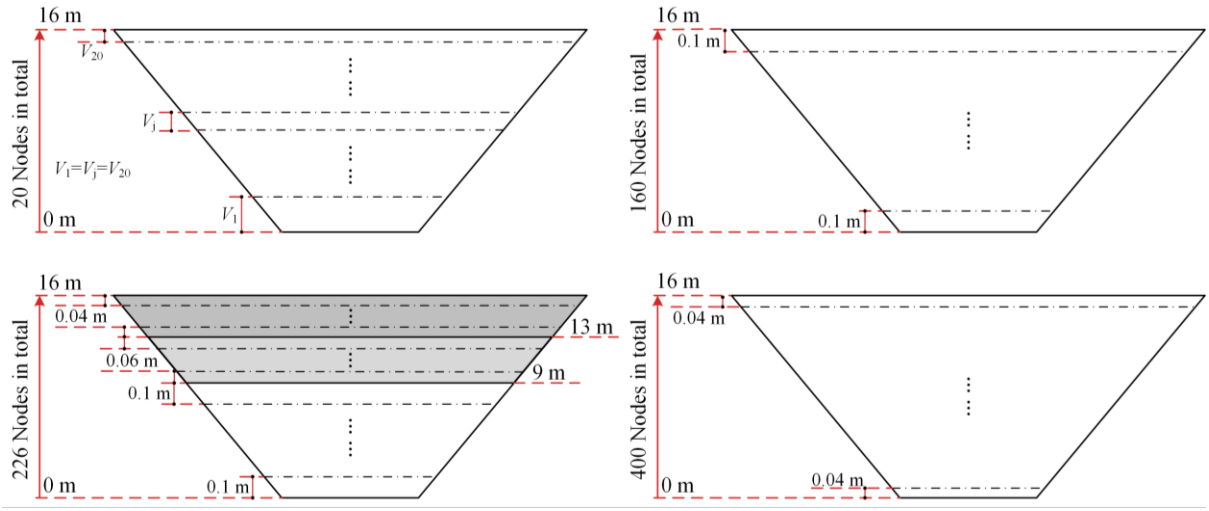

Figure 4.5 Schematic of different grid size distribution.

4.4.3 Improvement of 1D model calculation accuracy

PTES temperature distribution

Figure 4.6 illustrates the development of the MIX number for the Dronninglund PTES from 2015 to 2017. The calculation accuracy of PTES temperature with the recommended node size is superior to that with 20 nodes and 160 nodes. Moreover, it is noteworthy that reducing the grid size to 0.04 m (400 nodes in total) achieves a similar level of calculation accuracy as the recommended node size distribution (226 nodes in total).

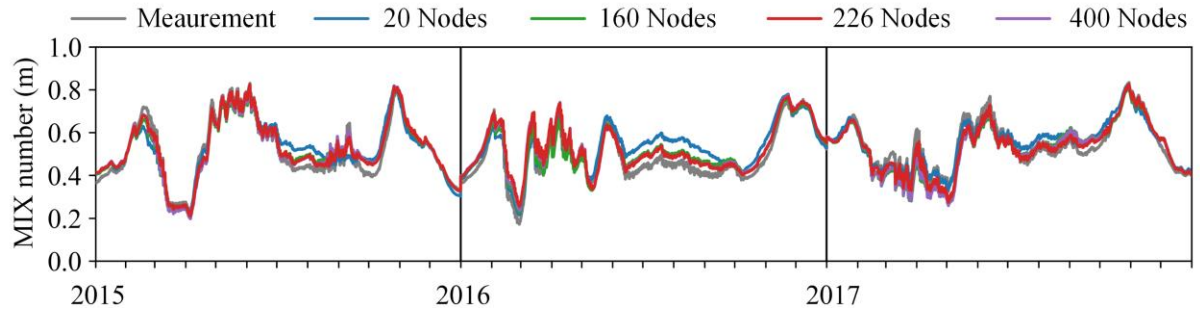

Figure 4.6 The development of calculated and measured MIX number from 2015 to 2017 **[Paper 2]**.

Furthermore, Figure 4.7 displays the model accuracy evaluation assessed by the RMSD of the MIX number, along with the calculation time for a one-year simulation. The results highlight the significant reduction in RMSD achieved when using the recommended grid size distribution (226 nodes in total). Notably, increasing the grid size with the same size along the PTES height does not necessarily yield the desired results but dramatically increases the computation time.

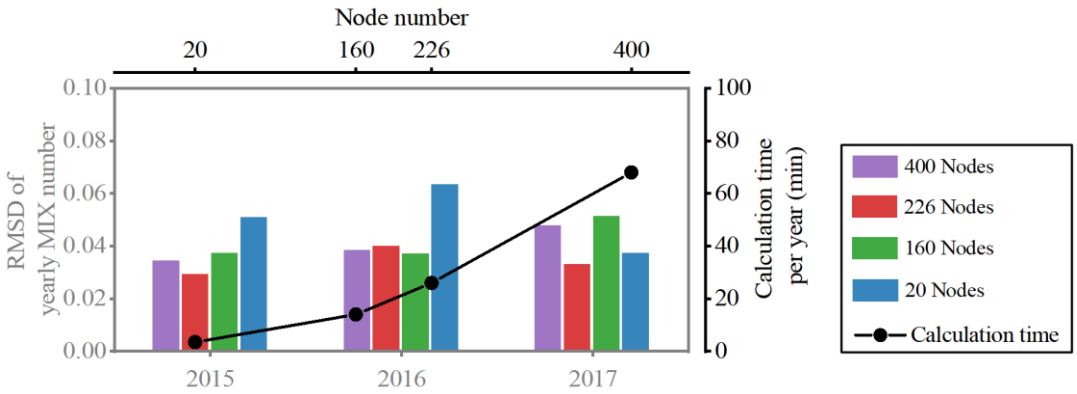

Figure 4.7 PTES temperature calculation accuracy and calculation time under different grid size distribution.

Charging and discharging energy

When planning a solar district heating system with PTES, energy flow is another critical factor influencing the selection of auxiliary energy units [58]. Figure 4.8 shows the monthly charge/discharge energy with different node numbers and the relative deviation ratios compared to the measurement. The relative deviation ratios are calculated using Eq. (4.7) and (4.8).

$$\vartheta_{ch} = (E_{ch,meas} - E_{ch,calc})/E_{ch,meas} \tag{4.7}$$

$$\vartheta_{disch} = (E_{disch,meas} - E_{disch,calc})/E_{disch,meas} \tag{4.8}$$

By increasing the node number, the maximum relative deviation ratio of monthly charged/discharged energy in these three years can be reduced to less than 5%. Remarkably, node number 226 outperforms node numbers 160 and 400 in monthly energy flow. The finding emphasizes the effectiveness of the proposed grid size determination in achieving higher calculation accuracy.

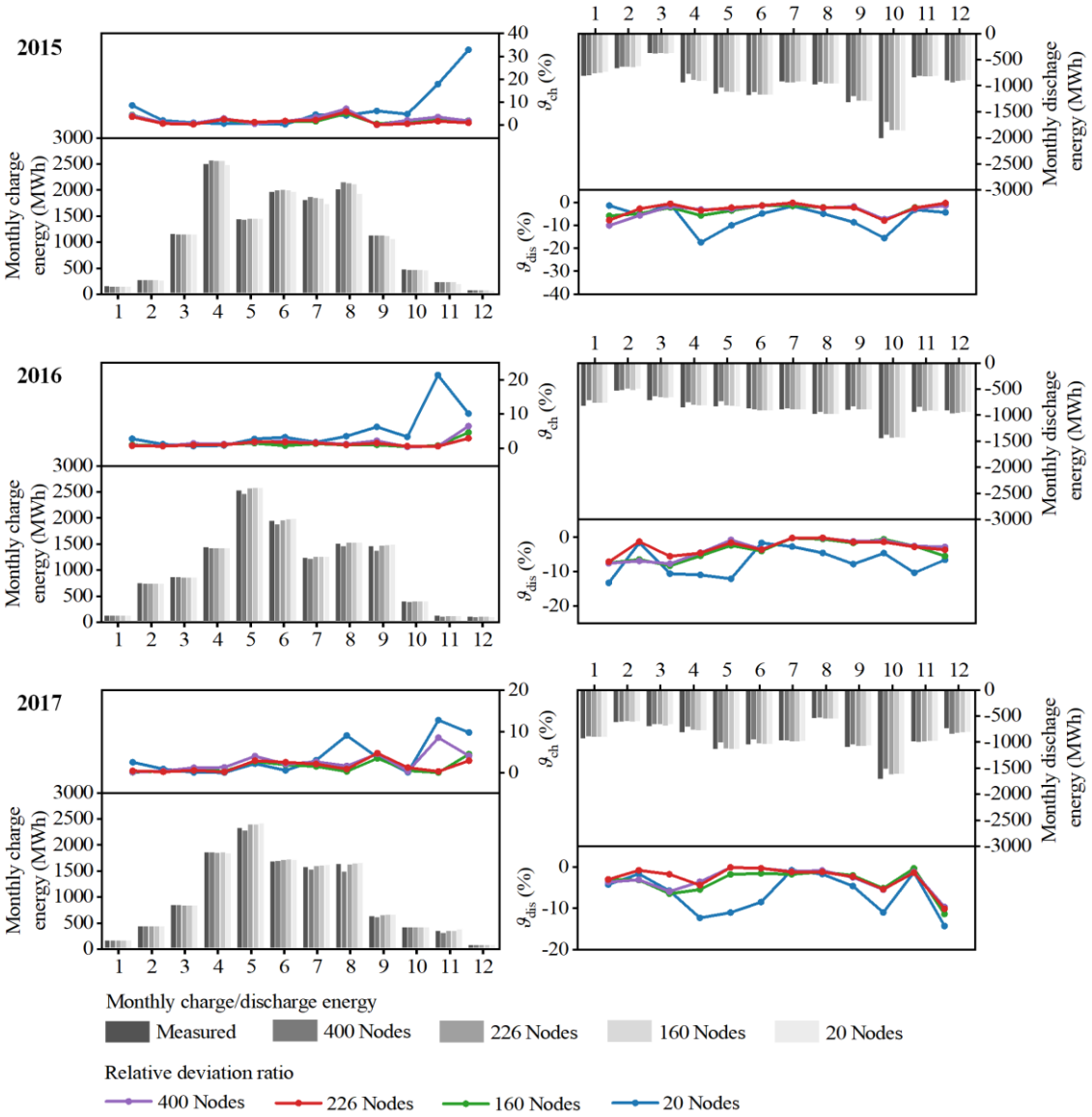

Figure 4.8 Comparison of monthly charge/discharge energy under different grid size distribution **[Paper 2]**.

Overall, the recommended grid size based on the $R_{\Delta T/\delta}$ criterion has shown substantial improvement in the calculation accuracy of TRNSYS Type 343 for PTES temperature distribution and energy quantities. This confirms the reliability of the proposed grid size selection approach. However, it is important to note that there may still be a slight difference between the measurement and the improved model, which can be further reduced by considering the inlet mixing effect.

5

Inlet mixing assessment within PTES

Hot and cold regions naturally form within pit thermal energy storage (PTES) because of the density differences between the hot and cold water. This natural phenomenon enables the extraction of hot water from the PTES top, while cold water is reintroduced at the PTES bottom. It is highly preferable to maintain these thermal regions with little mixing to prevent destratification.

For direct charge/discharge of PTES, the introduction of inlet mixing can result in destratification [68]. Extensive efforts have been made to develop proper inlet/outlet configurations to minimize the inlet mixing effect [32,46,47,69–71]. But, under certain conditions, inlet mixing may still occur. As a result, incorporating a modeling approach to account for the mixing effect can result in a more accurate PTES temperature prediction.

However, recent one-dimensional (1D) models are unable to consider mixing effects caused by the inflow, leading to numerical errors in predicting PTES thermal stratification [66]. One of the reasons is the insufficient research conducted on the impact of inlet mixing on PTES performance. Additionally, the mixing effect is influenced by both the PTES design and operating conditions [72], thereby posing a challenge in incorporating the three-dimensional (3D) characteristics of inlet mixing into a one-dimensional model.

Therefore, it is essential to fully understand the impact of inlet mixing on PTES performance and to develop a straightforward method to incorporate it into the 1D. This section aims to address the question '*What are the specific characteristics of inlet mixing that occur inside PTES during actual operation?*' and '*Can the characteristics of the inlet mixing be quantified?*'. By answering these questions, a deeper understanding of the inlet mixing dynamics can be achieved, enabling the improvement of 1D models.

5.1 Investigation method and scenarios

Inlet mixing in a PTES can be attributed to factors such as high inlet flow rates or significant temperature differences between the incoming water and the water within the PTES. In a study conducted on the Dronninglund PTES in 2017, the operational analysis revealed the occurrence of both positive and negative buoyant jets [73].

To assess the inlet mixing characteristics under dynamic operation, the full-scale 3D CFD model described in Section 3.3 was utilized. Twelve cases were selected for both positive and negative buoyant jets to access the dynamic characteristics of the buoyant jet under varied

conditions. The cases varied in terms of inflow rate (V_{in}), temperature difference (ΔT), diffuser diameter (D_d), and diffuser disc distance (H_d). For each case, the simulation was conducted over ten minutes, with results recorded at ten-second intervals to capture the transient behavior of the inlet mixture.

5.2 Quantization parameters

In this study, two parameters were introduced as effective measures to quantify the inlet mixing impact. These parameters are the penetration height (Z) and the energy distribution ratio (η_j). As illustrated in Figure 5.1, Z refers to the maximum height at which the inflow can affect, while η_j presents the inflow energy distributed to each layer inside the PTES. The Z and η_j were calculated based on the CFD simulation results.

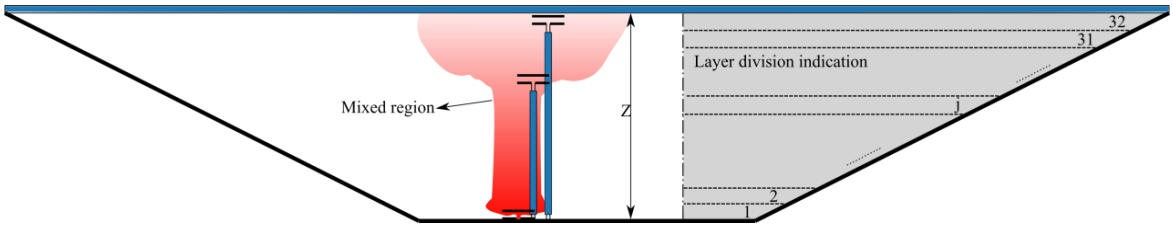

Figure 5.1 Illustration of the mixed region in the PTES (The grey background highlights the layer division for access the energy distribution ratio) **[Paper 3]**.

To obtain quantitative results for the inlet mixing effect under different cases, four dimensionless parameters were selected to evaluate the performance of PTES during dynamic operations [74–77]. These parameters include the inlet Reynolds (Re) number, the Froude (Fr) number, the momentum (M), and the buoyancy flux (F). The Re and Fr numbers are utilized to characterize the inflow forces and inertial forces, indicating the range of applicability for different cases. M and F are employed to establish a correlation for Z and η_j.

5.3 Physical natural of inlet mixing

Figure 5.2 visually describes the development of the jet within the PTES for two cases. In addition, the figure includes the energy distribution ratio along the PTES height at a specific time. Notably, the grey columns in the energy distribution ratio diagram indicate the actual energy distribution ratio in the 32 layers. The red curves represent a hypothetical scenario where the delivered energy is evenly distributed among all 32 layers inside the PTES.

Indeed, the behavior of positive and negative buoyancy jets follows a similar pattern. Initially, the jets concentrated near the inlet region. As time progresses, the jet moves upward and expands to the top of the PTES under positive buoyancy. In contrast, the jet moves downward, penetrating towards PTES bottom under negative buoyancy. Finally, both jets reach their maximum penetration height within the PTES.

Furthermore, most energy is initially distributed near the inlet diffusers. As the jet progresses, there is a noticeable shift in the energy distribution ratio. More energy is transferred from the

bottom layers to the top layers for the positive buoyancy jet. On the other hand, a greater proportion of energy is transferred from the middle layers to the bottom layers for the negative buoyancy jet.

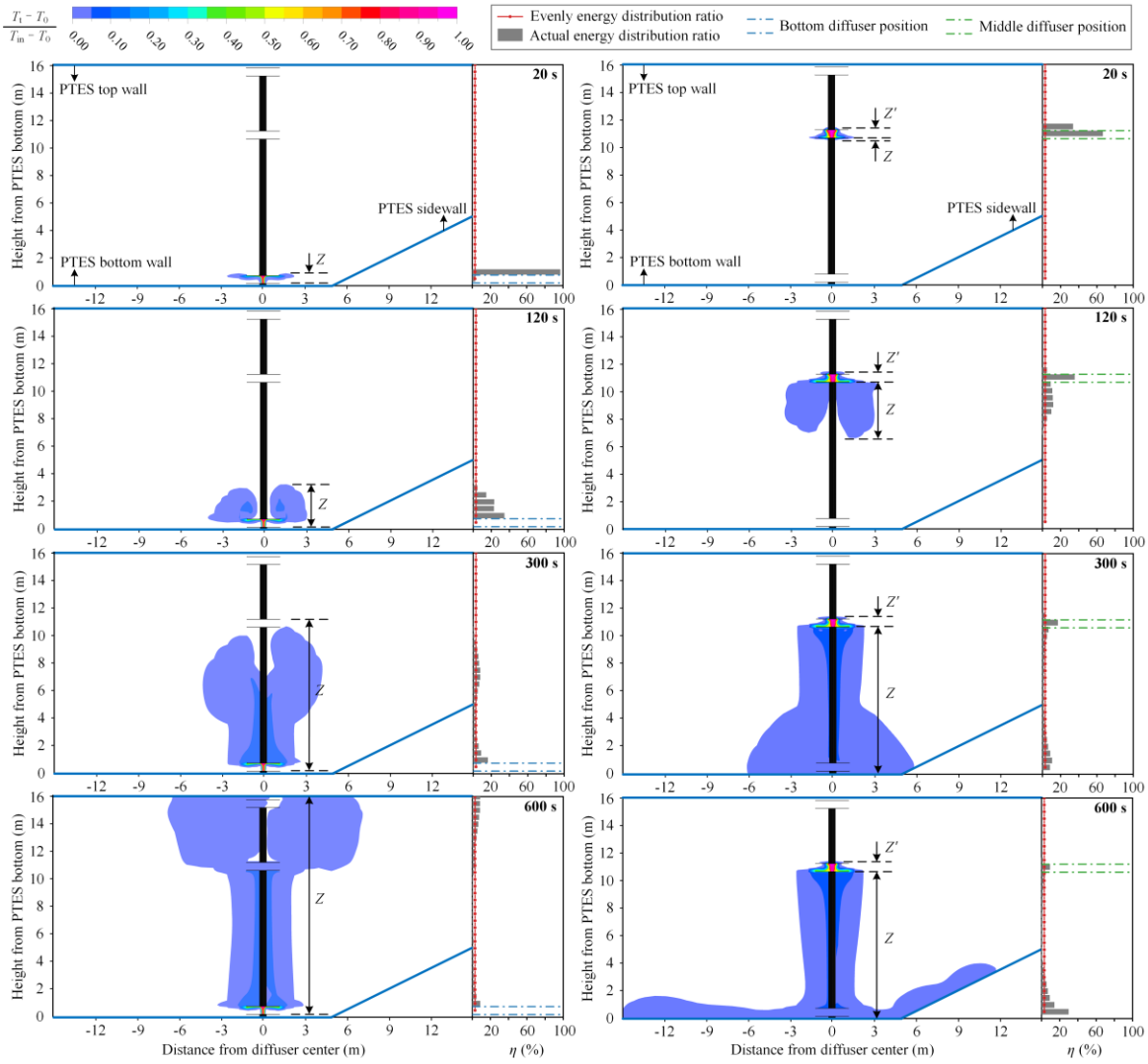

Figure 5.2 Flow visualization of buoyant jet (Left: positive buoyant jet, with T_0 = 10°C, T_{in} = 20°C, V_{in} = 50 m^3/h, D_d = 2.5 m and H_d = 0.58 m; Right: negative buoyant jet, withT_0 = 70°C, T_{in} = 60°C, V_{in} = 50 m^3/h, D_d = 2.5 m and H_d = 0.58 m) **[Paper 3]**.

5.4 Quantization of the penetration height

5.4.1 Growth trends of the penetration height

The penetration height within the PTES grows faster when there is a larger inflow rate (V_{in}), a greater temperature difference (ΔT), and a smaller diffuser diameter (D_d). However, changes in the diffuser disc distance (H_d) have a minimal impact on the penetration height.

The increased V_{in}, and decreased D_d diameter contribute to a higher Re number, while increased ΔT leads to a higher Fr number. Therefore, both a large Re numer and Fr number can accelerate the growth of the penetration height.

5.4.2 Quantitative relationships between penetration height and time

Based on the dimensional theory, Figure 5.3 presents the relationship between the dimensionless penetration height and time for a positive buoyant jet. The inlet Re number falls within the range of $1292 \leq Re \leq 25348$, and the Fr number in the range of $6.5 \times 10^{-6} \leq |Fr| \leq 5.2 \times 10^{-3}$. Figure 5.4 presents the relationship between the dimensionless penetration height and time for a negatively buoyant jet. The inlet Re number falls within the range of $1292 \leq Re \leq 25348$, and the Fr number in the range of $6.5 \times 10^{-6} \leq |Fr| \leq 5.2 \times 10^{-3}$.

Both figures reveal that the Re number has a more significant impact on the penetration height than the Fr number when dimensionless. A power-law relationship between the dimensionless height and the dimensionless time is observed for all the investigated cases. However, ensuring the range of inlet Re number falls within the applicable range of the correlations is crucial.

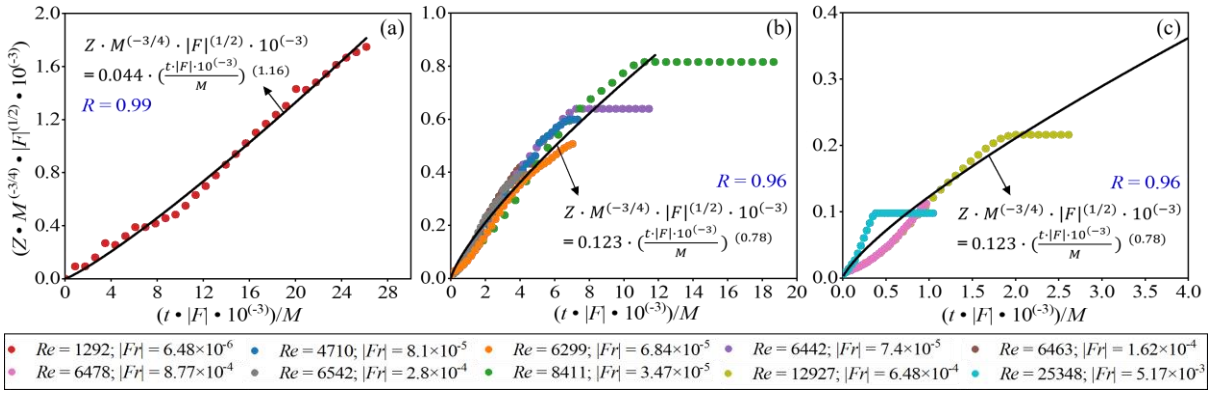

Figure 5.3 Relationship between the dimensionless penetration height and time for a positive buoyant jet **[Paper 3]**.

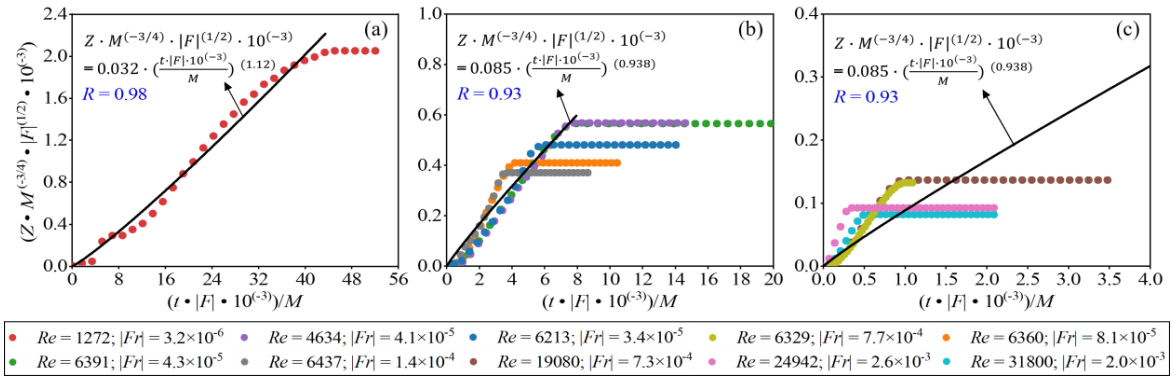

Figure 5.4 Relationship between the dimensionless penetration height and time for a negative buoyant jet **[Paper 3]**.

In sum, the correlation to predict the penetration height of a positive buoyancy jet during operation can be represented by Eq. (5.1), while the penetration height prediction of a negative buoyancy jet can be summarized in Eq. (5.2).

$$Z \cdot M^{\left(-\frac{3}{4}\right)} \cdot |F|^{\left(\frac{1}{2}\right)} \cdot 10^{(-3)} = \begin{cases} 0.044 \cdot \left(\frac{t \cdot |F| \cdot 10^{(-3)}}{M}\right)^{1.16} & Re \leq 1292 \\ 0.123 \cdot \left(\frac{t \cdot |F| \cdot 10^{(-3)}}{M}\right)^{0.78} & Re > 1292 \end{cases} \quad (5.1)$$

$$Z \cdot M^{\left(-\frac{3}{4}\right)} \cdot |F|^{\left(\frac{1}{2}\right)} \cdot 10^{(-3)} = \begin{cases} 0.085 \cdot \left(\frac{t \cdot |F| \cdot 10^{(-3)}}{M}\right)^{0.938} & Re \leq 1272 \\ 0.031 \cdot \left(\frac{t \cdot |F| \cdot 10^{(-3)}}{M}\right)^{1.124} & Re > 1272 \end{cases} \quad (5.2)$$

5.5 Quantization of the energy distribution ratio

5.5.1 Energy distribution ratio variation trend

In the case of positive buoyancy jets, the inflow water energy is primarily transferred toward the upper layer of the PTES. The layer above the bottom inlet (i.e., 2nd layer) consistently exhibits a large η_j in the first 100s of the calculation. Over time, η_j of the 2nd layer gradually decreases and varies depending on the conditions. As more mixed water enters the top layer, η_j of the 32nd layer increases. For the remaining layers inside the PTES, η_j is less than 10% throughout the calculation.

Regarding negative buoyancy jets, the energy from the inflow water is mainly transferred to the bottom layer of the PTES. The layers near the middle inlet (i.e., the 22nd and 23rd layers) demonstrate a significantly higher η_j in the first 100s. During the calculation, the η_j of other layers remains below 10%, except for the layers close to the middle inlet and the PTES bottom.

It is worth noting that increasing the Fr number by decreasing D_d and increasing the Re number through a higher temperature difference between the inflow water and the water inside PTES results in an intensified transfer of inlet water energy for both positive and negative buoyancy jets.

5.5.2 Quantitative relationships between energy distribution ratio and time

For positive buoyancy jets, most charged heat is stored in layers either close to the bottom inlet or in the top layer of the PTES. In this context, efforts were made to derive the correlations for η_j in the 2nd and 32nd layers based on the dimensional theory, as depicted in Figure 5.5. In contrast to positive buoyant jets, negative buoyant jets rise upward and then sink. Therefore, the fitting of the relational expression showcased in Figure 5.6 focuses on the inlet layer (22nd layer), the layer above the middle inlet (23rd layer), and the bottom layer (1st layer).

Most of the datasets demonstrate good agreement when fitted as a function in the form of Eq. (5.3). However, it has proven challenging to obtain ideal correlations by fitting the datasets in

the 1st layer under negative buoyancy to Eq. (5.3). To address this, Eq. (5.4) is proposed, which provides a perfect fit for the data from the 1st layer.

Notably, the time variable for the 32nd layer under positive buoyancy and the 1st layer under negative buoyancy is adjusted from (t) to $(t - t_{start})$ to account for the time delay associated with the start of energy distribution in those layers.

$$\eta_j = a \cdot \left(\frac{t \cdot |F| \cdot 10^{-3}}{M}\right)^b \tag{5.3}$$

$$\eta_j = a - b \cdot c^{\left(\frac{t \cdot |F| \cdot 10^{-3}}{M}\right)} \tag{5.4}$$

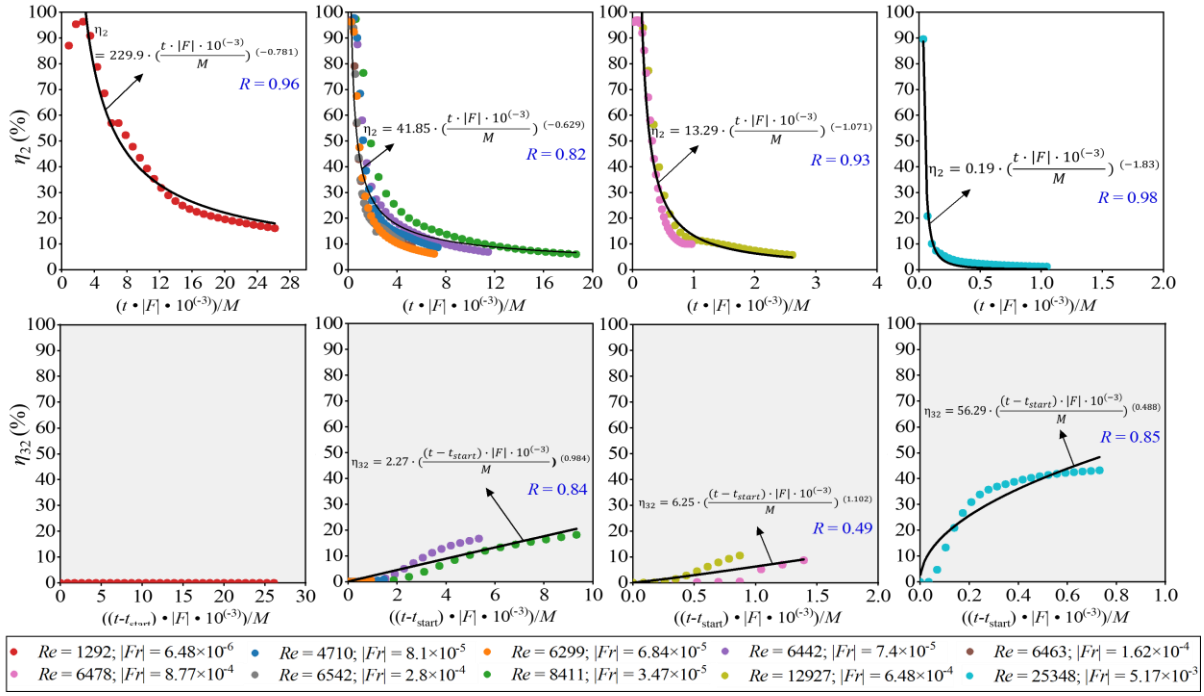

Figure 5.5 Relationship between the energy distribution ratio and the dimensionless time for a positive buoyant jet (white background represents the results of the 2nd layer, and light grey background represents the results of the 32nd layer) **[Paper 3]**.

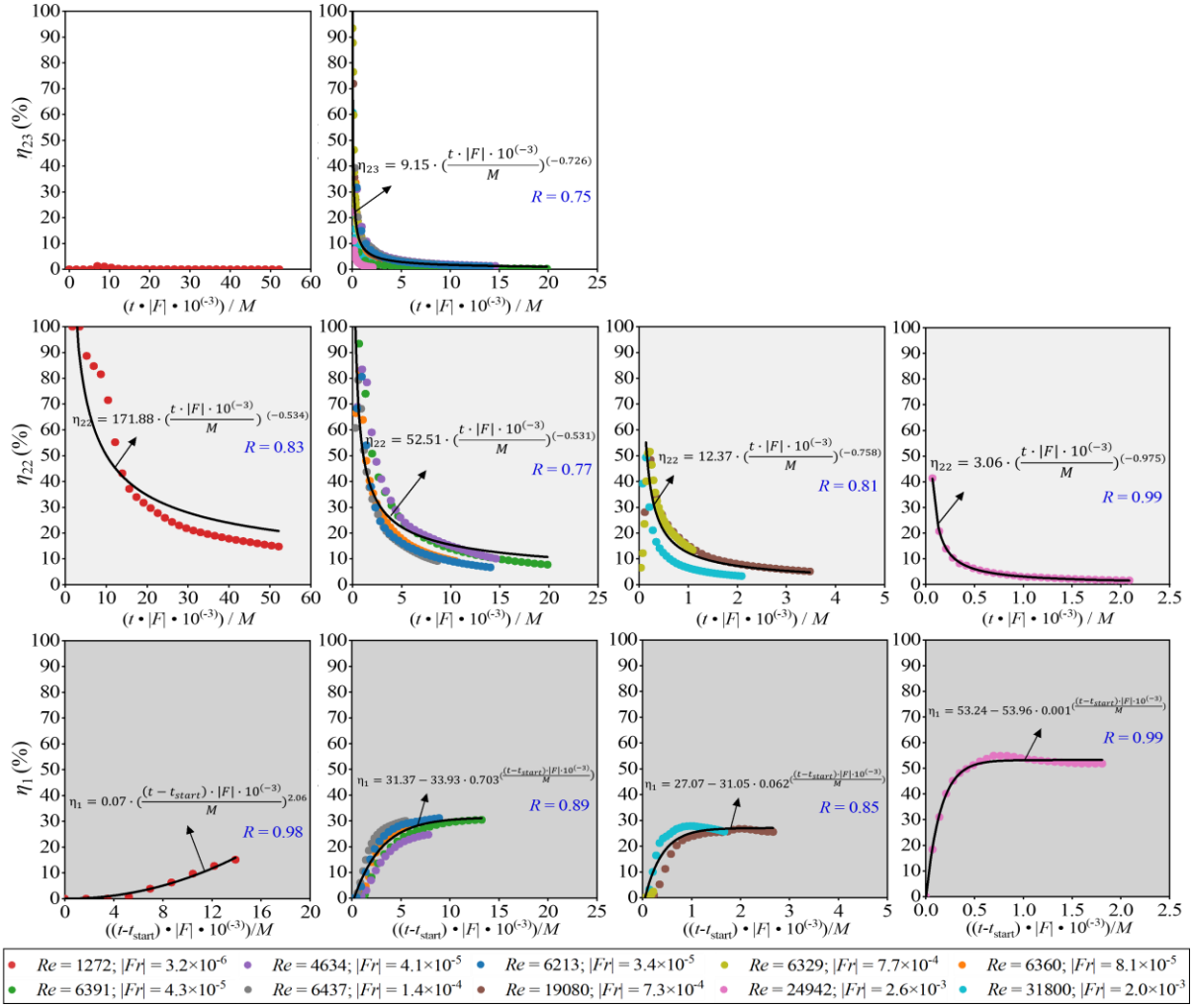

Figure 5.6 Relationship between the energy distribution ratio and dimensionless time for the negative buoyant jet (white background represents the results of the 23rd layer, light grey background represents the results of the 22nd layer, and dark grey background represents the results of 1st layer) **[Paper 3]**.

In summary, Table 5.1 provides detailed information regarding the coefficients and application range for a positive buoyant jet, while Table 5.2 presents the corresponding information for a negative buoyant jet. It is essential to note that the η_j of these layers depends on both the inlet Re number and the Fr number. In cases where the Re number is insufficiently large, it is necessary to consider the combination of the Re number and Fr number to determine η_j accurately.

Table 5.1 Coefficients and application range for a positive buoyant jet **[Paper 3]**.

Layer	Fitted equation	Coefficients		Application range
		a	b	
2nd	(5.9)	0.19	-0.183	$Re \geq 25348$
		13.29	-1.071	$Re \geq 6478$ & $6.84\times10^{-4} \leq \lvert Fr \rvert \leq 8.77\times10^{-4}$

		41.85	-0.629	$Re > 1292$ & $\|Fr\| < 8.77\times10^{-4}$
		229.9	-0.781	$Re \leq 1292$
32nd	(5.9)	56.29	0.488	$Re \geq 25348$
		6.25	1.102	$Re \geq 6478$ & $6.84\times10^{-4} \leq \|Fr\| \leq 8.77\times10^{-4}$
		2.27	0.984	$Re > 1292$ & $\|Fr\| < 8.77\times10^{-4}$
		0	0	$Re \leq 1292$

Table 5.2 Coefficients and application range for the negative buoyant jet **[Paper 3]**.

Layer	Fitted equation	Coefficients			Application range
		a	b	c	
1st	(10)	52.24	53.96	0.001	$Re \geq 24942$ & $\|Fr\| \geq 2.6\times10^{-3}$
		27.07	31.05	0.062	$Re \geq 6329$ & $7.3\times10^{-4} \leq \|Fr\| \leq 2\times10^{-3}$
		31.37	33.93	0.703	$Re > 1272$ & $\|Fr\| < 7.3\times10^{-4}$
	(9)	0.07	2.06	-	$Re \leq 1272$
22nd	(9)	3.06	-0.975	-	$Re \geq 24942$ & $\|Fr\| \geq 2.6\times10^{-3}$
		12.37	-0.758		$Re \geq 6329$ & $7.3\times10^{-4} \leq \|Fr\| \leq 2\times10^{-3}$
		52.51	-0.531	-	$Re > 1272$ & $\|Fr\| < 7.3\times10^{-4}$
		171.88	-0.534	-	$Re \leq 1272$
23rd	(9)	9.15	0.726	-	$Re > 1272$
		0	0	-	$Re \leq 1272$

In conclusion, this study emphasizes the significance of understanding and quantifying the influence of inlet mixing on PTES performance. Researchers and engineers can gain valuable insights into the thermal dynamics of PTES and make well-informed decisions about its design and operation by utilizing the suggested performance indicators. Furthermore, the proposed correlations can be used to improve existing one-dimensional PTES models targeting higher prediction accuracy of thermal stratification in storage.

6

Interaction between PTES and surrounding soil

Due to economic constraints and construction challenges, insulation is typically not applied to the side and bottom walls of large-scale pit thermal energy storage (PTES) [14]. In this situation, the large interface between the water body and surrounding soil may experience significant thermal losses because of the heat transfer mechanism. Therefore, the soil's thermal properties can strongly influence the PTES performance resulting in inefficient PTES operation.

It is well recognized that various parameters related to soil thermal properties have a great impact on thermal losses, and subsequently the stored thermal energy [78]. These parameters include thermal conductivity, heat compacity, and density [23]. However, the thermal properties are often assumed to be constant in research, even though they are largely dependent on the soil's water content. Additionally, due to heat loss to the surrounding, the sidewalls of a closed PTES system have lower temperatures compared to the water near the PTES center, resulting in natural convection. As the convection coefficient increases, the overall heat transfer coefficient also increases. However, this phenomenon is commonly neglected in TRNSYS models, where a constant heat transfer coefficient is used along the sidewalls. In this context, the heat loss as well as changes in soil temperature distribution may be overestimated.

Hence, a long-term calculation was conducted using the one-quarter 3D model to address the question '*How is the interaction between buried PTES and surrounding soil?*'. The investigation in this section focuses on three main aspects: transient natural convection, soil temperature distribution, and the influence of different geometries. By assessing these factors, valuable correlations were developed to improve the calculation accuracy of 1D models.

6.1 Investigation method and scenarios

The interaction between PTES and the surrounding soil was investigated using the one-quarter CFD model described in Chapter 3. The primary objectives were to gain comprehensive insights into the PTES performance and the heat transfer characteristics between the water and soil regions. For this purpose, three scenarios were proposed in this study.

Figure 6.1 visually presents the three-dimensional characteristics of these scenarios. In scenarios 2 and 3, the initial soil temperature was set to a constant value of 8.5°C. In addition, scenario 3 differed from scenarios 1 and 2 regarding the water region geometry while

maintaining the same storage height and volume. For more detailed information of these scenarios, refer to Table 6.1.

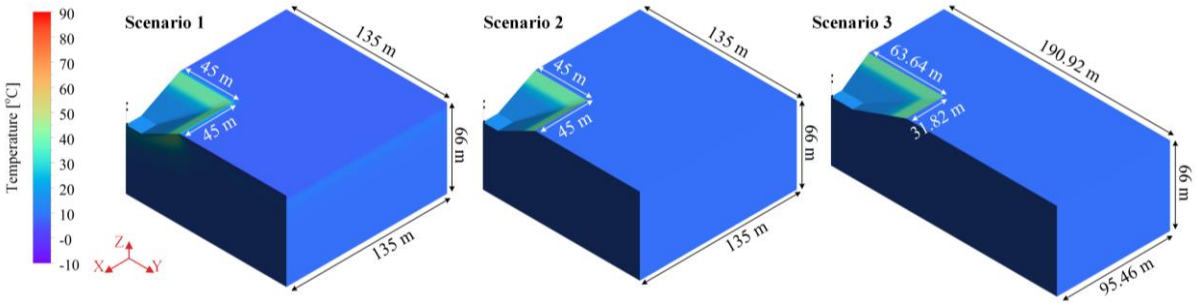

Figure 6.1 Visual illustration of different scenarios.

Table 6.1 Detailed parameters for different scenarios **[Paper 4]**.

Parameter	Scenario 1	Scenario 2	Scenario 3
Top dimension [m × m]	90 × 90	90 × 90	127.28 × 63.64
Bottom dimension [m × m]	26 × 26	26 × 26	36.76 × 18.38
PTES height [m]	16	16	16
Slope angle [°]	26.6	26.6	35.3/19.5
Top surface area [m^2]	8100	8100	8100
Bottom surface area [m^2]	676	676	676
Side surface area [m^2]	8300	8300	8484
PTES volume [m^3]	59285	59285	59281
Initial soil temperature [°C]	Temperature distribution starting 2017	8.5	8.5

All three scenarios underwent yearly calculations using the same boundary conditions for yearly calculations. The operation conditions for these calculations were based on the measurements of inlet/outlet temperature and flow rate of the Dronninglund PTES in 2017.

6.2 PTES performance

The yearly calculation results highlight the significant discrepancies observed in the side heat loss among the three scenarios. Scenarios 2 and 3 experience a notable increase in heat loss compared to scenario 1. This discrepancy can be attributed to the fact that the temperature distribution within the soil has not yet been established in scenarios 2 and 3, while scenario 1 establishes a stable soil temperature distribution. Thus, the yearly calculation results indicate that at the beginning of the operation, the proportion of side heat loss constitutes approximately 60% of the total heat loss. However, as the soil temperature distribution gradually stabilizes, the side heat loss decreases to approximately 40% of the total heat loss.

Table 6.2 summarizes the PTES thermal performance across the different scenarios. It is worth noting that all three scenarios achieve similar PTES temperature levels. However, scenarios 2 and 3 exhibit approximately 43% higher heat loss than scenario 1, resulting in a reduction in storage efficiency of about 3.7%. This finding suggests that side heat loss plays a significant role in the initial stages. As the soil temperature distribution gradually stabilizes, the relative contribution of side heat loss diminishes. Furthermore, changes in storage geometry will not significantly impact the PTES performance as long as the system operates under the same boundary conditions.

Table 6.2 Thermal performance comparison under different scenarios **[Paper 4]**.

Parameters	Scenario1	Scenario2	Scenario3
Maximum PTES temperature (°C)	85.8	85.8	85.8
Minimum PTES temperature (°C)	8.2	8.6	8.6
Heat capacity (MWh)	5281	5253	5253
Charged energy (MWh)	11,625	11,770	11,768
Discharged energy (MWh)	11,184	10,873	10,873
Internal energy change (MWh)	-564	-550	-584
Thermal loss (MWh)	1005	1448	1479
Storage cycle	2.12	2.07	2.07
Storage efficiency (%)	91.4	87.7	87.4

6.3 Soil temperature distribution

The absence of insulation in the side and bottom walls of underground storage pose a risk of the underground temperature exceeding certain limits set by national or local environmental standards [79]. This failure to maintain the desired underground environment standards can lead to various environmental challenges. Therefore, it is crucial to understand the soil temperature distribution under different scenarios.

As described in Section 6.1, scenarios 1, 2, and 3 exhibit different storage geometries. In this end, Figure 6.2 illustrates the soil temperature distribution along the X-Z symmetrical plane for scenarios 1 and 2. Figure 6.3 displays the temperature distribution of the X-Z symmetrical plane and the Y-Z symmetrical plane for scenario 3. Notably, the figures highlight the maximum area where the soil temperature is influenced over time. It is evident that the ambient temperature significantly affects the soil temperature within 1 m below the ground level. Additionally, the soil temperature adjacent to the water region demonstrates variations throughout the year, depending on the water temperature distribution within the PTES.

In scenario 1, the maximum area where the soil temperature is affected remains relatively consistent throughout the year, specifically at a depth of 20 m below the PTES. This area is approximately 1.5 times the size of the PTES top surface in the radial direction. Conversely, in scenario 2, where the soil temperature stratification is in the early stages of establishment, the area of influence gradually expands over the year. The depth affected ranges from 2 m to 10 m

below the PTES bottom. In the radial direction, the influence area extends from the boundary of the PTES top surface to approximately 1.2 times the size of the PTES top surface. The observed trend of soil temperature variation in scenario 3 is essentially similar to that of scenario 2. This reveals that changing the storage geometry slightly impacts the soil temperature distribution.

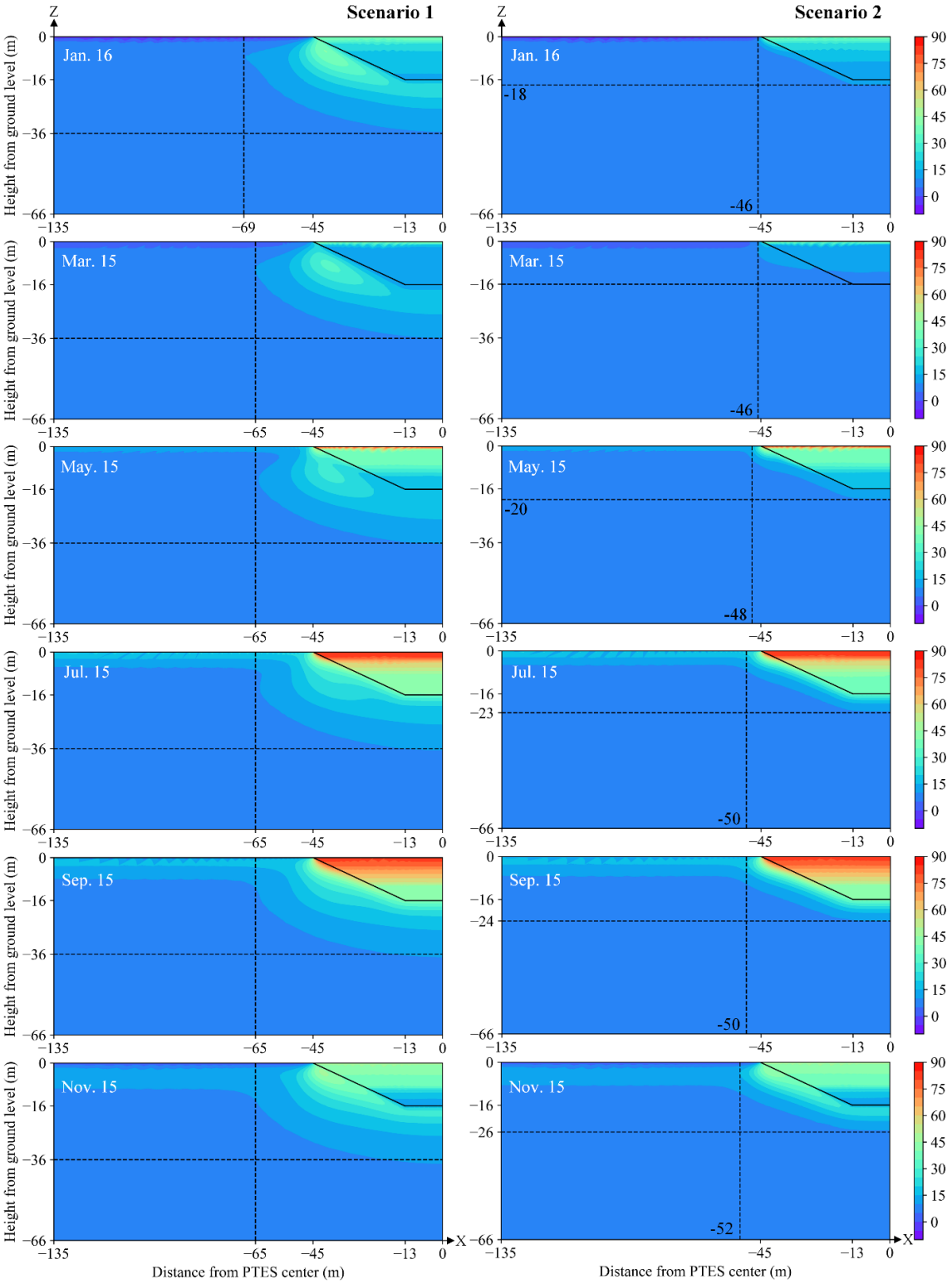

Figure 6.2 The temperature distribution for typical dates. Left: scenario 1; Right: scenario 2 **[Paper 4]**.

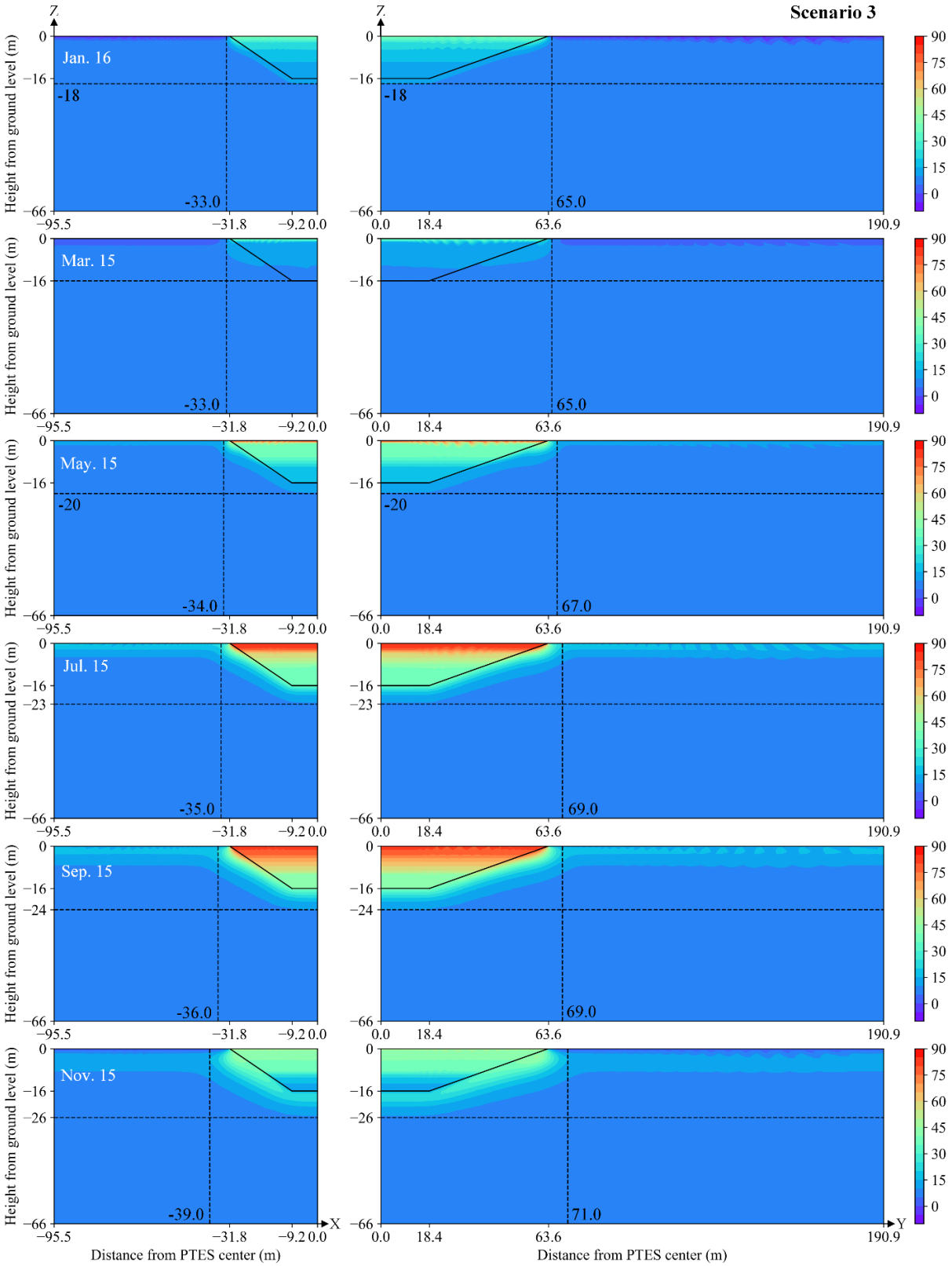

Figure 6.3 The temperature distribution for typical dates under scenario 3. Left: X-Z symmetrical plane; Right: Y-Z symmetrical plane **[Paper 4]**.

6.4 Heat transfer coefficient along the side walls

The overall heat transfer coefficient along the side walls is crucial to accurately simulate the heat flux through the side walls under dynamic operation. Using a constant parameter along the side walls may overestimate the heat loss prediction. Figure 6.4 has been included to address this issue, presenting the overall heat transfer coefficient along the side walls for typical days throughout the year. The water and soil temperatures adjacent to the side walls are presented together to illustrate the factors contributing to sudden changes in the heat transfer coefficient.

The negative values of the overall heat transfer coefficient indicate that heat is transferred from the water body to the soil. Conversely, positive values indicate that the water body gains heat from the soil. Throughout the year, the overall heat transfer coefficient along the side walls fluctuates from -20 to -30 $W/m^2 \cdot K$. However, significant fluctuations occur at certain heights, and these can be explained as follows:

1) Due to the heat losses through the PTES cover, a drop in temperature is observed near the top of PTES. This leads to an “inverse thermocline”, where the temperature of the upper layer is lower than that of the lower layer. As a result, driven by the buoyancy force, the high-temperature fluid moves upwards while the low-temperature fluid moves downward. This flow along the side wall results in an increase in the heat transfer coefficient. The magnitude of this influence depends on the temperature difference, and the maximum overall transfer coefficient can reach around -250 $W/m^2 \cdot K$ over the year.

2) At specific heights, such as around 12 m inside the PTES on June 15, the soil temperature is significantly lower than the water temperature. This temperature difference causes the water near the side wall to be cooled down to a lower temperature than the water in the lower layer. Therefore, a downward flow is induced along the side wall, increasing the overall heat transfer coefficient.

3) There is a significant temperature gradient in certain locations within the PTES, such as at a height of 14.5 m on March 15. Simultaneously, the soil temperature is higher than the water temperature. This temperature difference leads to the water near the side wall being warmed up to a higher temperature than the water in the upper layer. In this case, disturbances occur along the side wall, enhancing the overall heat transfer coefficient.

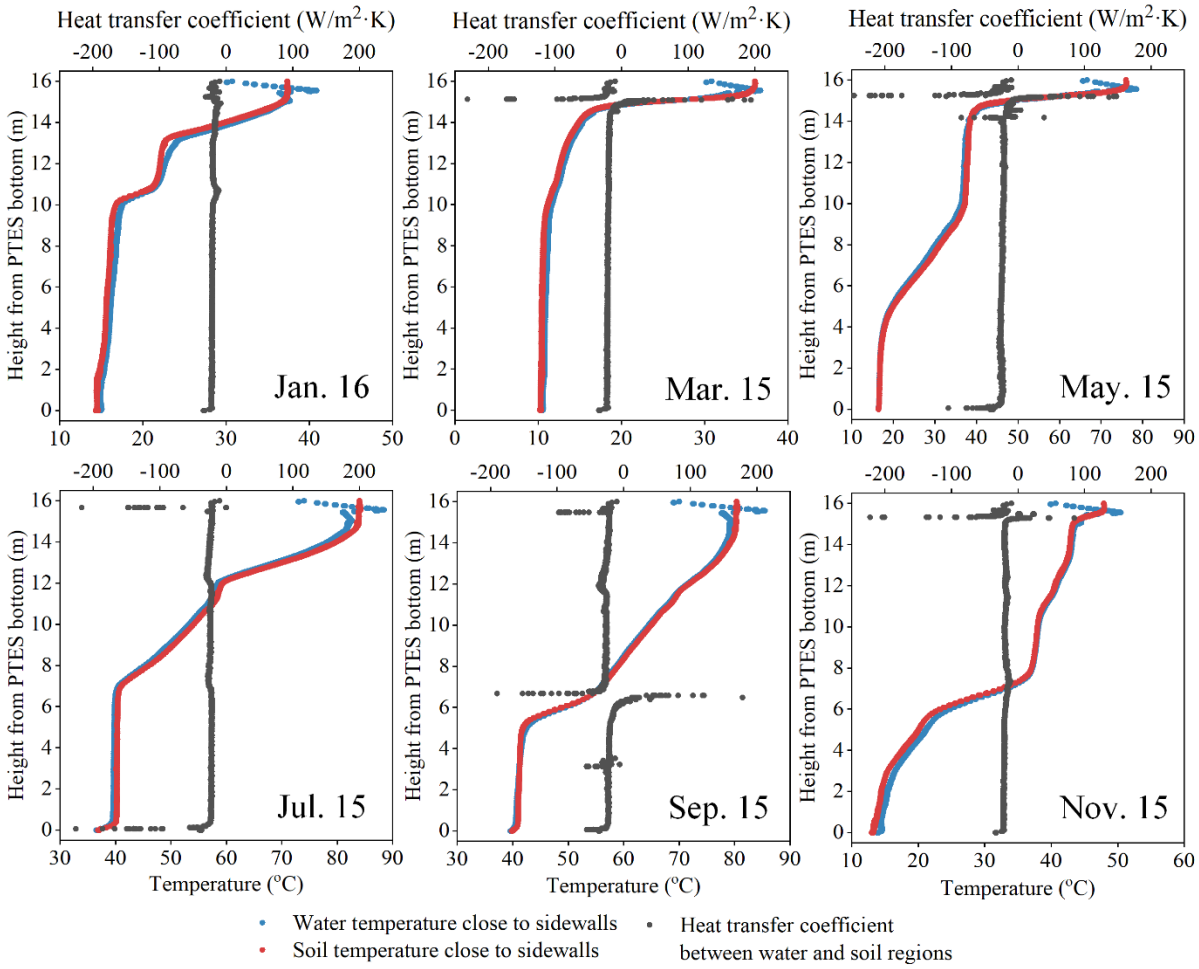

Figure 6.4 Overall heat transfer coefficient, water temperature, and soil temperature along the PTES side walls for typical dates under scenario 1 **[Paper 4]**.

Additionally, when comparing scenarios 1 and 2, it is observed that the initial temperature distribution of the soil has no significant effect on the heat transfer coefficient. This is primarily because the soil temperature distribution adjacent to the sidewalls in these two scenarios is almost identical. Simultaneously, the water temperature distribution adjacent to the sidewalls is also similar due to the same operation conditions.

Furthermore, when comparing scenarios 2 and 3, it is evident that changing the PTES geometry has a minor impact on the heat transfer coefficient along the sidewalls. However, it should be noted that increasing the slope angle of PTES sidewalls results in a slight increase in the overall heat transfer coefficient at specific heights within the PTES.

Overall, this study highlights the influence of different soil temperature distributions and PTES geometries on PTES performance. Additionally, it emphasizes the heat transfer characteristics between the water and soil regions under different scenarios. The findings, particularly the observed overall heat transfer coefficient along the PTES sidewalls, can serve as a valuable reference for developing and improving one-dimensional models.

7

Discussion

The Dronninglund solar district heating (SDH) plant is a remarkable example of successful integration with pit thermal energy storage (PTES). By utilizing PTES, the Dronninglund SDH plant achieves a solar fraction of around 40% over multi-year operations. Accurate simulation models have become vital in planning the PTES and effectively designing system components and operation strategies for large-scale SDH projects. However, improving the calculation accuracy of current one-dimensional models remains a challenge. A comprehensive investigation of PTES using a full-scale three-dimensional model can offer invaluable insights to researchers and developers, enabling a profound understanding of PTES characteristics during dynamic operations. Furthermore, this study proposed possible solutions for improving the calculation accuracy of one-dimensional models by incorporating three-dimensional phenomena in a simplified manner.

There is still untapped potential for future advancements in PTES. Additionally, numerous aspects related to PTES warrant further investigation, particularly in finding a balance between technical performance and economic viability. Overall, the integration of PTES into large-scale SDH plants holds great promise in diversifying system configurations and enhancing overall energy efficiency.

8

Conclusion

Pit thermal energy storage (PTES) has gained increasing attention as a promising technology. However, its rapid development has been hindered by several technical challenges that have not been adequately addressed. In light of this, this study aimed to investigate the large-scale PTES for solar district heating (SDH) plants, which the authors consider to be crucial for driving the future development of PTES. The followings are the conclusions drawn from addressing the research questions:

(1) What are the key challenges and problems that need to be solved in the development of PTES?

- The design and construction of the floating cover poses the most significant challenge in PTES projects, primarily due to the substantial heat loss and investment. Additionally, the reliability and durability of the thermal insulation and lining materials play a critical role, particularly in the case of large-scale buried PTES systems operating in high-temperature environments. The maximum temperature of most PTES projects is generally controlled below 90^{o}C to prevent a significant reduction in the lifetime of liner materials. These findings underscore the importance of exploring more reliable materials that can extend the lifetime of PTES while maintaining its performance during long-term operation.
- The calculation deviation of different models for the annual charged and discharged energy are generally within ±10%. However, it is important to note that the accuracy of PTES numerical approaches is currently insufficient, especially regarding the prediction of heat loss, PTES temperature distribution, and soil temperature. To improve the accuracy of PTES numerical models, several aspects have been addressed. However, it is worth noting that these attempts are primarily based on one-dimensional features and may not fully capture the three-dimensional characteristics of PTES systems. Consequently, the current improvements may still not accurately reflect the actual operating conditions and behavior of PTES.
- The operation characteristics of PTES have a significant impact on the overall efficiency of SDH systems. However, there is notable lack of research on simulation approaches for system integration. As a result, there is a pressing need for system-level investigations to identify the optimal system design and operation strategies.

(2) ***What grid size can achieve improved calculation accuracy without a significant increase in computation time?' and 'Whether a criterion that can be used for the guidance of selecting appropriate grid sizes*****?'**

- Grid size in the horizontal directions has a negligible effect on temperature distribution prediction. However, the vertical grid size plays a significant role in accurately capturing the temperature variations. Through the analysis of heat transfer characteristics during PTES dynamic operation, it has been determined that the thermocline's temperature gradient serves as a suitable criterion for determining the grid size distribution.
- By analyzing the dynamic variation characteristics of the thermocline over a three-year operation, an optimal grid size distribution has been determined. A three-year simulation was conducted using a multi-node model (TRNSYS Type 343) to verify the reliability of choosing the appropriate grid size distribution. The results of this simulation demonstrated the superior calculation accuracy achieved when using the appropriate grid size distribution, compared to other grid size distributions. By utilizing the recommended grid size distribution, the RMSD of the yearly MIX number remained below 0.04, and the relative deviation ratio of monthly charge/discharge energy was consistently below 5% each year. It is essential to highlight that the optimal grid size distribution strikes a balance between computational efficiency and accuracy.

(3) ***What are the specific characteristics of inlet mixing that occur inside PTES during actual operation?' and 'Can the characteristics of the inlet mixing be quantified?***

- Through the analysis of the dynamic behavior of inlet mixing inside PTES systems, several key factors influencing the penetration area of the inlet mixing have been identified. These factors include the inlet volume flow rate, the temperature difference between the inlet and the PTES temperature, and the diffuser disc diameter. Based on these findings, two performance indicators, the penetration height, and the energy distribution ratio, have been proposed to effectively quantify the inlet mixing impact within the PTES.
- The dimensionless height and time are applicable for characterizing the buoyancy jet phenomenon that occurs within PTES. These dimensionless quantities were typically fitted using a power law relationship, which enabled a more comprehensive understanding of the penetration height and time-dependent behavior of the buoyancy jet. Furthermore, the correlations derived from this study highlighted that the transient dimensionless penetration height was primarily dependent on the inlet Reynold number for both the positive and negative buoyancy jets. By incorporating dimensionless parameters and the derived correlations into existing one-dimensional PTES models, it becomes possible to improve their accuracy and effectiveness.

(4) ***How is the interaction between buried PTES and surrounding soil?***

- During the initial stages of operation, a considerable amount of heat is lost through the sidewalls, accounting for approximately 60% of the total heat loss in the PTES system. However, as the system continues to operate and the soil temperature distribution gradually stabilizes over three years, the proportion of side heat loss decreases to around 40% of the total heat loss. By conducting a comparison investigation across various scenarios, it was observed that an increase of around 43% in heat loss could lead to a reduction in storage efficiency of about 3.7%. This finding highlights the significant impact of heat loss on the overall performance and efficiency of the PTES system.

- In the case of the Dronninglund PTES, after three years of operation, the established soil temperature distribution reveals that the maximum area of soil temperature influence remains relatively consistent throughout the year, particularly at a depth of 20 m below the PTES. This area of influence is approximately 1.5 times the size of the PTES top surface in the radial direction. Conversely, during the early stages of soil temperature stratification, the range of influence gradually expands over the year. The depth affected ranges from 2 m to 10 m below the PTES bottom. In the radial direction, the influence extends from the PTES top surface boundary to approximately 1.2 times the size of the PTES top surface.
- The overall heat transfer coefficient along the PTES sidewalls typically ranges from -20 to -30 $W/m^2 \cdot K$ for most of the height throughout the year. However, it is crucial to pay special attention to situations where an "invert thermocline" occurs, resulting in a maximum overall heat transfer coefficient along the sidewalls of -250 $W/m^2 \cdot K$. The observed overall heat transfer coefficient along the PTES sidewalls can be a valuable reference for developing and improving one-dimensional models.

9

Future directions

This study aimed to enhance the understanding of PTES performance by developing a full-scale three-dimensional model. The model addressed three important aspects: heat transfer within PTES, inlet mixing assessment within PTES, and the interaction between PTES and surrounding soil. The proposed method offers a potential solution for improving the accuracy of one-dimensional models in a straightforward manner.

However, it is important to acknowledge that there are certain uncertainties and limitations associated with the model due to factors such as measurement uncertainties and mathematical methods employed. In this case, these conclusions drawn from this study may not be directly applicable to all operational scenarios and may require additional validation in a broader range of working conditions. Therefore, further research is needed to get a more complete picture of PTES technology.

First, as discussed in Chapter 2, the construction of PTES is influenced by various factors, and currently, PTES projects are predominantly concentrated in a few countries. While many other countries may not be aware of the potential for implementing PTES systems. Therefore, it is recommended to conduct a macro analysis that take into account factors such as heat demand, geological conditions, construction costs and policy frameworks. This can be used to assess the applicability and viability of PTES in different regions.

Second, as analyzed in Chapter 4, the proposed method for determining the grid size distribution in multi-node models provides a fast and effective way to enhance their accuracy. However, in the context of one-dimensional models, there are other methods that can be applied to reduce numerical diffusion within PTES. These methods are plug flow and adaptive-grid method. It is recommended to explore and compare the effects of these methods under the same boundary conditions. In this case, their effectiveness in capturing the dynamic behavior of PTES systems can be assessed.

Third, as mentioned in Chapter 5 the research conclusions are obtained under limited representative cases due to the computational effort of CFD calculation. The wider applicability of these correlations needs to be further evaluated. To address this, a hybrid approach that combines CFD calculation and machine learning can be employed. By using a hybrid approach, the fundamental dataset can be quickly enhanced for a variety of situations, improving the accuracy and applicability of the findings. Moreover, it is essential to consider the non-uniform temperature distribution of PTES under actual operating conditions. The practical significance of this study's findings can be strengthened by including suitable performance indexes for non-uniform temperature distribution, assuring their applicability in the actual PTES applications.

Fourth, the development of a three-dimensional model to study the interaction between PTES and the surrounding soil is a significant contribution of this study. Although three-dimensional modelling has often been avoided in the past due to the computational effort involved, the model developed in this study strikes a balance between computational efficiency and accuracy. Groundwater can significantly impact the heat transfer processes within the PTES system. Therefore, conducting investigations to better understand the influence of groundwater on PTES performance using the developed three-dimensional model would be of great interest.

Fifth, there is still a limited study focused on system-level modeling. However, conducting system-level modeling is critical for understanding the impacts and benefits of integrating PTES in various contexts. The system-level studies can include evaluating the optimal sizing and placement of PTES within the district heating system, identifying the potential challenges and opportunities associated with different system configurations, and assessing the techno-economic viability. Such investigations can provide valuable insights for decision-makers and stakeholders when considering the adoption of PTES in different system configurations.

References

[1] Ritchie H, Roser M, Rosado P. Energy. Published online at OurWorldInData.org. http://ourworldindata.org/energy.

[2] IEA. Greenhouse gas emissions from energy data explorer, IEA, Paris 2021. https://www.iea.org/data-and-statistics/data-tools/greenhouse-gas-emissions-from-energy-data-explorer.

[3] BP p.l.c. Statistical review of world energy 2022 (71st edition). http://www.bp.com/en/global/corporate/energy-economics/statistical-review-of-world-energy.

[4] REN21. Renewables 2022 global status report. 2022. http://www.ren21.net/gsr-2022/.

[5] IEA. Renewables 2021 analysis and forecast to 2026, 2021. http://doi.org/10.1787/96bc279a-en.

[6] Buonomano A, Forzano C, Palombo A, Russo G. Solar-assisted district heating networks: Development and experimental validation of a novel simulation tool for the energy optimization. Energy Conversion and Management 2023;288:117133. https://doi.org/10.1016/j.enconman.2023.117133.

[7] Tschopp D, Tian Z, Berberich M, Fan J, Perers B, Furbo S. Large-scale solar thermal systems in leading countries: A review and comparative study of Denmark, China, Germany and Austria. Applied Energy 2020;270:1–31. https://doi.org/10.1016/j.apenergy.2020.114997.

[8] Xu J, Wang RZ, Li Y. A review of available technologies for seasonal thermal energy storage. Solar Energy 2014;103:610–38. https://doi.org/10.1016/j.solener.2013.06.006.

[9] Ann Cruickshank C, Baldwin C. Sensible thermal energy storage: diurnal and seasonal. Elsevier Inc.; 2016. https://doi.org/10.1016/B978-0-12-803440-8.00015-4.

[10] Olsthoorn D, Haghighat F, Mirzaei PA. Integration of storage and renewable energy into district heating systems: A review of modelling and optimization. Solar Energy 2016;136:49–64. https://doi.org/10.1016/j.solener.2016.06.054.

[11] Egging-Bratseth R, Kauko H, Knudsen BR, Bakke SA, Ettayebi A, Haufe IR. Seasonal storage and demand side management in district heating systems with demand uncertainty. Applied Energy 2021;285. https://doi.org/10.1016/j.apenergy.2020.116392.

[12] Mahon H, O'Connor D, Friedrich D, Hughes B. A review of thermal energy storage technologies for seasonal loops. Energy 2022;239:122207. https://doi.org/10.1016/j.energy.2021.122207.

[13] Bott C, Dressel I, Bayer P. State-of-technology review of water-based closed seasonal thermal energy storage systems. Renewable and Sustainable Energy Reviews 2019;113:109241. https://doi.org/10.1016/j.rser.2019.06.048.

[14] Ochs F, Dahash A, Tosatto A, Bianchi Janetti M. Techno-economic planning and construction of cost-effective large-scale hot water thermal energy storage for Renewable District heating systems. Renewable Energy 2020;150:1165–77. https://doi.org/10.1016/j.renene.2019.11.017.

[15] Guelpa E, Verda V. Thermal energy storage in district heating and cooling systems: A review. Applied Energy 2019;252:113474. https://doi.org/10.1016/j.apenergy.2019.113474.

[16] Pelay U, Luo L, Fan Y, Stitou D, Rood M. Thermal energy storage systems for concentrated solar power plants. Renewable and Sustainable Energy Reviews 2017;79:82–100. https://doi.org/10.1016/j.rser.2017.03.139.

[17] Sarbu I, Sebarchievici C. A comprehensive review of thermal energy storage. Sustainability (Switzerland) 2018;10. https://doi.org/10.3390/su10010191.

[18] Schmidt T, Pauschinger T, Sørensen PA, Snijders A, Djebbar R, Boulter R, et al. Design aspects for large-scale pit and aquifer thermal energy storage for district heating and cooling. Energy Procedia 2018;149:585–94. https://doi.org/10.1016/j.egypro.2018.08.223.

[19] Mauthner F, Herkel S. Technology and demonstrators - technical teport subtask C - part C1. 2016:1–31. http://task52.iea-shc.org/data/sites/1/publications/IEA-SHC-Task52-STC1-Classification-and-benchmarking-Report-2016-03-31.pdf.

[20] Jensen MV, PlanEnergi. Task 45 Large systems seasonal pit heat storages - Guidelines for materials & construction 2014. https://task45.iea-shc.org/fact-sheets.

[21] Amiri L, de Brito MAR, Baidya D, Kuyuk AF, Ghoreishi-Madiseh SA, Sasmito AP, et al. Numerical investigation of rock-pile based waste heat storage for remote communities in cold climates. Applied Energy 2019;252. https://doi.org/10.1016/j.apenergy.2019.113475.

[22] Xiang Y, Xie Z, Furbo S, Wang D, Fan J. A comprehensive review on pit thermal energy storage: recent application, design and simulation approaches. Journal of Energy Storage 2022;55,105716. http://doi.org/10.1016/j.est.2022.105716.

[23] Dahash A, Ochs F, Janetti MB, Streicher W. Advances in seasonal thermal energy storage for solar district heating applications: A critical review on large-scale hot-water tank and pit thermal energy storage systems. Applied Energy 2019;239:296–315. https://doi.org/10.1016/j.apenergy.2019.01.189.

[24] Renaldi R, Friedrich D. Techno-economic analysis of a solar district heating system with seasonal thermal storage in the UK. Applied Energy 2019;236:388–400. https://doi.org/10.1016/j.apenergy.2018.11.030.

[25] Kubiński K, Szabłowski Ł. Dynamic model of solar heating plant with seasonal thermal energy storage. Renewable Energy 2020;145:2025–33. https://doi.org/10.1016/j.renene.2019.07.120.

[26] Winterscheid C. Dronninglund District Heating Monitaring Data Evaluation for the Years 2015-2017 2017.

[27] Ochs F, Nußbicker J, Marx R, Koch H, Heidemann W, Müller-Steinhagen H. Solar assisted district heating system with seasonal thermal energy storage in Eggenstein-Leopoldshafen. Conference Proceedings 2008.

[28] Schmidt T, Pauschinger T, Sørensen PA, Snijders A, Djebbar R, Boulter R, et al. Design aspects for large-scale pit and aquifer thermal energy storage for district heating and cooling. Energy Procedia 2018;149:585–94. https://doi.org/10.1016/j.egypro.2018.08.223.

[29] Novo A V., Bayon JR, Castro-Fresno D, Rodriguez-Hernandez J. Review of seasonal heat storage in large basins: Water tanks and gravel-water pits. Applied Energy 2010;87:390–7. https://doi.org/10.1016/j.apenergy.2009.06.033.

[30] Chang C, Leng G, Li C, Nie B, She X, Peng X, et al. Investigation on transient cooling process in a water heat storage tank with inclined sidewalls. Energy Procedia 2017;142:142–7. https://doi.org/10.1016/j.egypro.2017.12.023.

[31] Furbo S. Hot water tanks for solar heating systems 2004.

[32] Deng Y, Sun D, Niu M, Yu B, Bian R. Performance assessment of a novel diffuser for stratified thermal energy storage tanks – The nonequal-diameter radial diffuser. Journal of Energy Storage 2021;35. https://doi.org/10.1016/j.est.2021.102276.

[33] Kim H, Park D, Park ES, Kim HM. Numerical modeling and optimization of an insulation system for underground thermal energy storage. Applied Thermal Engineering 2015;91:687–93. https://doi.org/10.1016/j.applthermaleng.2015.08.070.

[34] Dahash A, Ochs F, Janetti MB, Streicher W. Advances in seasonal thermal energy storage for solar district heating applications: A critical review on large-scale hot-water tank and pit thermal energy storage systems. Applied Energy 2019;239:296–315. https://doi.org/10.1016/j.apenergy.2019.01.189.

[35] Ochs F. Modelling large-scale thermal energy stores.University of Stuttgart, 2009.

[36] Jiaqi. TRNSYS modelling and simulations of thermal storage water pits. Technical University of Denmark, 2020.

[37] TESSLibs 18, Component libraries of the TRNSYS simulation environment - Volume 12 solar library mathmatical reference.

[38] Xie Z, Xiang Y, Wang D, Kusyy O, Kong W, Furbo S, et al. Numerical investigations of long-term thermal performance of a large water pit heat storage. Solar Energy 2021;224:808–22. https://doi.org/10.1016/j.solener.2021.06.027.

[39] Pan X, Xiang Y, Gao M, Fan J, Furbo S, Wang D, et al. Long-term thermal performance analysis of a large-scale water pit thermal energy storage. Journal of Energy Storage 2022;52:105001. https://doi.org/10.1016/j.est.2022.105001.

[40] Bai Y, Wang Z, Fan J, Yang M, Li X, Chen L, et al. Numerical and experimental study of an underground water pit for seasonal heat storage. Renewable Energy 2020;150:487–508. https://doi.org/10.1016/j.renene.2019.12.080.

[41] Buoro D, Pinamonti P, Reini M. Optimization of a Distributed Cogeneration System with solar district heating. Applied Energy 2014;124:298–308. https://doi.org/10.1016/j.apenergy.2014.02.062.

[42] Campos Celador A, Odriozola M, Sala JM. Implications of the modelling of stratified hot water storage tanks in the simulation of CHP plants. Energy Conversion and Management 2011;52:3018–26. https://doi.org/10.1016/j.enconman.2011.04.015.

[43] PlanEnergi, Niras. Dronninglund solar thermal plant. 2014:1–12. https://www.dronninglundfjernvarme.dk/media/2984/brochure_dronninglund_2015_booklet_eng_web_.pdf

[44] PlanEnergi. Sunstore 3. Fase 1: Projektering og udbud 2011.

[45] Kallesøe AJ, Vangkilde-Pedersen T. Underground Thermal Energy Storage (UTES) – state-of-the-art, example cases and lessons learned. 2019.

[46] Chung JD, Cho SH, Tae CS, Yoo H. The effect of diffuser configuration on thermal stratification in a rectangular storage tank. Renewable Energy 2008;33:2236–45. https://doi.org/10.1016/j.renene.2007.12.013.

[47] Shah LJ, Furbo S. Entrance effects in solar storage tanks. Solar Energy 2003;75:337–48. https://doi.org/10.1016/j.solener.2003.04.002.

[48] Dimention of pipe. CAD drawing.

[49] Hight of pipe. CAD drawing.

[50] Gauthier G. Benchmarking and improving models of subsurface heat storage dynamics. Comparison of Danish Ptes and BTES installation measurements with their corresponding TRNSYS models. 2020.

[51] Sifnaios I, Jensen AR, Furbo S, Fan J. Performance comparison of two water pit thermal energy storage (PTES) systems using energy, exergy, and stratification indicators. Journal of Energy Storage 2022;52:104947. https://doi.org/10.1016/j.est.2022.104947.

[52] Sifnaios I, Gauthier G, Trier D, Fan J, Jensen AR. Dronninglund water pit thermal energy storage dataset. Solar Energy 2023;251:68–76. https://doi.org/10.1016/j.solener.2022.12.046.

[53] ANSYS Fluent Theory Guide 2019 R2, ANSYS.

[54] Song J, Bahnfleth WP, Cimbala JM. Parametric study of single-pipe diffusers in stratified chilled water storage tanks (RP-1185). HVAC and R Research 2004;10:345–65. https://doi.org/10.1080/10789669.2004.10391108.

[55] Fan J, Huang J, Chatzidiakos A, Furbo S. Experimental and theoretic investigations of thermal behavior of a seasonal water pit heat storage. ISES Solar World Congress 2017. 2017:714–25. https://doi.org/10.18086/swc.2017.13.03.

[56] Chatzidiakos A. CFD Calculations for Solar Water Pond Heat Storages. Technical University of Denmark. 2016.

[57] NMC. Nomalen 28N 2011.

[58] Dahash A, Ochs F, Tosatto A, Streicher W. Toward efficient numerical modeling and analysis of large-scale thermal energy storage for renewable district heating. Applied Energy 2020;279:115840. https://doi.org/10.1016/j.apenergy.2020.115840.

[59] KAT. Experimental investigation of possible use of hdpe as thermal storage material in thermal storage type solar cookers. International Journal of Research in Engineering and Technology 2015;04:92–9. https://doi.org/10.15623/ijret.2015.0412019.

[60] SOLMAX. Produktinformation Hypernet.

[61] Dannemand Andersen J, Bødker L, Jensen M V. Large thermal energy storage at Marstal district heating. 18th International Conference on Soil Mechanics and Geotechnical Engineering 2013;4:3351–4.

[62] Moradifam A, Nachman A, Tamasan A. Determination of thermal conductivity of

coarse and fine sand soils. SIAM Journal on Mathematical Analysis 2012;44:3969–90. https://doi.org/10.1137/120866701.

[63] Pagola MA, Jensen R. L, Madsen S, Poulsen SE. Measurement of Thermal Properties of Soil and Concrete Samples. Department of Civil Engineering Aalborg University DCE Technical Reports, No 235 2017.

[64] Łukawska A, Ryzynski G, Zerun M. Serial laboratory effective thermal conductivity measurements of cohesive and non cohesive soils for the purpose of shallow geothermal potential mapping and databases - methodology and testing procedure recommendations. Energies 2020;13:914. https://doi:10.3990/en13040914.

[65] Bulnes FK, Gluesenkamp KR, Rendall J. Comparison of plug flow and multi-node stratified tank modeling approaches regarding computaional efficiency and accuracy. Inetrnational Mechanical Engineering Congress and Exposition 2020:1–9.

[66] Unrau C. Numerical investigation of one-dimensional storage tank models and the development of analytical modelling techniques. McMaster University, 2017.

[67] Xiang Y, Gao M, Furbo S, Wang D, Tian Z, Fan J. Heat transfer of a large-scale water pit heat storage under transient operations. Journal of Energy Storage 2022;55:105455. https://doi.org/10.1016/j.est.2022.105455.

[68] Karim MA. Experimental investigation of a stratified chilled-water thermal storage system. Applied Thermal Engineering 2011;31:1853–60. https://doi.org/10.1016/j.applthermaleng.2010.12.019.

[69] Zachár A, Farkas I, Szlivka F. Numerical analyses of the impact of plates for thermal stratification inside a storage tank with upper and lower inlet flows. Solar Energy 2003;74:287–302. https://doi.org/10.1016/S0038-092X(03)00188-9.

[70] Zurigat YH, Ghajar AJ, Moretti EM. Stratified Thermal Storage Tank Inlet Mixing Characterization 1988;30:99–111.

[71] Yee CK, Lai FC. Effects of a porous manfold on thermal stratification in a liquid storage tank. Solar Energy 2001;71:241–54. https://doi.org/10.1016/S0038-092X(01)00043-3.

[72] Davidson JH, Adams DA, Miller JA. A coefficient to characterize mixing in solar water storage tanks. Journal of Solar Energy Engineering, Transactions of the ASME 1994;116:94–9. https://doi.org/10.1115/1.2930504.

[73] Xiang Y, Gao M, Furbo S, Fan J, Wang G, Tian Z, et al. Assessment of inlet mixing during charge and discharge of a large-scale water pit heat storage. Submit to Renewable Energy. 2023.

[74] Xu C, Liu M, Jiao S, Tang H, Yan J. Experimental study and analytical modeling on the thermocline hot water storage tank with radial plate-type diffuser. International Journal of Heat and Mass Transfer 2022;186. https://doi.org/10.1016/j.ijheatmasstransfer.2021.122478.

[75] Baeten B, Confrey T, Pecceu S, Rogiers F, Helsen L. A validated model for mixing and buoyancy in stratified hot water storage tanks for use in building energy simulations. Applied Energy 2016;172:217–29. https://doi.org/10.1016/j.apenergy.2016.03.118.

[76] Rendall J, Abu-Heiba A, Gluesenkamp K, Nawaz K, Worek W, Elatar A. Nondimensional convection numbers modeling thermally stratified storage tanks: Richardson's number and hot-water tanks. Renewable and Sustainable Energy Reviews 2021;150:111471. https://doi.org/10.1016/j.rser.2021.111471.

[77] Njoku HO, Ekechukwu O V., Onyegegbu SO. Analysis of stratified thermal storage systems: An overview. Heat and Mass Transfer/Waerme- Und Stoffuebertragung 2014;50:1017–30. https://doi.org/10.1007/s00231-014-1302-8.

[78] Abu-Hamdeh NH. Thermal properties of soils as affected by density and water content. Biosystems Engineering 2003;86:97–102. https://doi.org/10.1016/S1537-5110(03)00112-0.

[79] Dahash A, Ochs F, Giuliani G, Tosatto A. Understanding the interaction between groundwater and large-scale underground hot-water tanks and pits. Sustainable Cities and Society 2021;71:102928. https://doi.org/10.1016/j.scs.2021.102928.

Part II Paper

Yutong Xiang, Zichan Xie, Simon Furbo, Dengjia Wang, Meng Gao, Jianhua Fan. (2022). A comprehensive review on pit thermal energy storage: Technical elements, numerical approaches and recent applications, Journal of Energy Storage, 55, 105716. https://doi.org/10.1016/j.est.2022.105716

A comprehensive review on pit thermal energy storage: technical elements, numerical approaches and recent applications

Yutong Xiang[1], Zichan Xie[1,2], Simon Furbo[1], Dengjia Wang[3], Meng Gao[1], Jianhua Fan[1*]

1. Department of Civil Engineering, Technical University of Denmark, Brovej 118, Kgs. Lyngby DK 2800, Denmark
2. Department of Mathematics and Systems Analysis, Aalto University, School of Science, P.O. BOX 11100, Aalto, Finland
3. State Key Laboratory of Green Building in Western China, Xi'an University of Architecture and Technology, Xi'an, Shaanxi 710055, China;

Abstract

Pit thermal energy storage (PTES) is one of the most promising and affordable thermal storage, which is considered essential for large-scale applications of renewable energies. However, as PTES volume increases to satisfy the seasonal storage objectives, PTES design and application are challenged. These difficulties triggered an interest in PTES investigations. This paper aims to identify the success factors and research gaps of PTES by an up-to-date evaluation of 160 recent publications. Existing technical elements that affect PTES thermal properties inclusive geometry design, inlet/outlet design, cover design, and materials, are outlined in depth. Numerical studies are categorized in terms of their mathematical theory and research purposes for a systematic discussion. The current application status of PTES systems worldwide is summarized from four aspects: storage material, geological design, operation strategy, and storage duration. For projects in operation, special attention is given to gathering and comparing operational data on solar fraction, storage efficiency, storage cycle, and PTES temperature. This review outlines the progress and potential directions for PTES design and numerical studies by identifying the research gaps that require further effort.

Keywords: pit thermal energy storage, recent applications, floating cover, liner and insulation material, simulation approaches

Nomenclature

AL	Aluminum	LDPE	Low-density polyethylene
ATES	Aquifer thermal energy storage	PTES	Pit thermal energy storage
BTES	Borehole thermal energy storage	PE	Polyethylene
DTES	Diurnal thermal energy storage	PIR	Polyisocyanurate
ECG	Expanded clay granules	PP	Polypropylene
EGG	Expanded glass granules	PUR	Polyurethane
EPS	Expanded polystyrene	PVC	Polyvinyl chloride
FGG	Foam glass gravel	STES	Seasonal thermal energy storage
GFG	Glass foam gravel	SST	Stainless steel
HDPE	High-density polyethylene	TTES	Tank thermal energy storage

1. Introduction

Buildings account for approx. 40% of the world's annual energy consumption. The operations of buildings, including ventilation, heating, and cooling, have the highest energy demand for buildings. However, the heating market is still dominated by fossil fuel-based equipment and less efficient traditional electric heating products, accounting for nearly 80% of new sales [1]. As a result, the transformation of the heating industry must be accelerated to meet the climate and energy goals.

As the most sustainable energy source at present, solar thermal can cover the heating demand of buildings. Many countries have taken active and effective measures to increase the applications of solar heating systems. Solar heating systems can be divided into two categories: solar heating systems for individual buildings (i.e., small and medium scale) and solar heating systems for a group of buildings via a thermal grid (i.e., large-scale) [2]. Large-scale solar heating systems perform better than small-scale systems in terms of system efficiency and energy cost. Therefore, the number of large-scale systems has grown significantly over the past decade, especially outside Europe (as shown in Fig.1 [3]) [4]. By the end of 2020, there are approximately 470 solar district heating systems (>350kW$_{th}$; 500m^2) in operation worldwide.

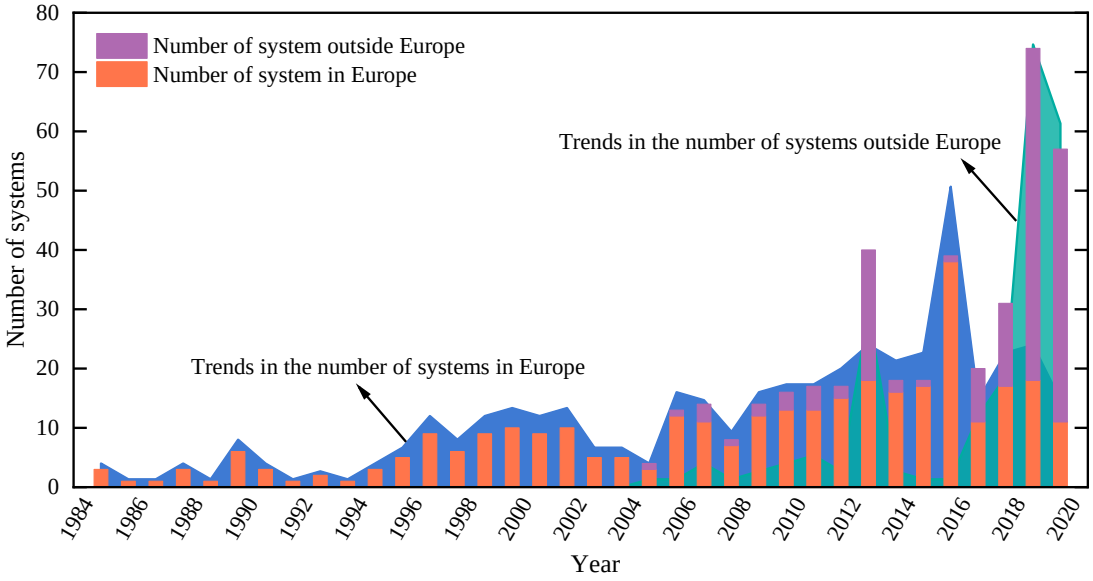

Fig.1 Number of existing solar district heating systems worldwide during the last 35 years [3].

However, solar thermal energy faces challenges in terms of stability and reliability, as it is intermittent. In this context, the integration of thermal energy storage into solar heating systems has been proposed to address these challenges [5,6]. Thermal energy storage can be classified into diurnal thermal energy storage (DTES) and seasonal thermal energy storage (STES) [5,7,8] according to the energy storage durations. Nevertheless, STES systems are often seen as challenging from a technical point of view. The requirement for large capacities for seasonal storage continues to drive up the construction STES systems. Fisch et al. [9] found that solar district heating systems with STES could deliver 50-70% of the yearly demand, whereas those with DTES could only provide 10-20% of the annual demand, demonstrated explicitly by summarizing twenty-seven large-scale solar district heating systems. The benefit of STES systems has also been shown in terms of solar fraction (defined as the percentage of the total thermal load satisfied by solar energy) [2,10–12], where utilizing STES could increase the solar

fraction from 5-15% to 25-50% compared to using DTES. Therefore, STES is an effective way to improve the efficiency of large-scale solar district heating systems [13].

The best-known types of STES in a solar district heating system can be generally categorized into four categories [14–18]: tank thermal energy storage (TTES), pit thermal energy storage (PTES), borehole thermal energy storage (BTES), and aquifer thermal energy storage (ATES). The research outputs of the above four systems is illustrated in Fig.2, together. Regarding these four types of STES systems, the majority of research has been done on BTES, followed by TTES, ATES, and PTES. This is because more projects for the BTES and ATES systems are undertaken as a results of low construction costs of the early years. Furthermore, the geometry of TTES is more flexible and less location dependent. As far as we know, TTES is normally insulated with an insulating layer due to its enormous surface area [19]. Additionally, its size is constrained when TTES is built above the ground.

Although the number of PTES investigations is lower than the number of other STES, it is broadly seen that PTES system is superior to other STES systems in terms of energy density, geometry size, construction site independence, operation characteristics, and construction costs, especially the investment costs per m^3 water equivalent of PTES have proven to be the lowest when the storage volume exceeds 60,000 m^3 [2,20]. Therefore, it has been regarded as a promising thermal storage technology in recent years due to the requirement for large storage capacity.

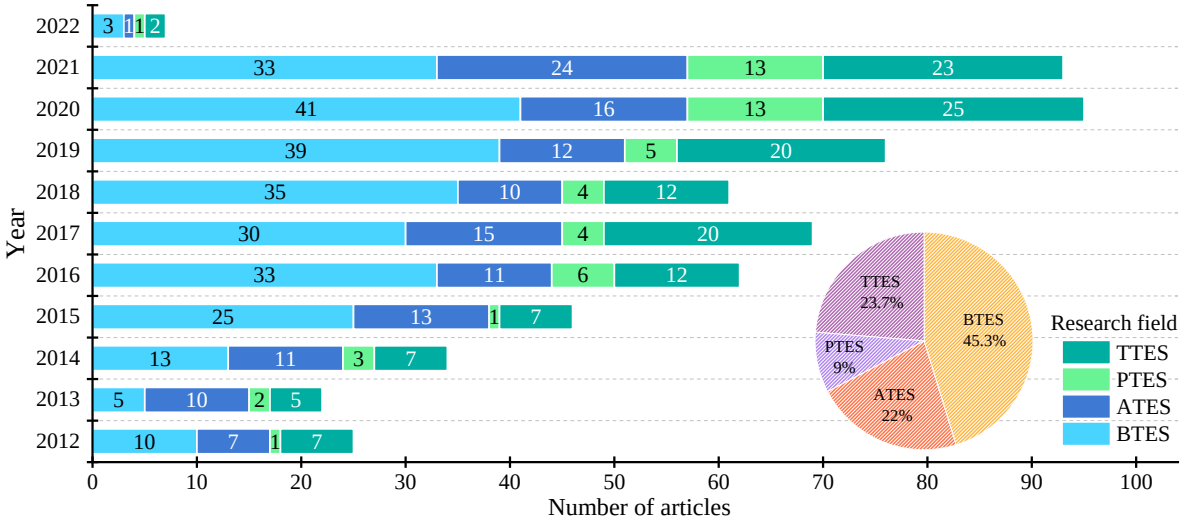

Fig.2 Number of articles related to seasonal thermal energy storage from 2012 to 2022.

Since 1985, the solar district heating system with PTES has been developed and reviewed in several documents [4,13,14,16,21–24]. However, most of these papers mainly focus on general information and comparisons with other types of STES, and discussions on PTES are not really in-depth. Only a few reviews are entirely relevant to PTES, including those by Novo et al. [22], Bott et al. [14], and Dahash et al. [24]. The technological basis and application status of waterproofing and thermal insulation materials were summarized [14,22]. As the key to determine the service life of PTES, comparative studies on material performance are not enough. Moreover, as constructing large-scale PTES systems trends to be costly, the importance of modeling these systems to ensure the economic viability of the system and the efficient planning layout is powerfully demonstrated. In this context, a typical research recently presented by Dahash et al. [24] paid more attention to discussing the PTES modeling parameters and models.

Despite the efforts by the authors mentioned above regarding introduction, construction, modeling method, and performance indicators, we detected there are still some deficiencies in the summary of PTES. Newly developed technical elements and modeling methods have not been updated. The technical challenges in practice have not been addressed properly. Furthermore, the different Numerical approaches developed for PTES have not been thoroughly analyzed and compared.

Therefore, this work aims to provide a thorough update to help better understand the research and development of PTES. Compared with the previous review works, the innovations of this paper are that:

- It covers all the technical aspects that affect PTES thermal performance, especially novel designs in recent years;
- It provides a list of thermal properties of a variety of materials currently used on PTES, along with their strengths, weaknesses and application status;
- It reviews systematically the numerical studies, focusing on the analysis of the mathematical theory concerning different methods;
- It discusses the application status of PTES and emphasizes the lessons learned from operational data across all projects.

This paper can be easily used by researchers and industry experts who need a quick and handy reference in PTES system design. Additionally, based on this review, readers may identify the existing research gaps in technical elements, numerical studies, and applications, which will aid them in proposing new research directions to fill the gaps.

The structure of this paper is illustrated in Fig.3.

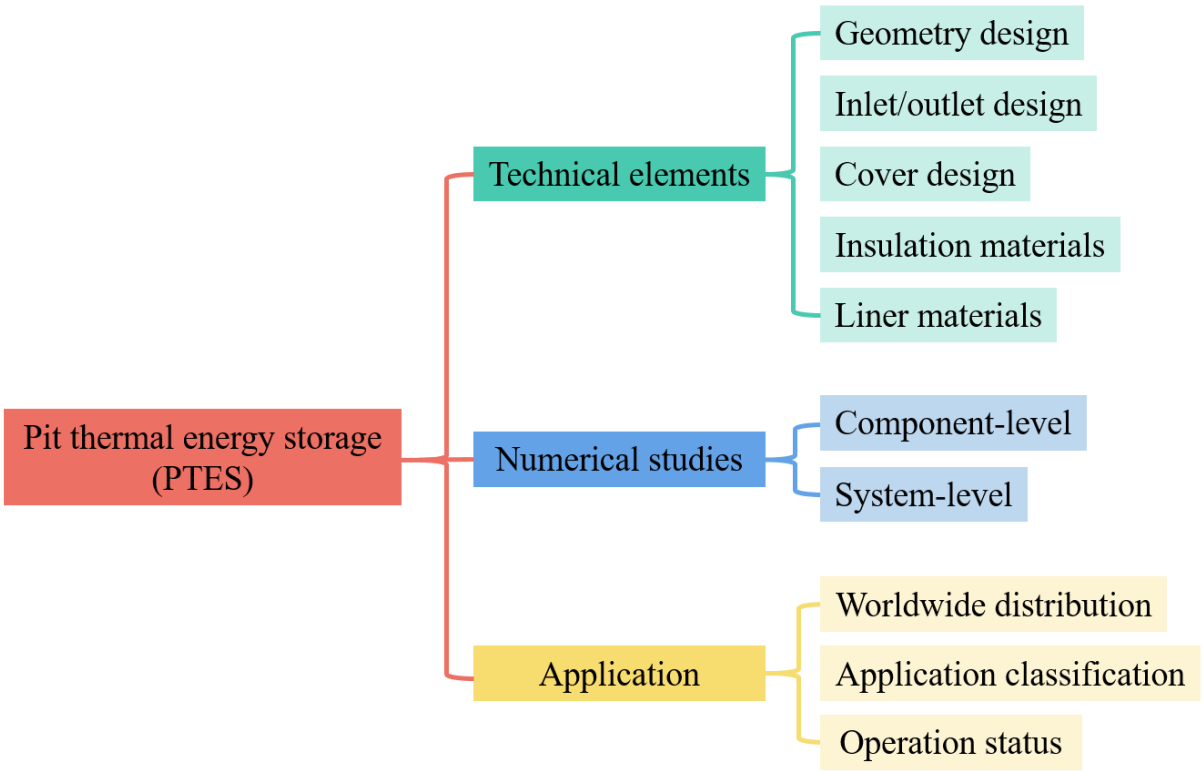

Fig.3 Research work conducted for PTES technology

First, a summary of the key technical elements of PTES design is provided, including geometry, inlet/outlet diffusers, cover, insulation material, and liner material, highlighting PTES structure design challenges to understand possible further solutions and improvements.

Recent research limitations are remarked by comparing recently used insulation and liner materials. The analysis of up-to-date numerical studies on PTES follows. They are categorized so the readers can understand the characteristics and applicability of various models. Additionally, models' calculation accuracy through experimental validation is compared, along with a detailed analysis of recent model assumptions and corrections with an aim to point out potential research directions. Finally, the implemented PTES systems worldwide are summarized with particular attention to storage material, geological design, operation strategy, and storage duration. In order to learn lessons from actual operations, particular efforts are paid to collect and compare operational data on system solar fraction, storage efficiency, and operation temperatures of PTES.

2. Technical elements of PTES

Due to the dispatchability and flexibility to incorporate various renewable energy systems, PTES is an essential part of solar district heating systems [25]. The thermal energy can be stored in an excavated ground enclosed with waterproof liners or can be stored in an artificial store composed of concrete or stainless steel for solar district heating systems with PTES [22,26].

The structure and the materials used on PTES are primarily the two factors that limit its development. Though conceptually comparable to TES, PTES is more difficult to implement because of its structure and installation location. Given that the thermal performance depends on a wide range of interrelated factors, the design of a PTES is frequently considered sophisticated. Such factors are geometry, inlet/outlet design, and cover design. In addition, the materials used for PTES (i.e., insulation and liner) can severely affect the performance and the lifetime. In the following section, a thorough summary of the current technological status of the structure and materials, discussion and recommendations for future development are provided.

2.1 Structure of PTES

2.1.1 Geometry of PTES

Due to lower construction cost, storage geometries with slopes have been developed, such as pyramid stumps with rectangular cross-sections (Fig.4 (a)) and truncated cones with circular cross-sections (Fig.4 (b)). Geometry (a) is more commonly used due to conventional construction than geometry (b). Additionally, to satisfy the greater PTES volume requirements, a complex pyramid stump was created and used in the Vojens plant (see Fig. 4 (c)).

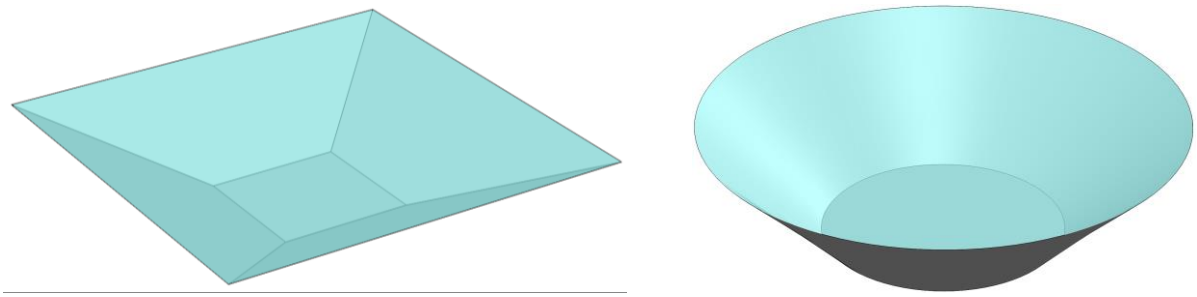

(a) (b)

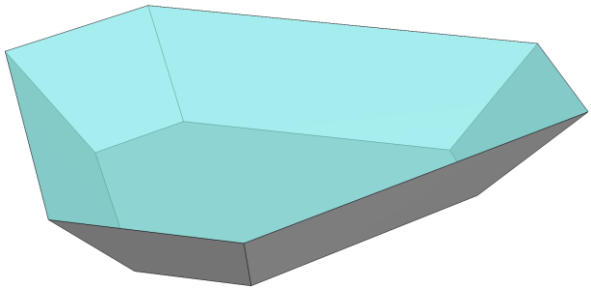

(c)

Fig.4 Geometries of PTES: (a) Truncated pyramid stump; (b) Truncated cone; (c) Complicated pyramid stump

The slope angle is the angle between the sidewall and horizontal plane. It should be noticed in Table 1 that the slope angle is around 30 for PTES larger than 10,000 m^3 to prevent sidewall collapse [22,27–29]. In addition to the influence of the construction site's geological conditions on the slope angle determination, the selection of slope angle is also constrained by the thermal performance of PTES since the slope angle impacts the surface-to-volume ratio, which in turn affects heat loss [5,14,30]. A simulated analysis by Chang et al. [26] revealed that high slope angles were better for establishing and maintaining thermal stratification, and the heat loss could be reduced by increasing the slope angle. In this case, it seems reasonable to use the highest possible slope angle from the standpoint of reducing heat loss, improving thermal stratification, and reducing costs.

However, moving groundwater can enormously increase heat loss from the lower parts of PTES. Therefore, future research is required to elucidate the ideal geometry for PTES installed in groundwater-moving sites.

Table 1 Information on PTES of the existing plants

Location	Heat store material	Volume (m^3)	Area[(1)] (m^2)	A/V[(2)]	Height (m)	Slope angle(°)	Inlet/outlet arrangement[(3)]	Liner material	Insulation material	References
Lambohov	Gravel& water	10000	1750	--	--	90	--	Butyl Rubber	Clay granules	[30,31]
Stuttgart	Gravel&pebbles&water	1050	835	0.84	5	45	Heat exchanger from bottom to top	HDPE	Pumice and PUR	[32–34]
Julich	Water	2500	--	--	--	--	Horizontal heat exchanger in the bottom, the middle and the top	PP	Mineralwolle	[35]
Augsburg	Gravel& water	6500	--	--	--	90	--	--	--	[36,37]
Chemnitz	Gravel& water	8000	3375	0.43	6.76	90	Heat exchanger from bottom to top	HDPE	XPS	[30,31]
Steinfurt	Gravel& water	1500	1305	0.87	--	50	Heat exchanger from bottom to top	Foil PP Film	FGG EGG	[30,38]
Eggenstein	Gravel&sand	4500	1924.9	0.428	9	26 (top) 35 (bottom)	One is embedded in the bottom, the other in the top	HDPE	FGG Cellular particles	[27,39,40]
Marstal	Water	75000	20298	0.233	16	32.78	(b)	HDPE	Nomalen	[22,25,41–43]
Dronninglund	Water	60000	17076	0.288	16	26.6	(a)	HDPE Al	Leca	[28,41,44–47]
Gram	Water	122000	28893	0.237	15	20	(b)	HDPE		[4,48,49]
Vojens	Water	200000	--	--	15	--	(b)	HDPE	Leca	[50–52]
Toftlund	Water	70000	19204	0.274	14.5	27	(b)	HDPE	Leca	[53–55]
Langkazi Tibet	Water	15000	6748	0.447	--	27	(a)	HDPE		[56–58]

[(1)] Surface area of PTES (including the top surface, sidewalls, and bottom surface)

[(2)] Ratio of PTES surface area to PTES volume

(3) The inlet and outlet arrangement of (a), (b) are shown in Fig.6

2.1.2 The inlet and outlet design

Thermal stratification in solar stores significantly impacts the thermal performance of solar district heating systems, regardless of the type of system [59]. Investigations have shown that water supplied to hot water tanks can create mixing that spoils the thermal stratification in the storage tanks. As a result, all inlets and outlets must be designed to make the mixing as small as possible [60]. Compared with the widely used domestic hot water tanks, the size of thermal energy storage in solar district heating systems is larger. Diffuser design is typically adopted to reduce the velocity of water entering the thermal energy storage and encourage stratification by promoting laminar flow during charging and discharging processes.

Various structural characteristics may have an impact on the performance of the diffuser, and different diffusers may be useful for different thermal energy storage. Some diffuser designs, including H-type, octagonal, and radial diffusers, have successfully been investigated [61]. Shah and Furbo [59] investigated the impact of three inlet designs (i.e., pipe design, Metro design, and plate design) on the thermal conditions inside the storage tank. Both simulation and experimental results proved that the plate type design had the highest degree of stratification. Chung et al. [62] studied the effect of design factors on the stratification of a rectangular storage tank by comparing three diffuser designs (i.e., the H-beam type, the radial plate type, and the radial adjusted plate type). Study results showed that the Reynolds number was the most critical parameter, and the radial plate type diffusers suppressed the local mixing more effectively than the H-beam type. Fagerlund Carlsson [63] compared the effect of different inlet designs and volume flows on mixing and found that the parallel plates were the best design that reduced mixing most, while the T-piece was the second-best design. The perforated and the direct pipe designs ranked third and fourth. Moncho-Esteve et al. [64,65] studied the influence of different inlet constructions on thermal stratification in the storage tank. In their case, the sintered bronze conical diffuser performed better than other inlet constructions. Also, Assari [66] investigated the influence of the inlet and outlet location inside the storage tank on thermal stratification by simulation and experiment, respectively. He discovered that better thermal stratification occurred with an inlet of hot water in the highest position and cold water outflow from the lowest part. Findeisen et al. [67–70] conducted comprehensive studies to investigate the influence of radial diffusers on thermal stratification using CFD. They pointed out that thermal stratification could be significantly improved due to an optimized position of the diffuser in the storage tank. Besides, they proposed a new radial diffuser with a flow-optimized shape. Recently, Deng et al. [61] proposed a novel non-equal diameter radial diffuser and demonstrated that it had nearly the same thermal stratification performance as the equal diameter radial diffuser but significantly reduced the cost. Besides, the thermal stratification was optimized when the ratio of the long baffle diameter and the tank diameter was 1/3, the ratio of the short baffle diameter and the long baffle diameter was 1/3, and the distance between the two baffles was as small as possible.

In summary, radial diffuser design has been adopted in most existing PTES due to its simple structure, convenient installation, low cost, and good thermal stratification [61]. Radial diffuser design typically consists of two circular plates mounted parallel to each other (shown in Fig.5 (a)), connected to the inlet/outlet pipe to form the water path. To help produce uniform flow, guiding elements can be build-in (shown in Fig.5 (b)). In real PTES application, diffusers are arranged at different heights at the top, the middle, and the bottom. Depending on the year-

round operating conditions and PTES temperature distribution throughout the year, diffusers are either taken as inlet or outlet.

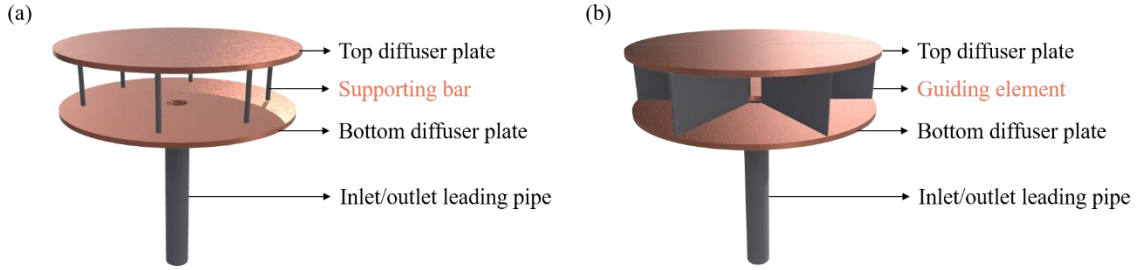

Fig.5 Diffuser design: (a) Diffuser design without guiding elements; (a) Diffuser design with guiding elements

At present, there are generally two ways for the leading pipes to enter the PTES to connect the diffusers. One way is to enter through the bottom of the PTES (Fig.6 (a) [71]), which is used in the Dronninglund and Langkazi plants. The other way is to enter through the side of the PTES (Fig.6 (b) [25]), which is used in the Marstal, Vojens, and Toftlund plants. Compared to the design entering through the side, leading pipes entering the bottom perpendicular to the liner makes it easier to connect the concrete structure and flange under the liner [72]. However, the leading pipes have to be buried deeper in the ground, which may increase the thermal loss.

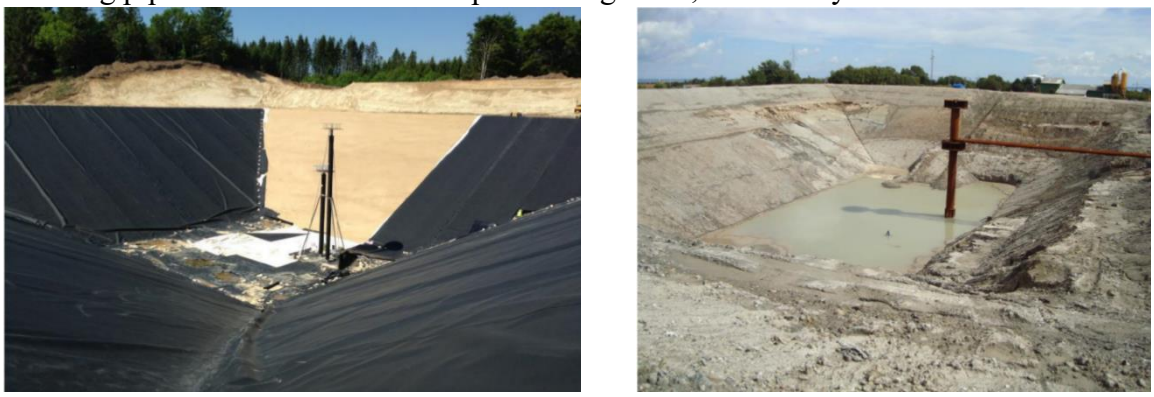

(a) (b)

Fig.6 Arrangement of inlet/outlet of existing PTES application: (a) Leading pipe enter PTES through the bottom [71]; (b) Leading pipe enter PTES through the side [25]

2.1.3 The cover

Most heat losses occur at the top of the PTES, based on the lessons learned from completed projects. Additionally, the cover accounts for most of the cost due to the complicated structure. For these reasons, much effort has been put into investigating different designs and materials [20,44,72–74]. There are now three main technical challenges.

One of the challenges is the insulation and liner material. Usually, the cover has three main layers (an insulation layer in the middle and two liner layers on both sides of the insulation). Fig.7 (a) [10,25] shows the cover design of the Marstal and Dronninglund projects. Three layers of 80 mm Nomalén insulation were installed in the middle. One 1.5 mm and one 2 mm HDPE line, correspondingly, were put above and below the insulation layers. Steel anchors were buried within the insulation layer to maintain the shape, and the hypenet CN-E layer was used to protect the liner. The cover design of Vojens and Gram projects is depicted in Fig.7 (b) [75]. For two reasons, Leca was chosen as the insulation material instead of Nomalén. One was that

Leca was flexible and easy to install. The other was that Leca outperformed Nomalén in terms of thermal performance. However, there is no document to state the improvement clearly.

One of the challenges is to remove the moisture inside the cover. Moisture may result from the implementation phase of the cover, water diffusion through the liner, or damage to the liners. In this case, the insulation material will be degraded, resulting in increased thermal conductivity and a short cover lifetime. Setting a ventilation gap (3-6 mm) between the liner and the insulation is a practical construction to remove moisture. At the same time, ventilation hoses are connected to the gap to help suck the moisture out in time.

The rainwater presents another challenge. Rainwater introduces a risk of puddles of water on the cover, which presses or even destroys the bulk insulation. Because of this, the cover is typically constructed with a 2 percent slope towards the center of the cover. Additionally, the weight pipes made of HDPE with concrete inside will place on the top of the cover [76]. On the one hand, to help keep the liners in position in case of wind. On the other hand, direct rainwater collected on the top of the cover to the center pump. The weight pipe layout on the top of the cover of the Marstal project is presented in Fig.8 (a) [77]. The diameter of the pipe increases with distance from the center. In this manner, rainwater can be gathered in the center to lessen the possibility of water puddles on the cover [28]. Worth pointing out that additional effort should be paid when the geometric shape of the cover is changed. The arrangement and dimensions of the weight pipes need to be adjusted, as seen in Fig.8 (b) [10].

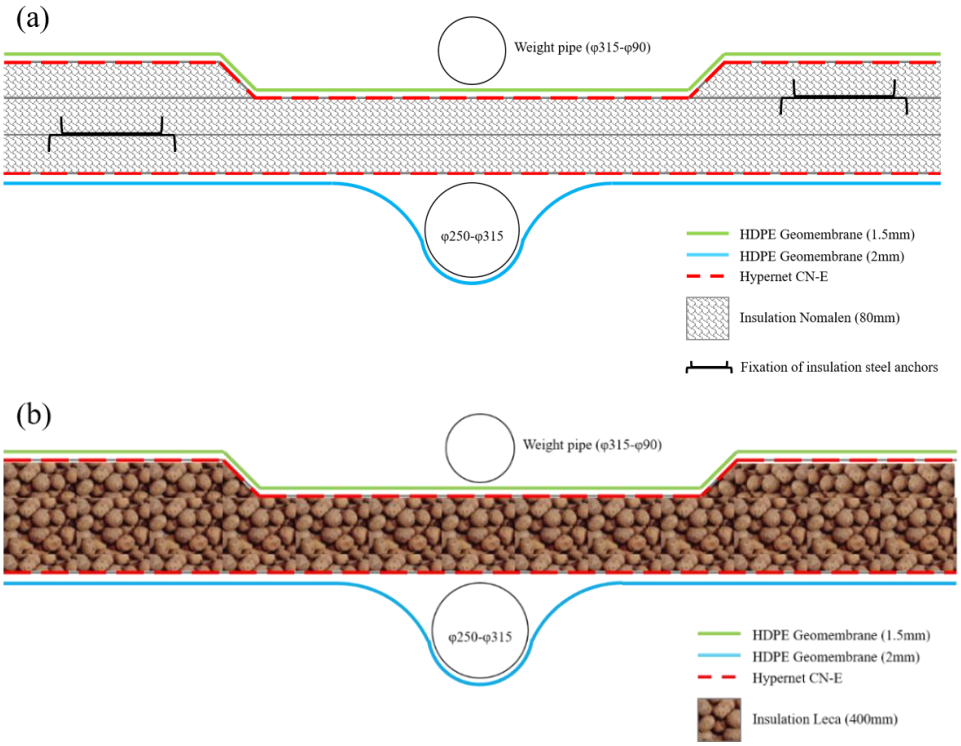

Fig.7 Cross-section of the cover: (a) Cross-section of the cover of Marstal and Dronninglund projects [10,25]; (b) Cross-section of the cover of Vojens and Gram's PTES [75]

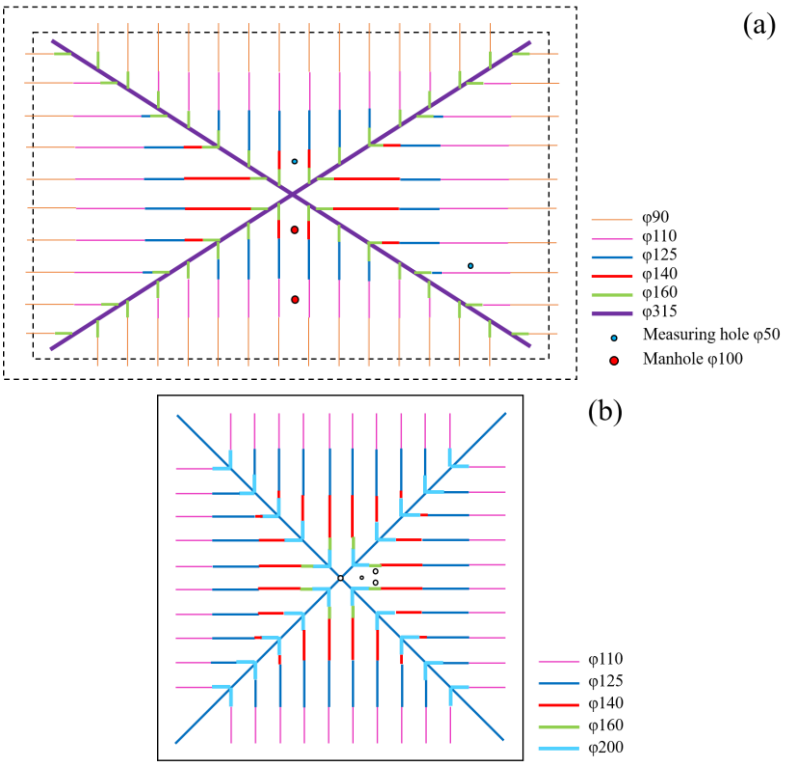

Fig.8 Weight pipe layout on the top of the cover: (a) Weight pipe layout of Marstal plant [77]; (b) Weight pipe layout of Dronninglund plant [10]

Recently, Aalborg CSP created a new cover design in which the cover was divided into smaller sections (Fig.9 (a) [78]), each with an individual drop towards the center pump (Fig.9 (b) [79]). This makes it considerably simpler to direct rainwater away from the surface and makes it possible to build larger PTES [78]. Additionally, the fall on the under and upper sides of each section shown in Fig.9 (b) [79] ensures that the air pockets are discharged [79]. Moreover, a diffusion-open structure is another innovation of the new design, preventing vapor accumulation inside the insulation layer. The functional performance of the new design has been inspected and verified, but no data exist to demonstrate the improvement effect.

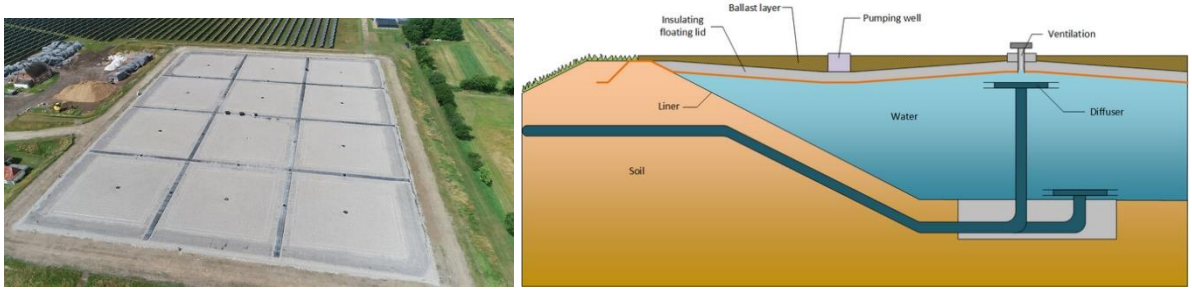

(a) Top view (b) Principle sketch

Fig.9 New cover solution developed by Aalborg CSP [78,79]

2.2 The materials used for PTES

2.2.1 Insulation materials

Most of the heat loss in uninsulated PTES is lost through the cover and upper edges [80]. As a result, a thicker layer of insulation will be added inside the cover, as previously mentioned. The side and bottom walls of PTES are rarely insulated because the surrounding soil can act as

a heat reservoir and transfer heat back to the PTES during discharge. However, insulation of the bottom wall is still recommended when it is closed to groundwater [81].

In the earlier stages of PTES design, the choice of insulation material is a crucial step that ultimately impacts PTES performance. The following desired specifications for insulation materials are generally agreed-upon: high thermal conductivity, high moisture resistance, high-temperature resistance, low density, low cost, and easy to install. There is, however, no perfect insulation material that satisfies all the requirements, and each material has its advantages and disadvantages. A list of tested insulation materials that met manufacturer requirements is shown in Table 2. Additionally, their thermal properties under specific experimental conditions, as well as strengths and weaknesses based on practical application, are included.

Together with Table 1, it can be observed that in earlier projects, sheets of rock wool, mineral wool, or polystyrene (Expanded Polystyrene *(*EPS) or extruded polystyrene (XPS)) were installed on the walls and the cover. But mineral wool and EPS will become too vulnerable if water infiltrates the insulation [81]. In this context, it is replaced by bulk insulation like expanded clay granules (EGG) or foam glass gravel (FGG). Bulk insulation has also the benefit of requiring less installation time and cost, particularly for large-scale PTES, since it can be installed by blowing from a silo truck [27,82]. Nomalén and Leca have lately been suggested to be more suited for insulation usage due to their superior thermal performance.

As far as we can obtain in the literature, the majority of insulating materials have their thermal properties tested under typical application conditions, and it is yet uncertain how thermal properties change under high temperature and high humidity conditions. Limited literature has revealed that, especially at higher temperatures, the thermal conductivity of the insulation increases dramatically with increasing moisture content [82,83]. Consequently, it has been found that the yearly thermal losses of most solar district heating plants with buried PTES are around 30-50% or even considerably greater than the design values [30,81,82,84,85].

Table 2 Properties for insulation materials

Material	Grain size (mm)	Thermal conductivity (W/(m·K)[1]	Density (kg/m^3)	Moisture effect on thermal conductivity	Advantages	Disadvantages	References
EGG	2-4	0.07[2] 0.08[3]	200[2] 190[3]	5 times (T= 60°C; M=200kg/m^3) [5] 10times (T=60°C; M=200kg/m^3)	Easy to install Cost-effective High temperature resistance	High cost	[25,81,82,86]
	4-8	0.08[2]	185[2]				
	8-16	0.08[2]	140[2]				
ECG	1-4	0.08[3]	300[3]	--	Lightness High strength High drainage capacity	Low moisture resistance Lack of demonstrated in reality	[20,44,81,82,87]
	4-8	0.1[2]	270[2]				
FGG	0-20	0.06[2]	150[2]	--	Lightness Dimensionally stable		[81,88,89]
GFG	10-50	0.09[3] 0.08[4]	195 [3] 170[4]	--	Lightness		[81,82]
PUR/PIR foam	--	0.02-0.03	80	Increase from 0.025 W/mK to 0.046 W/mK with increasing moisture content from 0 vol% to 10 vol%.	High temperature resistance High moisture resistance	High temperature expansion	[25,37,89,90]
Nomalén28 N	--	--	28	--	High heat resistant High-temperature resistance High moisture resistance		[44,91]
Mineral wool	--	0.03-0.04	160	Increase from 0.037 W/mK to 0.055 W/mK with increasing moisture content from 0 vol% to 10 vol%.		Low moisture resistance Hard to dry out	[20,89,90,92]

EPS	--	0.03-0.04	15-40	Increase from 0.036W/mK to 0.054W/mK with increasing moisture content from 0 vol% to 10 vol%.	Low thermal conductivity High water resistance	Stiff Become fragile after absorbing water	[20,90,93]
Perlite	0-1	0.05[(2)]	90[(2)]	--	Suitable for high temperature	Light-weight Difficult to control during implementation Difficult to make solid enough for treading on	[81,84]
Mussel shells	--	0.11-0.15	1070	--	Low material cost	Heavier than water; Higher thermal conductivity Difficult to be self-sustaining	[20,25,94]
Poraver	--	--	--	--	--	High material cost	[20]

(1) The thermal conductivity is under manufacturer specification
(2) Type I
(3) Type II
(4) Type III
(5) Moisture content at temperature 60°C

2.2.2 Liner materials

The liner encloses the water body on both sides of the cover to protect the insulation materials so that it has a significant role in determining the lifetime of a PTES. Moreover, by preventing vapor from traveling through insulation, the liner can help reduce heat loss [24]. The most common liners used for PTES are made of stainless steel, polymers, and elastomers [24,30,44]. Stainless steel was used as the liner in early plants (as shown in Table 1), but it was replaced by polymeric liners due to lower material costs and installation costs, especially for storage volumes larger than 20.000 m^3 [95,96]. However, offers for pilot storage in Rottweil had pointed out that a stainless steel liner with 0.5 mm thickness could be installed for roughly the exact cost as a thicker PP liner. In this context, a novel approach for assessing the liner material should be developed to consider many objectives. Otherwise, thicker polymer liners could be more expensive than thinner stainless steel with the same water resistance.

The thermal properties of liner material used to date are listed in Table 3. All listed polymer liners realized high water vapor permeability except for high-temperature polymer liners (HDPE). As a result, the demand for HDPE liners has accelerated [30]. However, the water vapor permeability of polymer liners is strongly independent of temperature [97], which can be seen from the change in water vapor permeability of HDPE at different temperatures. When HDPE is tested at 1 mm thickness under 20°C, the water vapor permeability is 0.03 $g/m^2/day$, while when HDPE is tested at 2.5 mm thickness under 80°C, the water vapor permeability can reach 1.5 $g/m^2/day$.

Considering the service life of liner materials, only three of them can be found in the literature, and most of the data are supplied by the Danish Technological Institute. Compared to the applications of such materials for hot water piping, the maximum service temperature and the exposure times are significantly higher for PTES. Therefore, reliable information on the service life of liners used for PTES under higher temperatures, especially under actual operation conditions, needs future investigations [30,72]. A newly developed high-temperature HDPE liner that can last more than 20 years at 90°C was claimed and guaranteed by the supplier recently. Still, it was not yet tested according to reliable methods [15].

Table 3 Properties for liner materials

Category	Material	Thermal conductivity (W/(mK) (at °C)	Water vapor permeability ($g/m^2/day$)	Lifetime (Years) [(1)]	Advantages	Disadvantages	References

Polymer liners	HDPE	0.44 (25 °C)	0.03 (σ[2]=1mm, T[3]=20°C) 1.5 (σ=2.5mm, T=80°C)	Less than 3 (T=90°C) 24.3 (T<70°C) 1.45 (T=100°C) 0.92 (T=107°C) 180 days (115°C) More than 20 (T =90°C)[4]	Low material cost Easy to install Low installation cost	Complicated temperature resistance Poor water vapor permeability	[20,30,44,72,74,98–100]
	PP	0.11 (25 °C)	4 times as high as for HDPE	Less than 6 (T=80°C) 22.6 (T<70°C) 1.1 (T=100°C) 0.55 (T=107°C) 0.33 (T=115°C) 16 (T=85°C)	Less degradation in contact with water Low material cost Easy to install Low installation cost		[20,44,72,95]
	PE	0.4 (23 °C)	--	15 (σ=2mm, T=95°C) 18 (σ=3mm, T=95°C) 1 (T=85°C)			[20,44,95,101]
	LDPE	0.33 (23 °C)	45 times as high as for HDPE	--	Low material cost Easy to install Low installation cost		[44,102]
	PVC	0.14-0.17 (25 °C)	115 times as high as for HDPE	--			[44,103]
Elastomer liners	EPDM	0.29 (25 °C)	2 times as high as for HDPE	--	Low material cost Higher temperature resistance	Not weldable Need special glue Higher installation cost	[44,72,104,105]
Metal liners	SST	25 (20 °C)	--	--	Long term stability Higher vapor tightness Highest temperature resistance	High material cost High installation cost	[44,72,106,107]
	AL[5]	239(20 °C)	--	--		Need special welding equipment	[44,72,107]

[1] Most of the results were tested by the Danish Technological Institute or assessed using a micro specimen
[2] Thickness of liner
[3] Experimental temperature
[4] It is offered by the supplier, but has not been tested yet
[5] Aluminum is not appropriate because of the pH in the storage water

2.3 Summary and outlook of PTES technical elements

The technical elements will determine the investment costs of PTES and, more importantly, will significantly affect the storage efficiency over its lifetime [84]. The optimal design of PTES still face several difficulties.

(1) Structure of PTES

At present, the geometry of PTES of most projects is regular, but due to the influence of geological conditions, more and more irregular-shaped PTES may appear. In this context, it is vital to understand the impact of geometry changes on PTES thermal and economic performance. Moreover, providing bottom insulation depends on many aspects, such as operation conditions, PTES bottom temperature, and soil parameters. These factors should be considered in the cost-benefit analysis of different insulation designs.

Investigations into the diffuser design have been conducted numerically and experimentally. The majority of studies, however, have focused on small-scale thermal energy storage. The structure of large-scale PTES with diffusers has not received much attention since it is time-consuming. The results from small-scale investigations must be carefully considered when scaling up because the PTES has a much bigger volume than a heat storage tank. What is more, the effect of inlet/outlet position or operating parameters on the performance of PTES has been partially understood, making engineers rely heavily on experience. Consequently, it is necessary to perform a full-scale simulation of PTES to identify the optimal inlet/outlet designs under different conditions.

As a crucial part of PTES, proper configuration and installation of the cover with insulation layers are challenging since thermal insulation and vapor permeability must be

considered simultaneously. To prevent damage to the insulation, the amount of moisture entering the insulation layer is reduced as much as possible. Additionally, more attention should be paid to thermal bridges caused by connection parts.

(2) The material used for PTES

The envelope of the buried PTES has to fulfill numerous vital purposes. As a summary and comparison of aforementioned materials, Fig.10 and Fig.11 plots thermal conductivity against density for insulation materials and test temperature for liner materials, respectively. Clearly, there are fewer materials available for PTES at the moment.

As demonstrated in Fig.10, except for mussel shells, the thermal conductivities of insulation materials range from 0.01 W/(m·K) to nearly 0.1 W/(m·K) and densities are lower than 300 kg/m^3. Changes in thermal conductivities are recorded for only four materials whose moisture changed. It is worth noting that the thermal conductivity change after water absorption by EGG appears to be unacceptably high. The applicability of other materials is still uncertain because no additional information is available.

No waterproofing membranes were developed especially for buried PTES, so liner materials used in other areas must be used. However, materials used in other fields often do not meet the high demands of temperature resistance. Currently, recorded thermal conductivity is limited to the range of 20 ºC to 30 ºC. The thermal conductivity of all other materials, excluding metal liners, is less than 0.6 W/(m·K). In addition, only the lifetime of three materials at different test temperatures can be collected, as shown in Fig.11. The service life of HDPE and PP liners appears to decrease with rising temperatures, but research findings are inconsistent, which may be due to differences in experimental parameters and methods. To elucidate the details, it is necessary to comprehend the aging mechanisms of liner materials, and particular focus must be placed on the investigation of polymeric accounting for the more severe temperature load profiles [101].

In conclusion, in order to reduce heat losses, new insulation materials with low thermal conductivity need to be developed. It is also desirable to compare various thermal insulation materials in terms of thermal conductivity, durability, water resistance, as well as installation costs [92]. Future research should focus on novel liner materials (e.g., bentonite, bitumen, geo-membranes, and high-performance concrete [24]), especially its long-term durability for temperatures higher than 90ºC. One aspect that needs special consideration is that the liner material research should take into account both the temperature and pH of water in the PTES.

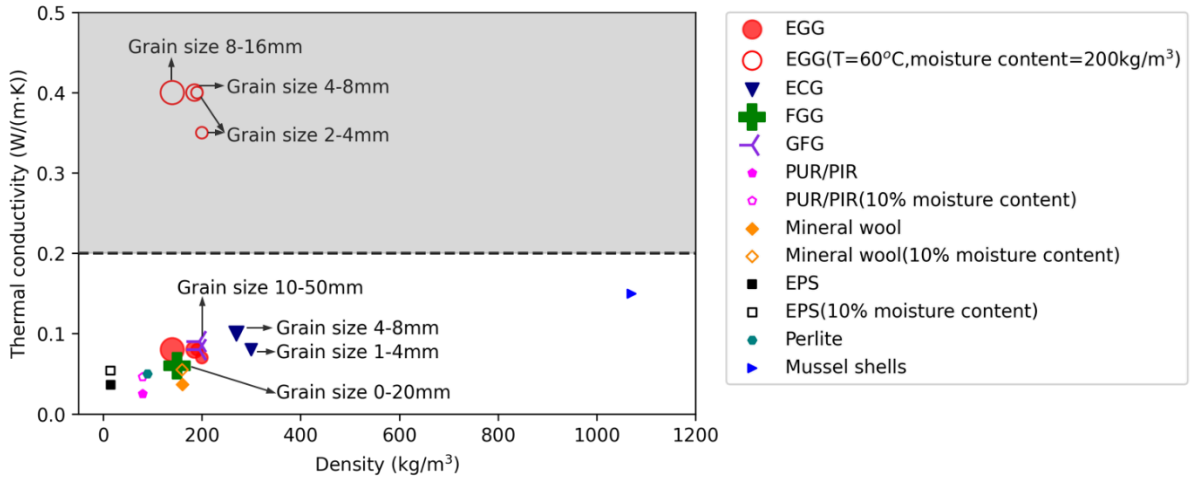

Fig.10 Thermal properties of insulation materials mentioned in the literature [81,82,84,88–90,92,94]

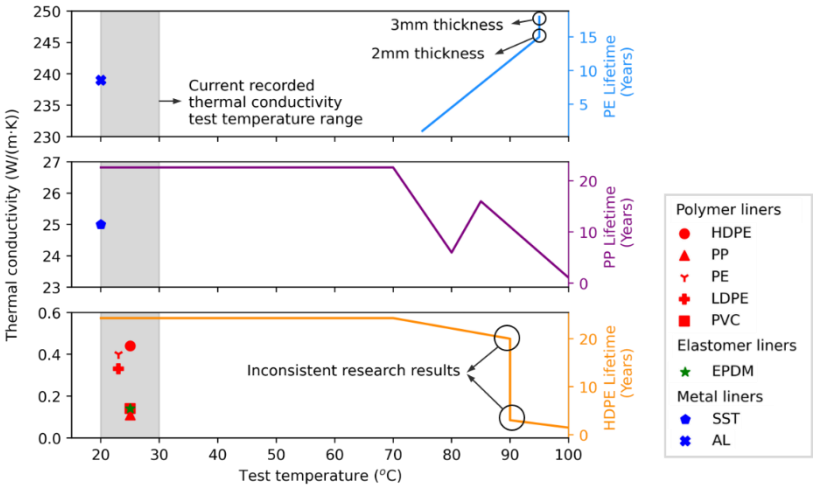

Fig.11 Thermal properties and lifetime of liner materials mentioned in the literature [44,72,74,95,99,102,103,105,107]

3. Numerical study of solar district heating plants with PTES

Proper planning is critical to commission the STES and assure the projects' economic viability [108]. As a result, the simulation methods for STES have received much attention [109], whereas most numerical research concentrates on TTES, BTES, and ATES because these three storage types are widely used in practice and have more mature simulation models. In contrast, PTES is a relatively new technology with limited available monitoring data, and modeling PTES is challenging due to complicated geometries. So far, only a few publications on PTES modeling studies can be found (see Table 4). The main findings and drawbacks of those studies are also added to Table 4 to provide a preliminary understanding.

Recent numerical studies can be clarified into component-level (i.e., considering only the performance of PTES) and system-level (i.e., integrating PTES into solar district heating systems). This section of the review presents all the available numerical models, with special attention to the mathematical theory and their calculation accuracy.

Table 4 Conclusion of the reference publications on PTES

Authors	Year of publication	Simulation approach/tool	Model dimension of PTES	Creativity and main findings	Drawbacks
Pan X. et al [110]	2022	PTES/TRNSYS	1D model (water part) 2D model (soil part)	(1) Validated a modified Type 342 with measurement data; (2) Storage cycle has a significant impact on storage efficiency;	(1) Limited to cylinder structure; (2) Large monthly differences heat loss between simulation and measurement;
Gauthier [111]	2020	PTES/TRNSYS	1D model (water part) 2D/3D model (soil part)	(1) Propose new model (Type 1300+1301 and Type 1302); (2) Type 1300+1301 and Type 1322 gave better results than Type 342; (3) Type 1300+1301 cost less calculation time;	(1) Limited to symmetrical structure; (2) Limited ports for Type 1300+1301 and Type 1302; (3) Large predicted side and bottom heat loss error for Type 342
Xie Z. et al [112]	2020	PTES/TRNSYS	1D model (water part) 2D model (soil part)	(3) Validated a modified Type 343 with measurement data; (4) Considerable heat extracted from the soil in winter; (5) The middle diffuser height affect the storage efficiency;	(1) Limited to symmetrical structure; (2) Large monthly differences heat loss between simulation and measurement;
Narula K. [113]	2020	System/Mathematical model	1D model (water part) 2D model (soil part)	(1) Validation with Marstal monitored data; (2) Preliminary assessment of the DH system without using specialized software;	(1) Can not replace detail simulation tools; (2) Large monthly differences between simulation and reported;
Kubinski K. et al [114]	2020	System/Aspen Hysys	1D model (water part)	(1) Model development on Aspen Hysys (2) Trnsys is recommended for system simulation	(1) Limited to cylinder structure; (2) Great simulation deviation;
Bai Y. et al [115]	2020	PTES/TRNSYS	1D model (water part) 2D model (soil part)	(1) Model development on Trnsys; (2) Validated with measurement data; (3) The PTES annual storage efficiency increases with sidewall slope; (4) Steeper slope gives better thermal stratification than smaller slope;	(1) Limited to symmetrical structure; (2) Limited to circular cross-section geometries; (3) Limited to two inlet/outlet diffusers;
Bai Y. et al [116]	2020	PTES/Mathematical model	1D model (water part) 2D model (soil part)	(1) Insulation on the side of PTES is also important;	(1) Limited to symmetrical structure;

				(2) Compared to MIX number, the stratification number is more representative;	(2) Limited to circular cross-section geometries; (3) Limited to two inlet/outlet diffusers;
Dahash A. et al [117]	2020	PTES/COMSOL	2D model (water part) 3D model (soil part)	(1) Validated with data from Dronninglund project; (2) Potential of improving the stratification by shifting from sloped-wall thermal energy storage;	(1) Limited to symmetrical structure; (2) Limited to circular cross-section geometries;
Dahash A. et al [118]	2019	PTES/COMSOL	2D model (water part) 3D model (soil part)	(1) Potential of improving the stratification by shifting from sloped-wall thermal energy storage; (2) Similar efficiency appears when tank without insulation and Pit with insulation after the ground pre-heating period;	Limited to the groundwater in the upper soil region;
Li X. et al [119]	2019	System/TRNSYS	1D model (water part) 2D model (soil part)	(1) Control strategies ; (2) The stratification of the seasonal storage; (3) Variable flow control is superior to temperature different control;	(1) Limited to circular cross-section geometries; (2) Groundwater is not considered; (3) Limited to two inlet/outlet diffusers;
Nageler P. et al [120]	2019	System/IDA+DYMOLA DHS+TRNSYS	1D model (water part) 2D model (soil part)	(1) Propose a co-simulation framework; (2) Climate is important for system selection;	(1) The co-simulation framework is not validated;
Dahash A. et al [121]	2018	PTES/COMSOL	1D model (water part) 2D model (soil part)	(1) Provide analysis for underground axisymmetric structures; (2) Model optimized with the respect to heat loss; (3) Low computation efforts;	(1) Limited to axial symmetric geometries; (2) Charging and discharging scenarios are simplified;
Sorknæs P. [109]	2018	System/Excel	1D model (water part)	(1) Validated with data from Dronninglund project;	(1) The system model only consists of the heat loss from the water pit storage and the heat pump itself; (2) Did not specify the errors between simulation and measurement results;

Chang C. et al [26,29,122]	2017	PTES/FLUENT	3D model (water part) 3D model (soil part)	(1) Downward flow appeared next to the sidewalls; (2) Steeper slope gives significant temperature stratification; (3) Intense heat transfer process appears at the beginning of cooling; (4) Average Nusselt numbers on the inner surface of the sidewalls and the bottom are higher than that of the top thermal insulation layer;	(1) Small scale simulation; (2) Short-term simulation; (3) Inlet and outlet are not considered;
Fan J. et al [123]	2017	PTES/FLUENT	3D model (water part) 2D model (soil part)	Thermal stratification strongly depend on the temperature of water returned to the PTES;	(1) Demond more calculation time; (2) Short period simulation;
Chatzidiakos A. [124]	2016	PTES/FLUENT	3D model (water part) 2D model (soil part)	(1) Thermal stratification can be maintained in most cases; (2) Backflow and mixing can be avoided by a pieced vertical disc at the end of the large pipe or a suitable nozzle;	(1) Groundwater is not considered; (2) Ground temperature fluctuation with time is not considered; (3) Demond more calculation time;
Reiter P. et al [125]	2016	System/TRNSYS	1D model (water part) 2D model (soil part)	(1) Heat price is competitive compared to heat from gas boilers for Graz; (2) Price stays in the economic sound range while solar district heating system size varying between 150,000 m² and 650,000 m²;	Lack of depth investigation
Ochs F. [126]	2014	PTES/Matlab+Simulink	2D model (water part) 2D model (soil part)	(1) Dynamic simulation; (2) Consider the variable distribution of the thermal insulation;	(1) limited to axial symmetric geometries; (2) Heat loss is not comparable to the measured data;
Raab S. et al [127]	2005	PTES/TRNSYS	1D model (water part) 3D model (soil part)	(1) Modeling one volume segment at the storage bottom is important; (2) Temperatures in the ground and the heat losses through the bottom are significantly overestimated without bottom segment model;	(1) Limited to geometries with vertical sides. (2) Limited to axial symmetric geometries;

3.1. Numerical study of PTES

Over the years, several models have been created to allow quick and trustworthy calculation of PTES performance. The energy balance equation is typically solved in such models using three approaches, the finite difference method, the finite element method, and the finite volume method. Based on these three approaches, this part discusses the numerical study on the component level in depth.

3.1.1 Approaches based on finite difference method

For the finite difference method, the water and soil regions are typically divided into nodes. The calculation algorithms consider the mass and energy flow, conduction between different nodes, and heat transfer through the walls. The commonly used finite difference method is implemented as TRNSYS models, including Type 342, Type 343, Type UGSTS, Type 1300-1301, and Type 1322. Fig. 12 [110–112,115,116,127] displays the geometric and grid characteristics of different models, as the grid division method determines the complexity of the model and impacts the model's calculation accuracy.

In terms of storage region (i.e., PTES marked in Fig.12 [110–112,115,116,127]), all of these models are simplified to one dimension. The storage region of Type 342 and Type UGSTS are restricted to cylinder geometry, while Type 343 and Type 1300-1301 extend the geometry to axisymmetric cones. The newly developed Type 1322 from TESS can also be used for symmetrical square pyramids. Besides, the storage region can be divided equally and unequally in height in all these models, which needs careful consideration when modeling, as calculation accuracy may be significantly affected.

For soil region, Type 1322 is three dimensions and other models are two dimensions. It is evident from Fig.12 [110–112,115,116,127] that the mesh division of the soil region varies significantly between models. For Type UGSTS, Type 343 and Type 1300-1301, the mesh density for part 1st and 2st in the z direction are determined by the nodes number in the PTES. However, the mesh density of part 2st for Type 342 can be set independently, with a factor towards the top and bottom contours of the storage region. Common to all models is that denser grid is applied in the adjacent area to more accurately calculate heat transfer between the storage and soil. Notably, there is an encryption above and below the baseline of the storage grid division interface for Type 1300-1301, designed to accurately simulate the thermal stratification intersection where temperature jump exists.

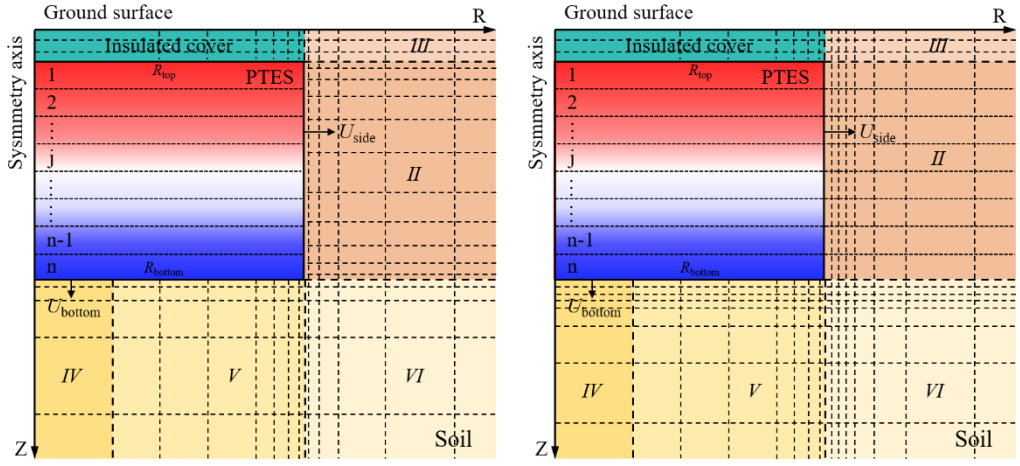

(a) Type 342 [110]

(b) Type UGSTS [115,116]

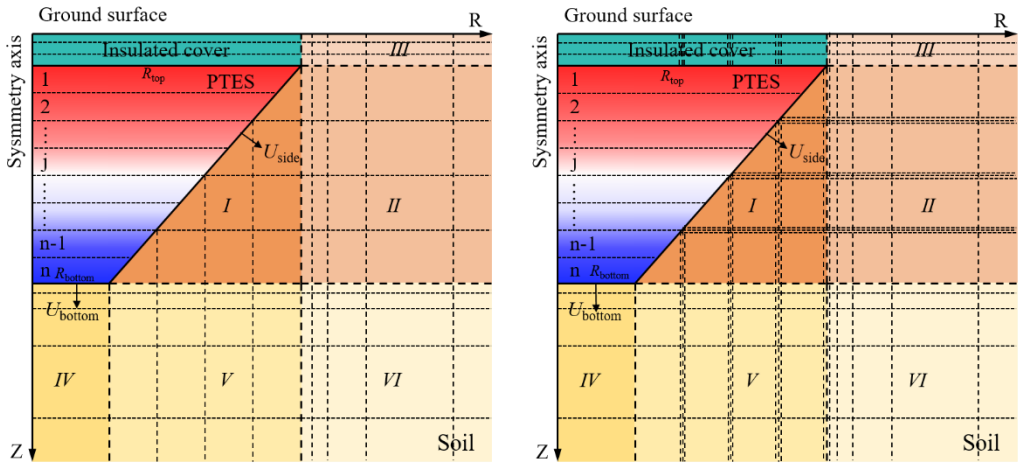

(c) Type 343 [112,127]

(d) Type 1300-1301[111]

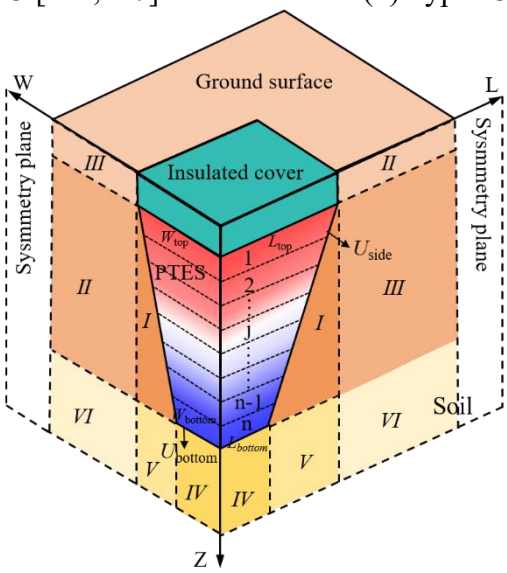

(e) Type 1322 [111]

Fig.12 Geometric characteristic and mesh method of models based on finite difference method

Several studies have been devoted to evaluating PTES performance using these finite different models. Raab et al. [127] validated Type 342 with the Hannover solar-assisted district system. Simulation results showed that the calculated temperature agreed well with the measured temperature, yet the heat loss through the bottom wall was severely overestimated. Pan et al. [110] also studied the performance of PTES using Type 342, with certain modifications made to fit the operation characteristics of the Dronninglund plant. The modified model predicted well the storage temperatures and the heat flow. For one year validation, the deviations of annual charged/discharged energy, internal energy content, and annual thermal loss between the model and the measurement were 2.0%, 1.9%, 2.5%, and 1.1%, respectively.

Xie et al. [112] developed a PTES for the Dronninglund plant based on Type 343. Their numerical findings demonstrated that the accuracy of the modified model was acceptable, and soil properties had an important influence on storage efficiency. However, the calculated deviation of PTES and soil temperature near the ground level could reach 16 K and 4 K, respectively.

Bai et al. [115,116] developed Type UGSTS and validated it with experimental data of an actual project in Huangdicheng, China. The results showed that the model could accurately

predict the temperature trend in the water and soil. At different heights from the PTES bottom, the average relative error of PTES temperature was around 2.5%. However, the maximum deviation in calculated soil temperature could reach 5 K. Furthermore, by examining the influence of height and sidewall slope on the thermal performance of PTES, they pointed out that there existed an optimum height to minimize the annual heat loss of PTES.

To assess the applicability of various models in the calculation accuracy and time efficiency, Gauthier [111] calibrated three models (i.e., Type 342, Type 1300-1301, Type 1322) with measurement data from the Dronninglund plant. Calibration analyses with variable parameters proved that Type 1300-1301 and Type 1322 gave superior results to Type 342, especially for heat losses through the cover. Under the conditions of this study, the relative error of Type 342 for bottom and side heat loss prediction could reach 87%. Moreover, Type 1300-1301 cost less calculation time than Type 1322, which was recommended for predicting the performance of PTES. Type 1322 could be used for detailed studies because of the sophisticated modeling theory. However, the heat loss from the bottom and sidewall of PTES could not be calculated accurately for all these models. Furthermore, more ports should be added to simplify the input file for Type 1300-1301 and Type 1322.

In addition to the models implemented in TRNSYS, Ochs [126] developed a dynamic model using the Matlab/Simulink platform that incorporated a one-dimensional finite-difference storage model and a two-dimensional finite element soil model. This model was adjusted to various symmetrical shapes. Fig.13 [126] indicates the difference between modeling TTES and PTES due to the surroundings based on the simulation results. It can be seen that the TTES was less affected by its surroundings because of the insulation on its side and bottom walls, while PTES was greatly affected by its surroundings since its lack of insulation. Therefore, the performance of insulation materials should be the main consideration for TTES, and the heat transfer between the water and soil region should be the primary concern for PTES.

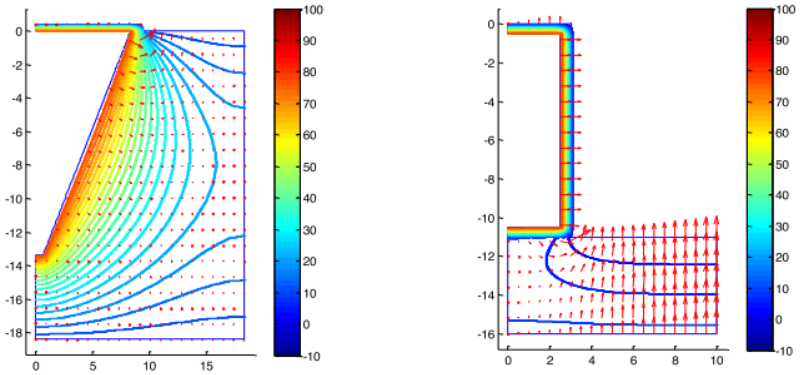

Fig.13 Temperature profile in the surrounding ground of a PTES and TTES with ground coupling [126]

3.1.2 Approaches based on finite element method

Commonly, the finite difference method is used for structure geometry since it is easier to implement than the finite element and finite volume method when the computational region can be divided into structure grids [128]. However, newly constructed PTES varies from symmetric pyramid stump to asymmetric pyramid stump because of local geological properties and construction investment, posing significant challenges to the finite difference method.

At this level, Dahash et al. [24,117,118,121,129] developed a new model for symmetric PTES shapes with surrounding soil region using COMSOL Multiphysics (Fig.14 (a) [121])

based on their previous investigation. They observed that PTES performance would drop under realistic conditions because of the existing groundwater. Accordingly, a new model considering groundwater (Fig.14 (b) [24]) was proposed and validated. Compared to the Dronninglund PTES measurements, the annual charge energy, discharge energy, internal energy, and heat loss deviate by less than 0.5%, indicating the new model's reliability. Yet, some slight discrepancies were seen due to uncertainties such as the cover's overall heat transfer coefficient and the soil region's thermal conductivity. Especially during November and December, the maximum deviations of charging energy were greater than 5%.

Moreover, the influence of STES geometry on thermal stratification was demonstrated by comparing the MIX number between Dronninglund PTES and a corresponding cylindrical TTES. For the cylindrical TTES, better stratification and lower thermal losses were observed, making it essential to find a compromise between technical performance and economic viability.

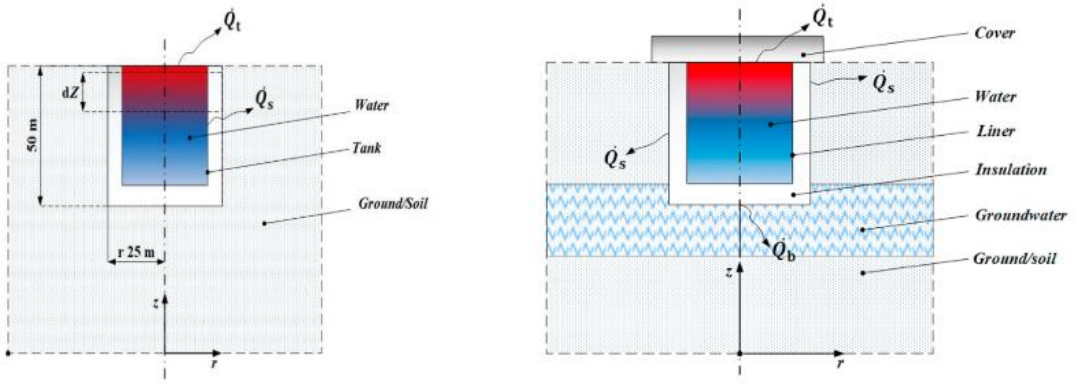

(a) (b)

Fig.14 Schematic of an underground tank with its surroundings: (a) Without groundwater [121]; (b) With groundwater [24]

3.1.3 Approaches based on finite volume method

Although approaches based on finite difference and finite element methods can be used to predict the performance of the PTES, they are not appropriate for detailed studies. The uncertainty in the boundary conditions will strongly impact the simulation results because they depend on numerous assumptions. As a result, some researchers used the finite volume-based ANSYS Fluent to conduct in-depth investigations.

Chatzidiakos and Fan [123,124] built a real-scale PTES model in ANAYS FLUENT (Fig.15 (a) [124]). Simulation results were presented for different typical cases (Fig.15 (b) [123]) and showed that the simulated model predicted PTES temperatures satisfactorily within a 10% difference for all these cases. Moreover, it proved that the mixing region was very limited in periods with slight temperature differences between inlet water and water inside PTES (Discharge case on October 7). But significant mixing occurred when the temperature differences were more considerable (Discharge case on February 18). Accordingly, powerful mixing would destroy thermal stratification and eventually affect the performance of PTES. The authors recommended paying more attention to investigating the position of inlet diffusers, the influence effect of inlet velocity, and the temperature difference between inlet water and water inside PTES.

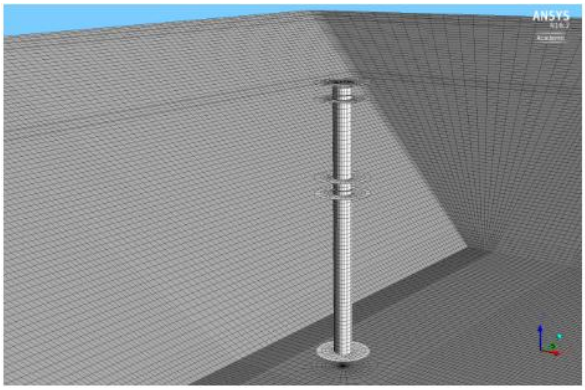

(a)

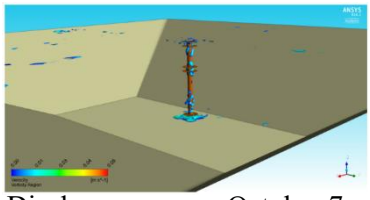

Discharge case on October 7

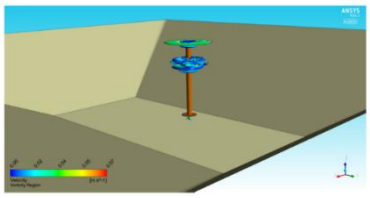

Charge case on August 3

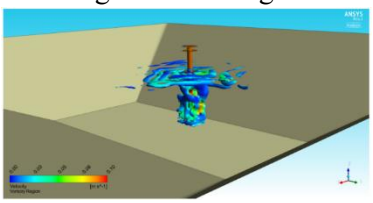

Discharge case on February 18

(b)

Fig.15 (a) Geometry and meshes for CFD model in Marstal [124]; (b) Illustration of regions for different cases [123]

Chang et al. [26,29,122] set up both experimental and simulation models of small-scale PTES. Natural convection along the sidewalls inside the PTES was investigated. The experiment proved that the simulation of the temperature curve was reasonable, and the maximum relative error was ±9.77%. Additionally, simulation results illustrated that both the sidewalls and the surrounding heat loss affected the natural convection inside the PTES, which might create downward flow along the sidewalls (Fig.16 [122]). It was worth noting that natural convection was more intense at the beginning of the cooling process. Furthermore, the influence of geometry on the thermal performance of PTES was studied. It concluded that a smaller depth and a smaller slope angle of PTES would decrease its thermal efficiency faster. However, the investigation time was as short as 40 minutes and could not demonstrate long-term reliability.

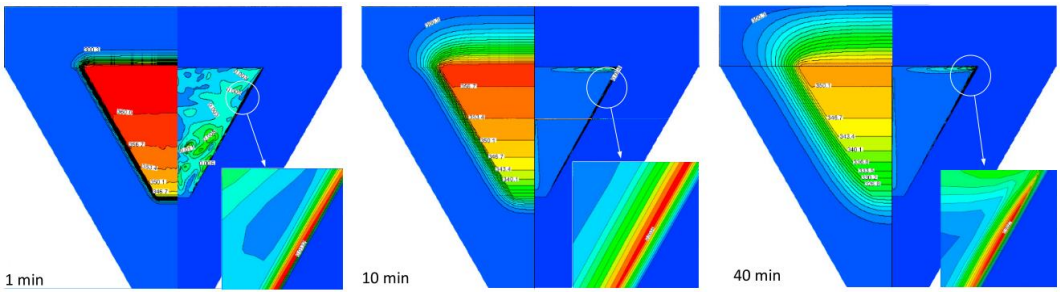

Fig.16 Isotherms and streamlines distributions on cross-section over time [122]

3.2 Numerical study for system integration

Future solar district systems will rely on variable renewable production and provide services for heating, cooling, and electricity [130]. Simulation and optimization should also be performed to ensure reliable design and operation of solar district heating systems integrated with PTES. Although such systems are highly dynamic and computationally complex, there is still some effort in the system-level investigation.

Reiter et al. [125] established the model of the Graz solar district heating plant using TRNSYS to predict the plant's performance while determining the optimum size of each component. Preliminary simulation results showed that the system had the best feasibility, with the solar collector field between 150000 m^2 and 650000 m^2, and the solar fraction could reach 9% to 26%. However, the performance and economic potential of the plant were affected by many parameters. Therefore, detailed simulations need to be done to clarify all relevant parameters further.

Sorknæs [109] presented a mathematical method in an excel spreadsheet to simulate the operation of PTES combined with a heat pump of the Dronninglund solar district heating plant. The model provided a tool that was sufficient to approximate the energy flow between components closely. However, the variation trend of the internal temperature of the PTES was quite different from the measurement, and the heat loss was overestimated by 36.5% compared with the actual operation. This was mainly due to the following simplifications: (1) The bottom temperature inside the PTES was set to be constant according to the operation period and the top temperature during the summer period. (2) The thermal exchanges between the soil and PTES were simplified by setting the soil temperature as constant all the year. (3) The fuel boiler provided a heat source to the heat pump was operating at full load.

Li et al. [119] set up a solar heating system with PTES in Hebei, China. Meanwhile, a TRNSYS model calibrated by the experimental data was established. The study was mainly focused on comparing three control strategies (i.e., constant flow control strategy, temperature difference control strategy, and variable flow control strategy) between the solar receiver and PTES. By comparing simulation and measurement results, it was found that a better stratification inside the PTES could be achieved in a variable flow control strategy. A reasonable control strategy was of extraordinary significance in improving the system efficiency since it could increase solar collection efficiency and enhance the exergy efficiency of the thermal energy storage. Nevertheless, the system scale was small compared to solar district heating plants, and the model for PTES was limited to tank storage. The research method can be considered a reference.

Narula et al. [113] developed a mathematical method to assess the hourly energy flow in a solar district heating system. Four configurations with different components could be considered. Simulation results were compared with the Marstal project for the configuration that included thermal energy storage and a heat pump (seen Fig.17 [113]). Based on the validation with the measured values, the annual energy flow could be closely replicated, demonstrating that the tool provided a simple alternative to preliminary evaluate the solar district heating system's yearly energy flow. However, the monthly energy flow deviations of different components were quite large. Two reasons could explain this. First, the energy supply and demand profiles used as input were incorrect. Second, the PTES was neither fully charged nor discharged due to the operation control strategy. To conclude, the developed model could not replace the specialized software, primarily detailed investigations. Further modification and exploitation need to be done to improve the model.

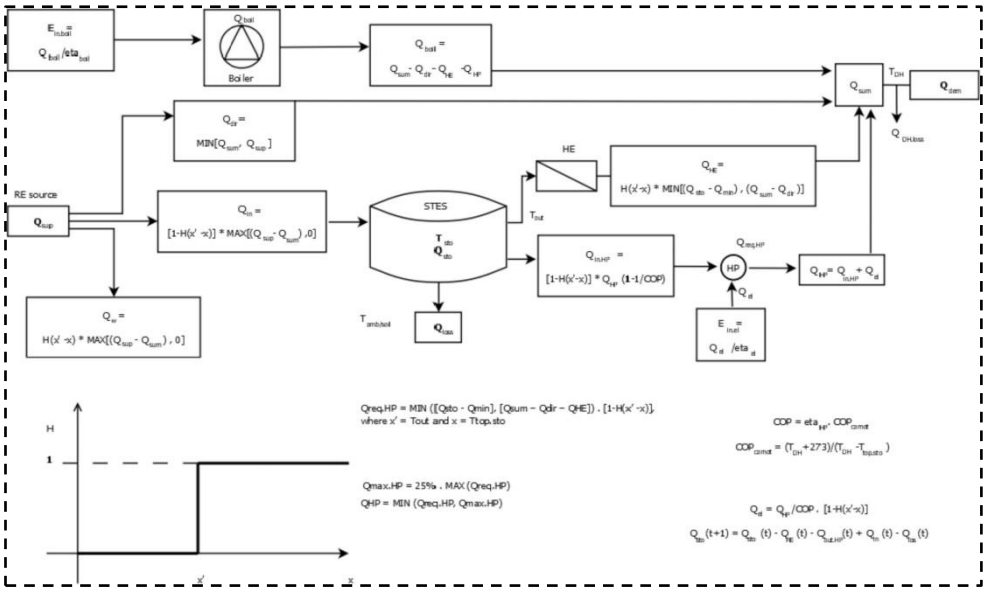

Fig.17 System framework with a renewable source, a boiler, a thermal storage, a heat exchange, and a heat pump [113]

Nageler et al. [120] developed a co-simulation framework shown in Fig.18 [120], which coupled with different tools (DYMOLA, IDA ICE, and TRNSYS) to assess energy supply. DYMOLA was used for the heating network simulation, IDA ICE was used for the building and substation simulation, and TRNSYS was used for the energy supply system simulation. Six cases were carried out to evaluate the tool, of which two cases included PTES aimed to overcome the seasonal fluctuating of waste heat. The co-simulation framework was reliable based on a virtual solar district heating system simulation. Significantly, the utilization of PTES was proved to be an effective way to balance the seasonal fluctuating waste heat. Moreover, climate conditions needed to be heavily considered to avoid oversizing the system components. This paper proposed a new way to evaluate the energy system by utilizing the advantages of different software. However, the accuracy needs to be further verified by comparing it with actual projects.

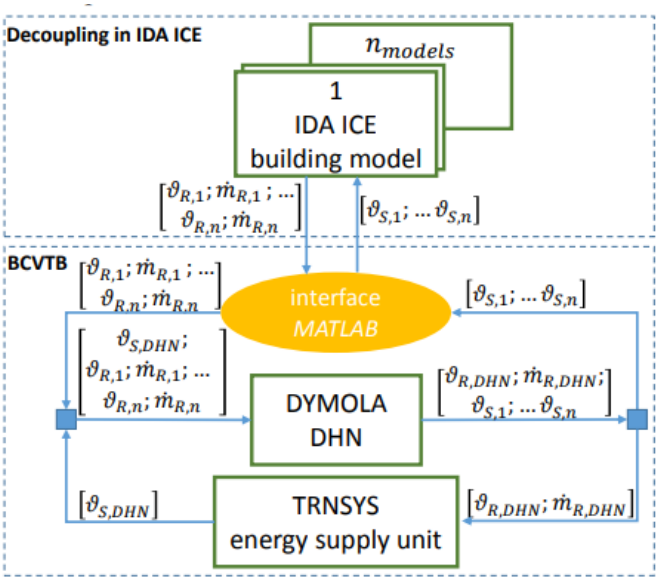

Fig.18 Co-simulation framework [120]

Kubinski and Szabłowski [114] developed a simplified dynamic model in the ASPEN HYSYS software based on the existing installation of the Vojents project. The model consisted of the collector field loop, the PTES application loop, and the heat distribution loop. The proposed model was expected to assess the achievable solar fraction. However, the simulation results, such as the solar fraction and water temperature distribution inside the PTES, differed significantly from the actual projects due to assumptions about the PTES and the system control strategy. It was recommended to change the software to TRNSYS, considering the inaccurate results, so that problems encountered in the proposed model, including missing components, detailed boundary conditions, and the time-varying parameters, can be easily resolved.

3.3 Summary and outlook on PTES numerical studies

3.3.1 Model classification and model accuracy

As an illustration, about 50% of the research conducted on FLUENT uses three-dimensional modes, 40% uses two-dimensional models, and the other 10% uses one-dimensional models.

Fig.19 shows that different simulation approaches have their characteristics and applicability. Recently research on PTES has concentrated on the TRNSYS platform, and the model dimensions are mostly one-dimensional and two-dimensional. In addition, it clarifies that not all geometries can be implemented in the current one-dimensional and two-dimensional models, bringing potential avenues for future research. Although FLUENT is known to implement various complex requirements, it is less utilized due to high time consumption. It is worth noting that the groundwater effect is only considered by Dahash et al. [118,131] successfully in a two-dimensional model. However, the asymmetric effect of groundwater in the two-dimensional model will be ignored, so its three-dimensional features need to be further corrected.

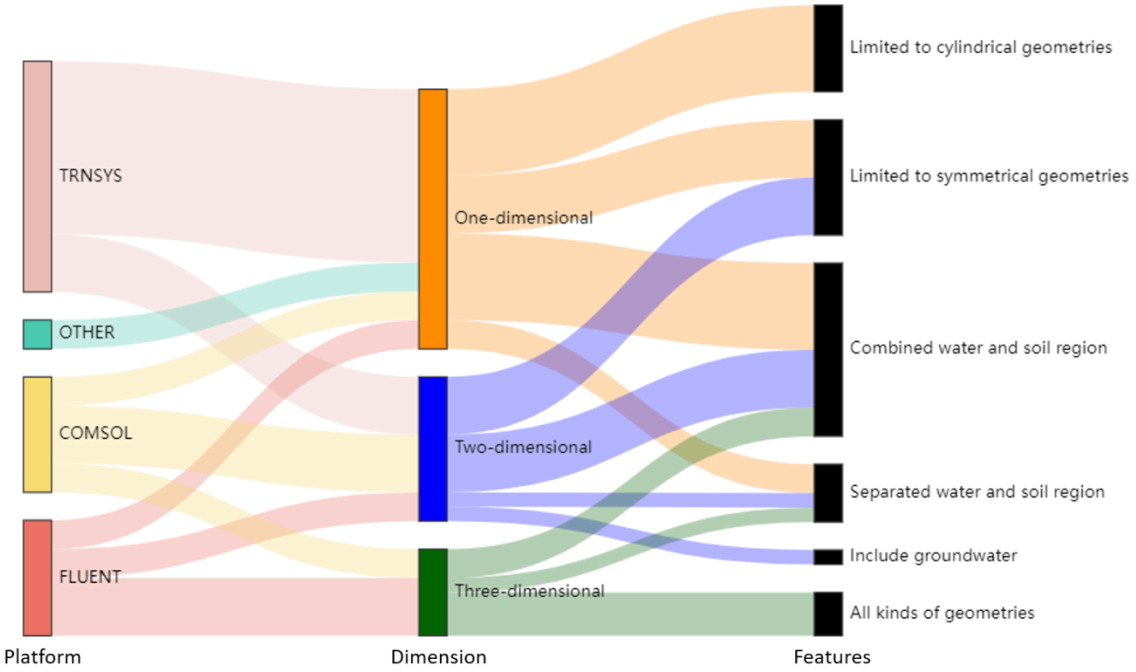

Fig.19 Classification of recent simulation approaches for PTES

It is also valuable to compare the calculation accuracy of previous studies. Therefore, three indicators of annual deviation, maximum monthly deviation, and maximum temperature

difference are used to compare the different numerical models. Fig.20 plots the relevant results from previous studies, where the models implemented in the TRNSYS platform are shown with a grey and white background, the model implemented in the COMSOL platform is shown with a pink background, and the models implemented in the FLUENT platform are shown with a brown background.

As shown in Fig.20, all the numerical models have good calculation accuracy regarding annual charge and discharge energy, with the annual deviations within 5%. However, some studies found large deviations beyond 10% in annual heat loss. It is important to note that even with the same model, there are significant differences in the annual heat loss calculation, which may be due to the settings of boundary conditions, including initial soil temperature, soil physical parameters, and heat transfer coefficients between water and soil. Moreover, three previous studies found large deviations in monthly calculations. The charge/discharge energy deviation in Fan's study is also an instantaneous result, as employing FLUENT for long-term simulations is challenging.

For calculation accuracy of PTES and soil temperature, there are considerable differences between different models. For one reason, a limited number of nodes are set using TRNSYS models in earlier studies. Another reason is that the relative position of soil measurements to the PTES walls changes after the PTES is transformed into cylinder geometry.

In conclusion, in the previous research, the model implemented on the COMSOL platform demonstrated good computational accuracy in all aspects. However, the model built based on COMSOL is not easy to link to system simulation software like TRNSYS. Furthermore, it is preferable to use the same setting to evaluate the suitability of various models further.

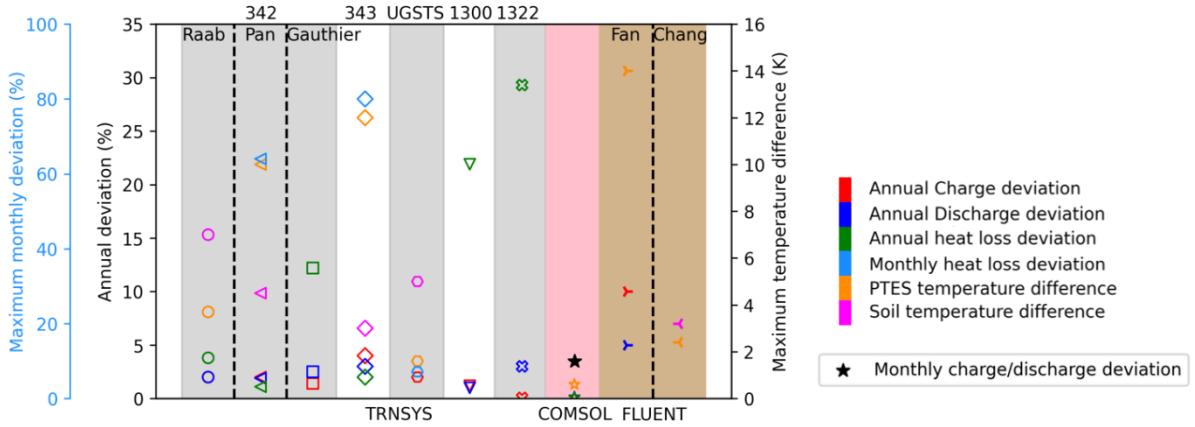

Fig.20 Numerical model calculation accuracy in previous studies [24,110–112,116,122,123,127]

3.3.2 Model assumptions

Numerous assumptions are used in different numerical models in an effort to improve computational efficiency. As discussed above, the calculation accuracy is acceptable for annual simulation. Still, more significant deviations appear when comparing the monthly or daily results with measurements since not all assumptions in the models are fully met in the actual project [7].

Table 4 summarizes the commonly adopted assumptions and categorizes them according to the aspects they consider. It is essential to point out that one of the common assumptions is axisymmetric flow and heat transfer. In this context, the temperature distribution inside the PTES and the heat loss through the sidewalls can be misleading without considering the

asymmetrical flow and heat transfer. The plug flow assumption is widely used in most simulation platforms without considering the inlet/outlet mixing. Moreover, the FLUENT platform commonly assumed a laminar flow inside PTES to achieve a stable and faster simulation. However, no studies have shown that more precise results can be obtained with the laminar flow than with turbulent flow.

Table 5 Main assumptions adopted in PTES numerical models

Aspects	TRNSYS	FLUENT	COMSOL	Others
Dimensional problem	Axisymmetric flow and heat transfer		Axisymmetric flow and heat transfer	Axisymmetric flow and heat transfer
Water properties	Constant thermal conductivity		Constant thermos-physical properties	Constant thermal conductivity
Soil properties	Constant thermos-physical properties	Constant thermos-physical properties	Constant thermos-physical properties	Constant thermos-physical properties
Heat transfer fluid from inlet/outlet diffusers	Neglect inlet mixing effect			Neglect inlet mixing effect
Heat transfer mechanism of water region	Neglect radial density gradients The water of each layer was considered thoroughly mixed before entering the adjacent layer Temperature inversion is not allowed Uniform temperature distribution of each layer Plug flow Uniform initial temperature	Laminar flow	Neglect radial density gradients The water of each layer was considered thoroughly mixed before entering the adjacent layer Uniform temperature distribution of each layer Laminar flow	Neglect radial density gradients Uniform temperature distribution of each layer Plug flow
Heat transfer mechanism of soil region	Neglect the influence of groundwater Uniform initial temperature	Neglect the influence of groundwater		Neglect the influence of groundwater
Heat transfer mechanism between soil and water region	Simplify the influence of natural convection			Neglect the influence of natural convection

3.3.3 Model correlations

Four primary corrections are tried in recent numerical models to overcome the disadvantages caused by the assumptions, and eventually improve the calculation accuracy. They are: (1) heat transfer coefficient of the surfaces; (2) eliminate inverse thermocline; (3) minimize numerical diffusion; (4) influence of groundwater.

(1) Heat transfer coefficient of the surfaces

The surface area of the PTES in the TRNSYS models differs from the surface area in reality since the actual shape needs to be converted to a cylinder or a reversed truncated cone in these models. In this case, a calculation error of heat loss will be introduced. Thus, to account for the surface variation, the heat transfer coefficient is corrected as Eq. (1) [112,117].

$$U_{simulation} = U_{original} * \frac{A_{original}}{A_{simulation}} \quad (1)$$

Where the $U_{simulation}$ and $U_{original}$ represent the surface heat transfer coefficient for the modeled PTES and the original PTES, respectively. $A_{simulation}$ and $A_{original}$ are the corresponding areas of the modeled PTES and the original PTES respectively.

However, some researchers use actual measurement results as constraints to obtain $U_{original}$, and some researchers assign $U_{original}$ empirically. Consequently, the deviation of

monthly heat loss is relatively large. Furthermore, during the planning phase, the heat transfer coefficient is unknown. Therefore, research is needed to propose an empirical formula suitable for different geological conditions.

(2) Eliminate inverse thermocline

Due to heat loss, a temperature drop may be observed at the very top layer near the cover. This drop may create an undesirable phenomenon called 'thermocline inversion'. To eliminate this, three methods have been used in recent approaches. The first method is to swap two adjacent nodes, which is suitable for the case where the volume of each node is equal. However, this method may introduce large errors when dividing PTES (with unequal top and bottom cross-section areas) into nodes of equal height. Thus a second method is proposed in several TRNSYS models, which defines a mixed temperature according to Eq. (2) and (3). When the thermocline inversion occurs, the temperature is replaced by the mass average temperature of the two adjacent nodes.

$$T_{mix} = (T_i * C_{p(i)} + T_{i+1} * C_{p(i+1)})/(C_{p(i)} + C_{p(i+1)}) \quad (2)$$

$$T_i = T_{i+1} = T_{mix} \quad (3)$$

However, this method deviates from the reality and miscalculates the heat loss through the sidewalls. Then, another method proposed by Dahash et al. [117] argued that correcting the thermal conductivity of water could better address this issue. Accordingly, the enhanced water thermal conductivity can be expressed as Eq. (4).

$$\lambda_{w,enh} = C * \left(\frac{\partial T_i}{\partial z_i}\right)^k \quad (4)$$

Both C and k are two constants that are usually determined experimentally. C is related to the dimensional parameters and thermophysical properties, and k depends on the application situation.

(3) Minimize numerical diffusion

For the one-dimensional models, the water region will be divided into several nodes in the vertical direction. The water temperature of the entire node near the inlet will be replaced by the thoroughly mixed average temperature of incoming water and existing water. Then, due to the plug flow assumption, artificial mixing will spread throughout the entire water region under different time steps. That causes significant numerical diffusion, especially when the mass per node is greater than the mass inlet flow within a time step.

In order to minimize the influence of numerical diffusion, two methods are generally adopted. One way is to increase the number of nodes, which can produce similar results to the actual situation. However, there is no straightforward rule for finding the appropriate number of nodes influenced by the storage dimensions and the operating condition. Furthermore, a large number of nodes may be required in some cases, which is undesirable due to a high computational cost.

The alternative way is the introduction of a virtual tank with a volume equal to that of the layer [132]. This method works only if all the layers have an equal volume. It assumes that the incoming water accumulates in the virtual tank first. When the virtual tank is full, all the accumulated water in the tank enters the storage node with the inlet [133]. Bai et al. [116] compared the influence of the plug flow method and found that the node's size still needed to be adjusted since it was related to the virtual tank's volume. Therefore, when water with

significant temperature differences in multiple time steps is mixed in the virtual tank, the predicted temperature will also significantly differ from the experimental results.

(4) Influence of groundwater

Awareness of the important impacts of groundwater on the planning and construction of PTES is increasing significantly. One concern is that groundwater challenges the excavation techniques and increases the construction investment. Another concern is that increased heat losses from the side and bottom walls of PTES will increase due to the enhanced heat transfer caused by groundwater. Additionally, significant temperature increases in the groundwater due to heat transfer from the water area may deteriorate groundwater quality [131]. However, most of the works discussed above neglect groundwater due to the model complexity.

Still, two efforts have been attempted to include the groundwater effect in the models. One attempt was to stratify the soil in height by different soil properties. In other words, the soil part with groundwater has a higher thermal conductivity. Yet, the soil properties of each layer of this method are still uniform without considering the groundwater flow. In this case, the interaction of PTES and groundwater cannot be predicted.

Another attempt was to take into account the hydraulic process of groundwater by introducing Darcy's law into the model. As proposed by Dahash et al. [131], the heat transfer equation in the soil layers was revised as Eq. (5).

$$\left(\rho c_p\right)_{eq} \frac{\partial T}{\partial t} + \rho_{gw} c_{p,gw} u * \nabla T = \nabla * \left(\lambda_{eq} \nabla T\right) \quad (5)$$

Where $\left(\rho c_p\right)_{eq}$ and λ_{eq} are the equivalent volumetric heat capacity and thermal conductivity of the porous medium in which the groundwater flows. ρ_{gw} and $c_{p,gw}$ represent the density and specific heat capacity of the groundwater respectively.

The second method can better predict the interaction between the groundwater and the PTES. This method can be implemented more easily on the COMSOL platform but is problematic in TRNSYS.

3.3.4 Outlook of numerical studies on PTES

Overall, the research stage of numerical studies for PTES has not yet reached a mature level. Therefore, there are several potential directions for future research in the numerical analysis of PTES, especially in developing sophisticated models that take into account geometrical suitability and geological conditions or in making full use of characteristics of different simulation platforms to improve the accuracy of existing models.

Few numerical studies have been conducted on PTES-integrated solar district heating systems. PTES complicates the operation of solar district heating systems. Consequently, there is a strong need for system-level investigation to determine the optimum system design and operation strategy [134].

4. Application of PTES

The first PTES with a volume of 500 m^3 was constructed at the Technical University of Denmark and extensive investigations were carried out [135–138]. The experience gathered from this project served the basis for constructing large-scale projects in Denmark and inspired the solar heating industry to establish more plants with PTES [139]. More recently, connecting PTES to large-scale solar district heating system has become one of the premier technologies to address the issue of solar thermal time-discrepancy. Although technical and economic

viabilities have been successfully demonstrated, only a small fraction of its potential has been exploited. To give a global perspective of PTES application, statistics on the application of PTES are essential.

4.1 Worldwide distribution

Fig.21 illustrates the global contribution of large-scale solar district heating systems with PTES, high-lighting PTES-active nations in different colors based on the number of publications. Over the past ten years, researchers in China and Austria produced more than ten articles, demonstrating the highest level of interest, followed by Denmark, Germany, Switzerland, and the United States.

Moreover, as depicted by the circles in Fig.4, countries have effectively integrated PTES into solar district heating plants, with Denmark accounting for around 47% of these installations, Germany 40%, and Sweden and China 13%. Together with Table 6, which summarizes the technical specifics of 15 solar district heating plants with PTES (PTES volume > 500 m^3), Denmark has emerged as a leader in the use of PTES, with significant growth in the installation of PTES reported over the past years. However, countries actively researched in the early years, such as Sweden and Germany, are now lagging.

Furthermore, the first solar heating plant with PTES in China was successfully realized in 2018 under severe weather conditions, thanks to the Danish PTES technology. In Austria, no PTES system has been built, but as far as we know, one is being planned. Due to the promotion of energy storage policy and the rising number of academics attempting to assess the technical feasibility and potential obstacles, more projects are anticipated in these two countries.

Planning and implementing PTES integration on such a large scale is problematic because it faces numerous challenges frequently. Despite the recent significant discrepancy in PTES worldwide, the application of PTES is moving from demonstration to commercialization, and the number of PTES is expected to increase in the future.

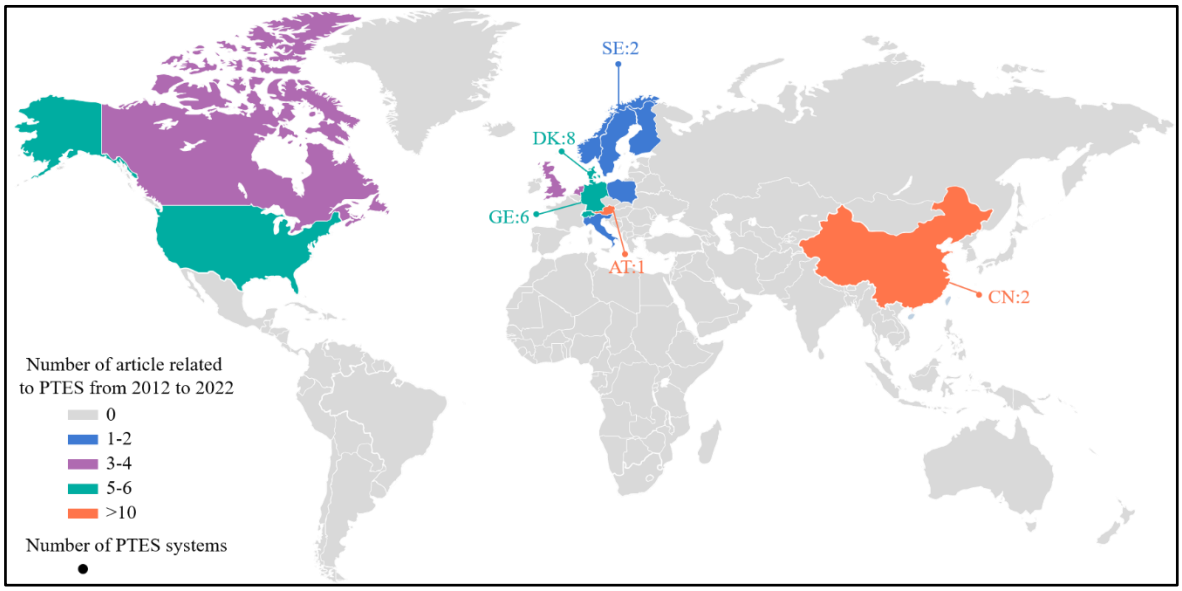

Fig.21 Global scientific publications on solar district heating plants with PTES

Table 6 Detail information of PTES projects (PTES volume > 500 m^3)

Position	Country	Year	Solar collector field area (m^2)	PTES volume (m^3)	Buffer tank volume (m^3)	Heat pump (type/capacity (kW))	Auxiliary energy (type/capacity/number)	Heat demand (MWh)	References
Lambohov	Sweden	1980	2700	10000	--	Compression/--	Gas Boiler/--/1	900	[140–142]
Stuttgart	Germany	1985	211	1050	1	Compression/66	Co generation plant/--	100	[32,33,143]
Julich	Germany	1996	1200	2500	1-2	--	Gas Boiler/750kW/1	590	[140,144]
Augsburg	Germany	1996	2000	6000	--	--	--	--	[35,36,143]
Steinfurt	Germany	1999	510	1500	1000	--	Gas Boiler/--/1	325	[11,24,38,140,143–145]
Chemnitz	Germany	2000	2000	8000	--	--	Gas Boiler/--/1	1200	[24,31,35,36,143,146,147]
Eggenstein	Germany	2008	1600	4500	30	Compression/60	Gas boiler/600kW/2	1400	[24,27,39,40,143]
Herlev	Denmark	1991	1050	3000	10	Compression/--	Gas boiler/--/1 Gas CHP/--/1	--	[74,143,148]
Ottrupgård	Denmark	1995	560	1500	--	--	--	43.5	[44,140]
Marstal	Denmark	2012	33300	75000	2100	Compression/1500	Biomass boiler/4MW/1 Bio-oil boiler/8.3MW/1 ORC/750kW/1	32000	[28,41,42,45,77,148,149]
Dronninglund	Denmark	2014	37573	60000	None	Absorption/4700	Bio-oil boiler/5MW/1 Bio-oil boiler/10MW/1 Gas boiler/8MW/1 Gas CHP/1.6MW/1	40000	[4,28,46,149,150]
Gram	Denmark	2015	44000	122000	2300	Compression/900	Electric boiler/10MW/1 Gas boiler/5.5MW/1 Gas CHP/5MW/6MWth/1 Industrial surplus heat/2MW	30000	[10,48,151,152]
Vojens	Denmark	2015	70000	200000	--	Absorption/5100	Electric boiler/10MW/1 Gas boiler/5.5MW/1 Gas CHP/5MW/6MWth/1 Industrial surplus heat/2MW	28000	[50–52]
Toftlund	Denmark	2017	27000	70000	--	Absorption/5100	Electric boiler/3MW/1 Gas boiler/4.5MW/1 Industrial surplus heat/1500-4000MWh/year	28000	[53–55]
Langkazi Tibet	China	2018	22275	15000	None	--	Electric boiler/1.5MW/2	37300	[56,57]

4.2 Classifications of PTES connected to solar district heating systems

Fig.22 shows four classification categories for PTES connected to solar district heating systems: storage material, construction type, operation strategy, and application method, according to Table 6.

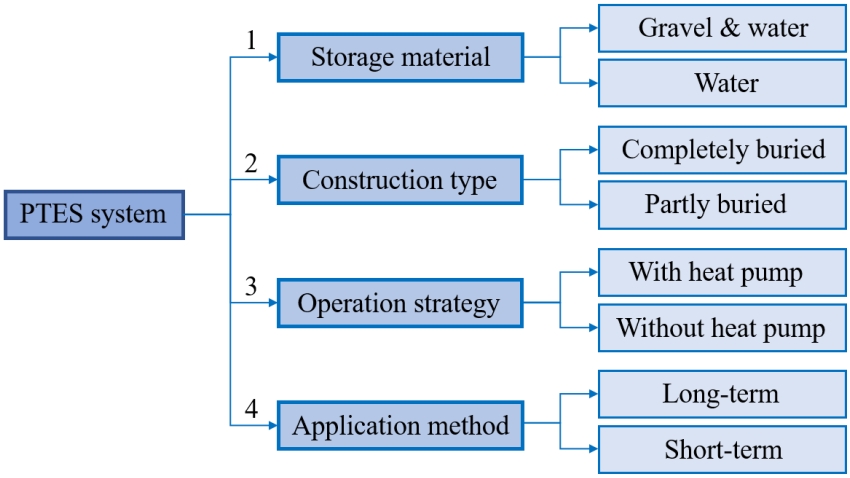

Fig.22 Classification categories of PTES connected to solar district heating systems

The first criterion is indicated in Fig.23. Earlier projects, like those in Lambohov, Stuttgart, Augsburg, Steinfurt, Chemnitz, and Eggenstein, commonly used gravel&water as storage material. However, it was replaced by water in the new projects for three reasons. One reason is that gravel&water have a lower energy density than water. The second reason is the requirement for indirect heat exchange coils of gravel&water PTES for charging and discharging, which add complexity to the system and is inconvenient to maintain. In addition, water can maintain an excellent thermal stratification [5,73]. It is worth noting that, depending on the quality of THE steel used, water may need to be treated after filling to prevent corrosion. Typically, if steel is utilized for the metal components of the PTES, the pH value of water will be raised to roughly 9.8 [5,20,44,72,73].

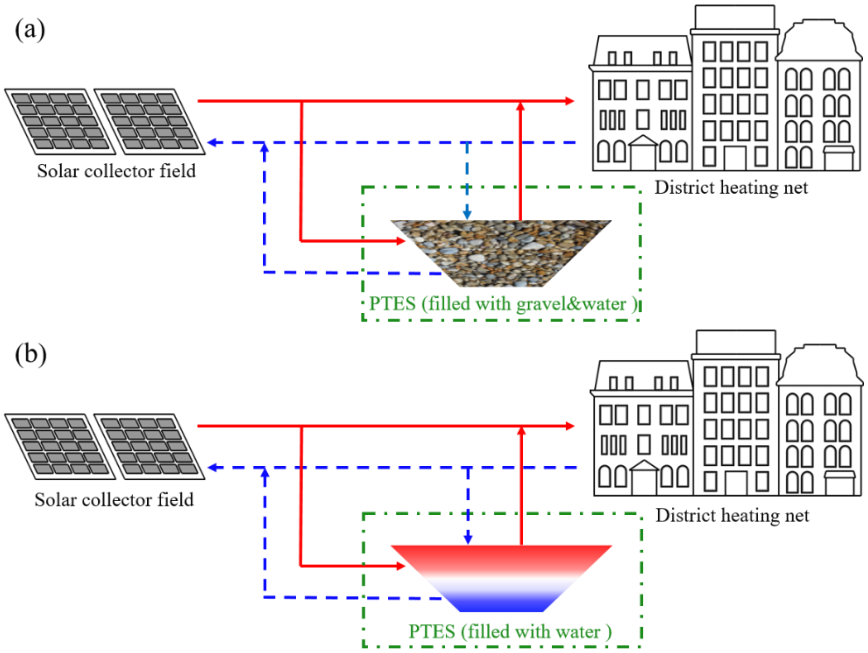

Fig.23 Criterion 1: Storage material filled inside PTES: (a) Filled with gravel & water; (b) Filled with water

The second criterion is represented in Fig.24. PTES volumes for projects before 2008 were completely buried under the ground level (see Fig.7 (a)) since their volumes are small, and their depth was all less than 7 m. However, as newly built PTES increased in volume and became deeper, the PTES were partly buried, and the above-ground part was supported by embankments made of the excavated soil (see Fig.7 (b)). In this case, heat losses due to groundwater are avoided through the sidewalls. To our knowledge, the sidewalls of PTES can account for around 40% of the heat loss [112], primarily due to groundwater effects, which increase further [15,16]. Therefore, an in-depth geological investigation is recommended before the construction of PTES.

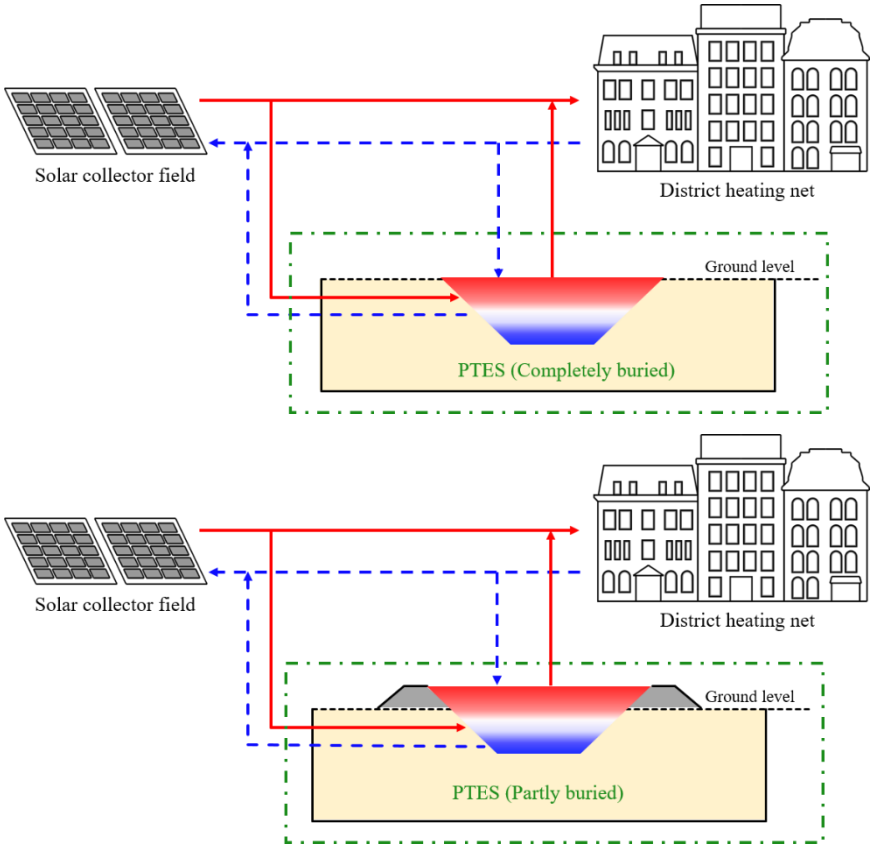

Fig.24 Criterion 2: Construction types of PTES: (a) Completely buried; (b) Partly buried

The third criterion, PTES operates with/without a heat pump, is displayed in Fig.25. For systems without a heat pump, the minimum PTES temperature is around 20°C. However, in systems with a heat pump, the heat pump extracts heat from the PTES to lower the minimum temperature to 10°C when the temperature inside the PTES is not high enough for direct heating. Therefore, the storage efficiency can be improved by using the heat pump property in this situation [153–158]. The achievement of lower storage temperature also allows for a reduction in heat losses.

Notably, the choice of the heat pump depends on the local energy structure and policy. The proportion of renewable energy share in the solar district heating systems can be increased with careful heat pump type selection. However, some researchers have pointed out that introducing heat pumps may not always help improve the overall energy perspective [159]. Thus, additional

investigations are still needed to determine the optimum design and operation strategies for integrating heat pumps with PTES.

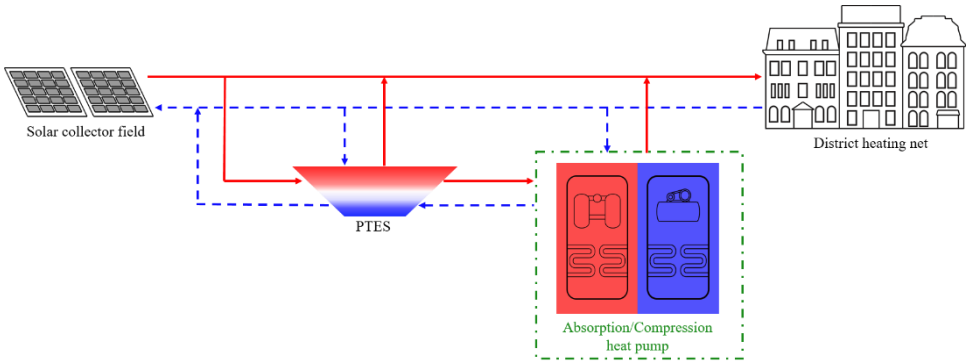

Fig.25 Criterion 3: Operational strategy

The fourth criterion of the PTES application method is shown in Fig.26. PTES has traditionally been proposed for long-term storage due to its large size. The primary processes for charging and discharging occur in summer and winter, respectively. As a result, an additional buffer tank is required to account for short-term variation in heat demand. However, in addition to the seasonal storage process from summer to winter, PTES can also be employed as short-term storage in summer [46]. In this context, storage efficiency is improved, and heat loss is reduced, as the average PTES temperature during summer is lower than that of the traditional application method. Additionally, the investment in the buffer tank can be saved.

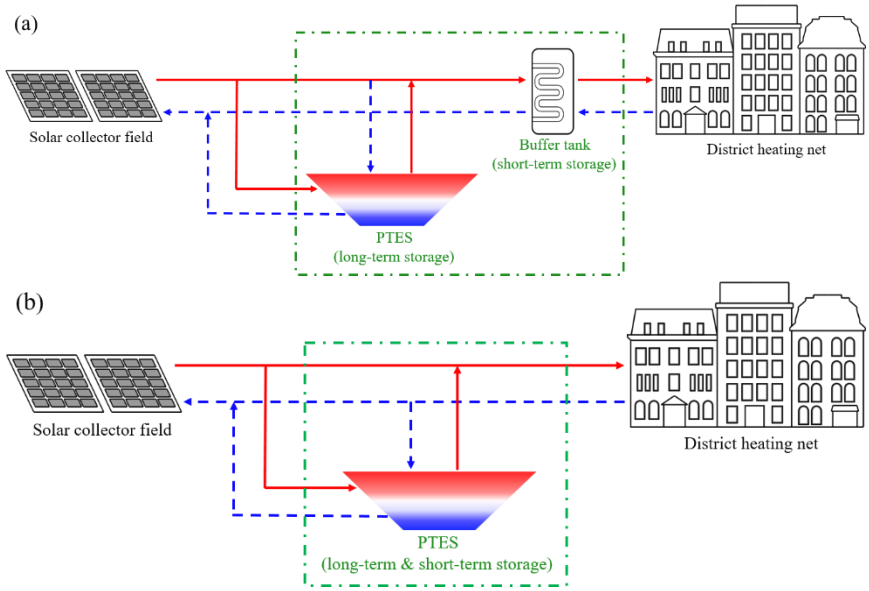

Fig.26 Criterion 4: Application method of PTES: (a) Long-term; (b) Short-term

4.3 Operation status of solar district heating plants with PTES

Integrating PTES into a solar district heating system has many advantages, such as achieving higher solar fraction and system efficiency. However, only 15 of the 470 large-scale solar district heating systems that have been successfully implemented worldwide integrated with PTES, which means the application of PTES remains challenging. The system will be more complicated than a system without PTES, and the desired efficiency may only be achieved with proper design and operation strategies [130,160]. In order to comprehend the operating statistics of existing PTES applications, and understand the current technical barriers and successful experiences, the project performance indicators, successes, and failures are

presented in Table 7. Based on Table 7, Fig.27 provides a comparison of performance metrics regarding solar fraction, storage efficiency, storage cycle, and PTES temperature.

As can be observed in Fig.27, the majority of projects have solar fractions between 30% and 50%, while the Lambohov and Langkazi Tibet projects have solar fractions exceeding 60%. Solar fraction is defined as the percentage of the total thermal load satisfied by solar energy. Therefore, the operational strategy and component design will both affect solar fraction. In the Stuggart and Tibet projects, the solar collector fields are slightly oversized, wasting extra heat during certain summer months. Notably, the Marstal project's solar fraction in 2017 fell below 30%. The reason is that rainwater has entered the cover construction through leakage, increasing the humidification of the cover and further increasing the heat loss through the cover.

In terms of storage efficiency, a significant gap can be observed. There are several points to be clarified. The ratio of the sum of the discharged and internal energy changes to the charged energy is known as storage efficiency. For the Dronninglund PTES, storage efficiency has increased slightly yearly, peaking at 96% in 2017. The higher storage efficiency, when compared to Marstal and Gram, is partly attributable to the storage cycle, which is defined as the ratio of the discharged heat to the maximum heat capacity of PTES. As demonstrated in Fig.27, Marstal and Gram have storage cycles lower than 1, while the typical storage cycle for the Dronninglund PTES is 2. In addition, the proper operation of the Dronninglund project lowers the minimum PTES temperature to approximately 10°C, reducing the heat losses from the side and bottom walls. The beneficial effect of the storage cycle on storage efficiency can also be proved with the Stuttgart projects. Even though the storage temperature is limited to around 30°C due to the use of unglazed collectors, the heat pump can fully utilize the storage capacity and achieve a large storage temperature difference.

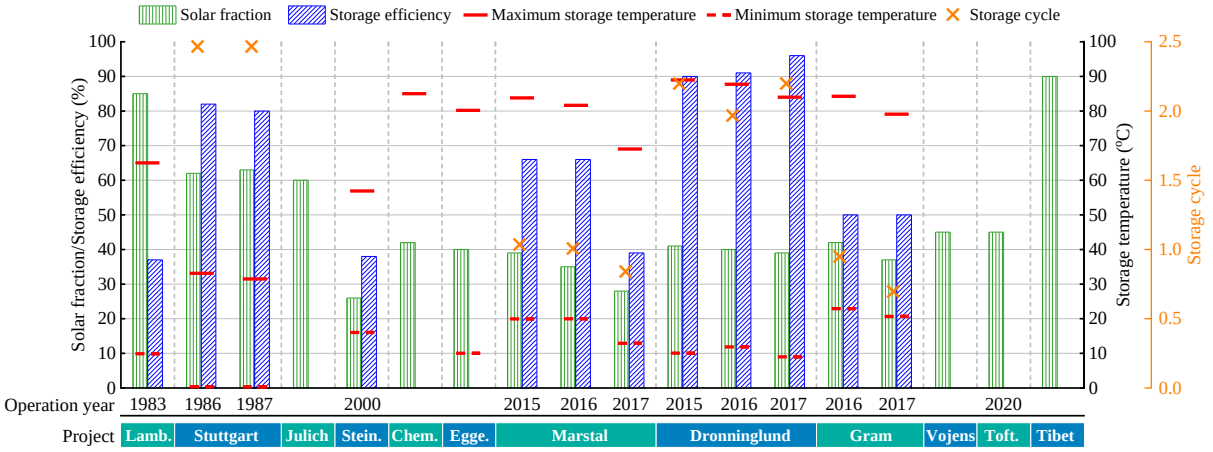

Fig.27 Comparison of performance metrics [11,31,32,38,46,48,52,54,57,141,144,147,161–164]

4.4 Summary and outlook of PTES application

As summarized in Table 7, successful projects demonstrated the applicability of PTES in different regions and climate zones. PTES can be seen as a major player in future district heating systems, incorporating a significant amount of renewable energy. In contrast, PTES grows in size to fulfill seasonal tasks, which brings more issues to the application. For instance, a thorough geotechnical and hydrogeological assessment is required prior to PTES construction. For larger volumes of PTES, a better cover design must be suggested to reduce heat loss and sustain service life. Additionally, the many more potential of using PTES when integrated with

different system components is not reflected in current operational statistics. So it is necessary to explore the adaptability of the combination with different systems further.

Table 7 Operational statistics of available PTES projects (PTES volume > 500 m^3)

Project	Solar fraction	Storage efficiency	Number of storage cycles	Storage max/min Temperature (°C)	Storage heat loss (MWh)	Success experience	Failure experience	References
Lambohov	85%	37%	--	65/10	395 (1983)		• Large heat loss due to wet insulation • No proper tools for predesign • Heat pump not working as expected • Unglazed collectors can not provide higher temperatures to increase the storage efficiency	[141,161]
Stuttgart	62% (1986) 63% (1987)	82% (1986) 80% (1987)	2.4 (1986) 2.4 (1987)	33/0 (1986) 31/0 (1987)	11.7 (1986) 13 (1987)	• PTES used as heat and cold storage • Water is well maintained, free from is fouling and corrosion	• Large energy waste from collectors • Solar fraction of operation is 18.9% lower than the design value • Leakage at the welded part of the sealing foil	[32,141]
Julich	60%	--	--	--	--		• High investment	[144]
Steinfurt	26% (2000)	38% (2000)	--	67/10 (1999) 57/16 (2000)	80 (2000)		• Increase moisture content of insulation due to drain pump failure • Storage efficiency of operation is 45.7% lower than the design value	[38]
Chemnitz	42%	--	--	85/	--		• Excavated with vertical walls accounts for a large part of the cost	[31,147]
Eggenstein	40%	--	--	80/10	--	• Successful heat pump operation strategies increase the efficiency of PTES		[11,31]
Herlev	--	--	--	85/10	--			[165]
Ottrupgård	--	--	--	60/35	70		• Fastening construction with clay was very weather dependent and expensive • Rain water seeps through the leak into the insulation of the cover	[43]
Marstal	39% (2015) 35% (2016) 28% (2017)	66% (2015) 66% (2016) 39% (2017)	1.1 (2015) 1.0 (2016) 0.7 (2017)	84/20 (2015) 82/20 (2016) 69/13 (2017)	2626 (2015) 2424 (2016) 4155 (2017)	• Backup boilers operate on the boi-oil enabling system to be 100% renewable energy	• Sensors are damaged during operation • Corrosion inside PTES due to mixing of iron and galvanized metal • Storage efficiency of operation is 28% lower than the design value	[28,149,162]
Dronninglund	41% (2015) 40% (2016) 39% (2017)	90% (2015) 91% (2016) 96% (2017)	2.2 (2015) 1.9 (2016) 2.2 (2017)	89/10 (2015) 87/12 (2016) 84/9 (2017)	1275 (2015) 1046 (2016) 388 (2017)	• PTES is also used for short-term storage • Lower storage temperature by rational use of heat pump	• Sensors are damaged during operation • Storage efficiency of operation is 28.8% lower than the design value	[28,46,149]

						• New liner guaranteed for 20 years when the temperature is less than 90°C • The inlet/outlet pipes are made of stainless steel • The pH of water remains at 9.8		
Gram	42% (2016) 37% (2017)	50% (2016) 50% (2017)	0.9 (2016) 0.7 (2017)	84/23(2016) 79/21 (2017)	7650 (2016) 6463 (2017)		• Large heat loss due to wet insulation • Corrosion inside PTES due to mixing of iron and galvanized metal	[48]
Vojens	45%	--	--	80/-	--		• Serious water absorption problem with insulation • Longer time to balance the heat transfer between the water and soil due to the largest volume	[52,164]
Toftlund	>45%	72 (2020)	--	--	4400 (2018) 2800 (2019) 2321 (2020)	• Excess heat from industry • Leca is used as the insulation layer of the cover • A special liner that can withstand temperatures above 90°C for a long time is used	• Rainwater entered the lid construction during the commissioning phase in 2018 • Heat loss in the first year of operation is 84% high than the design value	[54,163]
Langkazi Tibet	>90%	--	--	--	--	• Successful use in harsh weather conditions	• Energy waste due to system matching problems	[57]

5. Conclusion and future research directions

PTES has attracted more and more attention. However, certain technical challenges that are not yet to be sufficiently covered have limited its rapid development. This paper has addressed three aspects, namely technical elements, numerical approaches, and applications, which the authors believe will be the key drivers for the future development of PTES. The main findings and the challenges can be summarized as follows:

Main Findings

- Due to the high energy density and ease of maintenance, 64.3% of the analyzed projects use water as heat storage. 42.8% of the analyzed projects are partly buried to avoid the groundwater level. In addition, 25.8% of the analyzed projects use PTES for both long-term and short-term storage, which will improve storage efficiency by about 50%. Moreover, 63.8% of the analyzed projects are coupled with a heat pump, reducing the PTES minimum temperature to around 10ºC, further improving the storage efficiency by around 40%.
- Due to the failure of cover design and construction, the design value of storage efficiency is commonly overestimated by 28% or even as high as 46%. In the past, the floating cover of PTES has caused technical problems and unnecessary heat loss (60% of total heat loss), in the worst cases, accidents. Another important practical issue is that the mismatch between solar collector field design and PTES size leads to considerable energy waste in summer.
- At present, the maximum temperature of PTES is generally controlled below 85ºC because of a significant decrease in the lifetime of liner materials with temperatures higher than 85ºC.
- The existing numerical models for PTES are improved from four aspects: correcting the heat transfer coefficient between soil and water region, eliminating the inverse thermocline, minimizing the numerical diffusion, and considering the influence of groundwater. The prediction errors of different models for annual charged and discharged energy are within ±10%.
- Simulation approaches for system integration are less studied, and most of the characteristic parameters such as solar fraction, total heat loss, and storage efficiency are significantly different from the actual projects due to the simplification of the operation strategy.

Main challenges

- The design and construction of the floating cover remains the biggest challenge in PTES construction as it generates the most considerable heat loss and accounts for a large portion of the investment. Additionally, the reliability and durability of the thermal insulation and lining materials are critical for such massively buried PTES in a high-temperature environment as several projects must be shut down to repair the damaged floating cover.
- At present, the accuracy of PTES numerical approaches is insufficient, especially the prediction deviation of heat loss, PTES temperature, and soil temperature is still significant. In some cases, PTES temperature deviation inside PTES can be as high as 14 K, and the heat loss to the side walls is always grossly overestimated.

This paper contributes to a certain extent to deepen the understanding of the development and the challenges of PTES. Future research should concentrate on the following investigations:

- Considerably more work needs to be done to develop reliable cover design and construction methods to maintain stability for long-term applications. Ongoing research needs to expand the knowledge of insulation and liner materials from multiple dimensions, such as physical properties in different physical environments, lifetime, cost, and installing method.
- It would be interesting to assess the effects of different inlet/outlet designs on the thermal performance of large-scale PTES as the current design of the inlet/outlet diffuser draws on the experience of small-scale energy storage.
- Groundwater is considered one of the important factors affecting the performance of PTES. Better modeling of the groundwater will help us achieve a higher degree of accuracy by the simulation models.
- Combining the advantages of different platforms of PTES models to build a co-simulation platform is intriguing and should be future explored. Furthermore, system modeling is considered necessary to integrate PTES in the energy system with different system structures and operation strategies.

Acknowledgments

The work is partly funded by the Danish Energy Agency EUDP project (no. 64020-2036) and the Chinese Scholarship Council (CSC). Without their support, the research would not be possible.

References

[1] IEA (2020), Heating, IEA, Paris https://www.iea.org/reports/heating.

[2] Mauthner F, Herkel S. Technology and demonstrators - technical teport subtask C - part C1. 2016:1–31. http://task52.iea-shc.org/data/sites/1/publications/IEA-SHC-Task52-STC1-Classification-and-benchmarking-Report-2016-03-31.pdf

[3] Weiss W, Spörk-Dür M. Solar heat worldwide - global market development and trends in 2019 / detailed market figures 2018. https://www.iea-shc.org/Data/Sites/1/publications/Solar-Heat-Worldwide-2020.pdf

[4] Tschopp D, Tian Z, Berberich M, Fan J, Perers B, Furbo S. Large-scale solar thermal systems in leading countries: A review and comparative study of Denmark, China, Germany and Austria. Applied Energy 2020;270:1–31. https://doi.org/10.1016/j.apenergy.2020.114997.

[5] Xu J, Wang RZ, Li Y. A review of available technologies for seasonal thermal energy storage. Solar Energy 2014;103:610–38. https://doi.org/10.1016/j.solener.2013.06.006.

[6] Alva G, Lin Y, Fang G. An overview of thermal energy storage systems. Energy 2018;144:341–78. https://doi.org/10.1016/j.energy.2017.12.037.

[7] Ann Cruickshank C, Baldwin C. Sensible thermal energy storage: diurnal and seasonal. Elsevier Inc.; 2016. https://doi.org/10.1016/B978-0-12-803440-8.00015-4.

[8] Olsthoorn D, Haghighat F, Mirzaei PA. Integration of storage and renewable energy into district heating systems: A review of modelling and optimization. Solar Energy 2016;136:49–64. https://doi.org/10.1016/j.solener.2016.06.054.

[9] Fisch MN, Guigas M, Dalenbäck JO. A review of large-scale solar heating systems in Europe. Solar Energy 1998;63:355–66. https://doi.org/10.1016/S0038-092X(98)00103-0.

[10] Planenergi. Best practice for implementation and operation of large sale borehole and pit heat thermal storage 2019:1–22. https://www.solar-district-heating.eu/wp-content/uploads/2019/10/Best-practice-Br%C3%A6dstrup-Marstal-Dronninglund-and-Gram-003.pdf

[11] Bauer D, Marx R, Nußbicker-Lux J, Ochs F, Heidemann W, Müller-Steinhagen H. German central solar heating plants with seasonal heat storage. Solar Energy 2010;84:612–23. https://doi.org/10.1016/j.solener.2009.05.013.

[12] Mangold D, Schmidt T. The next generations of seasonal thermal energy storage in Germany. Engineering, Environmental Science 2009:8.

[13] Yang T, Liu W, Kramer GJ, Sun Q. Seasonal thermal energy storage: A techno-economic literature review. Renewable and Sustainable Energy Reviews 2021;139:110732. https://doi.org/10.1016/j.rser.2021.110732.

[14] Bott C, Dressel I, Bayer P. State-of-technology review of water-based closed seasonal thermal energy storage systems. Renewable and Sustainable Energy Reviews 2019;113:109241. https://doi.org/10.1016/j.rser.2019.06.048.

[15] Ochs F, Dahash A, Tosatto A, Bianchi Janetti M. Techno-economic planning and construction of cost-effective large-scale hot water thermal energy storage for

Renewable District heating systems. Renewable Energy 2020;150:1165–77. https://doi.org/10.1016/j.renene.2019.11.017.

[16] Guelpa E, Verda V. Thermal energy storage in district heating and cooling systems: A review. Applied Energy 2019;252:113474. https://doi.org/10.1016/j.apenergy.2019.113474.

[17] Pelay U, Luo L, Fan Y, Stitou D, Rood M. Thermal energy storage systems for concentrated solar power plants. Renewable and Sustainable Energy Reviews 2017;79:82–100. https://doi.org/10.1016/j.rser.2017.03.139.

[18] Sarbu I, Sebarchievici C. A comprehensive review of thermal energy storage. Sustainability. Sustainability 2018;10:191. https://doi.org/10.3390/su10010191.

[19] Li G. Sensible heat thermal storage energy and exergy performance evaluations. Renewable and Sustainable Energy Reviews 2016;53:897–923. https://doi.org/10.1016/j.rser.2015.09.006.

[20] chmidt T, Pauschinger T, Sørensen PA, Snijders A, Djebbar R, Boulter R, et al. Design aspects for large-scale pit and aquifer thermal energy storage for district heating and cooling. Energy Procedia 2018;149:585–94. https://doi.org/10.1016/j.egypro.2018.08.223.

[21] Mahon H, O'Connor D, Friedrich D, Hughes B. A review of thermal energy storage technologies for seasonal loops. Energy 2022;239:122207. https://doi.org/10.1016/j.energy.2021.122207.

[22] Novo A V., Bayon JR, Castro-Fresno D, Rodriguez-Hernandez J. Review of seasonal heat storage in large basins: water tanks and gravel-water pits. Applied Energy 2010;87:390–7. https://doi.org/10.1016/j.apenergy.2009.06.033.

[23] Zhou X, Xu Y, Zhang X, Xu D, Linghu Y, Guo H, et al. Large scale underground seasonal thermal energy storage in China. Journal of Energy Storage 2021;33:102026. https://doi.org/10.1016/j.est.2020.102026.

[24] Dahash A, Ochs F, Janetti MB, Streicher W. Advances in seasonal thermal energy storage for solar district heating applications: A critical review on large-scale hot-water tank and pit thermal energy storage systems. Applied Energy 2019;239:296–315. https://doi.org/10.1016/j.apenergy.2019.01.189.

[25] Planenergi. Design of the pit heat storage of the demonstration plant at Marstal fjernvarme 2013:1–19.

[26] Chang C, Nie B, Leng G, Li C, She X, Peng X, et al. Influences of the key characteristic parameters on the thermal performance of a water pit seasonal thermal storage. Energy Procedia 2017;142:495–500. https://doi.org/10.1016/j.egypro.2017.12.077.

[27] Ochs F, Nußbicker J, Marx R, Koch H, Heidemann W, Müller-Steinhagen H. Solar assisted district heating system with seasonal thermal energy storage in Eggenstein-Leopoldshafen. EuroSun 2008, Lisboa.

[28] Sørensen A, Schmidt T. Design and construction of large scale heat storages for district heating in Denmark. 14th International Conference on Energy Storage 2018, Turkey.

[29] Chang C, Leng G, Li C, Nie B, She X, Peng X, et al. Investigation on transient cooling

process in a water heat storage tank with inclined sidewalls. Energy Procedia 2017;142:142–7. https://doi.org/10.1016/j.egypro.2017.12.023.

[30] Ochs F, Heidemann W, Müller-Steinhagen H. Seasonal thermal energy storage: A challenging application for geosynthetics. Environmental Science 2008:1–8.

[31] Pavlov GK, Olesen BW. Seasonal ground solar thermal energy storage - review of systems and applications. 30th ISES Biennial Solar World Congress 2011;6:4864–74. https://doi.org/10.18086/swc.2011.29.24.

[32] Hahne E. ITW solar heating system: An oldtimer fully in action. Solar Energy 2000;69:469–93. https://doi.org/10.1016/S0038-092X(00)00115-8.

[33] Hornberger M, Fisch N, Hahne E. Solar assisted low temperature heating system with seasonal storage. International Solar Energy Society; 1988. https://doi.org/10.1016/b978-0-08-034315-0.50250-0.

[34] Ochs F, Heidemann W, Koch H. Erdreich / wasser-erdbecken-wärmespeicher mit direktem beladesystem. 16. OTTI Symposium Thermische Solarenergie 2006:88–93.

[35] Schmidt T, Mangold D, Müller-Steinhagen H. Seasonal thermal energy stroage in germany. ISES Solar World Congress 2003:1–7.

[36] Guadalfajara M, Lozano M, Serra L. Analysis of large thermal energy storage for solar district heating. Advances in Thermal Energy Storage 2014:1–10. https://doi.org/10.13140/2.1.3857.6008.

[37] Ochs F, Heidemann W, Koch H. Soil-water pit heat store with direct charging system - technology and economy. EuroSun 2006, United Kingdom.

[38] Bodmann M, Koch H, Pfeil M. Solare nahwärmeversorgung mit kies / wasser-wärmespeicher in Steinfurt-Borghorst 1998. https://www.tu-braunschweig.de/index.php?eID=dumpFile&t=f&f=30209&token=ebaebef0a2f25a0f30ea24a15a563150c82f5507

[39] Bauer D, Marx R, Drück H. Solar district heating for the built environment technology and future trends within the european project Einstein. Energy Procedia 2014;57:2716–24. https://doi.org/10.1016/j.egypro.2014.10.303.

[40] BINE informationsdienst. School refurbishment combined with local solar heating. https://api.deutsche-digitale-bibliothek.de/binary/41b6cd75-2ed6-4379-923e-56b4d3df3f92.pdf

[41] Jensen L, Rutz D, Doczekal C, Gjorgievski V, Batas-Bjelic I, Kazagic A, et al. Best practice examples of renewable district heating and cooling. Market uptake of small modular renewable district heating and cooling grids for communities 2016. https://www.coolheating.eu/images/downloads/D2.1_Best_Practice.pdf

[42] Fan J, Huang J, Andersen OL, Furbo S. Thermal performance analysis of a solar heating plant. ISES Solar World Congress 2017, Abu Dhabi, United Arab Emirates https://doi.org/10.18086/swc.2017.06.05.

[43] Epp B. Seasonal pit heat storage: cost benchmark of 30 EUR/m^3. 2019. https://solarthermalworld.org/news/seasonal-pit-heat-storage-cost-benchmark-30-eurm3/

[44] Jensen MV. Seasonal pit heat storages - Guidelines for materials & construction. IEA - SHC TECH SHEET 45 2014;1-31. http://task45.iea-shc.org/data/sites/1/publications/IEA-SHC%20T45.B.3.2%20TECH%20Seasonal%20storages%20-%20Water%20Pit%20Guidelines.pdf

[45] Danish District Heating Association, PlanEnergi. Solar district heating - inspiration and experiences from Denmark 2018. http://task55.iea-shc.org/Data/Sites/1/publications/SDH%20Inspiration%20Experience%20DK%20v5.pdf

[46] Winterscheid C. Dronninglund district heating monitaring data evaluation for the years 2015-2017. 2017. https://www.solar-district-heating.eu/wp-content/uploads/2019/10/Dronninglund-evaluation-report-2015-2017_20190531.pdf

[47] Epp B. Denmark: Dronninglund inaugurates 26 MWth solar district heating plant 2014;6. https://www.solarthermalworld.org/news/denmark-dronninglund-inaugurates-26-mwth-solar-district-heating-plant.

[48] Winterscheid C. Gram district heating monitaring data evaluation for the years 2016-2017 2019. https://www.solar-district-heating.eu/wp-content/uploads/2019/10/Gram-evaluation-report-2016-2017_20190531.pdf

[49] PlanEnergi. A presentation of the Danish pit and borehole thermal energy storages in Brædstrup, Marstal, Dronninglund and Gram. 2019. https://ens.dk/sites/ens.dk/files/Forskning_og_udvikling/sol_til_fjernvarme_brochure_endelig.pdf

[50] Ramboll. Heat pumps : the future of district heating?

[51] Epp B. Denmark 37MW field with 203000m^3 storage underway. 2014;8. https://www.solarthermalworld.org/news/denmark-37-mw-field-203000-m^3-storage-underway.

[52] Ramboll. World largest thermal heat storage pit in Vojens. https://stateofgreen.com/en/partners/ramboll/solutions/world-largest-thermal-pit-storage-in-vojens/.

[53] Ved D, Fjernvarme T. Large fyldes med 70.000 kubikmeter varmt vand 2017. https://jv.dk/artikel/lager-fyldes-med-70-000-kubikmeter-varmt-vand.

[54] Ramboll. Toftlund fjernvarme udvidelse solvarme project 2015.

[55] Pedersen MBS. Energilager tager form i Toftlund. 2017. https://www.energy-supply.dk/article/view/341832/energilager_tager_form_i_toftlund.

[56] Solar district heating. Solar district heating on the roof of the world. 2018. https://www.solar-district-heating.eu/solar-district-heating-on-the-roof-of-the-world/.

[57] Jiao Q, Li S, Gao F, Wang W, Qin K. The performance of a high altitude and high solar fraction large-scale district heating project.Proceedings of the ISES Solar World Congress 2019, 2019:459–69. https://doi.org/10.18086/swc.2019.11.01.

[58] Asian Development Bank. Solar district heating in the People'S Republic of China status and development potential. 2019. https://www.adb.org/sites/default/files/publication/514916/solar-district-heating-

peoples-republic-china.pdf

[59] Shah LJ, Furbo S. Entrance effects in solar storage tanks. Solar Energy 2003;75:337–48. https://doi.org/10.1016/j.solener.2003.04.002.

[60] Furbo S. Hot water tanks for solar heating systems 2004.

[61] Deng Y, Sun D, Niu M, Yu B, Bian R. Performance assessment of a novel diffuser for stratified thermal energy storage tanks - the nonequal-diameter radial diffuser. Journal of Energy Storage 2021;35. https://doi.org/10.1016/j.est.2021.102276.

[62] Chung JD, Cho SH, Tae CS, Yoo H. The effect of diffuser configuration on thermal stratification in a rectangular storage tank. Renewable Energy 2008;33:2236–45. https://doi.org/10.1016/j.renene.2007.12.013.

[63] Fagerlund Carlsson P. Temperaturstratificering i varmelagre. Technical University of Denmark, Depeartment of Civil Engineering 1995.

[64] Moncho-Esteve IJ, Gasque M, González-Altozano P, Palau-Salvador G. Simple inlet devices and their influence on thermal stratification in a hot water storage tank. Energy and Buildings 2017;150:625–38. https://doi.org/10.1016/j.enbuild.2017.06.012.

[65] García-Marí E, Gasque M, Gutiérrez-Colomer RP, Ibáñez F, González-Altozano P. A new inlet device that enhances thermal stratification during charging in a hot water storage tank. Applied Thermal Engineering 2013;61:663–9. https://doi.org/10.1016/j.applthermaleng.2013.08.023.

[66] Assari MR, Basirat Tabrizi H, Savadkohy M. Numerical and experimental study of inlet-outlet locations effect in horizontal storage tank of solar water heater. Sustainable Energy Technologies and Assessments 2018;25:181–90. https://doi.org/10.1016/j.seta.2017.12.009.

[67] Findeisen F, Urbaneck T, Platzer B. Raidal diffusers - simulation of three-dimensional flow effects with CFD (Part 1). Chemie-Ingenieur-Technik 2018;90:956–68. https://doi.org/10.1002/cite.201700023.

[68] Findeisen F, Urbaneck T, Platzer B. Radial diffusers - simulation of three-dimensional flow effects with CFD (Part 2). Chemie-Ingenieur-Technik 2018;90:969–78. https://doi.org/10.1002/cite.201700070.

[69] Findeisen F, Urbaneck T, Platzer B. Radial diffusers - simulation of three-dimensional flow effects with CFD (Part 3). Chemie-Ingenieur-Technik 2018;90:1065–72. https://doi.org/10.1002/cite.201700126.

[70] Findeisen F, Kroll U, Urbaneck T, Plazer B. Radial diffusers in stratified hot water stores: Ecomtry optimization with CFD. ISES Solar World Congress 2017:726–34. https://doi.org/10.18086/swc.2017.13.04.

[71] PlanEnergi, Niras. Dronninglund solar thermal plant. 2014:1–12. https://www.dronninglundfjernvarme.dk/media/2984/brochure_dronninglund_2015_booklet_eng_web_.pdf

[72] Kallesøe AJ, Vangkilde-Pedersen T. (eds). Underground Thermal Energy Storage (UTES) - state - of - the - art, example cases and lessons learned. HEATSTORE project report, GEOTHERMICA-ERA NET Cofund Geothermal. 2019.

[73] Ochs F, Heidemann W, Müller-Steinhagen H. Performance of large-scale seasonal thermal energy stores. Journal of Solar Energy Engineering, Transactions of the ASME 2009;131:0410051–7. https://doi.org/10.1115/1.3197842.

[74] Ellehauge K. Pedersen TE. Solar heat storages in district heating networks. 2007. https://www.osti.gov/etdeweb/servlets/purl/928828.

[75] Saint-Gobain Weber A/S. Weber leverer isolerende dyne til verdens største damvarmelager. 2015;11.

[76] PlanEnergi. Sunstore 3 phase 2 implementation. 2015. http://planenergi.dk/wp-content/uploads/2018/05/26-Sunstore-3-Final-report.pdf

[77] PlanEnergi. Summary technical description of the sunstore 4 plant in Marstal. 2013. https://www.solarmarstal.dk/media/6600/summary-technical-description-marstal.pdf

[78] Aalborg CSP. Pit thermal energy storage (PTES). https://www.aalborgcsp.com/business-areas/thermal-energy-storage-tes/pit-thermal-energy-storage-ptes/

[79] Aalborg CSP. Aalborg CSP improves bankability of thermal storage technology with certificate from Lloyd's register for unique lid technology. 2021. https://www.aalborgcsp.com/news-events/newstitle/news/aalborg-csp-improves-bankability-of-thermal-storage-technology/.

[80] Weinhold K., Werner T., Groß, S., Hellfritsch, S., Haas, D. Green Heat^3 Entwicklung innovativer Energieversorgungstechniken und - strukturen mit den Kernkomponenten modularer Großwärmespeicher und Maxianlage Solarthermie. 2019. https://tu-dresden.de/ing/maschinenwesen/iet/gewv/ressourcen/dateien/forschung_und_projekte/projekte/200220_Endbericht_GH3_freigegeben.pdf?lang=en.

[81] Ochs F, Heidemann W, Müller-Steinhagen H. Effective thermal conductivity of moistened insulation materials as a function of temperature. International Journal of Heat and Mass Transfer 2008;51:539–52. https://doi.org/10.1016/j.ijheatmasstransfer.2007.05.005.

[82] Ochs F, Heidemann W, Muller-Steinhagen H. Effective thermal conductivity of the insulation of high temperature underground thermal stores during operation. Environment Science 2006:1–7.

[83] Abdou A, Budaiwi I. The variation of thermal conductivity of fibrous insulation materials under different levels of moisture content. Construction and Building Materials 2013;43:533–44. https://doi.org/10.1016/j.conbuildmat.2013.02.058.

[84] Villasmil W, Fischer LJ, Worlitschek J. A review and evaluation of thermal insulation materials and methods for thermal energy storage systems. Renewable and Sustainable Energy Reviews 2019;103:71–84. https://doi.org/10.1016/j.rser.2018.12.040.

[85] Mangold D., Deschaintre L., Seasonal thermal energy storage - report on state of the art and necessary further R + D. IEA-SHC Task 45 Large Systems 2015:1–48. http://task45.iea-shc.org/data/sites/1/publications/IEA_SHC_Task45_B_Report.pdf

[86] Yatsenko EA, Goltsman BM, Smoliy VA, Kosarev AS. Investigation of a porous structure formation mechanism of a foamed slag glass based on the glycerol foaming mixture. Research Journal of Pharmaceutical, Biological and Chemical Sciences 2016;7:1073–81.

[87] Zukri A, Nazir R, Said KNM, Moayedi H. Physical and mechanical properties of lightweight expanded clay aggregate (LECA). MATEC Web of Conferences 2018;250. https://doi.org/10.1051/matecconf/201825001016.

[88] Bianchi Janetti M, Plaz T, Ochs F, Klesnil O, Feist W. Thermal conductivity of foam glass gravels: A comparison between experimental data and numerical results. Energy Procedia 2015;78:3258–63. https://doi.org/10.1016/j.egypro.2015.11.713.

[89] Ochs F. Temperature and Moisture Dependence of the Thermal Conductivity of Insulation Materials 2005:1–5. http://wevik.hu/file/lambdavaltozas2.pdf

[90] Jelle BP. Traditional, state-of-the-art and future thermal building insulation materials and solutions - properties, requirements and possibilities. Energy and Buildings 2011;43:2549–63. https://doi.org/10.1016/j.enbuild.2011.05.015.

[91] NMC, Nomalen 28N, NMC Termonova Oy, 2015. https://dms.etra.fi:9900/72192/conversions/original?version=0.

[92] Kim H, Park D, Park ES, Kim HM. Numerical modeling and optimization of an insulation system for underground thermal energy storage. Applied Thermal Engineering 2015;91:687–93. https://doi.org/10.1016/j.applthermaleng.2015.08.070.

[93] Ademović Z, Suljagić J, Zulić J. Zahida Ademović, et al., Influence of physical properties on thermal conductivity of polystyrene insulation materials. Contemporary Materials 2017;1:42–7. https://doi.org/10.7251/COMEN1701042A.

[94] Luis J, Ordóñez P. Characterization of mussel shells as a bio-based building insulation material. 3rd International Conference on Bio-Based Building Materials 2019;37:525–31. https://doi.org/10.26168/icbbm2019.76.

[95] Grabmann MK, Wallner GM, Buchberger W, Nitsche D. Aging and lifetime assessment of polyethylene liners for heat storages - effect of liner thickness. ISES Solar World Congress 2017 2017:753–60. https://doi.org/10.18086/swc.2017.13.07.

[96] Koehl M, Meir M, Papillon P, Wallner G, Sandrin S. Polymeric materials for solar thermal applications. 2015. https://doi.org/10.1002/9783527659609.

[97] Scheirs J. A guide to polymeric geomembranes wiley series in polymer science. 2009. United States.

[98] Kübler R, Fisch N, Hahne E. High temperature water pit storage projects for the seasonal storage of solar energy. Solar Energy 1997;61:97–105. https://doi.org/10.1016/S0038-092X(97)00040-6.

[99] KAT. Experimental investigation of possible use of hdpe as thermal storage material in thermal storage type solar cookers. International Journal of Research in Engineering and Technology 2015;04:92–9. https://doi.org/10.15623/ijret.2015.0412019.

[100] Patti A, Acierno D. Thermal conductivity of polypropylene - based materials. polypropylene - polymerization and characterization of mechanical and thermal properties 2020. https://doi.org/10.5772/intechopen.84477.

[101] Grabmann MK, Wallner GM, Grabmayer K, Nitsche D, Lang RW. Aging behavior and lifetime assessment of polyolefin liner materials for seasonal heat storage using micro-specimen. Solar Energy 2018;170:988–90. https://doi.org/10.1016/j.solener.2018.06.046.

[102] Polyethylene - Low density (LDPE) material information. https://www.goodfellow.com/E/Polyethylene-Low-Density.html

[103] Titow WV. PVC technology (fourth edition). 1984, USA. https://doi.org/10.1007/978-94-009-5614-8.

[104] McKeen LW. Elastomers and rubbers. Permeability Properties of Plastics and Elastomers 2017:209–47. https://doi.org/10.1016/b978-0-323-50859-9.00010-5.

[105] Ma A, Wang X, Chen Y, Yu J, Zheng W, Zhao Y. Largely enhanced thermal conductivity of ethylene-propylene-diene monomer composites by addition of graphene ball. Composites Communications 2019;13:119–24. https://doi.org/10.1016/j.coco.2019.04.005.

[106] Gasque M, González-Altozano P, Maurer D, Moncho-Esteve IJ, Gutiérrez-Colomer RP, Palau-Salvador G, et al. Study of the influence of inner lining material on thermal stratification in a hot water storage tank. Applied Thermal Engineering 2015;75:344–56. https://doi.org/10.1016/j.applthermaleng.2014.10.040.

[107] Carvill J. Thermodynamics and heat stransfer. Mechanical Engineer's Data Handbook Butterworth-Heinemann, 1993;102-145. https://doi.org/10.1016/B978-0-08-051135-1.50008-X.

[108] Ochs F, Dahash A, Tosatto A, Reisenbichler M, O'Donovan K, Gauthier G, et al. Comprehensive comparison of fifferent models for large-Scale thermal energy storage. Proceedings of the International Renewable Energy Storage Conference 2021 (IRES 2021) 2022;8:36–51. https://doi.org/10.2991/ahe.k.220301.005.

[109] Sorknæs P. Simulation method for a pit seasonal thermal energy storage system with a heat pump in a district heating system. Energy 2018;152:533–8. https://doi.org/10.1016/j.energy.2018.03.152.

[110] Pan X, Xiang Y, Gao M, Fan J, Furbo S, Wang D, et al. Long-term thermal performance analysis of a large-scale water pit thermal energy storage. Journal of Energy Storage 2022;52:105001. https://doi.org/10.1016/j.est.2022.105001.

[111] Gauthier G. Benchmarking and improving models of subsurface heat storage dynamics, comparison of Danish PTES and BTES installation measurements with their corresponding TRNSYS models. 2020. https://www.heatstore.eu/documents/HEATSTORE_WP2_D2.3-Danish%20PTES%20and%20BTES%20installations_Final_2020.11.02.pdf

[112] Xie Z, Xiang Y, Wang D, Kusyy O, Kong W, Furbo S, et al. Numerical investigations of long-term thermal performance of a large water pit heat storage. Solar Energy 2021;224:808–22. https://doi.org/10.1016/j.solener.2021.06.027.

[113] Narula K, de Oliveira Filho F, Villasmil W, Patel MK. Simulation method for assessing hourly energy flows in district heating system with seasonal thermal energy storage. Renewable Energy 2020;151:1250–68. https://doi.org/10.1016/j.renene.2019.11.121.

[114] Kubiński K, Szabłowski Ł. Dynamic model of solar heating plant with seasonal thermal energy storage. Renewable Energy 2020;145:2025–33. https://doi.org/10.1016/j.renene.2019.07.120.

[115] Bai Y, Yang M, Fan J, Li X, Chen L, Yuan G, et al. Influence of geometry on the thermal performance of water pit seasonal heat storages for solar district heating.

Building Simulation 2020. https://doi.org/10.1007/s12273-020-0671-9.

[116] Bai Y, Wang Z, Fan J, Yang M, Li X, Chen L, et al. Numerical and experimental study of an underground water pit for seasonal heat storage. Renewable Energy 2020;150:487–508. https://doi.org/10.1016/j.renene.2019.12.080.

[117] Dahash A, Ochs F, Tosatto A, Streicher W. Toward efficient numerical modeling and analysis of large-scale thermal energy storage for renewable district heating. Applied Energy 2020;279:115840. https://doi.org/10.1016/j.apenergy.2020.115840.

[118] Dahash A, Michele Bianchi Janetti M, Ochs F. Numerical analysis and evaluation of large - scale hot water tanks and pits in district heating systems. Proceedings of Building Simulation 2019: 16th Conference of IBPSA 2020;16:1692–9. https://doi.org/10.26868/25222708.2019.210566.

[119] Li X, Wang Z, Li J, Yang M, Yuan G, Bai Y, et al. Comparison of control strategies for a solar heating system with underground pit seasonal storage in the non-heating season. Journal of Energy Storage 2019;26:100963. https://doi.org/10.1016/j.est.2019.100963.

[120] Nageler P, Schweiger G, Schranzhofer H, Heimrath R, Mach T, Fochler LM, et al. Co-simulation workflow for the dynamic modelling and simulation of large-scale district energy systems institute of thermal engineering, 16th IBPSA international conference and exhibition 2019. Rome, Italy. https://doi.org/10.26868/25222708.2019.211048.

[121] Dahash A, Janetti MB, Ochs F, Science M. Detailed 3-D models of a large-scale underground thermal energy storage with consideration of groundwater conditions. International sustainable energy conference 2018:597–604. Graz, Austria.

[122] Chang C, Wu Z, Navarro H, Li C, Leng G, Li X, et al. Comparative study of the transient natural convection in an underground water pit thermal storage. Applied Energy 2017;208:1162–73. https://doi.org/10.1016/j.apenergy.2017.09.036.

[123] Fan J, Huang J, Chatzidiakos A, Furbo S. Experimental and theoretic investigations of thermal behavior of a seasonal water pit heat storage. ISES Solar World Congress 2017 2017:714–25. https://doi.org/10.18086/swc.2017.13.03.

[124] Chatzidiakos A. CFD Calculations for Solar Water Pond Heat Storages. Technical University of Denmark. 2016.

[125] Reiter P, Poier H, Holter C. BIG Solar Graz: solar district heating in Graz - 500,000 m^2 for 20% solar Fraction. Energy Procedia 2016;91:578–84. https://doi.org/10.1016/j.egypro.2016.06.204.

[126] Ochs F. Large-Scale Thermal energy stores in district heating systems - simulation based optimization 2015:1–8. https://doi.org/10.18086/eurosun.2014.19.09.

[127] Raab S, Mangold D, Müller-Steinhagen H. Validation of a computer model for solar assisted district heating systems with seasonal hot water heat store. Solar Energy 2005;79:531–43. https://doi.org/10.1016/j.solener.2004.10.014.

[128] Yamaguchi E. Finite element method. Bridge Engineering Handbook: Fundamentals, Second Edition 2014:225–51. https://doi.org/10.1201/b15616.

[129] Dahash A, Janetti MB, Ochs F. Detailed axial symmetrical model of large - scale underground thermal energy storage. COMSOL 2018 Conference 2018. Lausanne,

Switzerland.

[130] Rutz D, Winterscheid C, Pauschinger T, Grimm S, Roth T, Doračić B, et al. Upgrading the performance of district heating networks. 2019. WIP Renewable Energies, Munich, Germany. https://www.upgrade-dh.eu/images/Publications%20and%20Reports/D2.5_2019-07-02_Upgrade-DH_Handbook_EN.pdf

[131] Dahash A, Ochs F, Giuliani G, Tosatto A. Understanding the interaction between groundwater and large-scale underground hot-water tanks and pits. Sustainable Cities and Society 2021;71:102928. https://doi.org/10.1016/j.scs.2021.102928.

[132] Duffie JA, Beckman WA, McGowan J. Solar Engineering of Thermal Processes. 1985. https://doi.org/10.1119/1.14178.

[133] L. Mazzarella, S. Holst, Multi-flow stratified thermal storage model with full mixed layers, TRNSYS Version (1992). https://www.trnsys.de/static/d747464ad7627a47a6610a89da64e9/Type_342.en.pdf

[134] Buoro D, Pinamonti P, Reini M. Optimization of a Distributed Cogeneration System with solar district heating. Applied Energy 2014;124:298–308. https://doi.org/10.1016/j.apenergy.2014.02.062.

[135] Hansen KK, Hansen PN. Heat storage in an uninsulated water pit: construction and testing of a 500 m^3 store. Technical University of Denmark, Department of Civil Engineering 1983:404–12. https://doi.org/10.1007/978-94-009-7924-6_54.

[136] Heller A. Floating lid constructions for pit water storage - a survey. Technical University of Denmark, Department of Civil Engineering 1997.

[137] Hansen PN, Hansen KK, Ussing V. Seasonal heat storage in underground warm water pit: design of a 500 m^3 store. Technical University of Denmark, Department of Civil Engineering 1984;4:490–501.

[138] Heller A. Development of seasonal storage in Denmark : status of storage programme 1997-2000. Terrastock 2000, Proceedings 2000:47–52.

[139] Hansen KK, Hansen PN, Ussing V. Seasonal heat storage in underground warm water pit: design of a 30.-50,000 m3 storage. Technical University of Denmark, Department of Civil Engineering 1984;4:490–501 https://doi.org/10.1007/978-94-009-6508-9_170.

[140] Ochs F, Müller-Steinhagen H. Abschlussbericht zum vorhaben: weiterentwicklung der Erdbecken-Wärmespeichertechnologie 2008. https://www.igte.uni-stuttgart.de/veroeffentlichungen/publikationen/publikationen_08-05.pdf

[141] Central solar heating plants with seasonal storage - status report. 1990;6. http://www.iea-shc.org/Data/Sites/1/publications/Task%207-%20Central%20Solar%20Heating%20Plants%20with%20Seasonal%20Storage-Status%20Report-June%201990.pdf

[142] Dalenbäck JO, Jilar T. Swedish solar heating with seasonal storage - design, performance and economy. International Journal of Ambient Energy 1985;6:123–8. https://doi.org/10.1080/01430750.1985.9675454.

[143] Ochs F. Stand der Technik erdvergrabener Wärmespeicher. FFG store4grid; 2013. http://www.aee-

now.at/cms/fileadmin/downloads/projekte/store4grid/store4grid_stand_der_technik.pdf

[144] Meliß M, Späte F. Solar heating system with seasonal storage at the Solar-Campus Juelich. Solar Energy 2000;69:525–33. https://doi.org/10.1016/S0038-092X(00)00116-X.

[145] Ochs F, Heidemann W, Müller-Steinhagen H, Kock H. Soil-water pit heat store with direct charging system. Geology, 2006:1–8.

[146] Urbaneck T, Platzer B, Schirmer U. Advanced monitoring of gravel water storage. 9th International Conference on Thermal Energy Storage 2003, Warschau, Polen.

[147] Urbaneck T, Schirmer U. Central solar heating plant with gravel water storage. Thermal Energy Storage; 2000. http://ptp.irb.hr/upload/mape/solari/08_Thorsten_Urbaneck_CENTRAL_SOLAR_HEATING_PLANT_WITH_GRAVEL_.pdf

[148] Schmidt T. Monitoring results from large-scale solar thermal plants with long term storage in Marstal, Brædstrup and Dronninglund, Denmark. https://businessdocbox.com/Green_Solutions/66372775-Monitoring-results-from-large-scale-solar-thermal-plants-with-long-term-storage-in-marstal-braedstrup-and-dronninglund-denmark.html

[149] Schmidt T, Sørensen A. Monitoring results from large scale heat storages for district heating in Denmark. 14th International Conference on Energy Storage 2018, Adana, Turkey. https://planenergi.dk/wp-content/uploads/2018/05/Schmidt-and-Soerensen_Monitoring-Results-from-Large-Scale-Heat-storages-....pdf

[150] Nielsen JE. Solar district heating experiences from Denmark. Eenegy platform workshop 3, Zurich 2014.

[151] Galindo Fernández, M, Roger-Lacan, C, Gährs, U, Aumaitre, V, Efficient district heating and cooling systems in the EU - case studies analysis, replicable key success factors and potential policy implications, 2016. https://doi.org/10.2760/371045.

[152] Ramboll. Large scale solar water heating and seasonal heat storage pit in Gram. https://stateofgreen.com/en/partners/ramboll/solutions/large-scale-solar-heating-and-seasonnal-heat-storage-pit-in-gram/.

[153] Marx R, Bauer D, Drueck H. Energy efficient integration of heat pumps into solar district heating systems with seasonal thermal energy storage. Energy Procedia 2014;57:2706–15. https://doi.org/10.1016/j.egypro.2014.10.302.

[154] Lindenberger D, Bruckner T, Groscurth HM, Kümmel R. Optimization of solar district heating systems: seasonal storage, heat pumps, and cogeneration. Energy 2000;25:591–608. https://doi.org/10.1016/S0360-5442(99)00082-1.

[155] Abokersh MH, Vallès M, Saikia K, Cabeza LF, Boer D. Techno-economic analysis of control strategies for heat pumps integrated into solar district heating systems. Journal of Energy Storage 2021;42. https://doi.org/10.1016/j.est.2021.103011.

[156] Abokersh MH, Saikia K, Cabeza LF, Boer D, Vallès M. Flexible heat pump integration to improve sustainable transition toward 4th generation district heating. Energy Conversion and Management 2020;225. https://doi.org/10.1016/j.enconman.2020.113379.

[157] Pinamonti M, Beausoleil-Morrison I, Prada A, Baggio P. Water-to-water heat pump integration in a solar seasonal storage system for space heating and domestic hot water production of a single-family house in a cold climate. Solar Energy 2021;213:300–11. https://doi.org/10.1016/j.solener.2020.11.052.

[158] Yumrutaş R, Ünsal M. Energy analysis and modeling of a solar assisted house heating system with a heat pump and an underground energy storage tank. Solar Energy 2012;86:983–93. https://doi.org/10.1016/j.solener.2012.01.008.

[159] Danish Energy Agency. Regulation and planning of district heating in Denmark 2016. https://ens.dk/sites/ens.dk/files/Globalcooperation/regulation_and_planning_of_district_heating_in_denmark.pdf

[160] Tian Z, Zhang S, Deng J, Fan J, Huang J, Kong W, et al. Large-scale solar district heating plants in Danish smart thermal grid: Developments and recent trends. Energy Conversion and Management 2019;189:67–80. https://doi.org/10.1016/j.enconman.2019.03.071.

[161] Dalenback JD, Jilar T. Swedish solar heating plants with seasonal storage - system design influence on thermal performance and economy. First E.C. Conference on Solar Heating, 1984, Amsterdam.

[162] Schemidt T. Marstal district heating monitoring data evaluation for the years 2015-2017. 2017. https://www.solar-district-heating.eu/wp-content/uploads/2019/10/Marstal-evaluation-report-2015-2017_2019.05.28.pdf

[163] Ramboll. Pit thermal energy storage update from toftlund, 2020. https://www.heatstore.eu/documents/20201028_DK-temadag_Ramb%C3%B8ll%20PTES%20project.pdf

[164] District heating with seasonal storage in Vojens Denmark. https://deepresource.wordpress.com/2020/12/16/district-heating-with-seasonal-storage-in-vojens-denmark/

[165] Pedersen PV, Mørck O. A total energy design for 92 houses with combined use of solar heating and energy conservation. Energy Conservation in Buildings 1991:1–5. https://doi.org/10.1016/b978-0-08-037215-0.50009-2.

Yutong Xiang, Meng Gao, Simon Furbo, Dengjia Wang, Zhiyong Tian, Jianhua Fan. (2022). Heat transfer of a large-scale water pit heat storage under transient operations, *Journal of Energy Storage, 55, 105455.* https://doi.org/10.1016/j.est.2022.105455

Heat transfer of a large-scale water pit heat storage under transient operations

Yutong Xiang[1], Meng Gao[1], Simon Furbo[1], Dengjia Wang[2], Zhiyong Tian[3], Jianhua Fan[1*]

1. Department of Civil Engineering, Technical University of Denmark, Brovej 118, Kgs. Lyngby DK 2800, Denmark
2. State Key Laboratory of Green Building in Western China, Xi'an University of Architecture and Technology, Xi'an, Shaanxi 710055, China;
3. School of Environmental Science and Engineering, Huazhong University of Science and Technology, Wuhan 430074, China

∗ Corresponding authors: E-mail addresses: jif@byg.dtu.dk (J. Fan).

Abstract

An accurate and less time demanding model is required when integrating pit thermal energy storage (PTES) into solar heating systems. Multi-node (1D) models are commonly used, but these models face challenges when calculating PTES thermal stratification and heat loss. Therefore, a full-scale computational fluid dynamics (CFD) model of PTES inclusive water and soil regions is developed using FLUENT to improve the accuracy of heat transfer calculation of a multi-node model. The CFD model is validated against the Dronninglund PTES measurements regarding PTES thermal stratification, inlet/outlet energy flow, and soil temperature distribution. The model corresponds well to the measurements in three aspects: (i) a maximum temperature difference of 1 K in the water region; (ii) a maximum temperature difference of 2 K in the soil region; (iii) a maximum outlet temperature difference of 3 K. An indicator $R_{\Delta T/\delta}$ defined as the ratio between the thermocline temperature difference and the thermocline thickness is proposed to assess suitable grid size for PTES models, and the quantitative relationship between $R_{\Delta T/\delta}$ and grid size is recommended. Investigations with a range of grid sizes show that by using the recommended grid size, the prediction accuracy of the multi-node model TRNSYS Type 343 is significantly improved. The root mean square deviations of the predicted MIX number are decreased by 11-43% for different years, and the relative differences of the monthly charge/discharge energy from the measurement are within 5%. The findings of this study provide guidance for selecting appropriate grid sizes to achieve better calculation accuracy for large-scale PTES.

Keywords: Pit thermal energy storage, computational fluid dynamics, multi-node model, grid size, thermocline, thermal stratification

Nomenclature

Latin characters *Subscripts*

C_p	Specific capacity, [J/kg·K]	bottom	Bottom diffuser
$C_{1\varepsilon}$, C_2	Turbulence constant, [-]	c	Cold water
E	Energy, [MWh]	ch	Charge
Fr	Froude number, [-]	calc	Calculated
g	Gravitational acceleration, [m/s^2]	disch	Discharge
k	Turbulence kinetic energy, [kg m^2/s^2]	h	Hot water
L	Location, [m]	i	Time step
M	Energy momentum, [J/m]	meas	Measured
m	Mass flow rate, [kg/min]	middle	Middle diffuser
N	Number of values for the simulation period, [-]	top	Top diffuser
		s	Soil
n	Node number, [-]	w	Water
P	Parameters, [-]		
T	Temperature, [°C]	*Greek*	
t	Time, [s]	ρ	Density, [kg/m^3]
$R_{\Delta T/\delta}$	Ratio of thermocline temperature difference to thermocline thickness, [K/m]	λ	Thermal conductivity, [W/m·K]
		μ	Dynamic viscosity, [kg/m·s]
		τ	Stress tensor, [kg/m^2·s^2]
Re	Reynolds number, [-]	ε	Turbulent energy dissipation rate, [m^2/s^3]
Ri	Richardson number, [-]	δ	Thermocline thickness, [m]
RMSD	Root mean square deviation, [-]	σ_k	Turbulence kinetic energy Prandtl number, [-]
u	Velocity of water, [m/s]	σ_ε	Turbulence energy dissipation Prandtl number, [-]
V	Volume, [m^3]	Δ	Difference, [-]
z	Height from the PTES bottom, [m]	ϑ	Relative deviation ratio, [%]
		θ	dimensionless temperature, [-]

1. Introduction

In compliance with the Paris Agreement, rapid uptake of renewable energies is necessary [1]. Thermal energy storage technologies can be used to integrate high proportions of renewable energy in electricity generation, industry, and buildings. Therefore, thermal energy storage is a critical component of the energy transition investment package and receives increasing attention [1].

Water-based large-scale heat storage has experienced rapid development over the last decade for three reasons: 1) Large-scale thermal energy storage outperforms economically small-scale thermal energy storage, especially when the storage size exceeds 10,000 m^3 [2–5]; 2) The increase in storage volume can reduce heat losses per m^3 storage volume by lowering surface area/volume ratios [6,7]; 3) Water has a high thermal capacity and a simple thermal storage structure that can be used [8,9].

Commonly, the most used types of large-scale thermal energy storage in practical applications can be divided into the following [10]: tank thermal energy storage (TTES), borehole thermal energy storage (BTES), aquifer thermal energy storage (ATES), and pit thermal energy storage (PTES). Notably, PTES is known for enabling higher charging/discharging energy rates and lower investment costs than other types [3,8]. With the successful construction and operation of large-scale PTES in Denmark, about ten projects integrated with PTES are in operation or planned [11]. The newly built PTES are partly buried under the ground level, with a height higher than 10 m and a volume larger than 10000 m^3. In this case, three inlet/outlet diffusers are equipped for better thermal stratification. It is challenging to set up actual experiments for such a large project to investigate the factors that affect the performance of PTES. Therefore, suitable modeling tools are preferred in the planning phase. For instance, the 1D models based on the finite difference and the finite element method are prevailing among researchers due to their less computational effort.

Dahash et al. [12–16] developed a model based on the finite element method. Compared to Dronninglund PTES measurements, numerical results such as annual charge/discharge energy, internal energy, and heat loss were all within 0.5% deviation. Moreover, the calculated temperature development inside the PTES also agreed well with the measured results. However, the model was implemented on the COMSOL platform, and linking with system simulation software was not easy. In this context, further system-level investigation using this model remains a challenge.

Published models for PTES studies based on the finite difference method include Type 342, Type 343, Type 1300, Type 1322, and Type UGSTS (Underground Seasonable Thermal Energy Storage), all developed in the TRNSYS environment. Raab et al. [17] carried out a validation study for Type 342, considering measured data from the Hannover TTES. Simulation results showed that the maximum deviation over the year between calculated and measured temperatures was 3.7 K which appeared at the height of the middle charging/discharging diffuser. Type 342 was also studied by Gauthier [18] and Pan et al. [19] using Dronninglund PTES measurements. Gauthier [18] compared Type 342, Type 1300, and Type 1322 under the same conditions. The coefficients of determination for all three types of energy flow and outlet temperature were above 95%. However, Type 342 showed significant deviations in predicting side and bottom heat losses. Pan et al. [19] modified Type 342 to consider the actual scale PTES with more than two inlet/outlets. The results showed a marked difference between the calculated and measured MIX number value between July and October, demonstrating that Type 342 overestimated mixing in the PTES. Xie et al. [20] developed a simulation model of PTES based on Type 343. The calculated yearly energy flow showed good agreement with the measurement data of the Dronninglund PTES. In addition, the influence of parameters, such as soil properties and inlet arrangement on the performance of PTES was elucidated. Bai et al. [21,22] developed the Type UGSTS and verified it by the experimental data of the Huangdicheng PTES. Good agreement was shown between the measured and the simulated results. The difference between the calculated and measured temperatures was 1.4 K for PTES and 7 K for soil temperature. Additionally, Fan et al. [23] modified a TRNSYS model to include a 75000 m^3 PTES for the Marstal district heating plant. Compared with the measured results, the simulation could reflect the temperature development trend of PTES but failed to reproduce the inner temperature distribution, especially from May to August.

The aforementioned literature shows that PTES simulation research is still in the model validation process. Building an experimental platform is a challenge because actual PTES is large and complex in shape, and detailed studies are time-consuming. Currently, 1D models have good accuracy in predicting annual performance, and the models developed in the TRNSYS environment are suitable for system simulation. However, due to model assumptions (such as plug flow simplification, neglect of the inlet mixing effect, and the effects of natural convection), the 1D models showed large deviations for several months and could not accurately calculate the temperature distribution under transient conditions [11]. If plug flow assumption is not used, artificial mixing will spread throughout the water at different time steps, which results in significant numerical diffusion when fewer nodes are used. In this case, it has

been proposed to use more nodes to reduce numerical diffusion effectively [24]. Instruction for Type 342 suggested that finer spacing must be used in storage regions with large temperature gradients [25]. The method was also tried by Cody [26] on Type 4, Type 60, and Type 534. The investigation results showed that by increasing the number of nodes, the thermal stratification could be determined in the best possible way. However, using more nodes means more computation time. Therefore, adaptive node models were further proposed. For Type 38, the size of the nodes was allowed to vary with flow inlet conditions [27]. For the new model developed by Powell and Edgar [24], a dynamic changing node was used to track the thermocline. Yet, these approaches were investigated based on a small-scale water storage tank with two inlet/outlets. In such systems, the thermal stratification might differ from that observed in the large-scale PTES. Moreover, the adaptive grid model does have disadvantages since it cannot accurately represent the second thermocline caused by inner natural convection during the standby.

Thus for simulation and optimization of integrated thermal energy systems, accurate and simplified models are required to improve computational efficiency while accurately representing the thermal behavior of PTES under transient conditions. To the authors' knowledge, no literature addresses the improvement of the 1D model for large-scale PTES in terms of the grid size. Additionally, no criteria are provided for selecting the proper grid size for large-scale PTES 1D models.

The current study developed a full-scale 3D model, including water and soil regions, to fully understand the thermal behaviors of PTES under different conditions. Since it is computationally intensive, the water and soil regions of the model were validated separately using measured data from the Dronninglund PTES. In this context, a four-year calculation was performed for the soil region, while four representative cases from 2017 were selected for the water region. Then, the focus was on the grid sizes in terms of calculation accuracy for PTES temperature distribution. The ratio of thermocline temperature difference to thermocline thickness was proposed as an indicator for selecting the appropriate grid size. Based on this finding, the year-round variation of the thermocline characteristic was analyzed to determine the grid size distribution for 1D models. Lastly, a three-year calculation was carried out using TRNSYS Type 343 to demonstrate the reliability of the recommended grid size distribution. The improvement was addressed by comparing the model accuracy in terms of MIX number and charge/discharge energy under different grid size distributions.

2. Numerical and experimental methodology

2.1 Pit thermal energy storage description

The 60,000 m^3 PTES of the Dronninglund plant was selected as the experimental case for validating the numerical model. Fig.1 shows a schematic of Dronninglund PTES, which is partly constructed as a truncated pyramid stump above the ground level. The depth of the PTES is 16 m, and the sidewalls have a slope of 26.6°. The outer dimensions of the top and the bottom surface are 90 m × 90 m and 26 m × 26 m, respectively [28,29]. On the top of the PTES, there is a floating lid consisting of five layers: (from top to bottom) 1.5 mm HDPE Geomembrane, 3 mm Hypernet CN-E, 240 mm Nomalén insulation, 3 mm Hypernet HF-E, and 2mm HDPE Geomembrane. For the side and the bottom wall, a 2.5 mm HDPE Geomembrane layer, as well as a fabric layer, are used to enclose the water [30].

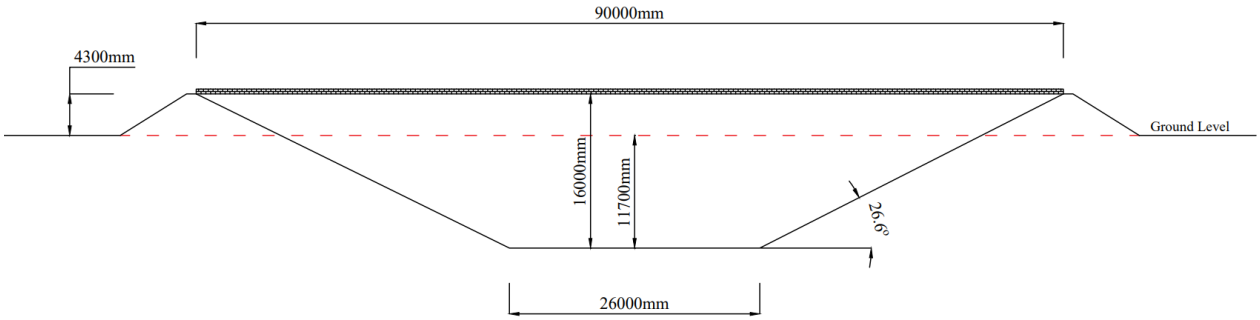

Fig.1 Schematic of Dronninglund PTES

Fig.2 shows the details of the arrangements of the inlet/outlet pipes. Three 273 mm diameter inlet/outlet pipes connect the PTES through the bottom and are arranged at different height levels. In order to maintain thermal stratification inside the PTES, the inlet/outlet diffusers consist of two horizontal discs with a diameter of 2500 mm.

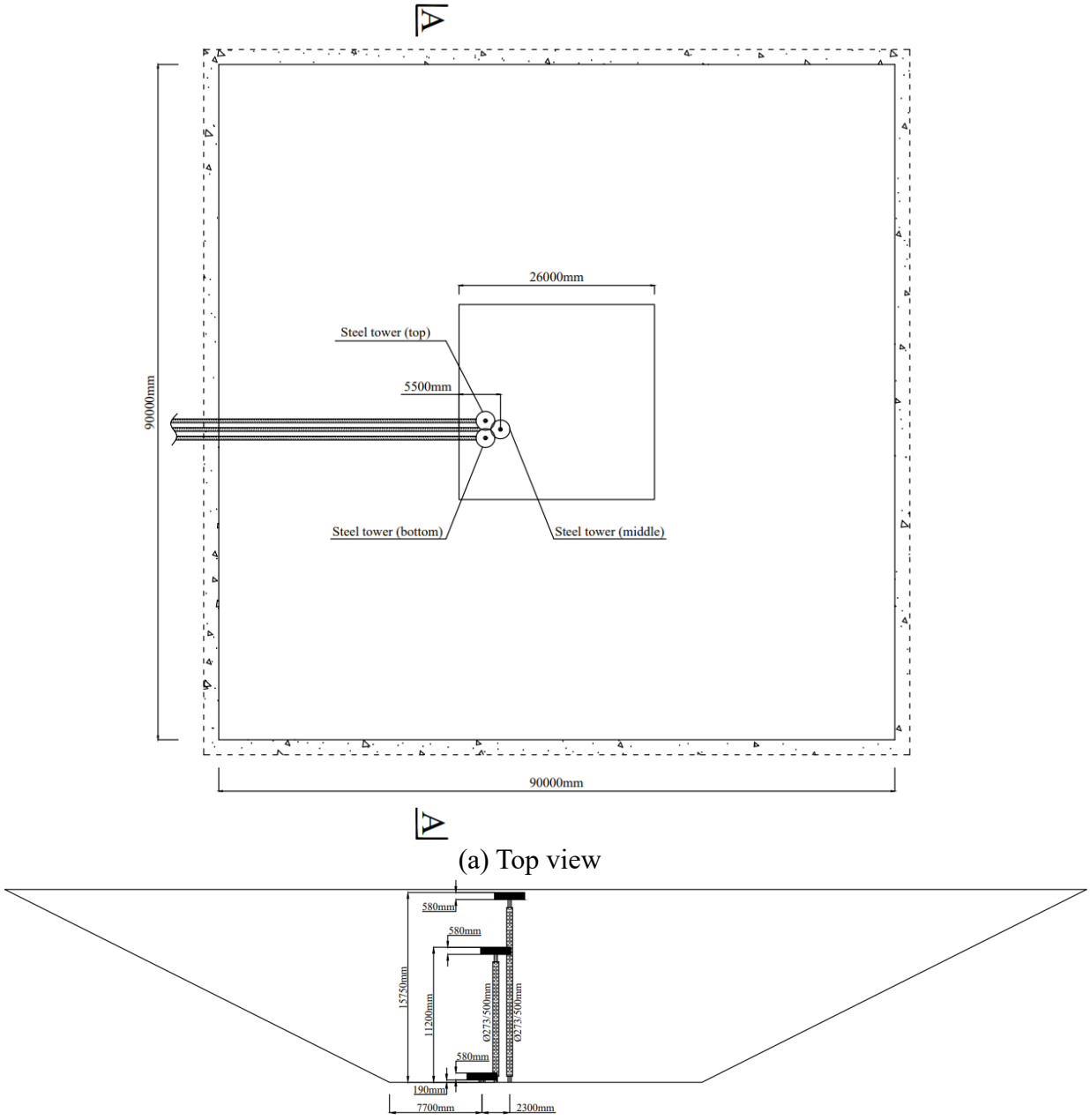

(a) Top view

(b) A-A view

Fig.2 Illustration of the inlet/outlet pipes arrangement inside the PTES [31,32]

Accordingly, the full-scale 3D model (shown in Fig. 3), including the water and soil region, was created based on Dronninglund PTES dimensions. Two simplifications were made to simplify the mathematical models: 1) The water flow inside the leading pipe (connected to the diffusers) was neglected; 2) The supporting structure of the diffusers was ignored. Notably, the soil region was built large enough to reduce the effect of the model's adiabatic boundaries on the soil temperature distribution around the water region. In addition, the geological investigation of the Dronninglund project indicates that the groundwater level is approximately 17 m under the ground level [28,33]. Thus, the soil region was divided into two parts at the height of 17 m, each of which can be assigned different soil properties.

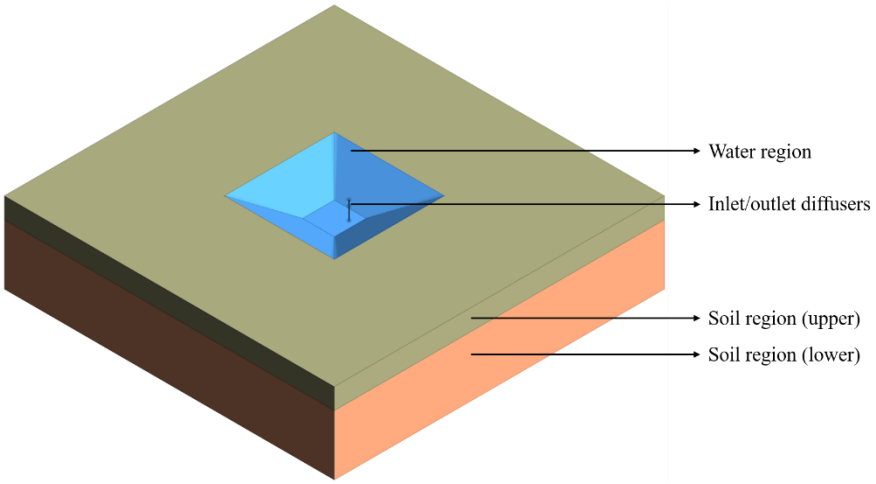

Fig.3 3D model of the water pit heat storage

2.2 Mathematical model

The water region was considered an incompressible fluid with temperature-dependent thermophysical properties. In this case, the governing equations of the water region are based on the laws of conservation of mass, momentum, and energy. The upper and lower soil region had constant thermal properties, while groundwater flow was not considered to reduce the computational effort. Therefore, the governing equation of the soil region is based on the law of energy conservation.

2.2.1 Governing equations

The 3D conservations of the flow and heat transfer in the water and soil region can be defined as follows [34]:

$$\nabla \cdot (\rho_w \vec{u}) = 0 \tag{1}$$

$$\frac{\partial(\rho_w \vec{u})}{\partial t} + \nabla \cdot (\rho_w \vec{u}\vec{u}) = -\nabla p + \nabla \cdot \tau_w - \rho_w g \tag{2}$$

The enthalpy equation of the water region is shown in Eq. 3.

$$\frac{\partial(\rho_w C_{p.w} T)}{\partial t} + \nabla \cdot (\rho_w C_{p.w} \vec{u} T) = \nabla \cdot (\lambda_w \cdot \nabla T) \tag{3}$$

The enthalpy equation of the soil region is shown in Eq. 4.

$$\rho_s C_{p.s} \frac{\partial T}{\partial t} = \lambda_s \nabla^2 T \tag{4}$$

Where ρ_w and ρ_s indicate the density of water and soil; u is the velocity of water; $C_{p.w}$ and $C_{p.s}$ represent the specific capacities of water and soil; λ_w and λ_s are the thermal conductivity of water and soil; τ_w presents the stress tensor of water.

2.2.2 Turbulence modeling

The flow pattern depends strongly on the configuration of the PTES (including the inlet/outlet design, the aspect ratio of the inlet/out to the storage) [35], as well as the operating conditions (such as inlet velocity, inlet temperature, the temperature difference between the incoming and internal water, and the internal stratification). Therefore, the fluid dynamic model should be selected carefully to better deal with the fluid mixing inside PTES.

The inlet *Re* number, *Fr* number, and *Ri* number (i.e., $Ri = Fr^{-2}$) have been used in previous studies as indicators by which flow state can be evaluated for different radial diffuser designs. A *Re* number criterion given by Blevins [36] predicted that for almost all full-scale tanks operating at a design flow rate, the flow entering the tank would be fully turbulent when an isothermal radial wall jet issued from a slot of finite height. Deng et al.[37] selected k-ε to study the performance of a thermal storage tank with radial diffusers since the *Re* number was much larger than 2300 in their study. Moreover, in the case of stratified flow, both the inlet *Re* and *Fr* number influence the turbulent transition. Keulegan [38] believed that the transition started when the ratio of *Re* number and *Ri* number exceeded 500. Investigations conducted by Cai et al. [39] also confirmed that it was essential to consider both the inlet *Fr* and *Re* number. Therefore, when the inlet *Re* number exceeds 2300, and the *Ri* number is greater than 500, it should be considered turbulent flow.

In this study, the turbulence model was used to simulate water flow inside PTES because the dynamic inlet *Re* number is more significant than 5000, and the *Ri* number is beyond 500 during most operating periods. Moreover, the realizable k-ε model was selected due to its ability to more accurately predict the spreading rate of round jets [34,40]. The transport equations in this model for the kinetic energy k and the dissipation rate ε are given as Eq. (5) and Eq. (6).

$$\frac{\partial(\rho_w k)}{\partial t} + \nabla \cdot (\rho_w k U) = \nabla \cdot \left[\left(\mu_w + \frac{\mu_t}{\sigma_k}\right) \cdot \nabla(k)\right] + G_k + G_b - \rho\varepsilon \quad (5)$$

$$\frac{\partial(\rho_w \varepsilon)}{\partial t} + \nabla \cdot (\rho_w \varepsilon U) = \nabla \cdot \left[\left(\mu_w + \frac{\mu_t}{\sigma_\varepsilon}\right) \cdot \nabla(\varepsilon)\right] + C_{1\varepsilon}\frac{\varepsilon}{k}C_{3\varepsilon}G_b - C_2\rho_w \frac{\varepsilon^2}{k+\sqrt{\frac{\mu_w}{\rho_w}\varepsilon}} \quad (6)$$

The turbulence constants $C_{1\varepsilon} = 1.44$ $C_2 = 1.9$ $\sigma_k = 1.0$ and $\sigma_\varepsilon = 1.2$ are established according to Ref. [34].

2.3 Model details

2.3.1 Meshing

The mesh scheme plays an essential role in the rationality of the simulation results. In this study, the soil and water regions were separated by interfaces so that the two regions could be calculated separately with different mesh densities (see Fig.4 (a)) to reduce the calculation

effort. The structure grids were used for both the water and the soil regions. It is evident in Fig.4 (b) that mesh in the region near the inlet/outlet diffuser was refined in order to capture its relatively high temperature and velocity gradients. Additionally, a boundary layer mesh was applied close to the adjacent walls to address heat transfer between the soil and water region. With appropriate grid size, truncation and discretization errors can be minimized, facilitating faster convergence [41]. Section 3 analyzes the calculation accuracy with different grid sizes.

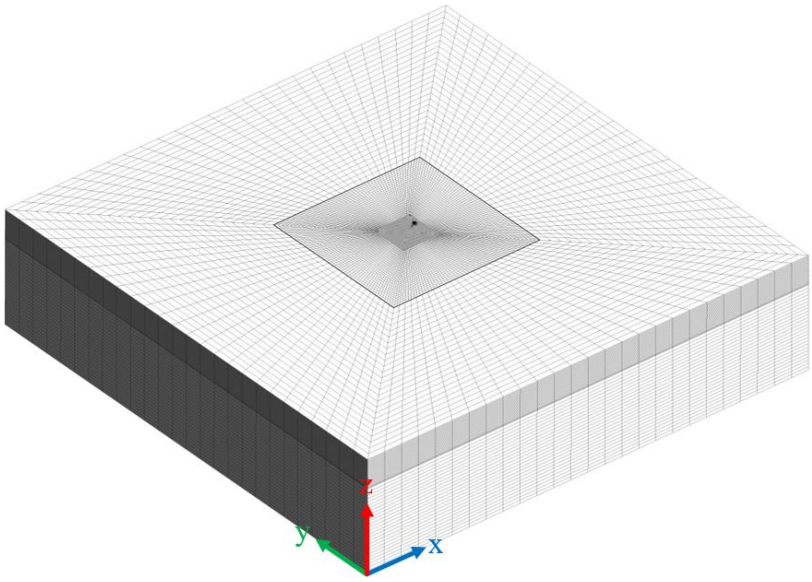

(a) Axonometric view

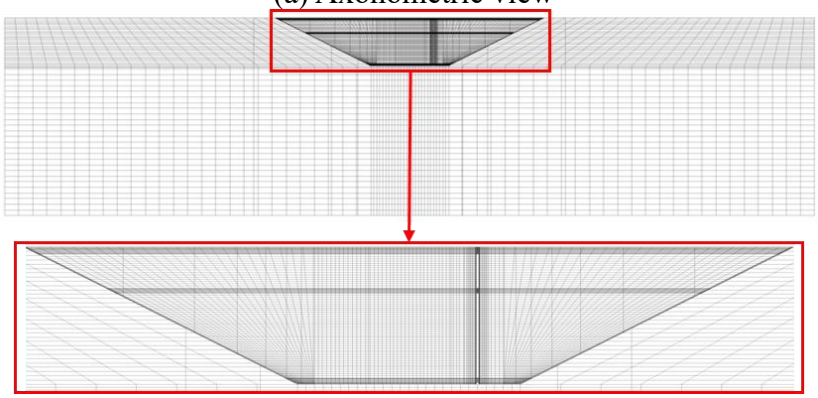

(b) Vertical cut plane

Fig.4 Grid scheme of the model

2.3.2 Numerical procedure

The governing equations were solved in each cell. A SIMPLE pressure-velocity coupling scheme was employed. The spatial discretization settings for pressure, momentum, and energy were PRESTO, second-order upwind, and second-order upwind, respectively. The pressure, density, momentum, and energy under relaxation value factors were 0.3, 0.8, 0.7, and 0.95, respectively. For energy, the convergence criteria were kept at 10^{-6}, while for velocity, continuity, and other variables, it was kept at 10^{-3}.

2.3.3 Thermal properties

Water was used as the heat storage media inside PTES. The following correlations provide the temperature dependence of the density, dynamic viscosity, thermal conductivity, thermal expansion coefficient, and specific heat capacity of water, respectively [42,43], where T is temperature in Kelvin.

Density, [kg/m^3] $$\rho = 863 + 1.21 * T - 2.57 * 10^{-3} * T^2 \quad (7)$$

Dynamic viscosity, [kg/m·s]

$$\mu = 9.67 * 10^{-2} - 8.207 * 10^{-4} * T + 2.344 * 10^{-6} * T^2 - 2.244 * 10^{-9} * T^3 \quad (8)$$

Thermal conductivity, [W/m·K] $$\lambda = 3.75 * 10^{-1} + 8.84 * 10^{-4} * T \quad (9)$$

Specific heat, [J/kg·K] $$C_p = 4432.6 - 1.819 * T + 3.3 * 10^{-3} * T^2 \quad (10)$$

According to the geological survey and reported soil properties [44–46], the soil properties for different parts are shown in Table 1, together with the physical properties of other solid materials used in this study [13,47–50]. The thermal conductivity of Nomalén 28N was assumed to be 0.02 higher than the standard value of 0.04 W/(m·K) [20,51], considering the 30% to 50% increase in thermal conductivity due to degradation of the insulation material caused by a long time exposure to high temperature and humidity.

Table 1 Physical properties of solid materials used in the numerical model

Material	ρ [kg/m^3]	λ [W/m·K]	C_p [J/kg·K]
Soil (upper part)	1840	1.8	900
Soil (lower part)	2200	2.3	1800
Nomalén 28N	28	0.06	2857
HDPE	940	0.4	1900
HF-E	940	0.4	1900
Stainless Steel	7600	15	490

2.4 Monitoring parameters

The distribution of the temperature measuring points in the Dronninglund PTES and the soil region can be seen in Fig. 5 [18,52]. Notably, all dimensions are in millimeters in the schematic diagram. In addition to the top sensor located 0.1m under the bottom of the cover, 32 temperature sensors are installed with an interval of 0.5 m from the bottom to the top of the PTES. On the north side of the PTES, four temperature sensors are placed in the soil at a depth of 10 m, 15 m, 20 m, and 25 m with the aim of monitoring soil temperature changes. Further, three inlet/outlet pipes are equipped with sensors that measure the water's temperature and volume flow rate. The measured temperatures are used to validate the developed CFD model.

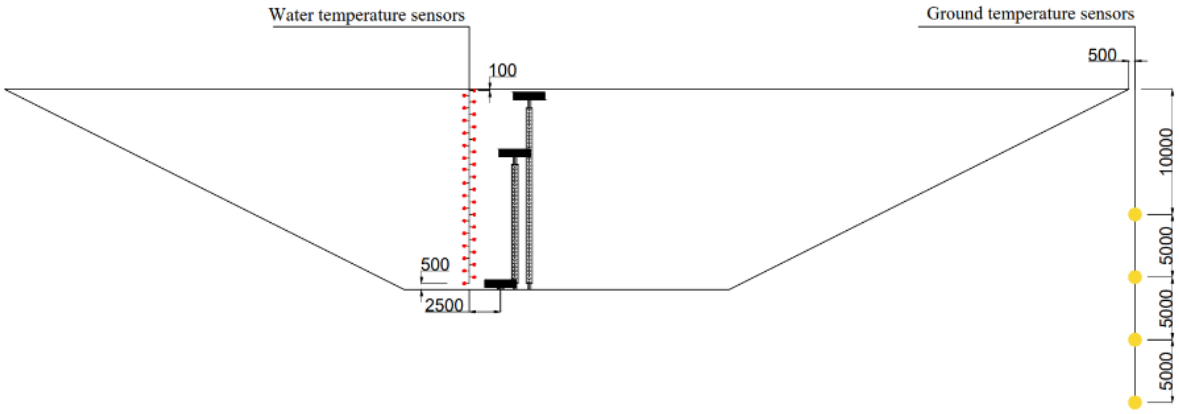

Fig.5 Scheme diagram of monitoring sensor position

3 Results and discussion

3.1 Uncertainty and calibration indicators

Before the validation process, it is essential to outline all uncertainties that arise from the measurements and the modeling approach.

The measurement uncertainties are owed to measurement equipment's accuracy and measurement method. In the Dronninglund project, the temperature sensors are Class A PT100, with an accuracy of ±0.15 K [53]. The volume flow rate is measured using electromagnetic flowmeters, with an accuracy of 0.4%. It is worth noting that the position of temperature sensors inside the PTES may change as the water level fluctuates. In addition, the inlet/outlet temperatures and volume flow rate are measured in the technical room a distance away from the PTES. Therefore, it takes time for the fluid in the leading pipes to flow between the PTES and the technical room, resulting in delay and inaccurate temperature measurements in case of frequent operation mode shifts [20].

The modeling uncertainties are related to the model assumptions. In this study, the water level is assumed constant, and the water enters the PTES directly from the diffusers without considering the flow process in the leading pipe. Additionally, the thermal properties of insulation and soil are constant regardless of changes in moisture content.

By comparing the calculated and the measured parameters, root mean square deviation (RMSD) is used. RMSD is defined as Eq. (11).

$$\mathrm{RMSD} = \sqrt{\frac{1}{N}\sum_{i=1}^{N}\left(P_{calc,i} - P_{meas,i}\right)^2} \tag{11}$$

Where $P_{calc,i}$ and $P_{meas,i}$ are respectively the calculated and the measured parameters logged every 10 min. N presents the number of obtained values for the simulation period.

3.2 Soil region

The calculation of the 3D model combining the soil and water region is very time-consuming due to the large volume and the calculation principle of the water region. Therefore, the 3D model of the soil region was tested separately under long-term simulations to find a suitable grid. Seven grid densities were formed by refining the mesh in different directions. The calculated soil temperatures were compared with the measured temperatures from 05-2014 to 12-2017.

Fig.6 illustrates the soil temperature variations at different locations. The discontinuity in the measurement results is due to a hardware failure of the SCADA system [52]. Overall, the model can reflect the development of measured soil temperatures. Even though the calculated soil temperatures at 15 m and 20 m are slightly different from the measured temperature, this can be explained by the change of soil thermal properties over time due to changes in soil moisture. The maximum differences between the measured and calculated soil temperatures at 10 m, 15 m, 20 m, and 25 m are 2 K, 1.8 K, 1.6 K, and 0.8 K, respectively. Moreover, the soil temperature calculation with different grid densities is basically unbiased, which means that increasing node numbers does not affect the calculated temperatures in the soil region.

Therefore, the heat transfer prediction accuracy of the surrounding soil model is considered acceptable. To reduce the computational requirements, a grid with 1.9×10^5 nodes was used for the soil-water combination model simulation.

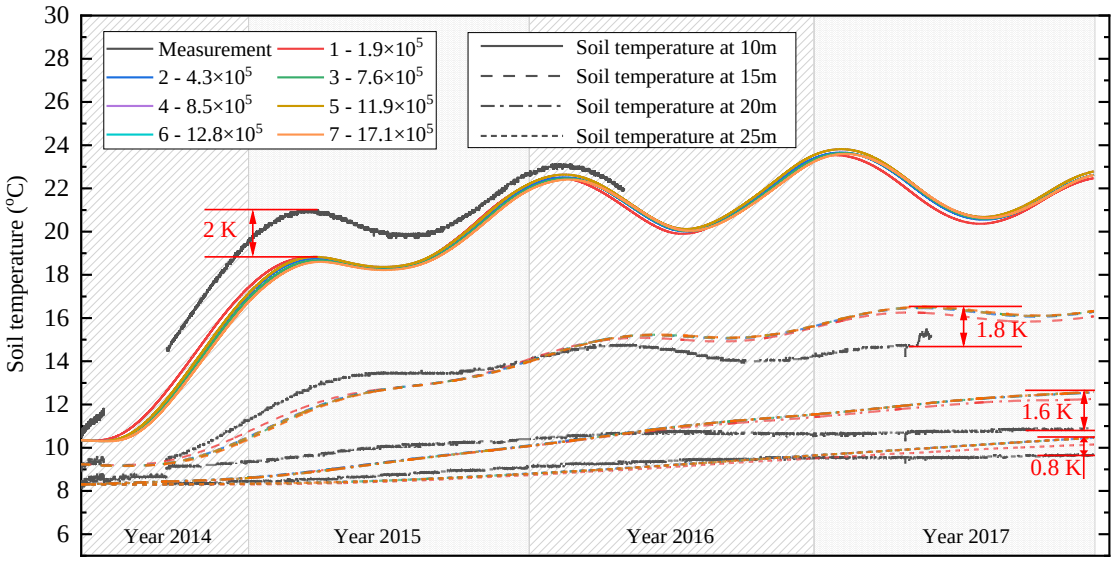

Fig.6 Soil temperature calculation for 7 mesh densities

3.3 Water region

3.3.1 Representative period selection

The charging/discharging conditions and the thermal stratification inside the PTES constantly change over the year. However, it is difficult to perform long-term simulations for

such a large 3D soil-water combination model due to the limitation of computing resources. Therefore, four representative cases in the year 2017 were selected to assess the accuracy of the 3D model, considering thermal stratification, charging/discharging characteristics, and the heat transfer between the water and soil region. Fig.7 shows the changes in PTES temperature distribution and operating conditions over 24 hours for the four cases. For Case 1, PTES temperature distribution barely changed over 24 hours, as is the PTES discharged at a mass flow rate below 15 kg/m^3 for most of the day. For Case 2, the temperature distribution at heights above 13 m varies greatly between 10:00 and 16:00 due to charge with a mass flow greater than 90 kg/m^3. For Case 3, the PTES temperature distribution does not change much either, but a significant temperature gradient is clearly seen between the heights of 14 m and 15 m. All heights of Case 4 have a slight temperature increase due to the inflow of hot water from the middle and top diffusers during the daytime.

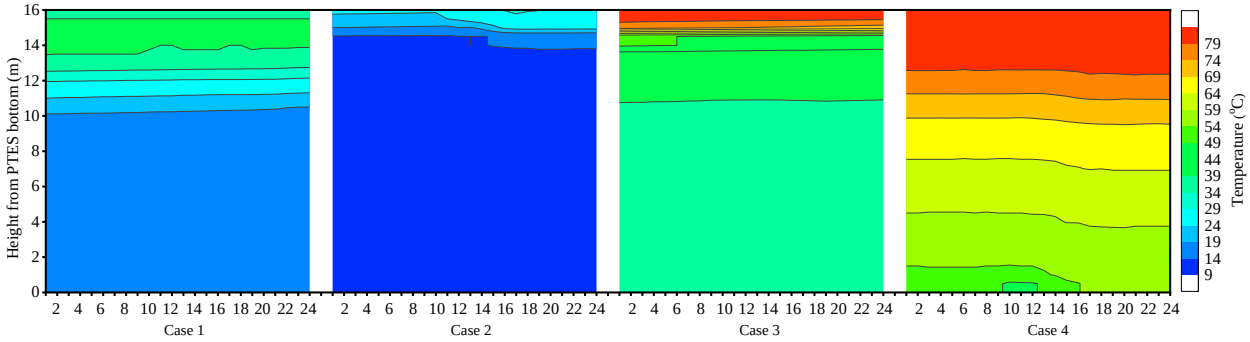

(a) Measured PTES temperature distribution

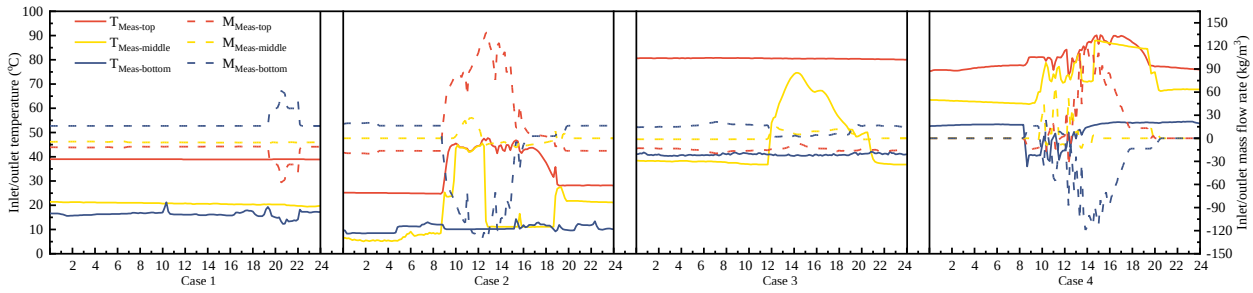

(b) Mass flow rates and temperatures of the three diffusers during the day

Fig.7 Cases description

Table 2 summarizes the operating conditions and thermocline characteristics. It is worth noting that, for Case 2, the thermocline thickness is decreasing, and the thermocline temperature difference is increasing from 16:00. The dimensionless temperature, defined by Eq. (12), is used to assess the thermocline thickness [26].

$$\theta(z) = \frac{T(z)-T_c}{T_h-T_c} \tag{12}$$

In Eq. (12) $\theta(z)$ is the dimensionless temperature, $T(z)$ is the average warm/cold water temperature at a certain height inside PTES, T_h is the PTES hottest temperature and T_c is the PTES coldest temperature.

The thermocline is defined where the dimensionless temperature is in the range 0.15-0.85 [54]. In this context, the thermocline thickness is calculated using Eq. (13). In the equation, z_h is the height where $\theta = 0.85$ and z_c is the height where $\theta = 0.15$.

$$\Delta z = z_h - z_c \tag{13}$$

Table 2 Characterization of different cases

Case	Date	Mode	Operation condition	Thermocline description
Case 1	January 5	Discharge	Flow out from top and bottom diffusers; Flow into middle diffuser;	Thermocline thickness: 3.5 m (basically unchanged the whole day); Thermocline temperature difference: 18.8 K (basically unchanged the whole day);
Case 2	March 15	Charge (daytime)	Flow out from bottom diffuser; Flow into top and middle diffusers;	Thermocline thickness: (2.5 m from 0:00, 1.8 m start 16:00); Thermocline temperature difference: (10.5 K from 0:00, 13.8 K start 16:00) ;
		Discharge (nighttime)	Flow out from top diffuser; Flow into bottom diffuser;	
Case 3	June 2	Discharge (daytime)	Flow out from top diffuser; Flow into middle diffuser;	Thermocline thickness: 2 m (basically unchanged the whole day); Thermocline temperature difference: 31.4 K (basically unchanged the whole day);
		Discharge (nighttime)	Flow out from top diffuser; Flow into bottom diffuser;	
Case 4	September 1	Charge (daytime)	Flow out from bottom diffuser; Flow into the top and middle diffusers;	Thermocline thickness: 9.5 m (basically unchanged the whole day); Thermocline temperature difference: 21 K (basically unchanged the whole day);
		Standby (nighttime)	--	

3.3.2 Effect of simulation time step and grid size

Firstly, all cases were investigated to determine the optimal time step and grid density. Fixed time steps of 0.5 s, 1 s, 1.5 s, and 2 s were tried, and the difference between calculated and measured results was less than 1% as the time step was decreased. Subsequently, the 2 s time step was used to save computing time. Then, seven grid densities were formed by refining the grid from the z-direction and x/y direction. With the increase of the grid density in the x/y

direction, the change in the calculation results is negligible. However, the grid size in the z-direction (vertical direction) significantly influences the accuracy of PTES temperature prediction. Fig.8 presents PTES temperature distribution calculation accuracy under different grid sizes using RMSD. Notably, the thermocline region is marked between the solid black lines, as previous investigations have shown that assigning a large number of grids to the thermocline region can effectively achieve higher accuracy [24,26].

From Fig.8, it is apparent that the grid size is negligible for temperature calculation accuracy in non-thermocline regions. Also, for non-thermocline heights, the RMSD over 24 hours of simulation is within 1 K. However, for these cases, the grid size influences the accuracy of temperature calculation within the thermocline region differently. For Case 1, the temperature calculation accuracy in the thermocline region improves slightly within 0.4 K as the grid size decreases. For Case 2 and Case 3, the PTES temperature in the thermocline region is significantly overestimated at large grid sizes, with the RMSD of approximately 1.9 K and 6.8 K for the 24-hours simulation, respectively. When the grid size is reduced to 0.04 m, the temperature calculation accuracy is improved by 1 K for Case2 and 3.2 K for Case 3. While the calculation results of Case 4 are independent of the grid size. In other words, for Case 4, grid size has little impact on temperature calculation accuracy.

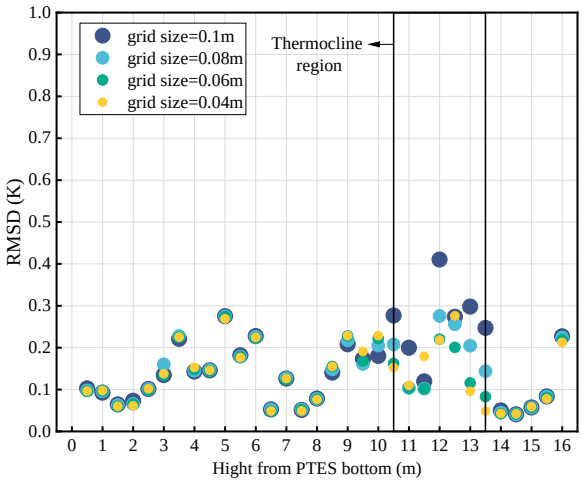

(a) Case 1

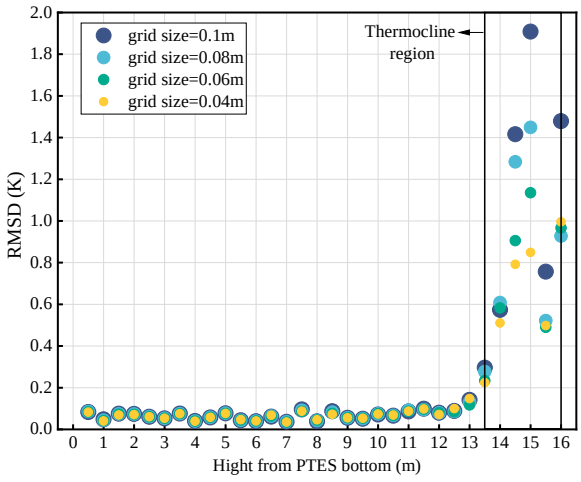

(b) Case 2

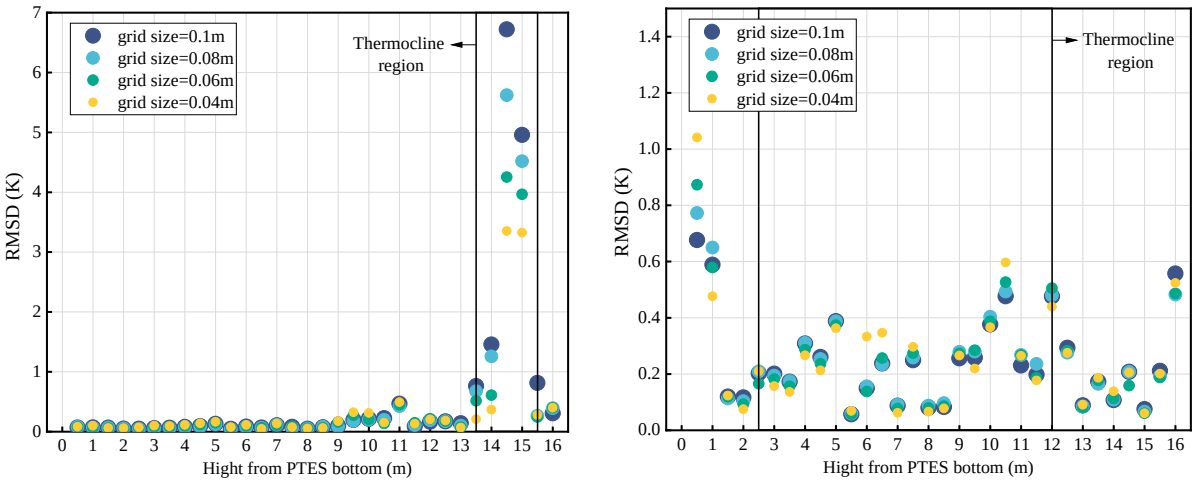

(c) Case 3 (d) Case 4

Fig.8 Effect of grid size on the calculation accuracy

To balance calculation accuracy and computational cost, a grid size of 0.06 m in the z-direction is used for all cases in the following study to demonstrate the model's reliability.

3.3.3 Water temperature

To further demonstrate the model's accuracy in calculating the PTES temperature development trend, Fig.9 visually shows the calculated and measured temperature development inside PTES with hourly resolution. The labels marked with 'Calc' and 'Meas' represent the calculated and the measured temperature at the corresponding heights. Only the heights mentioned above have greater fluctuation over a 24-hour period are plotted.

Fig. 9 shows a remarkable matching between calculated and measured PTES temperature for Case 1 and Case 4, with maximum temperature difference within 0.5 K and 1 K, respectively. However, for Case 2 and Case 3, a temperature difference larger than 2 K appeared at 14.5 m and 15 m. Two reasons can explain this:

1) The monitored temperature points inside PTES are assumed to be fixed in the CFD calculation. In contrast, the uncertainty of the actual temperature sensor position varies within ±0.3 m due to the water contraction and expansion. In this case, calculated temperatures at 14.4 m and 15.05 m are added, revealing that the calculated accuracy can be improved by considering the uncertainty of temperature measurement.

2) There is a considerable temperature difference within a smaller thickness. Together with Table 2, the temperature difference to thickness ratio (temperature gradient) for Case 2 changed from 4.2 at 14:00 to 7.7, while it reached 15.7 for Case 3 at the start of the day. In this context, two measurement points are not enough to reflect the actual temperature gradient within such a large ratio because the temperature of the adjacent heights has a significant impact on its temperature prediction.

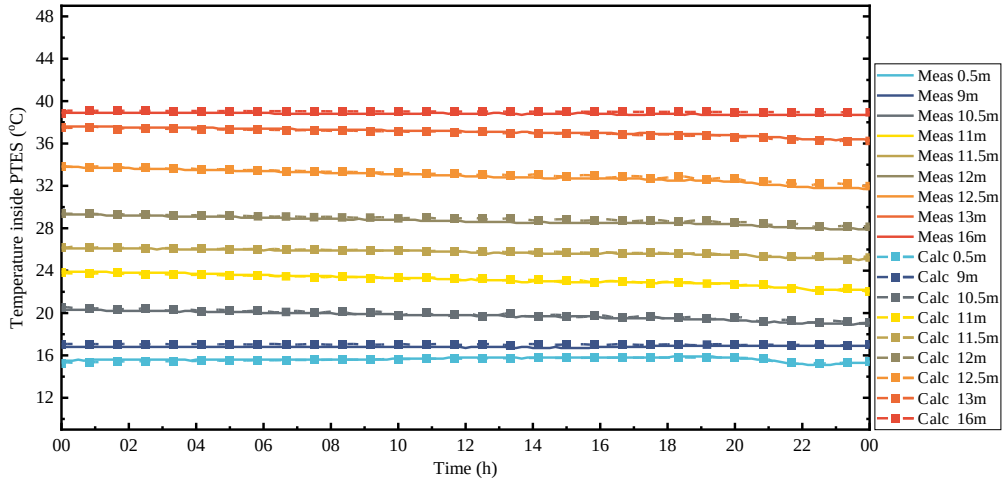

(a) Case 1

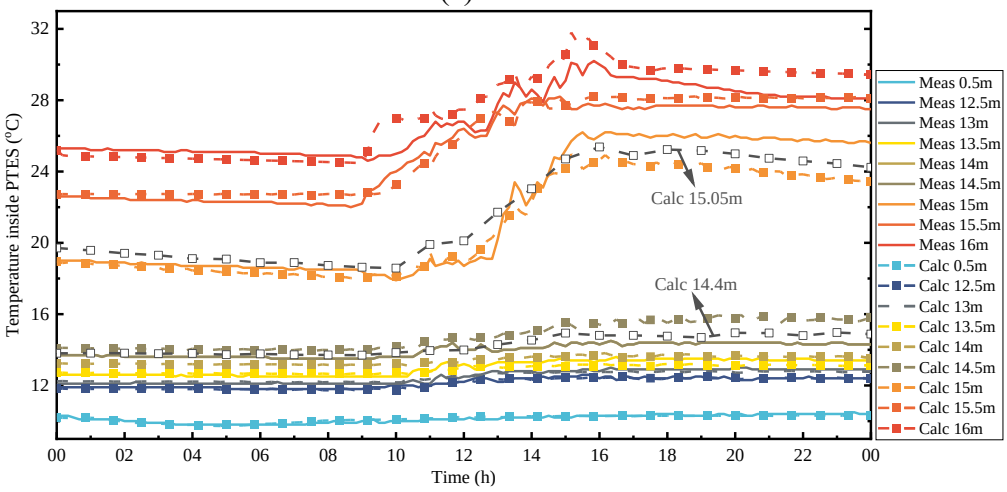

(b) Case 2

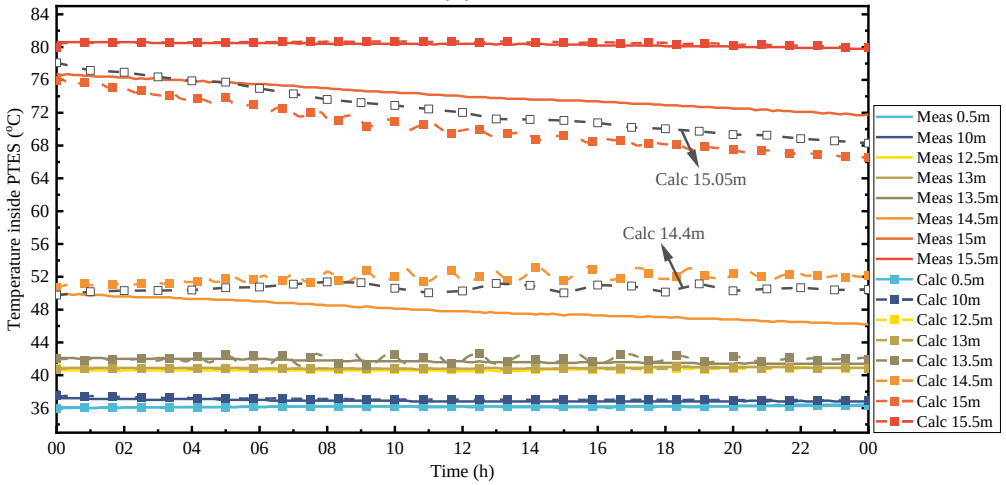

(c) Case 3

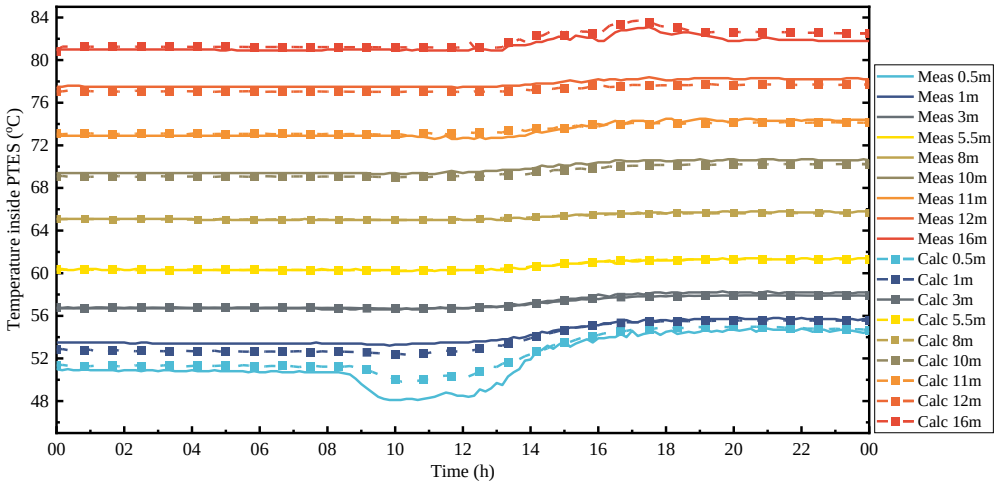

(d) Case 4

Fig.9 Comparison of PTES calculated and measured temperatures with hourly resolution

3.3.4 Charging/discharging conditions

In addition to the PTES temperature distribution, the charge/discharge energy under transient calculation can also be used to examine the model accuracy. In view of the fact that the charge/discharge energy is calculated using the inlet/outlet mass flow rate and temperature, Fig.10 presents the hourly inlet/outlet temperature and mass flow rate variation under different cases.

Slight deviations can be observed in the calculation results compared to the measurements. The maximum difference between the calculation and measurement is within 3 K for temperature and 10 kg/m^3 for mass flow rate. The calculation accuracy is acceptable considering the differences between the actual measured and calculated positions of the inlet/outlet sensors and uncertainties of the measurement in case of frequent shifts of operation mode [20].

Moreover, it is found that the outlet temperature is influenced by the temperature distribution near the outlet diffusers. In other words, the accuracy of the outlet temperature calculation will depend on the prediction of PTES temperature distribution since the calculated outlet temperature is a mixture of the temperatures near the diffusers. Therefore, it is recommended to set more measuring sensors along the PTES height to precisely capture the temperatures near the diffusers.

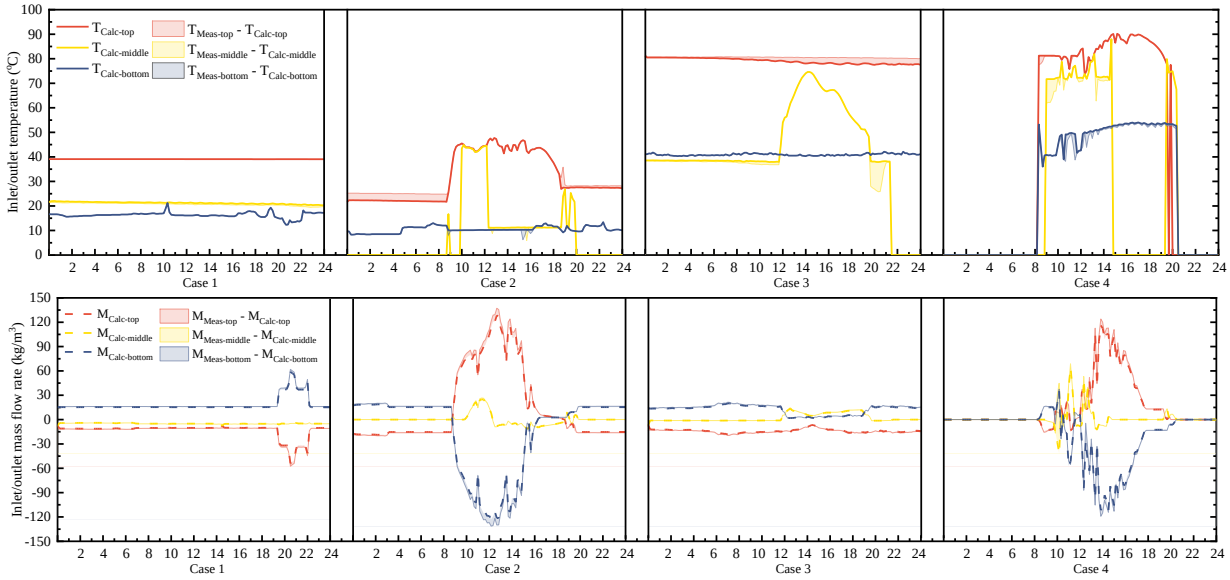

Fig.10 Comparison of charging/discharging conditions with hourly resolution

3.4 Discussion

Overall, it can be concluded that the developed 3D model is adequate to predict the thermal performance of a large-scale PTES.

Furthermore, it is important to note that the main factor affecting the accuracy of PTES temperature calculation is the thermocline's temperature rather than the thermocline's position. The results show that Case 2 and Case 3 have almost the same thermocline position between 13.5 m and 16 m, but the RMSD of Case 3 is roughly three times that of Case 2 due to more significant temperature differences.

Therefore the temperature gradient, $R_{\Delta T/\delta}$, defined as the ratio of thermocline temperature difference to thermocline thickness, is proposed in this study. $R_{\Delta T/\delta}$ can be used to guide the selection of suitable grid sizes for 1D models. For a higher calculation accuracy, the recommended grid sizes are summarized as follows, depending on $R_{\Delta T/\delta}$:

1) A grid size of 0.1 m is recommended when $R_{\Delta T/\delta}$ is lower than 5 K/m.

2) A grid size of 0.06 m is recommended when $R_{\Delta T/\delta}$ is between 5 and 7 K/m.

3) A grid size of 0.04 m is recommended when $R_{\Delta T/\delta}$ is larger than 7 K/m.

It is shown that a higher temperature gradient of the thermocline requires a smaller grid size, in other words, a higher number of grid points in the 1D models. The explanation is that a higher temperature gradient means larger temperature difference and/or a smaller thickness of the thermocline. In order to capture the temperature change in a small distance, a smaller grid size is needed. However, the grid shall not be too coarse or too fine, because a coarser grid will sacrifice the calculation accuracy, while an unnecessarily finer grid will significantly increase

the computational cost. The recommended grid sizes aim to keep a balance between these factors.

4. Application

The appropriate grid size for different heights is chosen by analyzing yearly thermocline conditions to thoroughly verify the conclusions based on the grid size estimation obtained from the 3D model calculation. Then the improvement of model accuracy under the grid size correction is demonstrated using TRNSYS Type 343.

4.1 Grid size determination based on yearly thermocline characteristics

Fig. 11 shows the development of thermocline temperature difference and thermocline positions of the Dronnonglund PTES in 2017, where the thermocline thickness is highlighted with slashes. It reveals that the temperature difference increases sharply from March to May and decreases slowly from May to June since hot water is charged from the top diffuser. During this period, the thermocline is located above 13 m. From July to August, with the continuous charging, the temperature difference inside the PTES gradually decreased, resulting in a downward movement of the thermocline. Beginning in September, the dominant process turns to the discharge process, with low-temperature water entering from the bottom diffuser. In this case, the thermocline position moves upward, and the thermocline thickness gets smaller. Moreover, during the period of end October through early November, cold water of about 20 ^{o}C entered from the bottom diffuser at night, resulting in a rapid drop in the bottom water temperature.

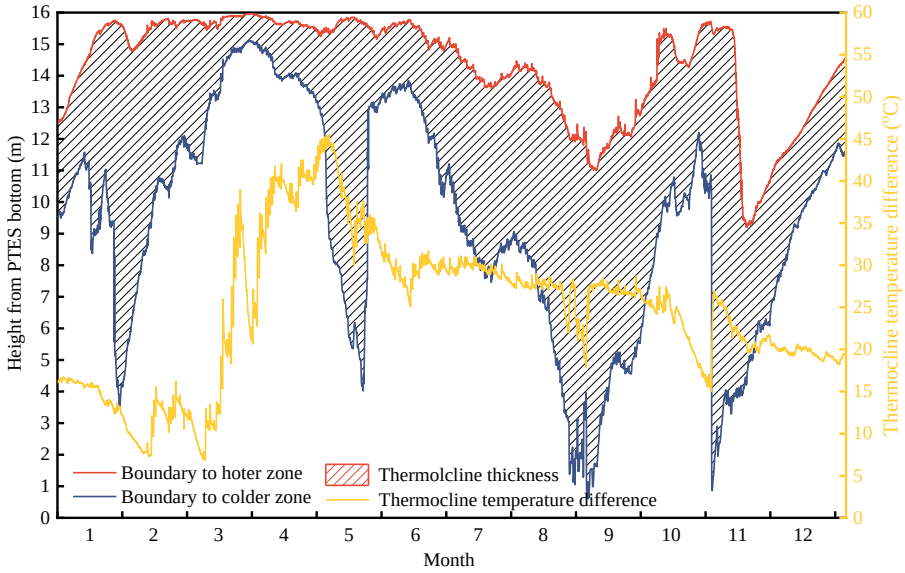

Fig.11 Annual variation of thermocline temperature difference and thermocline thickness

Furthermore, the annual variation of $R_{\Delta T/\delta}$ (shown in Fig. 12) is calculated based on the annual thermocline temperature difference and thermocline thickness. Fig.12 demonstrated that $R_{\Delta T/\delta}$ is greater than 7 in zone 1 and 2. Meanwhile, the thermocline is located above 13 m, according to Fig.11. In addition, $R_{\Delta T/\delta}$ is between 5 and 7 for zone 3 and 4, with the thermocline located between 9 m and 15 m. Except for these zones, the $R_{\Delta T/\delta}$ is less than 5. Therefore, the grid size required for different heights for the 1D model can be summarized in Table 3 according to the recommended grid size for $R_{\Delta T/\delta}$ proposed in section 3.2.5. In this context, PTES temperature distribution and charged/discharged energy quantities are expected to be more accurate.

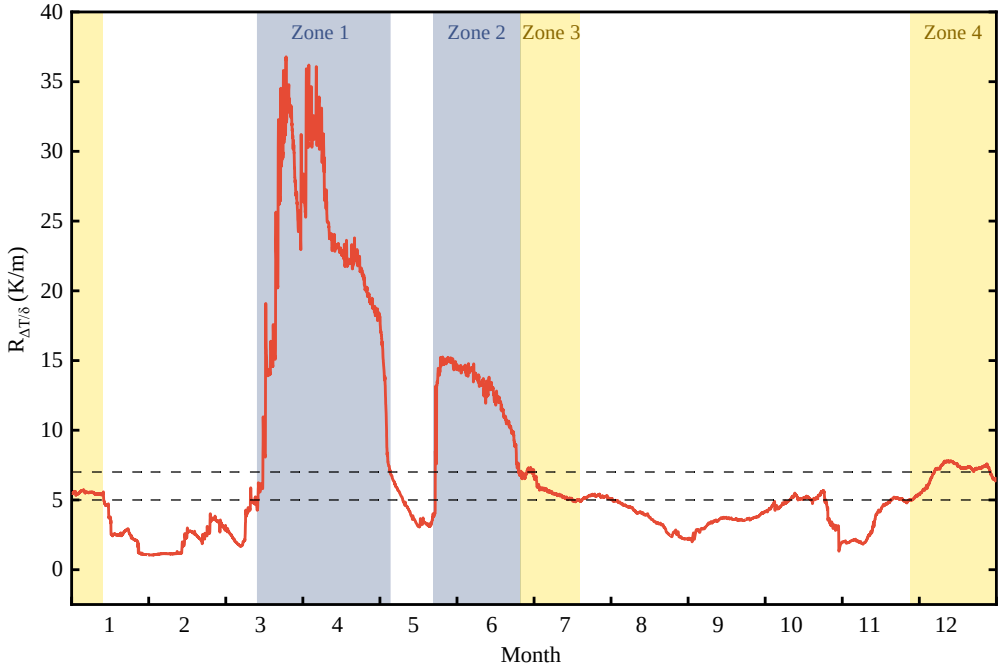

Fig.12 Annual variation of $R_{\Delta T/\delta}$

Table 3 Recommended grid size for different height

Height from PTES bottom (m)	Grid size (m)
13-16	0.04
9-13	0.06
0-9	0.1

4.2 Improvement of TRNSYS Type 343

A TRNSYS model Type 343 was developed for PTES and verified with the measurement of the Dronninglund PTES [20]. The grid size of the model is further improved by implementing the aforementioned recommendations. Calculations for different grid size distributions (listed in Table 4) were performed using Type 343. Furthermore, the MIX number and charge/discharge energy are used to examine the advantage of the recommended grid size in terms of calculation accuracy and time.

Table 4 Grid size distributions

Total nodes number	Node size distribution
400	0.04 m from bottom to top
226	0.04 m from 13 m to 16 m; 0.06 m from 9 m to 13 m; 0.1 m from 0 m to 9 m;
160	0.1 m from bottom to top
20	PTES is divided into 20 equal volumes

4.2.1 MIX number

The MIX number was calculated according to Eq. (14) and (15) [55].

$$\mathrm{MIX} = \frac{M_E^{stratified} - M_E^{exp}}{M_E^{stratified} - M_E^{fully-mixed}} \tag{14}$$

$$M_E^{exp} = \sum_{i=1}^{n} z_i \cdot (\rho_i \cdot V_i \cdot c_p \cdot T_i) \tag{15}$$

Where $M_E^{stratified}$ represents the energy momentum for perfectly stratified conditions and $M_E^{fully-mixed}$ represents the energy momentum for thoroughly mixed conditions. M_E^{exp} is calculated based on actual temperature distribution inside PTES. For calculating the MIX, the moment of energy must be calculated for each of the nodes in the PTES [53]. Therefore MIX number can indirectly reflect the PTES temperature calculation accuracy.

Fig.13 exhibits the development of the MIX number of the Dronninglund PTES from 2015 to 2017. As depicted in this Figure, the MIX number using 20 nodes over three years deviates significantly in March and from June to August. With decreasing the node size to 0.1 m (i.e., 160 nodes in total), the difference in MIX number between the measurement and the calculation is getting smaller. According to the recommended node sizes, further reducing the node size for positions above 9 m inside the PTES (i.e., 226 nodes in total), an improvement of the MIX number of 0.01 can still be observed. However, reducing the grid size to 0.04 m (i.e., 400 nodes in total) seems to have the same calculation accuracy as the recommended node sizes.

Reducing the grid size can improve the calculation accuracy for two reasons. One of the reasons is that as the grid size decreases, temperature distribution can be captured at large $R_{\Delta T/\delta}$, allowing accurate heat transfer calculation between adjacent nodes. Another reason is related to how Type 343 calculates the temperature of the inlet node. As shown in Eq. (14), the temperature of the node at the inlet in a time step depends on the inlet mass flow rate and the mass content of the node. A false numerical diffusion will be introduced in the calculation, and the magnitude of the false diffusion decreases with a decrease in grid size (layer volume). When charging with a significant mass flow rate of higher temperature from June to August, the false

numerical diffusion overestimates the mixing effect with a large grid size (20 nodes), resulting in an overestimated mix number. A decrease in the grid size will significantly improve prediction accuracy for the MIX number.

$$T_{n,i+1} = m_{inlet}T_{inlet}/m_n + ((m_n - m_{inlet}) * T_{n,i})/m_n \quad (14)$$

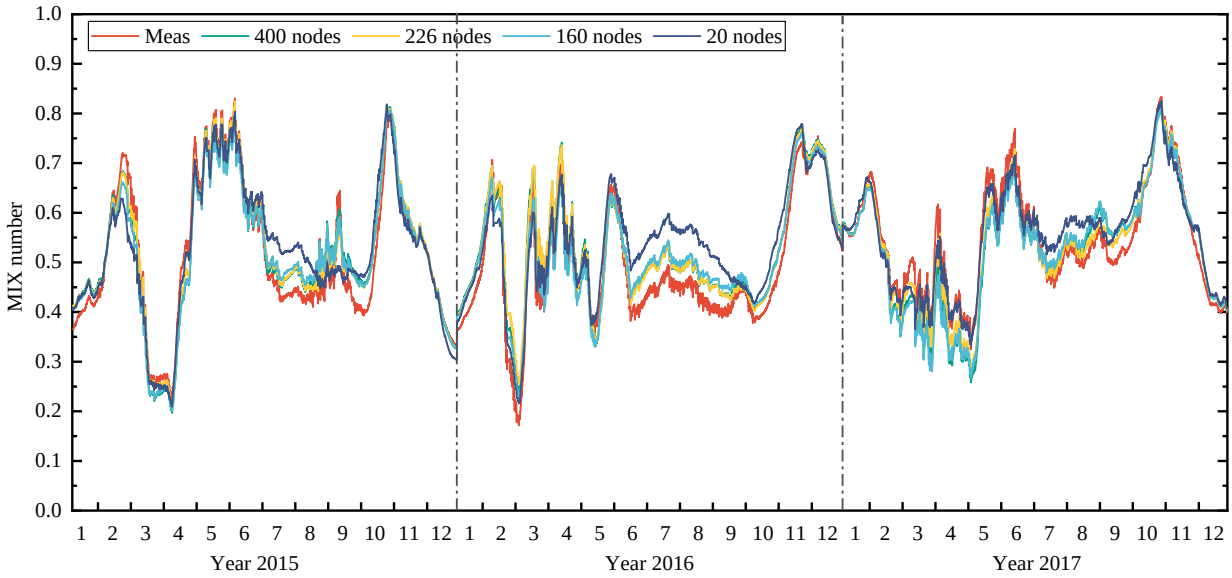

Fig.13 Development of calculated and measured MIX number 2015-2017

Table 5 shows the model accuracy assessed by RMSD of the MIX number and the calculation time used for the one-year simulation. This highlights that reduction of RMSD is significant using the recommended grid size distribution (i.e., 226 nodes in total), and it can reach 43%, 37%, and 11% for 2015, 2016, and 2017 respectively. Moreover, refinement of grid size with the same size along the PTES height does not necessarily lead to desired results, increasing computation time.

Table 5 Model accuracy and calculation time under different grid size distribution

Total node number	RMSD (2015)	RMSD (2016)	RMSD (2017)	Calculation time/per year
400	0.0339	0.0381	0.0475	68min
226	0.0288	0.0395	0.0326	26min
160	0.0369	0.0366	0.0510	14min
20	0.0505	0.0631	0.0368	3.5min

4.2.2 Charge/discharge energy

When planning a solar district heating system with PTES, energy flow is another critical factor influencing the selection of auxiliary energy units [13]. Fig.14 shows the monthly charge/discharge energy with different node numbers compared to the measurement. Therein, the positive values present the charge energy, whereas the negative values present the discharge energy. Note that the relative deviation ratio for charge and discharge energy compared to measurement follows Eq. (16) and (17).

$$\vartheta_{ch} = (E_{ch,meas} - E_{ch,calc})/E_{ch,meas} \quad (16)$$

$$\vartheta_{disch} = (E_{disch,meas} - E_{disch,calc})/E_{disch,meas} \quad (17)$$

As depicted in Fig.14, the maximum relative deviation ratio of monthly charged/discharged energy in these three years can be reduced to less than 5% by increasing the node number. Remarkably, node number 226 also outperforms node numbers 160 and 400 in monthly energy flow, as it is discovered that in some months. For example, in February and December 2016, as well as March and November 2017, the calculation deviations of node numbers 160 and 400 are higher than that of node number 226.

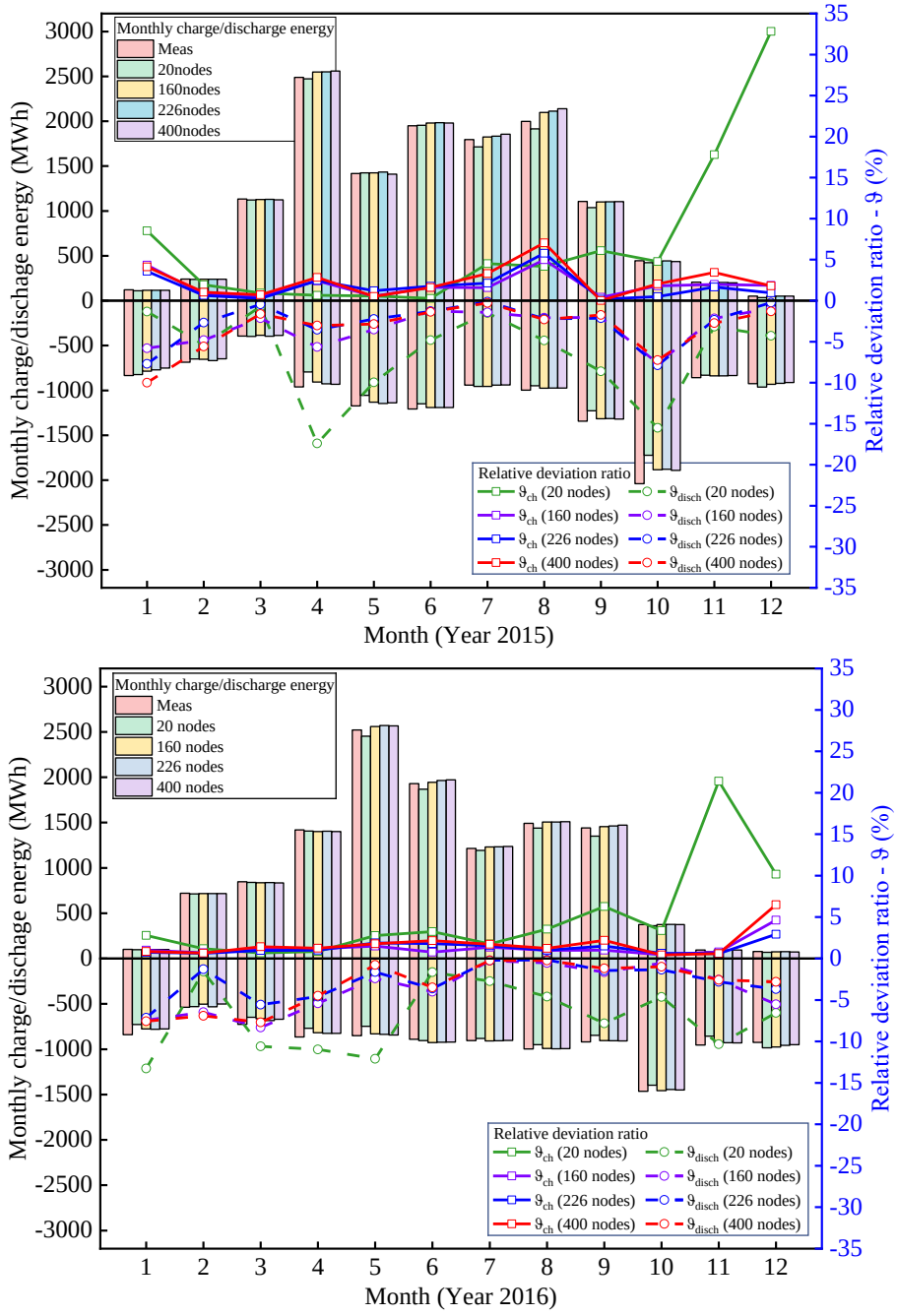

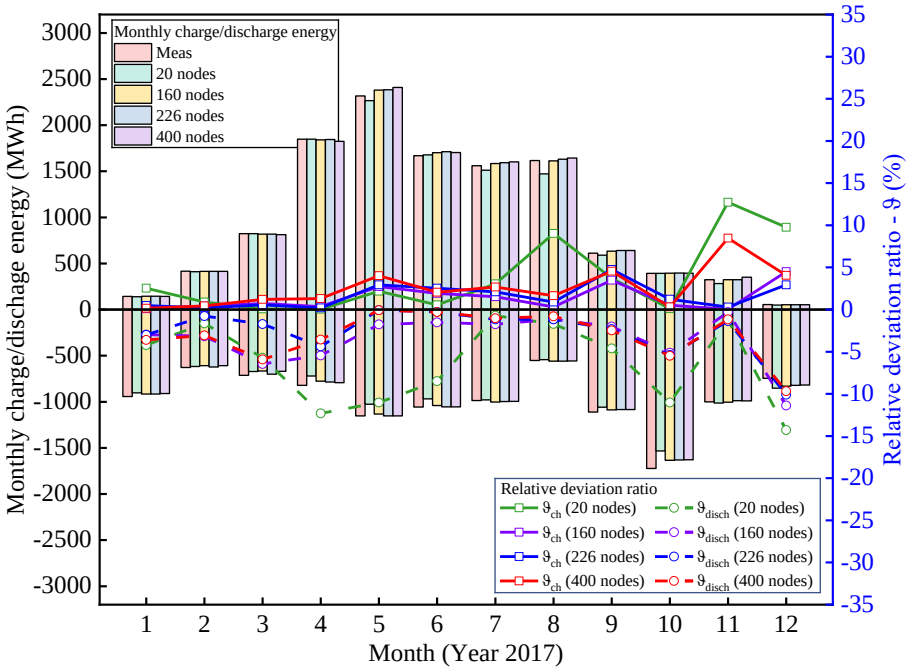

Fig.14 Monthly charge/discharge energy under different node sizes compared with measurement

Overall, the recommended grid size has significantly improved the calculation accuracy of TRNSYS Type 343 in terms of PTES temperature distribution and energy quantities, proving the reliability of the proposed grid size selection based on $R_{\Delta T/\delta}$. However, there is still a small difference between the measurement and the improved model, which can be further reduced by considering the inlet mixing effect.

5. Conclusion

This study developed a full-scale 3D CFD model of PTES including water and soil regions. The proposed CFD model was calibrated using measurements of the Dronninglund PTES. The CFD model was used to determine the optimal grid size for the 1D PTES model. The influence of grid size on the prediction accuracy of the 1D PTES model was examined. The major conclusions are summarized as follows:

1) The difference between the measured and the calculated temperatures for the soil and water region is less than 2 K and 1 K, respectively. In addition, the energy flow is in good agreement with the measurements, with a maximum temperature difference of 3 K and a maximum mass flow rate difference of 10 kg/m^3 between measurements and CFD calculation. Therefore, the accuracy of the 3D model is considered acceptable.

2) Grid size in the horizontal directions has a negligible effect on temperature distribution prediction, but the vertical grid size has a considerable impact. For cases with significant temperature differences within a thinner thermocline thickness, the reduction in RMSD can

reach 50% by reducing the grid size. The temperature gradient of the thermocline $R_{\Delta T/\delta}$ is proposed as a criterion to guide the grid size selection for 1D multi-node models.

3) An optimal grid size distribution was determined by analyzing the dynamic variation characteristics of the thermocline throughout the year. A three-year simulation was performed on a multi-node model TRNSYS Type 343 to verify the reliability of choosing the appropriate grid size distribution using $R_{\Delta T/\delta}$. The calculation accuracy using the appropriate grid size distribution is superior to other grid size distributions in both temperature distribution and energy flow. The RMSD reduction in MIX numbers in 2015, 2016, and 2017 can reach 43%, 37%, and 11%, respectively. Moreover, the monthly charge/discharge energy deviation ratio can be reduced to less than 5%.

Further, two aspects are proposed for future work:

i) Aside from the influence of grid size analyzed above, the mixing effect around the diffusers caused by inlet jet flow should also be investigated.

ii) Despite the model's ability to predict soil temperature, the influence of groundwater on the heat loss of the PTES remains unknown. The CFD model could be used to develop a simplified 1D PTES model considering the influence of groundwater.

Acknowledgments

The work is partly funded by the Danish Energy Agency EUDP project for participation of the IEA ECES Annex 39: "Large Thermal Energy Storages for District Heating" (no. 64020-2036) and the Chinese Scholarship Council (CSC). Without their support, the research would not be possible.

References

[1] IRENA (2020). Innovation Outlook: Thermal Energy Storage. International Renewable Energy Agency. Abu Dhabi.

[2] Lottner V, Schulz ME, Hahne E. Solar-assisted district heating plants: status of the German programme Solarthermie-2000. Solar Energy 2000;69:449–59. https://doi.org/10.1016/S0038-092X(00)00125-0.

[3] Planenergi. Best practice for implementation and operation of large sale borehole and pit heat thermal storage 2019:1–22.

[4] Schmidt T, Pauschinger T, Sørensen PA, Snijders A, Djebbar R, Boulter R, et al. Design aspects for large-scale pit and aquifer thermal energy storage for district heating and cooling. Energy Procedia 2018;149:585–94. https://doi.org/10.1016/j.egypro.2018.08.223.

[5] Mangold D. Seasonal storage – a German success story. Sun & Wind Energy 2007;1:48–58.

[6] Dahash A, Ochs F, Giuliani G, Tosatto A. Understanding the interaction between groundwater and large-scale underground hot-water tanks and pits. Sustainable Cities and Society 2021;71:102928. https://doi.org/10.1016/j.scs.2021.102928.

[7] Duffie JA, Beckman WA, McGowan J. Solar engineering of thermal processes. 1985. https://doi.org/10.1119/1.14178.

[8] Novo A V., Bayon JR, Castro-Fresno D, Rodriguez-Hernandez J. Review of seasonal heat storage in large basins: water tanks and gravel-water pits. Applied Energy 2010;87:390–7. https://doi.org/10.1016/j.apenergy.2009.06.033.

[9] Mahmoud M, Ramadan M, Naher S, Pullen K, Baroutaji A, Olabi AG. Recent advances in district energy systems: a review. Thermal Science and Engineering Progress 2020;20:100678. https://doi.org/10.1016/j.tsep.2020.100678.

[10] Yang T, Liu W, Kramer GJ, Sun Q. Seasonal thermal energy storage: A techno-economic literature review. Renewable and Sustainable Energy Reviews 2021;139:110732. https://doi.org/10.1016/j.rser.2021.110732.

[11] Xiang Y, Xie Z, Furbo S, Wang D, Fan J. A comprehensive review on pit thermal energy storage recent application design and simulation approaches. Journal of Energy storage.

[12] Dahash A, Ochs F, Janetti MB, Streicher W. Advances in seasonal thermal energy storage for solar district heating applications: a critical review on large-scale hot-water tank and pit thermal energy storage systems. Applied Energy 2019;239:296–315. https://doi.org/10.1016/j.apenergy.2019.01.189.

[13] Dahash A, Ochs F, Tosatto A, Streicher W. Toward efficient numerical modeling and analysis of large-scale thermal energy storage for renewable district heating. Applied Energy 2020;279:115840. https://doi.org/10.1016/j.apenergy.2020.115840.

[14] A. Dahash, M. B. Janetti FO. Detailed axial symmetrical model of large-scale underground thermal energy storage. Proceedings of COMSOL 2018 Conference 2018.

[15] Dahash A, Janetti MB, Ochs F, Science M. Detailed 3-D models of a large-scale underground thermal energy storage with consideration of groundwater conditions 2017:597–604.

[16] Dahash A, Michele Bianchi Janetti M, Ochs F. Numerical analysis and evaluation of large-scale hot water tanks and pits in district heating systems. Proceedings of Building Simulation 2019: 16th Conference of IBPSA 2020;16:1692–9. https://doi.org/10.26868/25222708.2019.210566.

[17] Raab S, Mangold D, Müller-Steinhagen H. Validation of a computer model for solar assisted district heating systems with seasonal hot water heat store. Solar Energy 2005;79:531–43. https://doi.org/10.1016/j.solener.2004.10.014.

[18] Gauthier G. Benchmarking and improving models of subsurface heat storage dynamics. Comparison of Danish Ptes and BTES installation measurements with their corresponding TRNSYS models. GEOTHERMICA-ERA NET Cofund Geothermal. 47 pp. 2020.

[19] Pan X, Xiang Y, Gao M, Fan J, Furbo S, et al. Measured and simulated thermal performance analysis of a large-scale water pit thermal energy storage. Journal of thermal storage 2022.

[20] Xie Z, Xiang Y, Wang D, Kusyy O, Kong W, Furbo S, et al. Numerical investigations of long-term thermal performance of a large water pit heat storage. Solar Energy 2021;224:808–22. https://doi.org/10.1016/j.solener.2021.06.027.

[21] Bai Y, Yang M, Fan J, Li X, Chen L, Yuan G, et al. Influence of geometry on the thermal performance of water pit seasonal heat storages for solar district heating. Building Simulation 2020. https://doi.org/10.1007/s12273-020-0671-9.

[22] Bai Y, Wang Z, Fan J, Yang M, Li X, Chen L, et al. Numerical and experimental study of an underground water pit for seasonal heat storage. Renewable Energy 2020;150:487–508. https://doi.org/10.1016/j.renene.2019.12.080.

[23] Fan J, Huang J, Andersen OL, Furbo S. Thermal performance analysis of a solar heating plant. ISES Solar World Congress 2017 - IEA SHC International Conference on Solar Heating and Cooling for Buildings and Industry 2017, Proceedings 2017:291–300. https://doi.org/10.18086/swc.2017.06.05.

[24] Powell KM, Edgar TF. An adaptive-grid model for dynamic simulation of thermocline thermal energy storage systems. Energy Conversion and Management 2013;76:865–73. https://doi.org/10.1016/j.enconman.2013.08.043.

[25] Mazzarella L. Multi-flow stratified thermal storage model with full-mixed layers PdM-XST. 1992.

[26] Unrau C. Numerical investigation of one-dimensional storage tank models and the development of analytical modelling techniques.McMaster University, Canada. 2017.

[27] Solar Energy Laboratory. Trnsys 17 a TRaNsient system simulation program volume 4 mathematical reference. 2009.

[28] PlanEnergi. Sunstore 3. Fase 1: Projektering og udbud 2011.

[29] Kallesøe AJ, Vangkilde-Pedersen T, et al. Underground thermal energy storage (UTES) – state-of-the-art, example cases and lessons learned. HEATSTORE project

report GEOTHERMICA-ERA NET Cofund Geothermal. 130 pp + appendices, 2019.

[30] Jensen MV, PlanEnergi. Task 45 Large systems seasonal pit heat storages - Guidelines for materials & construction 2014. https://task45.iea-shc.org/fact-sheets.

[31] Rørindføring alternativ 2, Sunstore 3 Dronninglund Fjernvarme A.m.b.a. 2010.

[32] Dampvarmelager snit.2013.

[33] PlanEnergi. Dronninglund. Lunderbjerg Damvarmelager Måling af grundvandstemperatur 2015.

[34] ANSYS Fluent Theory Guide 2019 R2, ANSYS.

[35] Chung JD, Cho SH, Tae CS, Yoo H. The effect of diffuser configuration on thermal stratification in a rectangular storage tank. Renewable Energy 2008;33:2236–45. https://doi.org/10.1016/j.renene.2007.12.013.

[36] Blevins R. Applied fluid dynamic handbook. 1984.

[37] Deng Y, Sun D, Niu M, Yu B, Bian R. Performance assessment of a novel diffuser for stratified thermal energy storage tanks – the nonequal-diameter radial diffuser. Journal of Energy Storage 2021;35. https://doi.org/10.1016/j.est.2021.102276.

[38] Keulegan GH. Interfacial instability and mixing in stratified flows. Journal of Research of the National Bureau of Standards 1949;43:487. https://doi.org/10.6028/jres.043.041.

[39] Cai L, Stewart WE, Sohn CW. Turbulent buoyant flows into a two dimensional storage tank. International Journal of Heat and Mass Transfer 1993;36:4247–56. https://doi.org/10.1016/0017-9310(93)90087-M.

[40] Song J, Bahnfleth WP, Cimbala JM. Parametric study of single-pipe diffusers in stratified chilled water storage tanks (RP-1185). HVAC and R Research 2004;10:345–65. https://doi.org/10.1080/10789669.2004.10391108.

[41] Manimaran R. Performance assessment of solar PV and thermal-driven humidification dehumidification systems: a CFD modelling approach. Energy Conversion and Management 2021;245:114574. https://doi.org/10.1016/j.enconman.2021.114574.

[42] Fan J, Huang J, Chatzidiakos A, Furbo S. Experimental and theoretic investigations of thermal behavior of a seasonal water pit heat storage. ISES Solar World Congress 2017 - IEA SHC International Conference on Solar Heating and Cooling for Buildings and Industry 2017, Proceedings 2017:714–25. https://doi.org/10.18086/swc.2017.13.03.

[43] Chatzidiakos A. CFD Calculations for Solar Water Pond Heat Storages. Technical University of Denmark. 2016.

[44] Moradifam A, Nachman A, Tamasan A. Determination of thermal conductivity of coarse and fine sand soils. SIAM Journal on Mathematical Analysis 2012;44:3969–90. https://doi.org/10.1137/120866701.

[45] Pagola MA, Jensen R. L, Madsen S, Poulsen SE. Measurement of Thermal Properties of Soil and Concrete Samples. Department of Civil Engineering Aalborg University DCE Technical Reports, No 235 2017.

[46] Soils N, Recommendations P. Serial laboratory effective thermal conductivity measurements of cohesive and non cohesive soils for the purpose of shallow

geothermal potential mapping and databases 2020.

[47] NMC. Nomalen 28N 2011.

[48] Thakare K, Vishwakarma H, Bhave A, Experimental investigation of possible use of HDPE as thermal storage material in thermal storage type solar cookers. International Journal of Research in Engineering and Technology 2015;04:92–9. https://doi.org/10.15623/ijret.2015.0412019.

[49] SOLMAX. Produktinformation Hypernet.

[50] Dannemand Andersen J, Bødker L, Jensen M V. Large thermal energy storage at Marstal district heating. 18th International Conference on Soil Mechanics and Geotechnical Engineering: Challenges and Innovations in Geotechnics, ICSMGE 2013 2013;4:3351–4.

[51] Ochs F, Heidemann W, Müller-Steinhagen H. Effective thermal conductivity of moistened insulation materials as a function of temperature. International Journal of Heat and Mass Transfer 2008;51:539–52. https://doi.org/10.1016/j.ijheatmasstransfer.2007.05.005.

[52] Winterscheid C. Dronninglund district heating monitaring data evaluation for the years 2015-2017 2017.

[53] Sifnaios I, Jensen AR, Furbo S, Fan J. Performance comparison of two water Pit thermal energy storage syatems using energy, exergy, and stratification indicators. Solar energy. 2015.

[54] Xu C, Liu M, Jiao S, Tang H, Yan J. Experimental study and analytical modeling on the thermocline hot water storage tank with radial plate-type diffuser. International Journal of Heat and Mass Transfer 2022;186. https://doi.org/10.1016/j.ijheatmasstransfer.2021.122478.

[55] Haller MY, Cruickshank CA, Streicher W, Harrison SJ, Andersen E, Furbo S. Methods to determine stratification efficiency of thermal energy storage processes - review and theoretical comparison. Solar Energy 2009;83:1847–60. https://doi.org/10.1016/j.solener.2009.06.019.

Yutong Xiang, Meng Gao, Simon Furbo, Jianhua Fan, Gang Wang, Zhiyong Tian, Dengjia Wang. (2023). Assessment of inlet mixing during charge and discharge of a large-scale water pit heat storage, *[Submitted to Renewable Energy]*

Assessment of inlet mixing during charge and discharge of a large-scale water pit heat storage

Yutong Xiang[1], Meng Gao[1], Simon Furbo[1], Jianhua Fan[1*], Gang Wang[2], Zhiyong Tian[3], Dengjia Wang[4]

1. Department of Civil and Mechanical Engineering, Technical University of Denmark, Koppels Allé
Building 404, Kgs. Lyngby DK 2800, Denmark
2. School of Energy Engineering, Xinjiang Institute of Engineering, Urumqi 830023, China
3. School of Environmental Science and Engineering, Huazhong University of Science and Technology, Wuhan 430074, China
4. State Key Laboratory of Green Building in Western China, Xi'an University of Architecture and Technology, Xi'an, Shaanxi 710055, China;

∗ Corresponding authors: E-mail addresses: jifa@dtu.dk (J. Fan).

Abstract

Pit thermal energy storage (PTES) is an efficient renewable energy storage technology widely used in large-scale solar district heating systems. Accurate modeling of mixing in a PTES due to inlet flow is key in calculating heat storage performance. However, the commonly used one-dimensional PTES models fail to consider inlet mixing due to the three-dimensional nature of the mixing flow. This research adopts a three-dimensional model to analyze the dynamic behavior of inlet mixing inside the PTES. The model is validated against measurements of the Dronninglund PTES. To quantify the inlet mixing impact, two performance indicators (i.e., the penetration height (Z) and the energy distribution ratio (η_j)) are proposed. The parametric analysis revealed that Z is more dependent on the Reynold (Re) number than the Froude (Fr) number, while both the Re and Fr numbers influence η_j. According to the dimensional theory, the penetration height Z shows a power-law relation with time. For the energy distribution ratio η_j, a power-law relation with time is seen, although an asymptotic formula is needed in the region of a negative buoyancy jet. Finally, the inflow mixing inside the PTES is characterized under various operating conditions by empirical correlations. The results of this study could be used to improve the current one-dimensional heat storage models in terms of inlet mixing.

Keywords: *Solar district heating, water pit heat storage, three-dimensional model, inflow mixing, penetration height, energy distribution ratio*

Nomenclature

Latin characters

a	Coefficient, [-]	Z	Penetration height, [m]

b	Coefficient, [-]	*Subscripts*	
CFD	Computational fluid dynamic, [-]	bottom	Bottom diffuser
C_p	Specific capacity, [J/kg·K]	d	Diffuser
c	Coefficient, [-]	h	Hydraulic diameter
D	Diameter, [m]	in	Inlet
F	Buoyancy flux, [m^4/s^3]	j	Number of layer in PTES
Fr	Froude number, [-]	m	Mixed water
Gr	Grashof number, [-]	middle	Middle diffuser
g	Gravity, [m/s^2]	out	Outlet
H	Distance between diffuser discs, [m]	start	Energy starts to distribute in a layer
M	Inlet momentum flux, [m^4/s^2]	top	Top diffuser
m	Mass flow rate, [kg/h]	0	Initial
Re	Reynolds number, [-]		
Ri	Richardson number, [-]	*Greek*	
PTES	Pit thermal energy storage, [-]	ρ	Density, [kg/m^3]
T	Temperature, [°C]	μ	Dynamic viscosity, [kg/m·s]
t	Time, [s]	η	Energy distribution ratio, [-]
V	Volume flow rate, [m^3/h]	θ	Dimensionless temperature, [-]
v	Inlet velocity, [m/s]		

1. Introduction

To reduce dependence on traditional fossil energy while achieving net-zero emissions, large-solar district heating system shows growing interest [1,2]. However, solar energy resource are insufficient in the heating seasons but abundant in the non-heating seasons [2]. The mismatch between thermal energy demand and solar thermal production can be addressed using seasonal heat storage, resulting in higher utilization of solar energy [3]. Water is recognized as the best sensible heat storage material below 100°C due to its low cost, high heat storage capacity, and environmental friendliness [4]. Therefore, water is widely used for different thermal energy storage techniques. Thermal stratification inside the storage is usually created by the buoyancy separation of hot and cold water inside the thermal storage, which significantly influences the thermal performance of solar heating systems [5–7].

Several heat transfer mechanisms can result in the loss or degradation of thermal stratification in thermal storage [8,9], for instance, thermal conduction in the storage due to the vertical temperature gradient, heat loss through the top insulation, and mixing at the inlet/outlet. Typically, the mixing effect is expected to occur in a small region near the inlet, but under unfavorable conditions, mixing may expand to the majority of the storage volume [10]. The leading cause of destratification, particularly for direct charge/discharge of thermal storage, is inlet mixing during the charge/discharge process [11].

Numerous experimental and numerical studies have been conducted to reduce inlet mixing. Some of them focused on creating correlations to guide the design of inlet configurations. For instance, a correlation for vertical inlet extraction efficiency based on the inlet Reynolds (Re) number, Grashof (Gr) number, and tank aspect ratio was established [12]. On that basis, the extraction efficiency for horizontal inlets was further adjusted [13]. Deng et al. [14] emphasized inlet configurations to where with water entering the thermal storage at a uniform low flow rate, favoring thermal stratification. In this context, inlet/outlet diffusers with baffle plates [14–18] and porous manifolds inlets [19–21] have been successfully suggested. Radial diffusers have recently been studied in detail using Computational Fluid Dynamic (CFD) and experiments by Findeisen et al [22–26]. They emphasized that when there was a large distance between the diffuser and storage top wall, the stratification quality could be significantly reduced due to strong mixing. Therefore, they suggested mounting the diffuser on the top of the storage tank to improve the thermal stratification.

1.1 Modeling of inlet mixing

Computational modeling of heat transfer and fluid flow in solar heating systems provide a valuable tool for evaluation of system performance [27]. Therefore, mathematical models of thermal storage are developed for integration into the system's dynamic simulations. The commonly used models are mostly based on simplified one-dimension energy balance approaches. These approaches significantly reduce the model complexity but also mean that the detailed flow structures, especially the three-dimensional phenomena of inlet mixing, cannot be directly modeled.

In the early years, some researchers considered the mixing processes by introducing an eddy conductivity factor into the energy equation to compensate for the discrepancy in one-dimensional models. Oppel et al. [28] established a functional relation of inlet eddy conductivity factor for circular inlets and solid circular plate inlets using the Re number and Richardson (Ri) number. When used with a one-dimensional model, the obtained correlations gave good predictions of the thermocline development. Zurigat et al. [17,29] further characterized the turbulent mixing for various inlet configurations using the same methods. Those inlet configurations included side inlet, side inlet with perforated baffle, impingement inlet, solid diffuser, perforated diffuser, and perforated diffuser with a solid center. Their study showed that the effective diffusivity factor could be a practical measure for quantifying mixing effects introduced by different inlet configurations. Najem and Rafaee [30] also incorporated an eddy conductivity factor into their finite element model, which agreed with the experimental results.

In recent years, researchers have attempted to characterize the mixing effect by quantifying the mixing region geometry or mixing coefficient. The ratio of the sum of the mixing zone and the inflow heat capacities to the mixing zone heat capacity is known as the mixing coefficient. It was found that the mixing coefficient can be expressed as a function of Re and Ri numbers [31]. Further, Karim et al. [32] found that after the thermocline formation, the inlet flow velocity could be increased without increasing the inlet mixing. They adjusted the mixing coefficient versus inflow velocity when achieving a fully developed thermocline. Shah and Furbo [16] carried out both theoretical and experimental analysis to characterize the inlets impact on the thermal conditions. The findings indicated that the Ri number, tapped water volume percentage, temperature difference, and thermal expansion coefficient all impacted the changes in entropy and exergy during discharge. However, the limited amount of experimentally obtained data could not propose the correlation of these parameters. Further research by Jordan and Furbo [33] revealed that the inlet height could be defined as a function

of the inlet mass flow rate and density difference in the storage tank. In this case, the degree of mixing under different operating conditions could be characterized in a one-dimensional model by changing the inlet position during the dynamic simulation. The simulated results of the storage temperature distribution were more consistent with the measured results when using a variable inlet height than when using a fixed inlet height.

Furthermore, Nizami et al. [27] developed a new one-dimensional model capable of considering the mixing characteristics created by vertical inflow. According to parametric CFD studies, jet penetration depth and entrainment mass flow rates were obtained as a function of the Ri number and inlet diameter. The temperature predictions of the new model were compared to the experimental results with good agreement. However, it could not easily be extrapolated to other inlet configurations. Most recently, a new one-dimension model for tank thermal storage was proposed by Brecht et al. [34]. The model included two parameters in the energy equations, mixing coefficient and mixing zone height. The mixing coefficient had a linear relationship with the Re number, and the mixing zone height was related to the inflow Fr number, inflow Re number, and the ratio of the inlet diameter to the tank diameter. The model demonstrated the significance of precisely modeling of the mixing effect generated by direct inflow in small-scale tank thermal storage, even with slight differences from the experimental results.

1.2 Motivation

According to the aforementioned literature, mixing may still occur under certain conditions, even with the proper inlet design. The one-dimension models can be adjusted to improve the calculation accuracy by introducing the inlet mixing empirical correlations. However, all the reported methods incorporating the mixing effect are based on limited data from experiments or CFD simulations of small-scale thermal storage. In other words, the empirical relationships proposed in the studies can only apply to specific situations and may not be applicable to other heat storage, for example, large-scale water pit heat storage.

The commonly used one-dimensional models for PTES are Type 342, Type 343, Type UGST, as well as the newly developed models Type 1535 and Type 1536, which are built in the TRNSYS simulation software [3]. However, it is important to note that these existing models do not currently account for the phenomenon of the inlet mixing within PTES. For one thing, there is a lack of research on the influence of inlet mixing on PTES performance. Additionally, the mixing effect depends not only on the design of the PTES but also on its

operating conditions [35], making it challenging to introduce the three-dimensional characteristics of inlet mixing into a one-dimensional model.

Therefore, it is crucial to fully understand the effect of inlet mixing on PTES performance and to develop a straightforward method to incorporate it into the one-dimensional model to improve its calculation accuracy.

1.3 Contribution and organization of the paper

To address the above-mentioned research gaps, this study aims to analyze the potential inlet mixing phenomenon in the context of the Dronninglund project's operational conditions. The primary focus is to develop a comprehensive understanding of the inlet mixing effect within the PTES, employing a full-scale three-dimensional CFD model.

The developed CFD model allows for the visualization of the inlet mixing phenomenon, providing insights into its dynamic behavior within the PTES. Various operating scenarios are simulated to thoroughly evaluate and quantify the impact of inlet mixing on PTES performance. In this instance, appreciate correlations are proposed to characterize the penetration height of the inlet mixing area and the energy distribution ratio for each layer.

The findings of the investigations will further contribute to understanding the inlet mixing phenomenon inside PTES and improving the calculation accuracy of one-dimensional models.

2. Experimental study

2.1 System overview

The Dronninglund solar district heating (SDH) plant has been demonstrated to be one of the most successful projects. The system can cover up to 70% of the heat demand using renewable energy [36]. A schematic diagram of the Dronninglund SDH system is shown in Fig.1. The system's major components are two solar collector fields with a total aperture area of 35,573 m^2, a 60,000 m^3 pit thermal energy storage (PTES), and an absorption heat pump. During charging, the top of the PTES is heated by the heat from the outlet of the solar collector fields. Notably, the middle inlet/outlet (yellow line in Fig.1) is used at certain times to help manage stratification within the PTES [37]. For instance, if the top of the PTES reaches 85^{o}C and the solar collector fluid is heated to 60^{o}C by the solar collector fields, the PTES is charged by the solar heat through the middle diffuser than the top diffuser. During discharge, when the PTES temperature is high enough, water is taken from the top of the PTES and used directly for the district heating grid. When the PTES temperature is too low for direct use, the heat pump extracts heat from the PTES, resulting in high storage efficiency [36]. In addition, the

system is equipped with a combined heat and power plat fed by four gas engines, a bio-oil boiler, and a natural gas boiler to supply the remaining heat requirements [38].

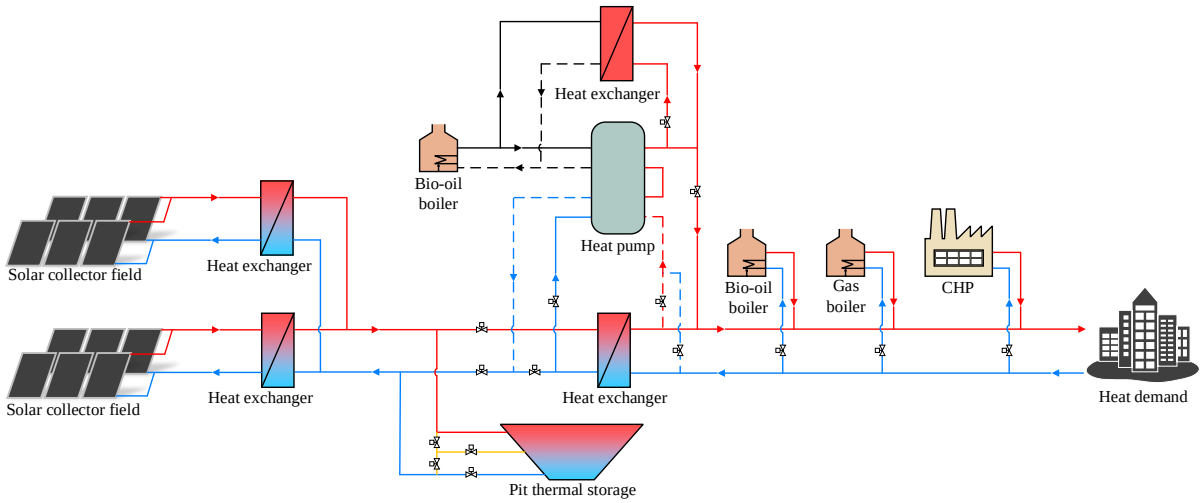

Fig. 1. A simplified schematic of the Dronninglund solar district heating plant

It should be noted that due to the proper utilization of the PTES, the average solar fraction of the system can reach 40% in the past few years of operation. Therefore, this study will focus on understanding the dynamic behaviors of the PTES during charging and discharging. An aerial view of the Dronninglund PTES and its inner structure during construction is shown in Fig.2.

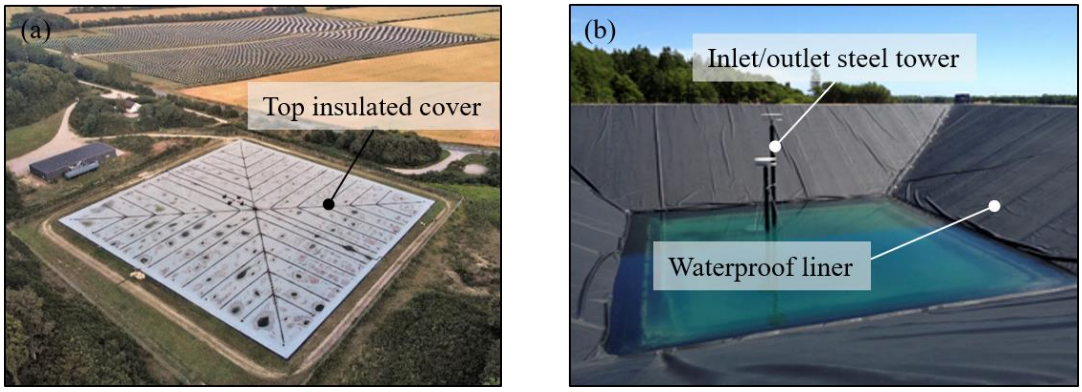

Fig. 2. Photo of Dronninglund PTES: (a) Aerial view (2019) [7], (b) Inner structure (Image source: PlanEnergi).

2.2 The PTES design

Dronninglund PTES consists of the water body, the cover, the connection pipes, and the inlet/outlet diffusers as depicted in Fig.3 (a). The water body is shaped like a regular quadrilateral pyramid with a base side length of 26 m, a top side length of 90 m, and a height of 16 m. A slope angle of 26.6^{o} to is specially chosen for the water body to reduce construction costs and prevent sidewall collapse [38–41]. In addition, an insulating cover is installed to seal

the water body, and a waterproof liner is applied to the sides and the bottom surface of the PTES to isolate the water from the surrounding soil.

PTES is typically designed large enough to accommodate long-term storage needs. Three diffusers are installed at the top, the middle, and the bottom of the PTES, respectively. The top diffuser is close to the top of the PTES, while the bottom diffuser is near the bottom of the PTES. Each diffuser is equipped with two radial discs. These designs help maintain thermal stratification by introducing water enters PTES at a uniform and slow rate at various temperatures [16,18]. Fig.3 (b) illustrates the detailed design of the Dronninglund PTES inlet.

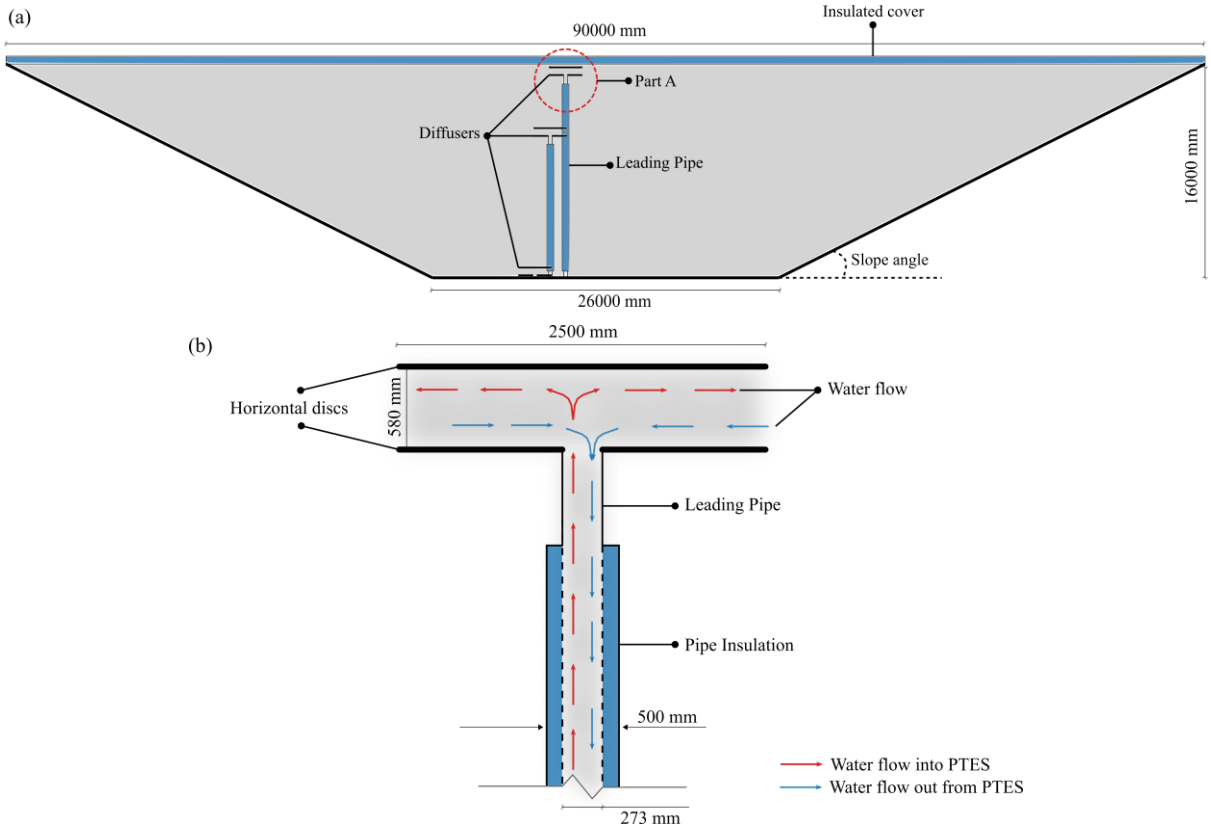

Fig. 3. Schematic of the Dronninglund PTES: (a) Main design of the PTES, (b) Enlarged view of Part A (inlet detailed dimensions), the red vectors indicate the flow when the diffuser is used as an inlet, the blue vectors indicate the flow when the diffuser is used as an outlet.

2.3 The measurements and uncertainties

In order to monitor the PTES's behavior, several sensors have been mounted in and around the PTES [36,37]. The different types of sensors used in this study and their locations are described as follows:

1) There are 32 temperature sensors installed inside the PTES, one of which is located 0.1 m below the insulating cover, and the other 31 are spaced 0.5 m from the bottom to the top of the PTES.

2) Two temperature sensors are placed on the top and the bottom surface of the insulating layer, respectively.

3) Three temperature sensors and three flow meters are installed in the pipes (sections in the technical building) connected to the three diffusers. It is worth mentioning that the flow meters measure both direction and flow rate.

The temperature sensors are Class A PT100, with an accuracy of ±0.15 K [7]. Electromagnetic flow meters are used to measure the volume flow rate, and their accuracy is 0.4%. All the measurements are recorded at 10-minute intervals.

2.4 The operation of the PTES

The Dronninglund PTES serves as long-term and short-term heat storage to balance the heat production by the solar collector fields and the heat demand of the district heating consumers. Water is used as the storage material, which means it will naturally stratify due to the density difference between hot and cold water [42]. It is important to note that inlet mixing caused by high inlet flow rates or large temperature differences between the incoming water and the water in the PTES may significantly contribute to the destruction of thermal stratification [43,44]. In this case, appropriate operating strategies should be selected to minimize mixing during the charge and discharge of the heat storage.

In practice, the operation of the inlet/outlet diffuser is complicated as it depends on the supply temperature from the solar collector field, the heat demand of the district heating network, and the PTES temperatures. Table 1 summarizes the inlet/outlet diffusers combinations of the PTES based on the measurements in 2017, where '1' means the diffuser operates as an outlet, '0' means the diffuser operates as an inlet, and '/' means on standby. As observed, the bottom diffuser is used as an inlet for most of the year. The top or the middle diffuser serves as an inlet in approximately 15% of the year.

Table 1

The inlet/outlet diffusers combinations of the PTES in the year 2017.

Flow path no.	Direction			Operation percentage
	Top	Middle	Bottom	
1	0	1	1	8.0%
2	0	0	1	2.9%
3	0	/	1	2.3%
4	0	1	0	4.2%
5	1	0	0	5.2%
6	1	0	1	3.9%
7	1	1	0	35.2%

8	1	/	0	27.6%
9	1	0	/	2.8%
10	/	0	1	1.2%
11	/	1	0	1.9%
12	/	/	/	4.8%

In order to identify typical operation conditions for the investigations of inlet mixing, Fig.4 shows the inlet temperatures, inlet volume flow rates, and the PTES temperatures at the levels of the inlet diffusers.

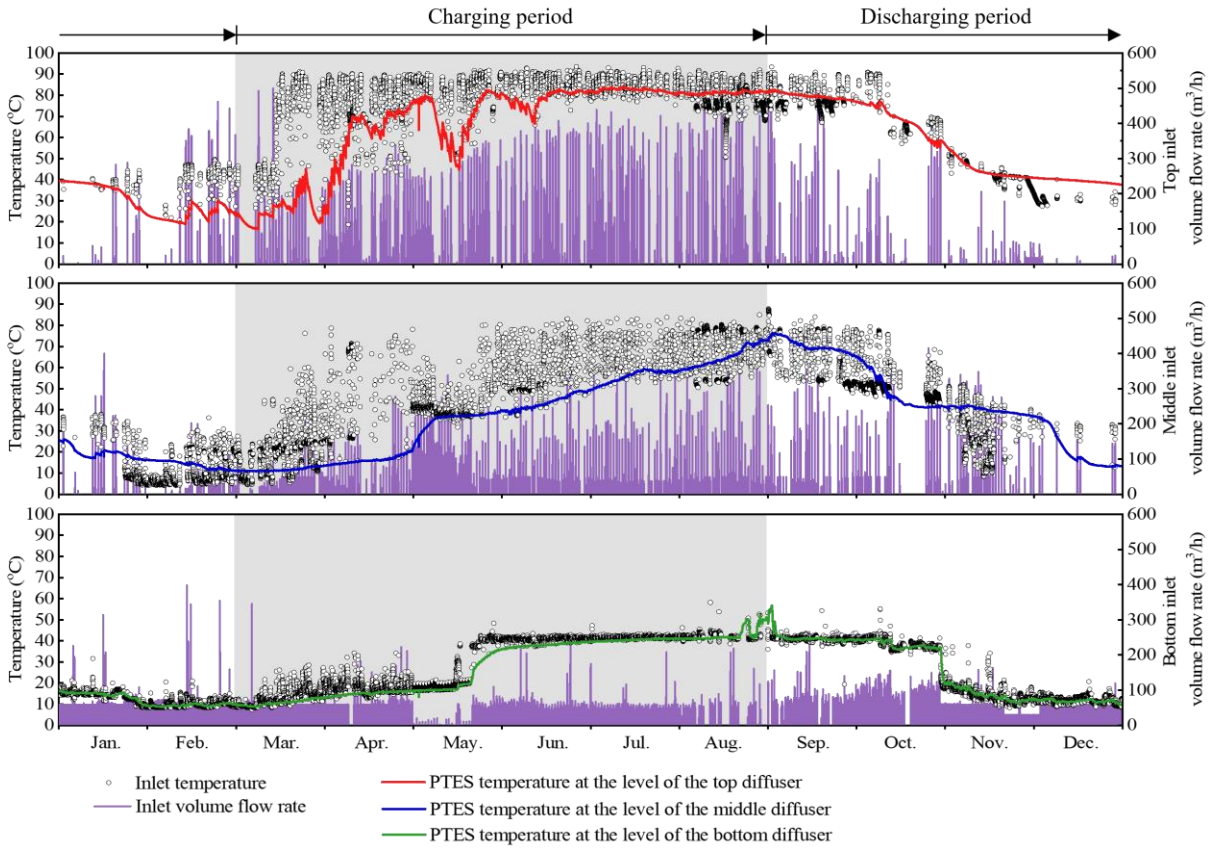

Fig. 4. Inlet volume flow rates, inlet temperatures and the PTES temperature at the levels of the inlet diffusers in 2017

The top diffuser operates mainly from March to August, with a volume flow range of 0-400 m^3/h. At certain times in March, July, and August, the inlet volume flow rate occasionally reaches 500 m^3/h. The inlet temperature is always higher than the PTES temperature at the level of the top diffuser, with a maximum temperature difference of over 60 K in March. However, in April and August, the inlet temperature is sometimes lower than the PTES temperature at the level of the top diffuser.

The middle diffuser operates mainly from March to August, but the inlet flow rate is lower than that of the top inlet. The volume flow rate typically varies between 0-250 m^3/h. The maximum volume flow rate is around 300 m^3/h. From April to July, the inlet temperature is

higher than the PTES temperature at the level of the middle diffuser, with a maximum temperature difference of 50 K. Most of the time, lower-temperature water with a maximum temperature difference of -30 K is introduced into PTES from August to March.

Except for May, the bottom diffuser operates as an inlet most of the year with a flow rate below 100 m^3/h. In addition, the inlet temperature is the same as the PTES temperature at the level of the bottom diffuser most of the time. Notably, there are periods from March to May when the inlet temperature is higher than the PTES temperature at the level of the bottom diffuser. The most noticeable temperature difference is around 10 K.

In conclusion, the inlet temperature may not always be the same as the PTES temperature at the level of the inlet diffuser due to the fixed position of the inlet/outlet diffusers. In this situation, even with the radial diffuser being used as the inlet stratification device, inlet mixing may still occur in a certain region within the PTES, especially when there is a notable temperature difference between the inlet and the PTES.

3. Numerical study

3.1 Model description

Based on the PTES size of the Dronninglund project described in Section 2.2, a full-scale three-dimensional model was developed in ANSYS. The model includes both the water and the soil region, as shown in Fig.5 (a). It should be noted that the soil region is created large enough to minimize the impact of soil boundaries on changes in soil temperature near the water body. The water region was considered an incompressible fluid with temperature-dependent thermophysical properties, while the soil region was treated as a solid region with constant thermal properties.

Reynolds-average transport equations were solved by ANSYS FLUENT for flow and energy fields using the realizable k-ε model to accurately reflect the inlet mixing process caused by inflow and outflow [45]. After a mesh study of 0.5, 0.7, 0.9, and 1.6 million cells, the numerical mesh with a density of 0.9 million cells was found to be a good compromise between accuracy and calculation time. The readers are recommended to refer to the literature [46] for more information on the developed CFD model, inclusive of the geometry, the mathematical method, the mesh, and the numerical procedure.

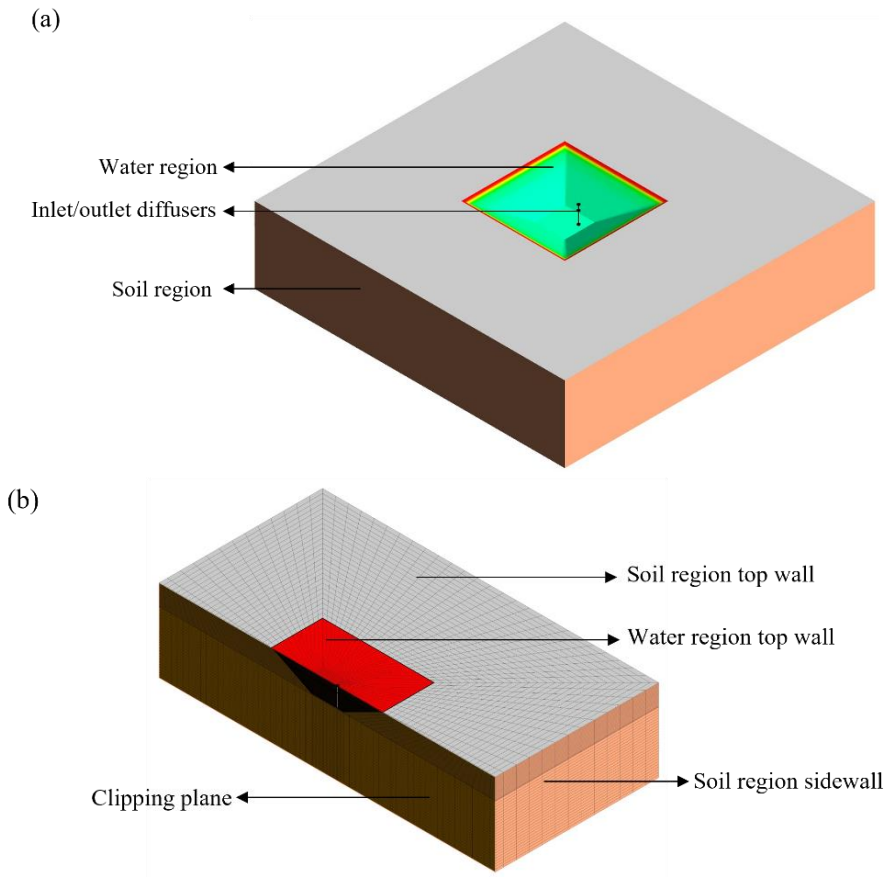

Fig. 5. Three-dimensional CFD model: (a) Model diagram; (b) Grid scheme (the clipping plane is positioned through the center of the diffusers to show the mesh inside the model)

3.2 Boundary conditions

The CFD model has been successfully verified using short-term operational measurements of the Dronninglund PTES [46]. However, it was observed that the case on June 2 had a lower PTES temperature calculation accuracy than the other cases. The discrepancy can be attributed to a considerable temperature gradient in the top of the PTES [46]. In this context, this validation focused on the period from June 1 to June 7 to further demonstrate the model's long-term reliability for accurately assessing the inlet mixing phenomenon.

As the boundary condition of the long-term validation, Fig.6 presents the operational conditions from June 1 to 7. The initial temperature distribution inside PTES is shown in Fig.6 (a), with a uniform temperature of 36 ^{o}C below 13 m and a significant temperature gradient of 22 K/m exists between 13.5 m and 15.5 m. During this time, hot water primarily enters from the top diffuser to charge PTES at daytime, while cold water enters from the bottom diffuser to discharge PTES at night. Additionally, hot water enters from the middle diffuser to charge PTES when the water temperature from the solar collector field is lower than that of the PTES top.

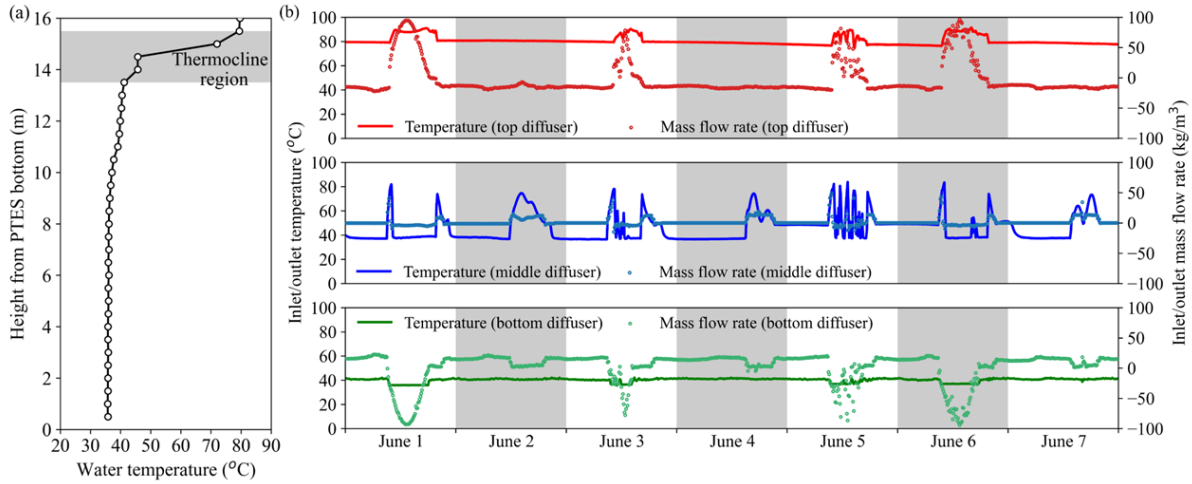

Fig. 6. Operational conditions during the validation period: (a) Initial PTES temperature distribution; (b) Inlet/outlet conditions (Positive flow rate: water enters the PTES; Negative flow rate: water flows out from the PTES)

3.3 Long-term validation

3.3.1 Water temperature

Fig. 7 compares the Dronninglund measurements with the calculated PTES temperature using the CFD model at a 10-minute resolution. The PTES temperature distribution at 0:00 from June 1 to June 8 is depicted in Fig.7 (a). It is evident that there is a good agreement between the calculated and measured temperatures. However, a significant temperature difference of 6 K is observed at 14.5 m. Due to the large temperature gradient between 14 m and 15 m, the uncertainty in the sensors' position along the PTES height has a great impact on the reported PTES temperature [46]. To further illustrate this effect, Fig. 7 (b) includes the calculated temperature at 14.4 m, in addition to the measured and calculated temperatures at 14.5 m. The results demonstrate that accounting for sensor vertical movement uncertainty reduces the temperature difference between the calculated and the measured values.

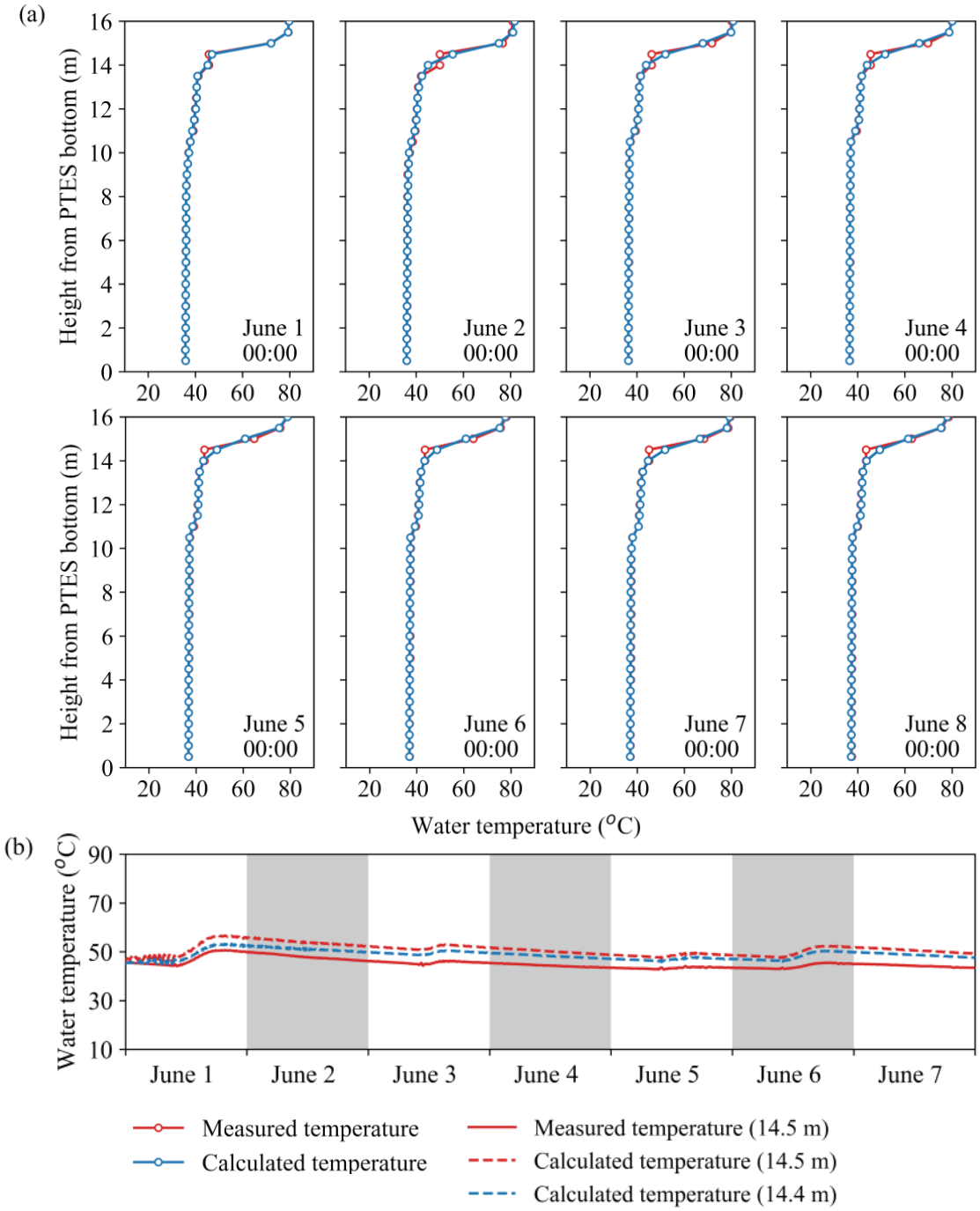

Fig. 7. Comparison of the measured and calculated PTES temperature from June 1 to June 7, 2017

3.3.2 Operation conditions

Fig.8 illustrates the variation in inlet/outlet temperature and mass flow rate variation from June 1 to June 7. There is qualitative agreement for the inlet/outlet operating conditions in terms of temperature and mass flow rate. The most significant deviation occurs when the top diffuser is used as the outlet. In theory, the outlet temperature should fall between the water temperatures at 15.12 m and 15.7 m, where the top diffuser is located. However, as mentioned earlier, there is considerable uncertainty in the actual temperature distribution between 14.5 m

and 15.5 m due to the large temperature gradient. Therefore, the difference between the calculated and the measured results regarding the top outlet temperature is acceptable.

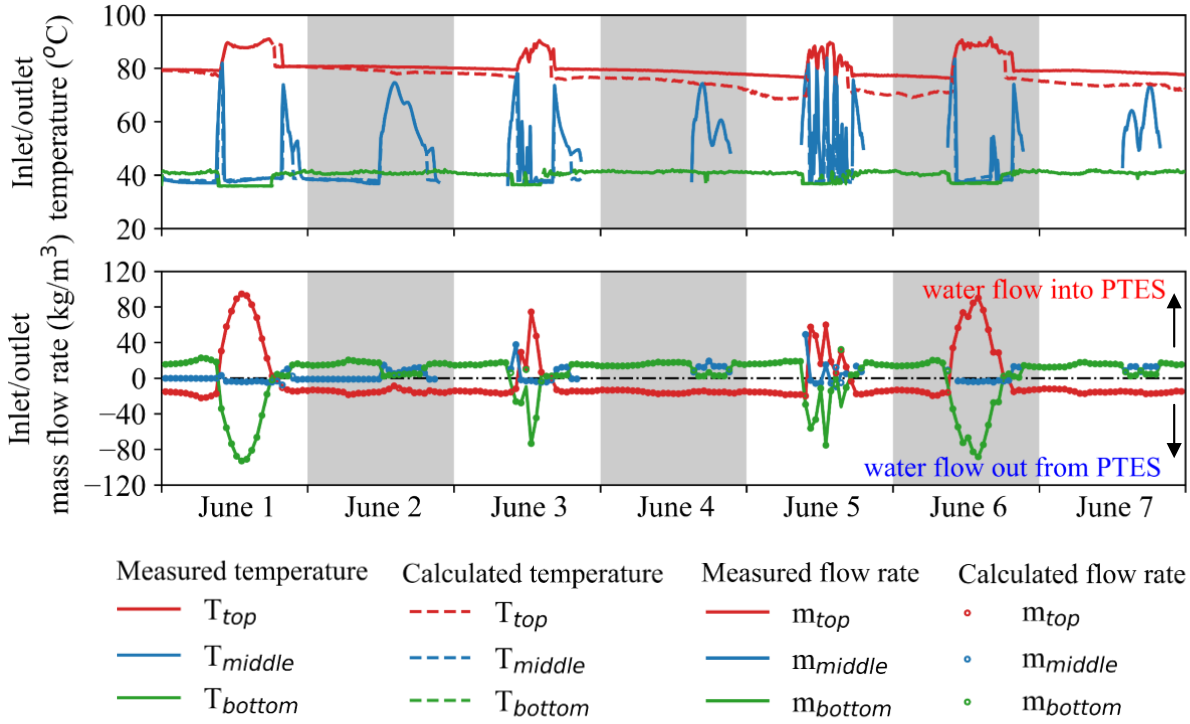

Fig. 8. Comparison of the measured and calculated inlet/outlet parameters from June 1 to June 7, 2017

It is worth mentioning that this study focuses on developing the inlet mixing correlations. As a result, the calculated temperatures of the soil region have not been presented in this section since they do not play a significant role in the inlet mixing investigation. Overall, the agreement observed in PTES temperature distribution and inlet/outlet parameters suggests that the model can be confidently used to correlate the inlet mixing parameters.

4. Numerical study scenarios and parameters

4.1 Numerical study scenarios

4.1.1 Positive buoyancy effect

Based on the operation of the PTES in 2017, twelve case studies were determined and used to investigate the impact of positive buoyant jet mixing. In all simulations, the bottom diffuser was used as the inlet, and the top diffuser served as the outlet. The bottom diffuser is far from the PTES top wall and provides enough space for the diffusion of the buoyant jet. In this case, more features of positively buoyant jet can be found in different situations. The initial temperature (T_0) was uniformly 10°C for all cases, while the inflow temperature (T_{in}), the inlet flow rate (V_{in}), the diameter of the diffuser disc (D_d), and the distance between the diffuser

discs (H_d) were varied. Key parameters of the 12 cases are presented in Table 2, with the referred case highlighted in red background and the parameter variations based on the reference case highlighted in blue background. The monitoring data indicated that the operation conditions changed every ten minutes, so the simulations ran for ten minutes. Additionally, the simulation results were recorded every ten seconds to fully characterize the transient behavior of the inlet mixture.

Table 2

Key parameters used in the investigations of positive buoyancy effect.

Case	Initial PTES temperature (T_0 (°C))	Inflow temperature (T_{in} (°C))	Inlet flow rate (V_{in} (m^3/h))	Diameter of diffuser disc (D_d (m))	Distance between diffuser discs (H_d (m))
1	10	20	10	2.5	0.58
2	10	20	50	2.5	0.58
3	10	20	100	2.5	0.58
4	10	12	50	2.5	0.58
5	10	30	50	2.5	0.58
6	10	40	50	2.5	0.58
7	10	20	50	0.5	0.58
8	10	20	50	1.5	0.58
9	10	20	50	3.5	0.58
10	10	20	50	2.5	0.48
11	10	20	50	2.5	0.68
12	10	20	50	2.5	0.78

4.1.2 Negatively buoyant effect

Similar to the positive buoyant effect study, a series of 12 cases were performed to investigate the mixing effect of negative buoyant jets. The bottom diffuser was employed as the outlet, while the middle diffuser was used as the inlet for two reasons: (1) When the middle diffuser is used as the inlet, the inflow temperature is lower than the PTES temperature at the level of the diffuser for more periods than the top diffuser operates. (2) There is enough space for the jet flow to develop. In addition, the initial temperature (T_0) was uniformly 70°C in the PTES, as shown in Table 3. Other simulation settings regarding simulation time and data sampling interval are the same as in Section 4.1.2.

Table 3

Key parameters used in the investigations of negative buoyancy effect.

Case	Initial PTES temperature (T_0 (°C))	Inflow temperature (T_{in} (°C))	Inflow rate (V_{in} (m^3/h))	Diameter of diffuser discs (D_d (m))	Distance between diffuser discs (H_d (m))

1	70	60	10	2.5	0.58
2	70	60	50	2.5	0.58
3	70	60	150	2.5	0.58
4	70	60	250	2.5	0.58
5	70	50	50	2.5	0.58
6	70	69	50	2.5	0.58
7	70	60	50	0.5	0.58
8	70	60	50	1.5	0.58
9	70	60	50	3.5	0.58
10	70	60	50	2.5	0.48
11	70	60	50	2.5	0.68
12	70	60	50	2.5	0.78

4.2 Performance index

To effectively quantify the inlet mixing impact, two parameters are introduced: the penetration height (Z) and the energy distribution ratio (η_j). These parameters aim to capture the changes in the affected areas and energy distribution variation resulting from inflow mixing under different scenarios.

4.2.1 The penetration height

Z represents the maximum height at which the inflow can affect, as illustrated shown in Fig.9. It measures the difference between the maximum height of the mixing area and the height of the inlet position. In this study, Z is determined based on the CFD calculations. A dimensionless temperature represented in Eq. (1) is used as the metric to determine whether a point in the PTES is affected by the inlet flow.

$$\theta = \frac{T_t - T_0}{T_{in} - T_0} \tag{1}$$

Where T_{in} is the inflow temperature, T_0 is the PTES initial temperature, and T_t is the PTES temperature at time t. $\theta = 1$ means that a point in the PTES is completely replaced by inflow water, while $\theta = 0$ means that a point in the PTES is not affected by inlet flow. In this context, the larger the θ, the greater the temperature change at a certain location of the PTES caused by the inlet flow. Conversely, the smaller the θ, the smaller the temperature change at a specific position inside the PTES.

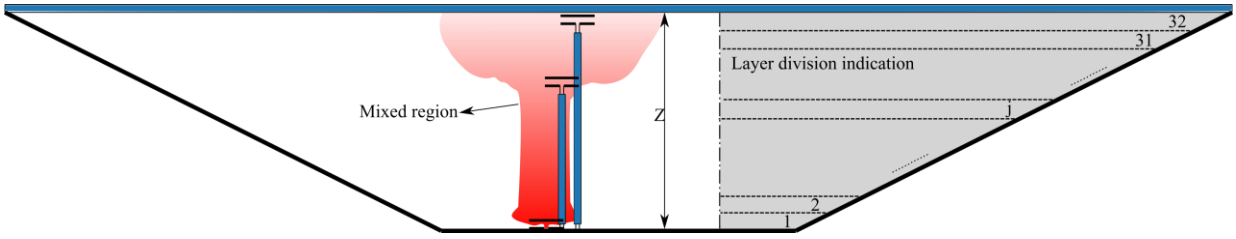

Fig. 9. Illustration of the mixed region in the PTES (The grey background illustrates the layer division in this study)

4.2.2 Energy change efficiency

Considering that the objective of this study is to quantify the degree of cross-layer mixing caused by fluid entrainment in the buoyant jet, the PTES was divided into 32 layers along the height, as shown in Fig.9. Then, the energy distribution ratio of a layer is defined as follows:

$$\eta_j = \frac{\sum_0^t C_{p.jm} m_{jm,t} (T_{jm,t} - T_{jm,0})}{\int_0^t m C_p (T_{in} - T_{out}) dt} \quad (2)$$

Where the numerator represents the energy stored in layer j and the denominator is the energy supplied to the entire PTES during the charge/discharge. $m_{jm,t}$ is the mixed water mass in layer j, and its specific heat is $C_{p.jm}$. $T_{jm,0}$ and $T_{jm,t}$ denote the initial temperature of the mixed water in the layer j and the temperature at time t, respectively. An energy distribution ratio of 1 for a layer means all the charged/discharged heat enters the layer, while an energy distribution ratio of 0 means the layer is not affected by the inlet flow. If the charged/discharged heat is evenly distributed over the 32 layers, the distribution ratio will be 1/32 for all layers. It is possible to determine the energy stored in each layer inside PTES resulting from inflow mixing based on the CFD simulations.

4.3 Dimensionless parameters

To obtain quantitative results for the inlet mixing effect, it is essential to establish a relationship with specific PTES characteristics. The characteristics of the PTES depend on the geometric configuration and operating conditions. The diffuser position and geometry are among the geometrical parameters. The inflow rate and the temperature difference between the incoming and resident water are the operating factors that are the most important.

4.3.1 Reynolds and Froude number

Dimensionless parameters are of great significance in the design and performance evaluation of stratified thermal storage and are used as indexes to evaluate the performance of stratified thermal storage [8,34,47,48]. Two dimensionless parameters are selected in this study to characterize the inflow forces and inertial forces. The inlet *Re* and *Fr* numbers are expressed as Eq. (3) and Eq. (4), respectively.

$$Re = \rho_{in} v D_h / \mu \quad (3)$$

$$Fr = v^2 / (D_h g (\frac{\rho_{in}}{\rho_0} - 1) \quad (4)$$

Where ρ_{in} and ρ_0 represent the inflow temperature and the PTES initial temperature, respectively. v is the average inflow velocity, μ is the kinematic viscosity, and g is the acceleration of gravity. $D_h = \frac{4\pi D_d H_d}{\pi D_d + H_d}$ is the characteristic length that is used instead of the inlet pipe diameter because the buoyant jet formation is also related to the diffuser geometry (with detailed analysis in Section 5).

4.3.2 Momentum and buoyancy flux

Inspired by previous studies, the mixing flow depends on the momentum M and the buoyancy flux F when the inlet diameter is small compared to the jet penetration height. In this case, it is expected that M and F can be used to determine the inlet mixing impact. The following equations give the expressions for momentum M and the buoyancy flux F:

$$M = \pi D_h^2 v^2 \tag{5}$$

$$F = \pi \left[\frac{g(\rho_{in} - \rho_0)}{\rho_0}\right] D_h^2 v \tag{6}$$

M characterizes the inertia force of the inlet flow while F describes the buoyancy force of the inlet flow. It is important to note that in the following sections, Fr and F are expressed in their absolute values to harmonize the format of buoyancy in positive and negative buoyancy jets.

4.3.3 Dimensionless penetration height and time

In the context of inlet mixing, it has been demonstrated that all inflow properties can be scaled in terms of combination of M and $|F|$. The penetration height (Z) should be scaled as the dimensionless penetration height ($Z \cdot M^{-3/4} \cdot |F|^{1/2}$) [49,50]. The time ($t$) should be scaled as the dimensionless time $t|F|/M$ [51]. These scaling relationships allow for a more generalized representation of the penetration height and the temporal evolution of the inlet mixing, considering the combined effects of the inflow momentum and buoyancy flux.

In summary, the mentioned indexes provide a framework for analyzing and comparing the inlet mixing behavior in a dimensionless manner. In particular, it makes it possible to quantify the inlet mixing effect across different cases, facilitating the evaluation of inlet mixing degree. Section 5 will present the correlations of these parameters for various cases.

5. Results and discussion

5.1 Physical nature

5.1.1 Positive buoyant effect

The development of a positive buoyant jet and the energy distribution ratio along the PTES height at the specific time (left) are shown in Fig.10. Note that the red curve in the energy distribution ratio diagram indicates the actual energy distribution ratio in the 32 layers. In comparison, the blue curve in the diagram represents that the delivered energy is evenly distributed among the 32 layers inside the PTES.

Initially, water enters the diffuser and reaches the upper diffuser disc. The jet starts to spread radially but remains concentrated near the inlet diffuser in the first 20s. Most of the energy provided is distributed near the bottom diffuser. The water flow starts to rise when it reaches the disc's outer edge, driven by the buoyancy force. Over time, the penetration height is getting larger, as well as the region of influence. The penetration height reaches the middle diffuser in around 300s. At the same time, the energy distribution ratio significantly changed, with more energy being distributed between 6 and 8 m inside PTES. At the end of the calculation, the jet reaches the top of the PTES, and part of the water flows downward, forming a recirculation region. More water is induced and brought to the top of the PTES, resulting in a larger distribution ratio.

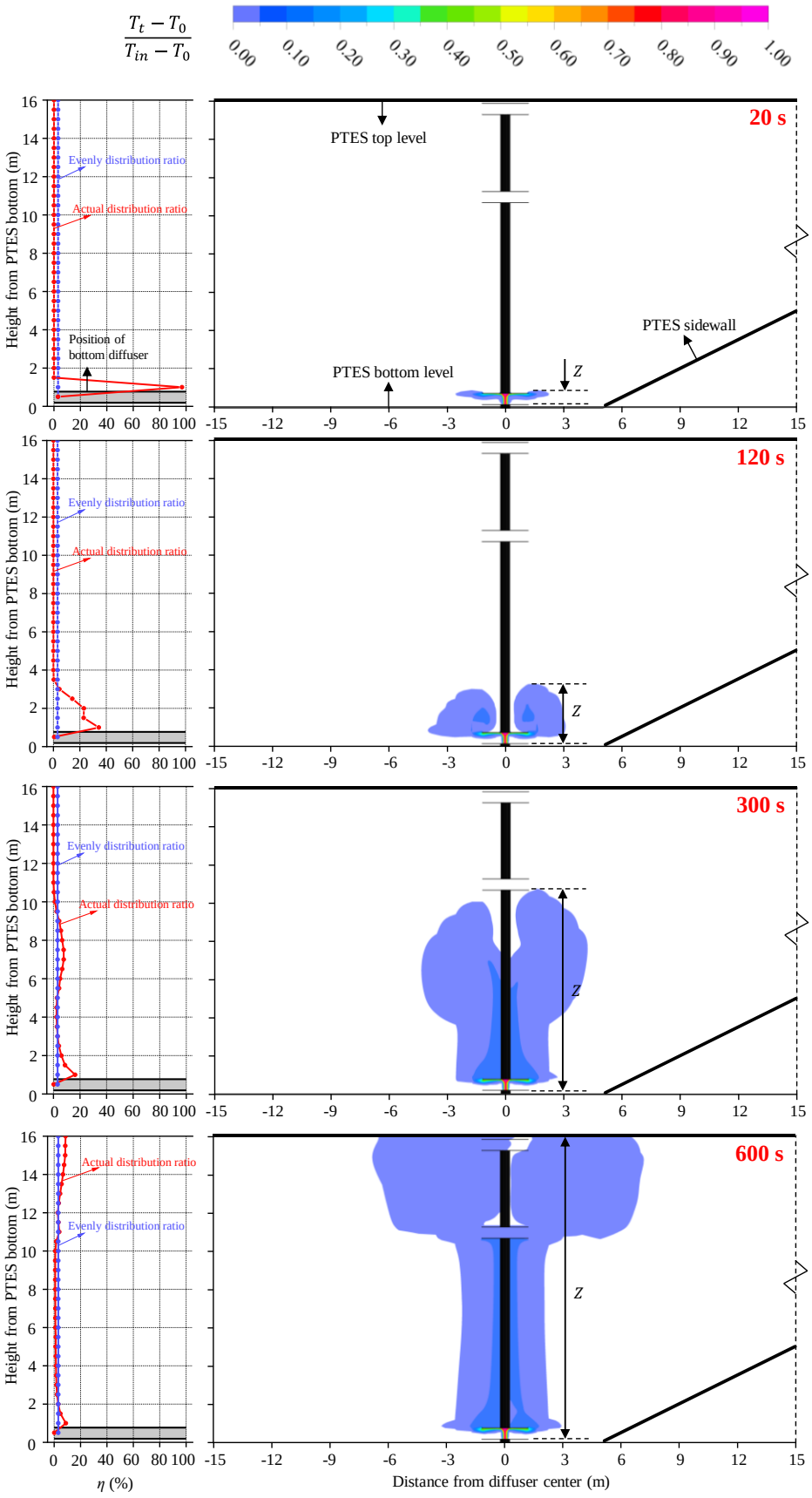

Fig. 10. Flow visualization of a positive buoyant jet. Based on Case2, with T_0 = 10°C, T_{in} = 20°C, V_{in} = 50 m^3/h, D_d = 2.5 m and H_d = 0.58 m.

5.1.2 Negative buoyant effect

Flow visualization of the transient behavior of a negatively buoyant jet is shown in Fig. 11, where Z is the downward penetration height, and Z' is the upward penetration height.

The jet flow reaches the upper diffuser disc in a short time, which weakens the upward momentum and changes the flow direction (20 s). During this period, the influenced area is confined near the middle diffuser. Then, driven by the negative buoyancy force, the water flows downward. As time progresses, the mixing region expands downwards, and the jet becomes noticeably asymmetric. The jet reaches the bottom of the PTES in about 300s. Additionally, it is evident that the location of the maximum energy distribution ratio shifts from the layers near the middle entrance to the layers of PTES bottom within the first 300s. Furthermore, it spreads radially until it reaches the PTES sidewall (t = 600s). Notably, the upward penetration height Z' is limited within the distance between the diffuser discs, since the upper diffuser disc blocks its upward path.

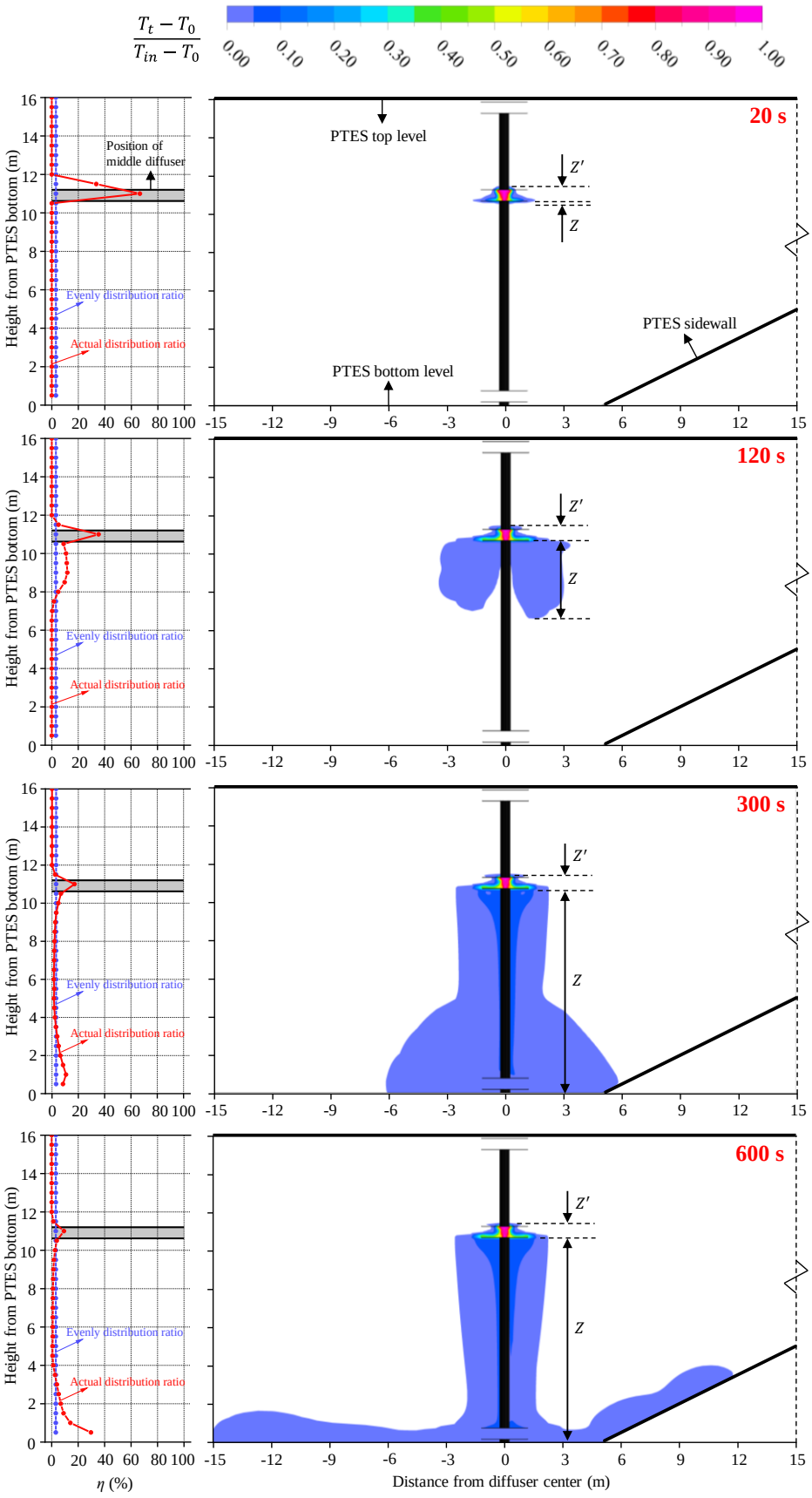

Fig. 11. Flow visualization of a negative buoyant jet. Based on Case2, with T_0 = 70°C, T_{in} = 60°C, V_{in} = 50 m^3/h, D_d = 2.5 m and H_d = 0.58 m.

5.2 Parametric analysis of penetration height

5.2.1 Positive buoyant jet

The inflow rate (V_{in}), the temperature difference (ΔT) between the inflow and the PTES, and the diffuser size (D_d and H_d) affect the extent of the inflow mixing zone. Fig.12 displays the time history of the penetration height for a positive buoyant jet under different conditions. The solid and dash lines represent the positions of the upper and lower discs of the bottom diffuser, respectively. Changes of V_{in}, D_d and H_d contribute to the change of the Re number, while change of ΔT contributes to the change of the Fr number.

The upward momentum of jet will be increased for positive buoyancy where the momentum and buoyancy are in the same direction. The inlet flow reaches PTES top in less than 600s, except for cases with an inflow rate of 10 m^3/h and a temperature difference of 2 K. In addition, the penetration to the top of the PTES occurs faster for higher Re numbers because of a larger jet momentum. A larger Fr number can also cause the jet to reach the PTES top faster due to greater buoyancy. Moreover, H_d does not significantly affect penetration since the disc distance varies very little to ensure that the diffuser distributes the inflow effectively.

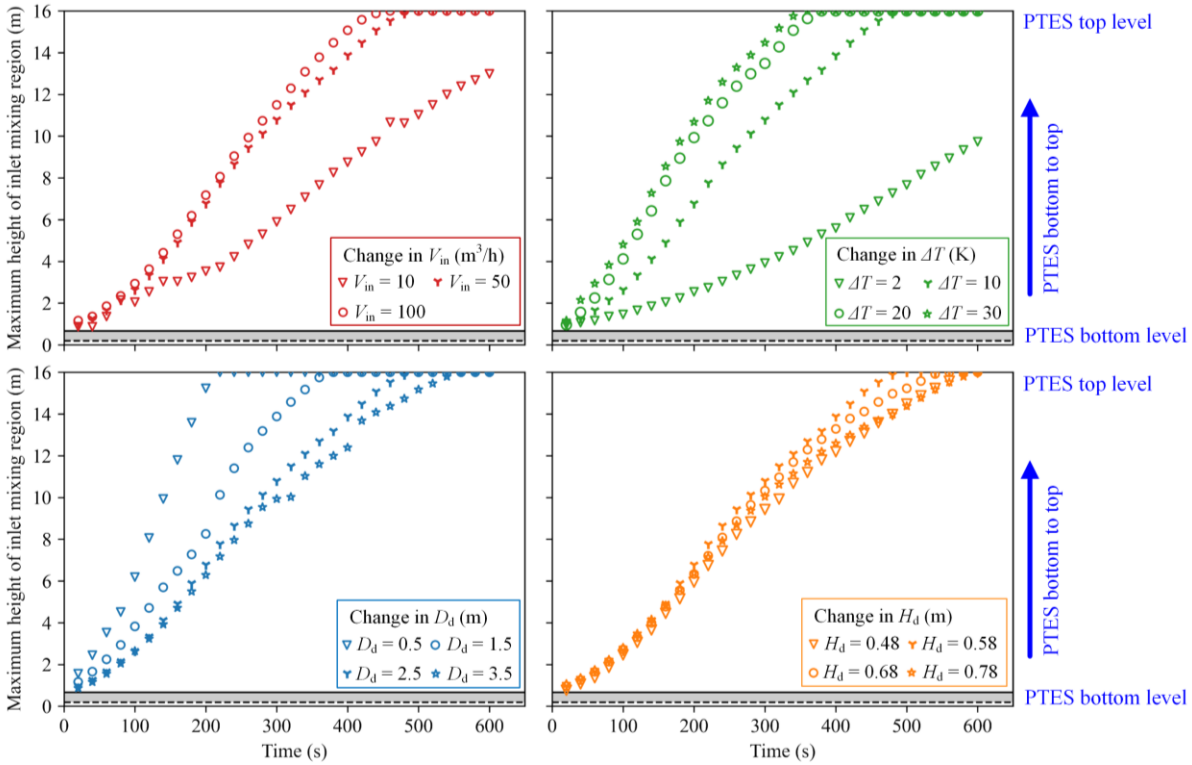

Fig. 12. Variation of the penetration height with time for a positive buoyancy jet under different operation conditions.

Based on the dimensional theory, the relation between the dimensionless penetration height and time for a positive buoyant jet is shown in Fig.13. The inlet Re number falls in the

range of $1292 \leq Re \leq 25348$ and the Fr number in the range of $6.5 \times 10^{-6} \leq |Fr| \leq 5.2 \times 10^{-3}$. A power-law relation between the dimensionless height and the dimensionless time is found for all the investigated cases. However, the coefficients fitted for the Re number of 1292 differ from those of the rest, as shown in Eq. (7). The different behavior of the inlet flow with a Re number of 1292 could be explained by its low inlet flow rate. As shown in Eq. (5) and Eq. (6), the influence of the inlet velocity on momentum is much greater than that of the buoyancy.

$$Z \cdot M^{\left(-\frac{3}{4}\right)} \cdot |F|^{\left(\frac{1}{2}\right)} \cdot 10^{(-3)} = \begin{cases} 0.044 \cdot \left(\frac{t \cdot |F| \cdot 10^{(-3)}}{M}\right)^{1.16} & Re \leq 1292 \\ 0.123 \cdot \left(\frac{t \cdot |F| \cdot 10^{(-3)}}{M}\right)^{0.78} & Re > 1292 \end{cases} \quad (7)$$

In conclusion, Eq. (7) can be used to predict the penetration height of a positive buoyancy jet during operation, but attention should be paid to the applicable range of the inlet Re number.

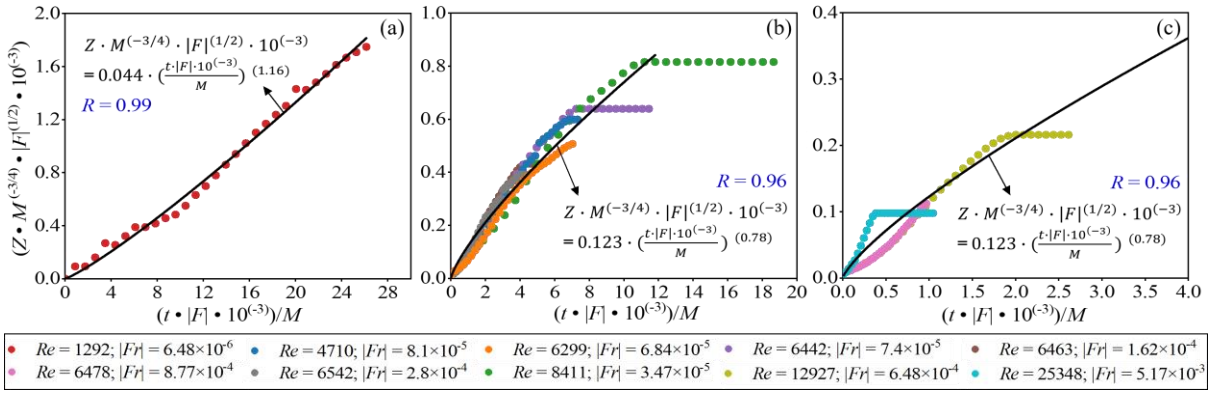

Fig. 13. Relationship between the dimensionless penetration height and time for a positive buoyant jet

5.2.2 Negative buoyant jet

Fig.14 display the penetration height over 600s for each case given in Table 3. The solid and dash lines represent the positions of the upper and lower discs of the middle diffuser, respectively.

The largest upward penetration height (Z') can be reached more quickly by water at a higher inlet volume flow rate (V_{in}), but for a smaller V_{in} of 10 m^3/h, it takes around 100s to reach the maximum Z'. For a more significant temperature difference (ΔT), Z' stabilizes earlier, while buoyancy takes longer to offset the effect of momentum at smaller ΔT.

When V_{in} and ΔT are increased, the penetration to the PTES bottom occurs more quickly, and the downward penetration height (Z) increases faster. Besides, lowering D_d results in a more considerable Re number, which can also speed up the increase of Z. However, the inlet

Re value changes by 1% for every 0.1 m increase in H_d. In this case, it affects the penetration height slightly.

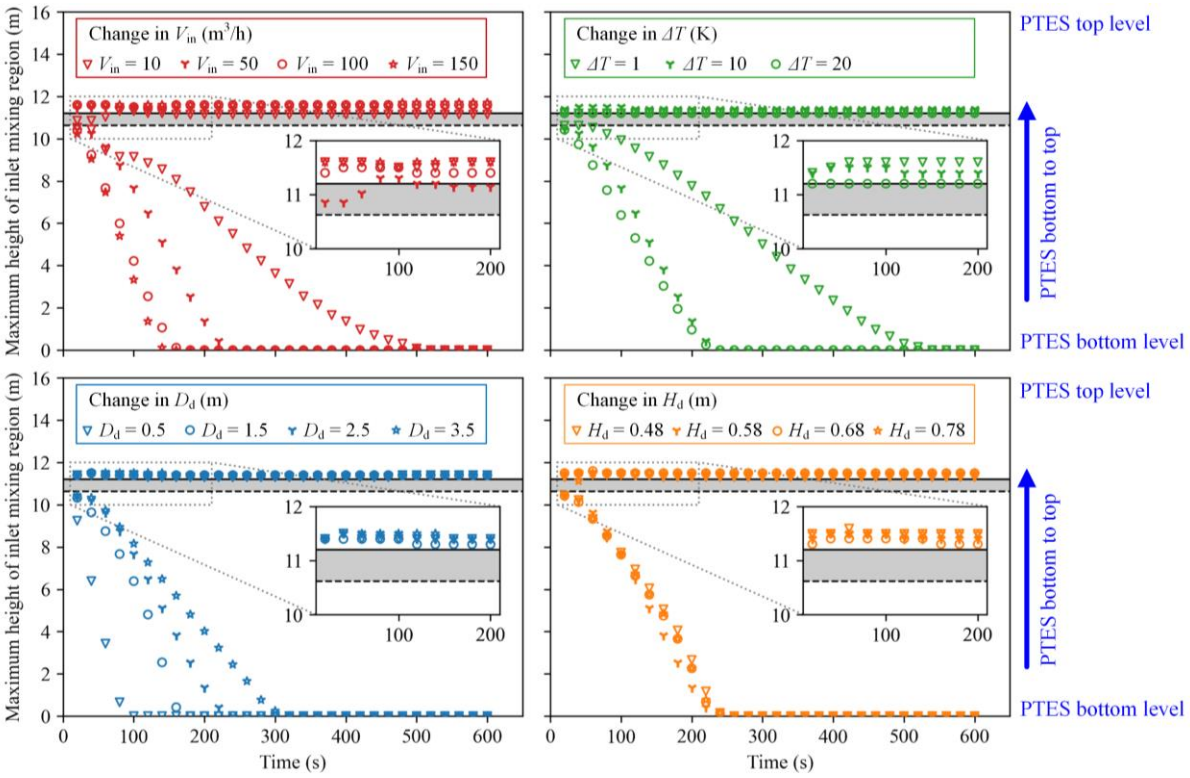

Fig. 14. Variation of the penetration height with time under different operation conditions for a negative buoyancy jet

However, the maximum upward penetration height Z' for all the cases are limited is only about 0.3 m above the middle diffuser upper disc, and there is no great tendency to spread radially within the diffuser region. Therefore, we assume that the mixing above the inlet is negligible when the flow enters with a temperature lower than that of the PTES at the level of the diffuser.

In this context, only the relationship between the downward penetration height Z and time is established based on the dimensional theory for the negative buoyancy jet. The relationship between the dimensionless time and penetration height is illustrated in Fig.15. Both the solid curves show a power-law fit, but they differ in terms of Re. The curve in Fig.15 (a) needs to be considered when the Re number is less than 1272, while the curve in Fig.15 (b) and (c) is considered when the Re number is higher than 1272. As a result, the prediction of the penetration height should follow Eq. (8) as specified in this study.

$$Z \cdot M^{\left(-\frac{3}{4}\right)} \cdot |F|^{\left(\frac{1}{2}\right)} \cdot 10^{(-3)} = \begin{cases} 0.085 \cdot \left(\frac{t \cdot |F| \cdot 10^{(-3)}}{M}\right)^{0.938} & Re \leq 1272 \\ 0.031 \cdot \left(\frac{t \cdot |F| \cdot 10^{(-3)}}{M}\right)^{1.124} & Re > 1272 \end{cases} \quad (8)$$

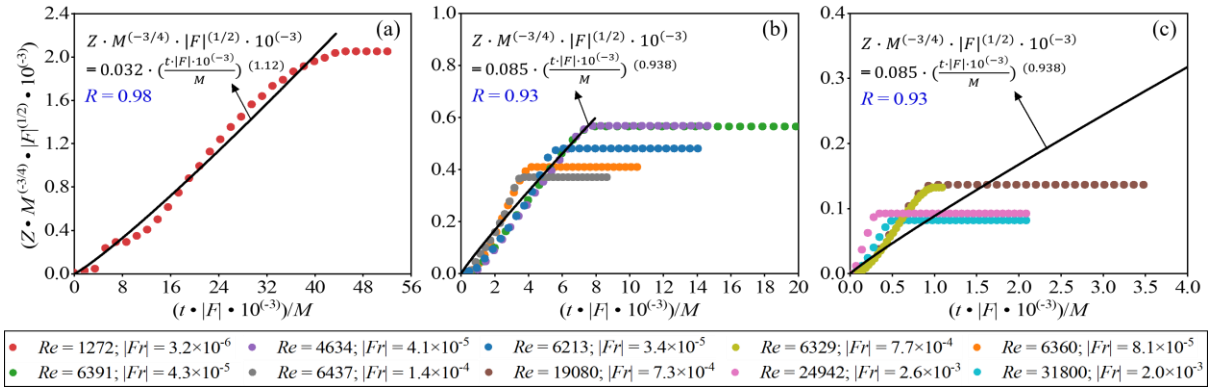

Fig. 15. Relationship between the dimensionless penetration height and time for a negative buoyant jet.

5.3 The energy distribution ratio

5.3.1 Positive buoyant jet

Fig.16 represents selected cases where there is a significant difference between the energy distribution ratio (η_j) of the layers inside the PTES. The circles are colored according to the value of the ratio. Smaller circles represent a smaller energy distribution ratio, while larger circles represent a more significant energy distribution ratio. It shows that the layer above the bottom inlet (i.e., the second layer) always has a large energy distribution ratio in the first 100s of the calculation because the inlet water continuously accumulates in this layer before being dispersed. Over time, the energy distribution ratio of the second layer decreases gradually and varies depending on the conditions. In addition, as more and more mixed water enters the top layer, the energy distribution ratio of the 32nd layer increases. Moreover, for the other layers inside the PTES, the energy distribution ratio is less than 10% during the calculation.

For comparison, we briefly describe the results for two cases. In Case 1, when V_{in} is reduced to 10 m^3/h, the large energy distribution ratio is obviously concentrated in the layers near the bottom inlet, while the upper layers of PTES are hardly affected. This is because it is challenging for the buoyancy jet to penetrate the top layers with small momentum during the calculation. The inlet momentum and buoyancy are significantly increased for Case 7 when D_d is reduced to 0.5 m. As a result, the inflow quickly spreads to the top layers, causing a sharp rise in the energy distribution ratio of the 32nd layer while maintaining a stable value of about 40%. At the same time, the energy distribution ratio of the second layer drops rapidly to below 10%.

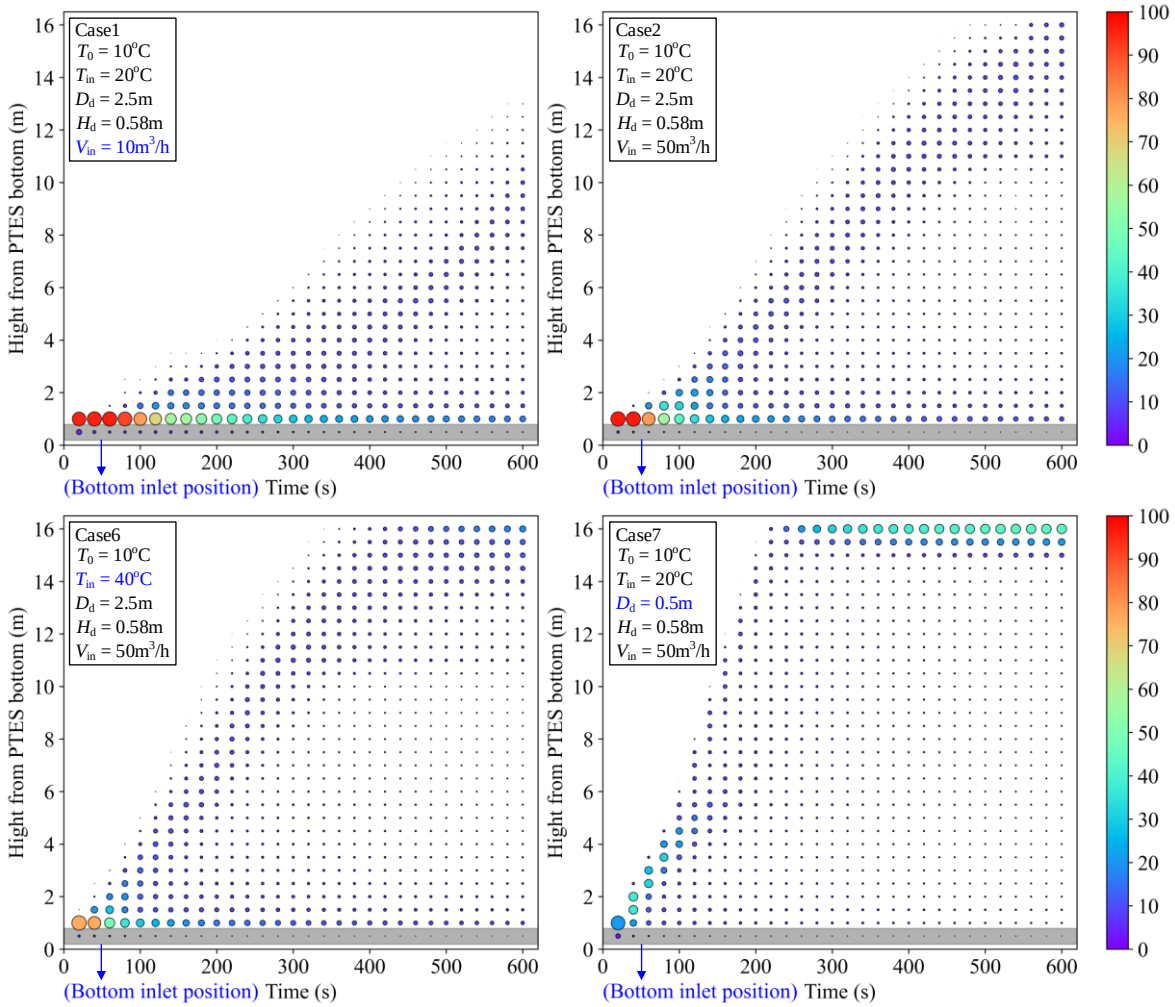

Fig. 16. Development of the energy distribution ratio under different conditions. Each circle represents the energy distribution ratio of the layer at different times.

Most of the charged heat is stored in layers either close to the bottom inlet or in the top layer of the PTES since a larger energy distribution ratio η_j is found in these layers. Therefore, efforts were made to derive the correlations of the energy distribution ratio for the second and 32nd layer based on the dimensional theory.

Fig.17 shows the energy distribution ratio for the 2nd and the 32nd layer, respectively. All datasets can be fitted as functions in the form of Eq. (9) but with different coefficients, a and b. Combined with Fig.16, it is evident that the start time of the energy distribution in the 32nd layer is highly affected by the inflow under different conditions, making it challenging to establish a correlation. In this case, it should be noticed that the time variable for the 32nd layer is adjusted from (t) to $(t - t_{start})$, considering the time delay associated with the start of energy distribution in that layer.

$$\eta_j = a \cdot \left(\frac{t \cdot |F| \cdot 10^{-3}}{M}\right)^b \tag{9}$$

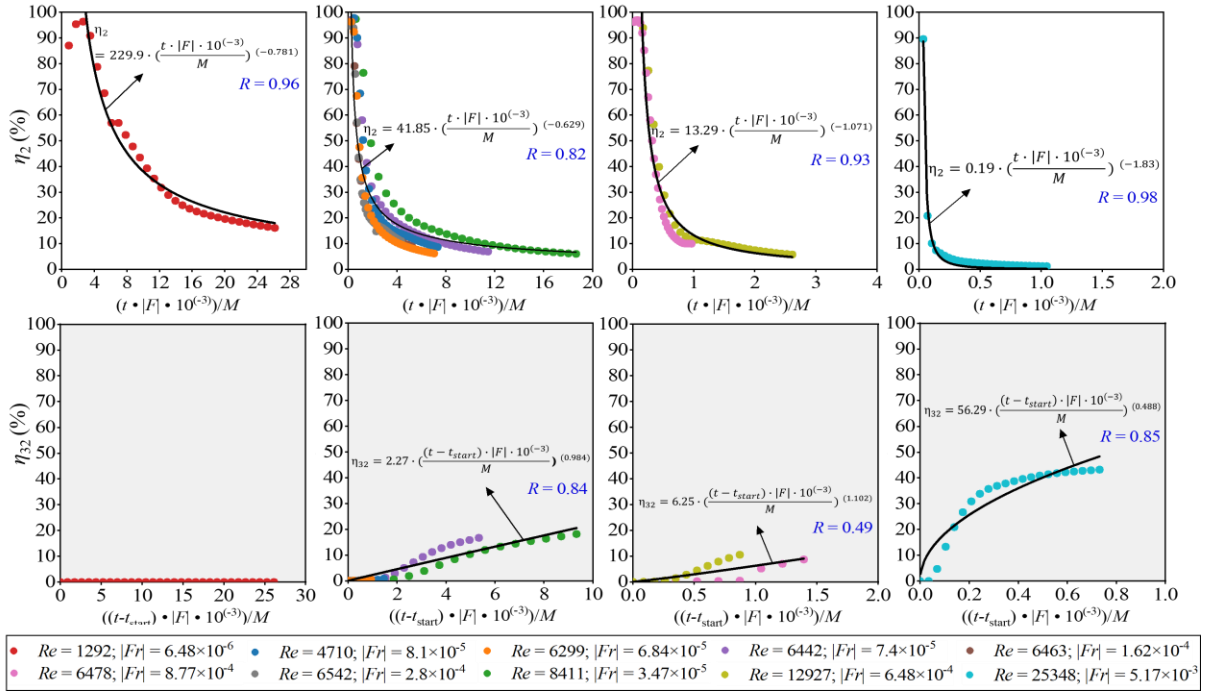

Fig. 17. Relationship between the energy distribution ratio and the dimensionless time for a positive buoyant jet (White background represents the results of the 2nd layer, and light grey background represents the results of the 32nd layer).

The coefficients for these situations, along with their range of application, are listed in Table 4. The application ranges of the 2nd and 32nd layers follow the same principle. It is essential to note that the energy distribution ratio of these layers depend both on the inlet Re number as well as the Fr number. When the Re number is insufficiently large, it is necessary to consider the combination of Re number and Fr number.

Table 4

Coefficients and application range for a positive buoyant jet.

Layer	Fitted equation	Coefficients		Application range
		a	b	
2nd	(9)	0.19	-0.183	$Re \geq 25348$
		13.29	-1.071	$Re \geq 6478$ & $6.84\times10^{-4} \leq \|Fr\| \leq 8.77\times10^{-4}$
		41.85	-0.629	$Re > 1292$ & $\|Fr\| < 8.77\times10^{-4}$
		229.9	-0.781	$Re \leq 1292$
32nd	(9)	56.29	0.488	$Re \geq 25348$
		6.25	1.102	$Re \geq 6478$ & $6.84\times10^{-4} \leq \|Fr\| \leq 8.77\times10^{-4}$
		2.27	0.984	$Re > 1292$ & $\|Fr\| < 8.77\times10^{-4}$

	0	0	$Re \leq 1292$

5.3.2 Negative buoyant jet

The visual representation in Fig.18 shows the cases with significant differences between the energy distribution ratio (η_j) of each layer inside the PTES. The circles are colored according to the value of the energy distribution ratio. Smaller circles represent a smaller energy distribution ratio, while larger circles represent a more significant energy distribution ratio. The layers near the middle inlet (i.e., the 22nd and 23rd layers) have a large energy distribution ratio in the first 100s. In Case 6, the energy distribution ratio of the 23rd layer is more noticeable compared to other cases. This is attributed to a significant upward penetration caused by the initial inlet momentum force being much larger than the buoyancy force. However, water at the PTES bottom for Case 6 takes longer to be affected by the inlet water because of a smaller ΔT. Moreover, the energy distribution ratio of all other layers are less than 10% during the calculation, with the exception of the layers close to the middle inlet and the PTES bottom.

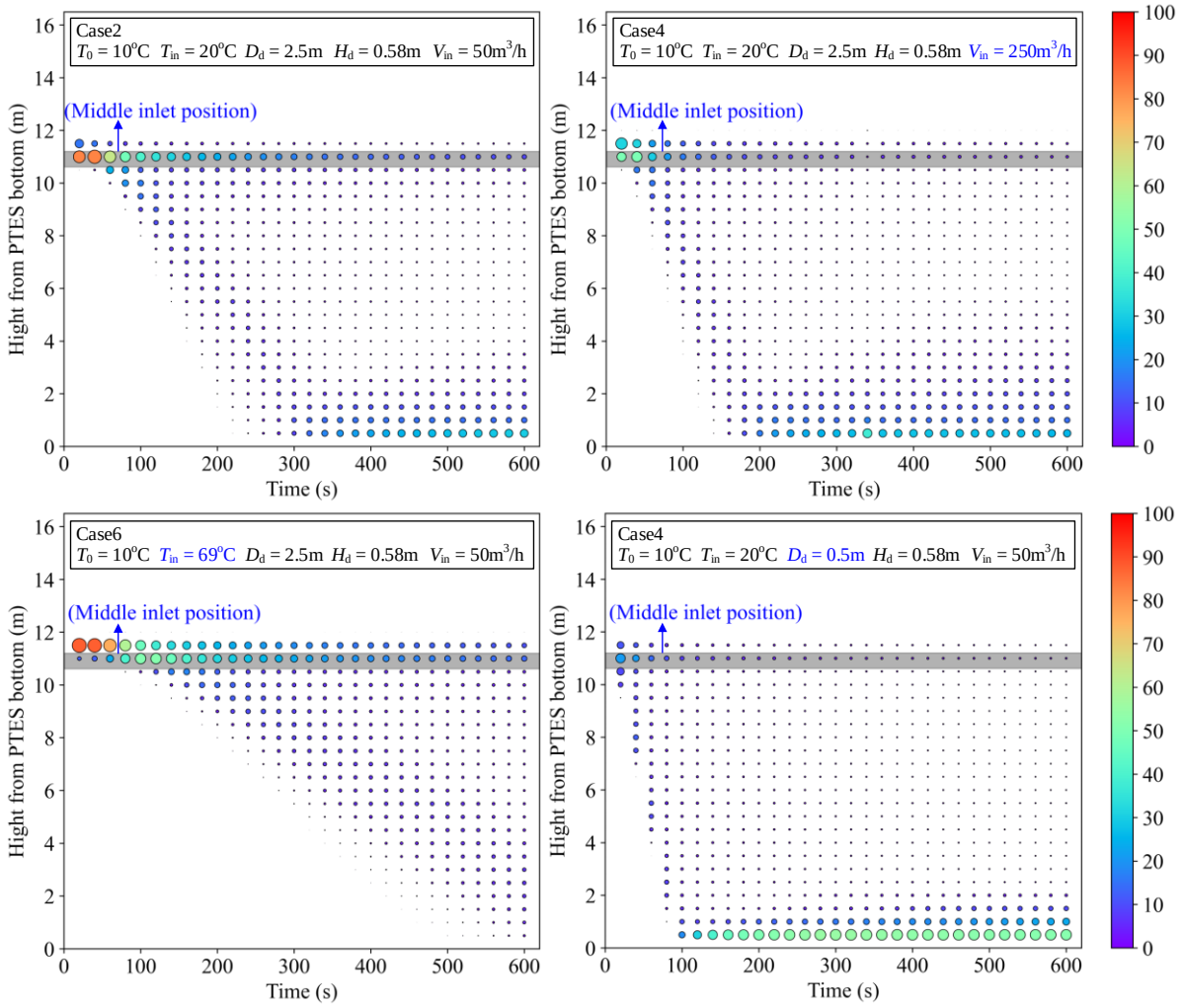

Fig. 18. Development of the energy distribution ratio under different conditions. Each circle represents the energy distribution ratio of the layer at different times.

Unlike the positive buoyant jets, the negative buoyant jets penetrate upward and then sink. Therefore, the fitting of the relational expression focuses on the inlet layer (22nd layer), the layer above the middle inlet (23rd layer), and the bottom layer (first layer).

Fig.19 demonstrates the relationship between the energy distribution ratio η_j and the dimensionless time for these three layers. All data related to the 22nd and 23rd layers can be fitted as functions in the form of Eq. (10). In particular, the curve is in good agreement with the data for the 22nd and the 23rd layers, which is a consequence of the application of diffuser discs. However, it is challenging to obtain ideal correlations by fitting most of the data in the 1st layer to Eq. (9). As a result, Eq. (10) is proposed, which fits all the data perfectly (as shown in Fig.17 (1st layer)). Detailed information related to the coefficients and application range is listed in Table 5.

$$\eta_j = a - b \cdot c^{\left(\frac{(t-t_{start})\cdot|F|\cdot 10^{-3}}{M}\right)} \tag{10}$$

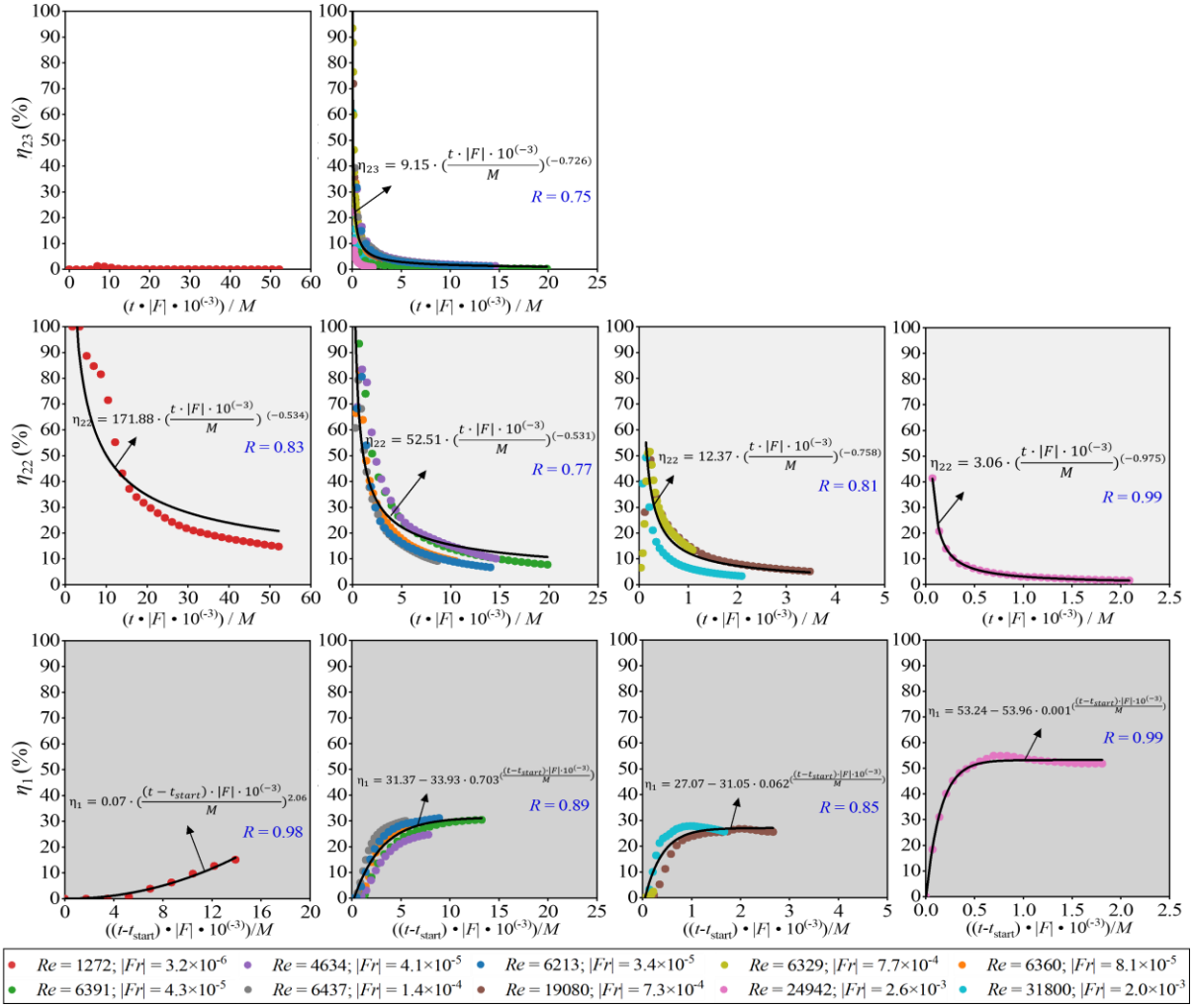

Fig. 19. Relationship between the energy distribution ratio and dimensionless time for the negative buoyant jet (White background represents the results of the 23rd layer, light grey background represents the results of the 22nd layer, and dark grey background represents the results of 1st layer).

Table 5 demonstrates that the energy distribution ratio of the 23rd layer is only depending on the inlet Re due to the application of diffuser inlet. But for the energy distribution ratio of the 22nd and 1st layers, both inlet Re number and Fr number should be considered.

Table 5

Coefficients and application range for the negative buoyant jet.

Layer	Fitted equation	Coefficients			Application range
		a	b	c	
1st	(10)	52.24	53.96	0.001	$Re \geq 24942$ & $\lvert Fr\rvert \geq 2.6\times10^{-3}$
		27.07	31.05	0.062	$Re \geq 6329$ & $7.3\times10^{-4} \leq \lvert Fr\rvert \leq 2\times10^{-3}$
		31.37	33.93	0.703	$Re > 1272$ & $\lvert Fr\rvert < 7.3\times10^{-4}$
	(9)	0.07	2.06	-	$Re \leq 1272$

22nd	(9)	3.06	-0.975	-	$Re \geq 24942$ & $\lvert Fr \rvert \geq 2.6\times10^{-3}$
		12.37	-0.758		$Re \geq 6329$ & $7.3\times10^{-4} \leq \lvert Fr \rvert \leq 2\times10^{-3}$
		52.51	-0.531	-	$Re > 1272$ & $\lvert Fr \rvert < 7.3\times10^{-4}$
		171.88	-0.534	-	$Re \leq 1272$
23rd	(9)	9.15	0.726	-	$Re > 1272$
		0	0	-	$Re \leq 1272$

5.4 Range of application

The selection of the investigated cases is based on the actual operation of the Dronninglund project. However, the correlations of the penetration height and the energy distribution ratio are obtained based on limited datasets. Therefore, the accuracy of the expressions proposed in this study is only guaranteed with the dimensionless parameters in the ranges shown in Table 4 and Table 5.

Furthermore, the model and correlations presented in this study do not consider the case of multiple diffusers serving as inlets simultaneously. As demonstrated in Table 1, when multiple diffusers are used as inlets at the same time, the proportion is only 8.18%, of which 2.94% are the top and middle diffusers working as inlets, 5.24% being the middle and bottom diffusers working as inlets. Therefore, the potential impact on the mixed region parameters may be insignificant when multiple diffusers operate as inlets. Nevertheless, the presented model should be used with caution in this situation.

Overall, the findings of this study are derived from the fundamental dataset used in this paper. It is important to note that the correlations established in this study may need revaluation and reassessment if there are changes in the underlying data, such as the changes in PTES geometry, alteration in the inlet position along the horizontal direction, utilization of multiple diffusers as inlets simultaneously, or non-uniform initial PTES temperature distribution.

5. Conclusion

To accurately predict the thermal performance of the PTES, it is crucial to develop a model that is precise and efficient. The inlet mixing effect is an important aspect to be considered in this modeling process, as it has a notable impact on the thermal stratification within the PTES. Therefore, it is essential to incorporate the consideration of inlet mixing into one-dimensional numerical models of the PTES. This study explores the inlet mixing phenomenon and its impact

on the overall thermal behavior of the PTES using a three-dimensional full-scale CFD model of Dronninglund PTES.

5.1 Core findings

Two performance indexes are proposed in this study to quantify the mixing area inside the PTES and evaluate its influence on the energy distribution within the PTES. The following conclusions are drawn:

- For Dronninglund PTES, the bottom diffuser is used as an inlet for about 74% of the year, indicating that it is crucial to PTES's overall operating performance. The maximum temperature difference between the inflow and the water inside PTES at the level of the bottom diffuser is about 10 K. This temperature indicates the potential for significant positive buoyant jets when the bottom diffuser operates as an inlet.
- The middle diffuser is employed as an inlet roughly 16.1% of the time for Dronninglund PTES. Notably, in September and November, inflow water that is up to 30 K colder than the PTES water temperature enters the PTES. In this scenario, a strong negative buoyancy jet is expected.
- The penetration height of the inlet mixing depends on the inlet volume flow rate (V_{in}), the temperature difference between the inlet and the level of the inlet diffuser inside the PTES (ΔT), and the diffuser disc diameter (D_d).
- The dimensionless height ($Z \cdot M^{(-3/4)} \cdot |F|^{(1/2)} \cdot 10^{(-3)}$) and time ($t \cdot |F| \cdot 10^{(-3)}/M$) are still applicable for the buoyancy jet that occurs within PTES. These dimensionless quantities are typically fitted using a power law relationship, allowing for a more comprehensive characterization of the penetration height and time-dependent behavior. In addition, the correlations derived from this study reveal that the transient dimensionless penetration height is primarily dependent on the inlet Re number for both the positive and negative buoyancy jets.
- For the positive buoyancy jet, the most thermally influenced layers of the PTES are the layers near the bottom inlet (2nd layer) and the top layer (32th layer). The energy distribution ratio can be found for a layer using the formula $\eta_j = a \cdot (t \cdot |F| \cdot 10^{(-3)}/M)^b$, however the coefficients vary with the Re number and the Fr number.
- For the negative buoyancy jet, the middle inlet layer (22nd layer), the layer just above the middle inlet (23rd layer), and the bottom layer (1st layer) experience the most significant thermal influence. The energy distribution ratio formula, $\eta_j = a \cdot (t \cdot |F| \cdot 10^{(-3)}/M)^b$, is

suitable for the 22nd and 23rd layers. However, a slightly modified formula $\eta_j = a - b \cdot c^{t\cdot|F|\cdot 10^{(-3)}/M}$ provides a good representation of the jet influence for the 1st layer and accounts for its specific characteristics.

In conclusion, this study emphasis the significance of understanding and quantifying the influence of inlet mixing on the PTES performance. Researchers and engineers can gain valuable insights into the thermal dynamics of PTES and make well-informed decisions about its design and operation by utilizing the suggested performance indicators. Furthermore, the proposed correlations can be used to improve existing one-dimensional PTES models targeting higher prediction accuracy of thermal stratification in the heat storage.

5.2 Forthcoming studies

Several gaps in this work deserve to be further studied. To quickly enrich the fundamental dataset, it is worth developing a hybrid approach that combines CFD calculation and machine learning. With this approach, the dataset may be quickly enhanced for a variety of situations, improving the accuracy and applicability of the findings. In addition, it is essential to consider the non-uniform temperature distribution of PTES under actual operating conditions. The practical significance of the study's findings can be strengthened by including suitable performance indexes for non-uniform temperature distribution, assuring their applicability in the actual PTES applications.

Acknowledgments

The work is partly funded by the Danish Energy Agency EUDP project titled Participation in the IEA SHC Task 68 on "Efficient Solar District Heating Systems"" (no. 134-21027) and the Chinese Scholarship Council (CSC). Without their support, the research would not be possible.

Reference

[1] International Energy Agency. World Energy Outlook 2022.

[2] Gao D, Kwan TH, Dabwan YN, Hu M, Hao Y, Zhang T, et al. Seasonal-regulatable energy systems design and optimization for solar energy year-round utilization. Applied Energy 2022;322:119500. https://doi.org/10.1016/j.apenergy.2022.119500.

[3] Xiang Y, Xie Z, Furbo S, Wang D, Fan J. A comprehensive review on pit thermal energy storage: Technical elements, numerical approaches and recent applications. Journal of Energy storage 2022; 55: 105716. https://doi.org/10.1016/j.est.2022.105716.

[4] Tatsidjodoung P, Le Pierrès N, Luo L. A review of potential materials for thermal energy storage in building applications. Renewable and Sustainable Energy Reviews 2013;18:327–49. https://doi.org/10.1016/j.rser.2012.10.025.

[5] Fan J, Furbo S. Thermal stratification in a hot water tank established by heat loss from the tank. Solar Energy 2012;86:3460–9. https://doi.org/10.1016/j.solener.2012.07.026.

[6] Li Q, Lin W, Huang X, Tai Y, Ding X, Zhang Y. Thermocline dynamics in a thermally stratified water tank under different operation modes. Applied Thermal Engineering 2022;212:118560. https://doi.org/10.1016/j.applthermaleng.2022.118560.

[7] Sifnaios I, Jensen AR, Furbo S, Fan J. Performance comparison of two water pit thermal energy storage (PTES) systems using energy, exergy, and stratification indicators. Journal of Energy Storage 2022;52:104947. https://doi.org/10.1016/j.est.2022.104947.

[8] Njoku HO, Ekechukwu OV, Onyegegbu SO. Analysis of stratified thermal storage systems: An overview. Heat and Mass Transfer 2014;50:1017–30. https://doi.org/10.1007/s00231-014-1302-8.

[9] Alizadeh S. An experimental and numerical study of thermal stratification in a horizontal cylindrical solar storage tank. Solar Energy 1999;66:409–21. https://doi.org/10.1016/S0038-092X(99)00036-5.

[10] Han YM, Wang RZ, Dai YJ. Thermal stratification within the water tank 2009;13:1014–26. https://doi.org/10.1016/j.rser.2008.03.001.

[11] Karim MA. Experimental investigation of a stratified chilled-water thermal storage system. Applied Thermal Engineering 2011;31:1853–60. https://doi.org/10.1016/j.applthermaleng.2010.12.019.

[12] Lavan Z, Thompson J. Experimental study of thermally stratified hot water storage tanks. Solar Energy 1977;19:519–24. https://doi.org/10.1016/0038-092X(77)90108-6.

[13] Hariharan K, Badrinarayana K, Srinivasa Murthy S, Krishna Murthy M V. Temperature stratification in hot-water storage tanks. Energy 1991;16:977–82. https://doi.org/10.1016/0360-5442(91)90057-S.

[14] Deng Y, Sun D, Niu M, Yu B, Bian R. Performance assessment of a novel diffuser for stratified thermal energy storage tanks – The nonequal-diameter radial diffuser. Journal of Energy Storage 2021;35. https://doi.org/10.1016/j.est.2021.102276.

[15] Zachár A, Farkas I, Szlivka F. Numerical analyses of the impact of plates for thermal stratification inside a storage tank with upper and lower inlet flows. Solar Energy

2003;74:287–302. https://doi.org/10.1016/S0038-092X(03)00188-9.

[16] Shah LJ, Furbo S. Entrance effects in solar storage tanks. Solar Energy 2003;75:337–48. https://doi.org/10.1016/j.solener.2003.04.002.

[17] Zurigat YH, Ghajar AJ, Moretti EM. Stratified thermal storage tank inlet mixing characterization 1988;30:99–111.

[18] Chung JD, Cho SH, Tae CS, Yoo H. The effect of diffuser configuration on thermal stratification in a rectangular storage tank. Renewable Energy 2008;33:2236–45. https://doi.org/10.1016/j.renene.2007.12.013.

[19] Yee CK, Lai FC. Effects of a porous manfold on thermal stratification in a liquid storage tank. Solar Energy 2001;71:241–54. https://doi.org/10.1016/S0038-092X(01)00043-3.

[20] Andersen E, Furbo S, Fan J. Multilayer fabric stratification pipes for solar tanks. Solar Energy 2007;81:1219–26. https://doi.org/10.1016/j.solener.2007.01.008.

[21] Shah LJ, Andersen E, Furbo S. Theoretical and experimental investigations of inlet stratifiers for solar storage tanks. Applied Thermal Engineering 2005;25:2086–99. https://doi.org/10.1016/j.applthermaleng.2005.01.011.

[22] Findeisen F, Urbaneck T, Platzer B. Radial diffusers in stratified hot water stores: Ecomtry optimization with CFD. ISES Solar World Congress 2017 2017:726–34. https://doi.org/10.18086/swc.2017.13.04.

[23] Findeisen F, Urbaneck T, Platzer B. Radial Diffusers – Simulation of Three-Dimensional Flow Effects with CFD (Part 1). Chemie-Ingenieur-Technik 2018;90:956–68. https://doi.org/10.1002/cite.201700023.

[24] Findeisen F, Urbaneck T, Platzer B. Radial Diffusers - Simulation of Three-Dimensional Flow Effects with CFD (Part 2). Chemie-Ingenieur-Technik 2018;90:1065–72. https://doi.org/10.1002/cite.201700126.

[25] Findeisen F, Urbaneck T, Platzer B. Radial Diffusers – Simulation of Three-Dimensional Flow Effects with CFD (Part 3). Chemie-Ingenieur-Technik 2018;90:969–78. https://doi.org/10.1002/cite.201700070.

[26] Findeisen F, Ullrich K, Thorsten Urbaneck, Bernd Platzer. Radial diffusers in stratified hot water stores simulation of three dimensional flow behavior with CFD.

[27] Nizami DJ, Lightstone MF, Harrison SJ, Cruickshank CA. Negative buoyant plume model for solar domestic hot water tank systems incorporating a vertical inlet. Solar Energy 2013;87:53–63. https://doi.org/10.1016/j.solener.2012.10.001.

[28] Oppel FJ, Ghajar, AJ, Moretti, PM. A numerical and experimental study of stratified thermal storage. Ashrae Transactions 1986; 92: 293-309.

[29] Zurigat YH. Turbulent mixing correclations for a thermocline thermal storage tank. Heat Transfer 1988.

[30] Al-Najem NM, El-Refaee MM. A numerical study for the prediction of turbulent mixing factor in thermal storage tanks. Applied Thermal Engineering 1997;17:1173–81. https://doi.org/10.1016/s1359-4311(97)00030-6.

[31] Nelson JEB, Balakrishnan AR, Srinivasa Murthy S. Experiments on stratified chilled-

water tanks. International Journal of Refrigeration 1999;22:216–34. https://doi.org/10.1016/S0140-7007(98)00055-3.

[32] Karim A, Burnett A, Fawzia S. Investigation of stratified thermal storage tank performance for heating and cooling applications. Energies 2018;11. https://doi.org/10.3390/en11051049.

[33] Jordan U, Furbo S. Thermal stratification in small solar domestic storage tanks caused by draw-offs. Solar Energy 2005;78:291–300. https://doi.org/10.1016/j.solener.2004.09.011.

[34] Baeten B, Confrey T, Pecceu S, Rogiers F, Helsen L. A validated model for mixing and buoyancy in stratified hot water storage tanks for use in building energy simulations. Applied Energy 2016;172:217–29. https://doi.org/10.1016/j.apenergy.2016.03.118.

[35] Davidson JH, Adams DA, Miller JA. A coefficient to characterize mixing in solar water storage tanks. Journal of Solar Energy Engineering 1994;116:94–9. https://doi.org/10.1115/1.2930504.

[36] Winterscheid C. Dronninglund District Heating Monitaring Data Evaluation for the Years 2015-2017 2017.

[37] Gauthier G. Benchmarking and improving models of subsurface heat storage dynamics, comparison of Danish PTES and BTES installation measurements with their corresponding TRNSYS models. 2020. https://www.heatstore.eu/documents/HEATSTORE_WP2_D2.3-Danish%20PTES%20and%20BTES%20installations_Final_2020.11.02.pdf.

[38] Sørensen A, Schmidt T. Design and construction of large scale heat storages for district heating in Denmark. 14th International Conference on Energy Storage 2018, Turkey.

[39] Novo A V., Bayon JR, Castro-Fresno D, Rodriguez-Hernandez J. Review of seasonal heat storage in large basins: Water tanks and gravel-water pits. Applied Energy 2010;87:390–7. https://doi.org/10.1016/j.apenergy.2009.06.033.

[40] Ochs F, Nußbicker J, Marx R, Koch H, Heidemann W, Müller-Steinhagen H. Solar assisted district heating system with seasonal thermal energy storage in Eggenstein-Leopoldshafen. Conference Proceedings 2008.

[41] Chang C, Leng G, Li C, Nie B, She X, Peng X, et al. Investigation on transient cooling process in a water heat storage tank with inclined sidewalls. Energy Procedia 2017;142:142–7. https://doi.org/10.1016/j.egypro.2017.12.023.

[42] Osman K, Al Khaireed SMN, Ariffin MK, Senawi MY. Dynamic modeling of stratification for chilled water storage tank. Energy Conversion and Management 2008;49:3270–3. https://doi.org/10.1016/j.enconman.2007.09.035.

[43] Chandra YP, Matuska T. Stratification analysis of domestic hot water storage tanks: A comprehensive review. Energy and Buildings 2019;187:110–31. https://doi.org/10.1016/j.enbuild.2019.01.052.

[44] Lou W, Luo L, Hua Y, Fan Y, Du Z. A review on the performance indicators and influencing factors for the thermocline thermal energy storage systems. Energies 2021;14:1–19. https://doi.org/10.3390/en14248384.

[45] Song J, Bahnfleth WP, Cimbala JM. Parametric study of single-pipe diffusers in

stratified chilled water storage tanks (RP-1185). HVAC and R Research 2004;10:345–65. https://doi.org/10.1080/10789669.2004.10391108.

[46] Xiang Y, Gao M, Furbo S, Wang D, Tian Z, Fan J. Heat transfer of a large-scale water pit heat storage under transient operations. Journal of Energy Storage 2022;55:105455. https://doi.org/10.1016/j.est.2022.105455.

[47] Xu C, Liu M, Jiao S, Tang H, Yan J. Experimental study and analytical modeling on the thermocline hot water storage tank with radial plate-type diffuser. International Journal of Heat and Mass Transfer 2022;186. https://doi.org/10.1016/j.ijheatmasstransfer.2021.122478.

[48] Rendall J, Abu-Heiba A, Gluesenkamp K, Nawaz K, Worek W, Elatar A. Nondimensional convection numbers modeling thermally stratified storage tanks: Richardson's number and hot-water tanks. Renewable and Sustainable Energy Reviews 2021;150:111471. https://doi.org/10.1016/j.rser.2021.111471.

[49] Turner JS. Jets and plumes with negative or reversing buoyancy. Journal of Fluid Mechanics 1966;26:779–92. https://doi.org/10.1017/S0022112066001526.

[50] Turner JS. Turbulent entrainment the development of the entrainment assumption, and its application to geophysical flows. Journal of Fluid Mechanics 1986;173:431–71.

[51] Middleton JH. The asymptotic behaviour of a starting plume. Journal of Fluid Mechanics 1975;72:753–71. https://doi.org/10.1017/S0022112075003266.

Yutong Xiang. (2023). Assessment of interaction between underground pit thermal energy storage and surrounding soil under transient conditions, *[Done preparation]*

Assessment of interaction between underground pit thermal energy storage and surrounding soil under transient conditions

Yutong Xiang

Done preparation.

Abstract

Large-scale pit thermal energy storage (PTES) systems are often considered vital components in district heating systems. Due to their significant size, these systems are commonly constructed underground. Therefore, the interaction between the water and soil regions will be essential for PTES performance. A three-dimensional PTES model based on Dronninglund PTES was developed in this paper. The model enables long-term simulation with reasonable computational time and has validated the measurements from Dronninglund PTES, showing good agreement. The relative deviations of annual charge/discharge energy, internal energy content, and total heat loss between the model and measurements were 0.5%, 0.9%, 4.2%, and 4.7, respectively. A comparative study was conducted across different scenarios by altering the initial soil temperature distribution and PTES geometry. The results demonstrated that heat loss has a significant impact on PTES performance. An increase of approximately 43% in heat loss could lead to a reduction in storage efficiency of around 3.7%. The overall heat transfer coefficient for most of the height along the PTES sidewalls fluctuates from -20 to -30 W/m^2·K. However, an overall heat transfer coefficient can reach a maximum value of -250 W/m^2·K when an "invert thermocline" occurs in the PTES top layers. The findings presented in this paper provide valuable insights for researchers and developers, offering a three-dimensional perspective on PTES characteristics under dynamic operation.

Keywords: *pit thermal energy storage, three-dimensional, CFD, soil temperature distribution, overall heat transfer coefficient*

Nomenclature

Latin characters

ATES	Aquifer thermal energy storage, [-]	in	Inlet flow
BTES	Borehole thermal energy storage, [-]	j	Number of layers inside PTES
CFD	Computational fluid dynamic, [-]	loss	Heat loss
C_p	Specific heat, [J/kg·K]	max	Maximum
g	Gravitational acceleration, [m/s^2]	meas	Measured
N_{cycle}	Storage cycle, [-]	min	Minimum
PTES	Pit thermal energy storage, [-]	out	Oulet flow

Q	Heat energy, [J]	top	PTES top
STES	Seasonal thermal energy storage, [-]	side	PTES side
T	Temperature, [°C]	simu	Simulated
TTES	Tank thermal energy storage, [-]	st	Storage
t	Time, [s]	start	Start time of operation
V	Volume flow rate, [m^3/s]		
		Greek	
Subscripts		ρ	Density, [kg/m3]
bottom	PTES bottom	μ	Dynamic viscosity, [kg/m·s]
capa	*Capacity*	λ	Thermal conductivity, [W/m·K]
char/dischar	Charge/discharge	Δ	Difference, [-]
end	End time of operation	η	Storage efficiency, [-]

1. Introduction

Seasonal thermal energy storage (STES) is emerging a crucial technology in the energy transition and decarbonization scenarios due to its capability to address both short-term and long-term energy demand and supply gaps [1,2]. Previous research has demonstrated that the application of STES has the potential to improve system safety [3], flexibility, and efficiency [4,5]. The most common categories of STES types are the following [6–10]: 1) aquifer thermal energy storage (ATES), 2) borehole thermal energy storage (BTES), 3) tank thermal energy storage (TTES), and 4) pit thermal energy storage (PTES). Regarding these four types of STES, TTES and PTES are widely known for being able to achieve high charging/discharging energy rates. In addition, the construction of TTES and PTES is less geographically demanding. Furthermore, PTES can be built on an unlimited size scale. Therefore, PTES technology has drawn an increasing amount of attention.

Recently, the volume of PTES has been rising for three reasons: 1) accomplish the long-term storage purposes; 2) lower investment cost per m^3 water equivalent when taking the same construction boundary conditions into account [11–13]; 3) improve the potential to integrate a significant amount of renewable resources [14]. Because of the considerable potential for space availability and the minimal impact from surrounding environment, most large-scale PTES are advantageously built completely or partly underground [15]. However, the large interface area between the PTES and the surrounding soil makes it crucial to identify the suitable construction sites, which creates new difficulties to the design and implementation of large-scale PTES. The site selection is dependent upon a variety of factors, such as geo-mechanical properties, hydrogeological characteristics, and thermo-physical properties [16]. The soil should be easy to excavate, otherwise, special excavation techniques may be required, resulting in a dramatic

increase in investment costs. [14]. Additionally, to ensure the stability to support large PTES volume, the design of PTES geometry should be based on the soil mechanical properties. Another main concern is the impact of soil characteristics on heat losses through the interfaces between PTES and surrounding soil, which will ultimately affect the technical performance of the solar district heating system, particularly on the storage and system efficiency. On a bright note, when the PTES is discharged in actual operation, the surrounding soil can also serve as a heat reservoir and transfer heat back to it [17]. In this case, it is anticipated that the significance of soil thermal properties will decline when implementing PTES [18]. Therefore, in addition to the on-site geological assessment, concerns may exist over how PTES actually interacts with the surrounding soil.

TRNSYS is a common modeling platform most widely used to study the effects of soil thermal properties on PTES performance because of its time-efficiency for long-term simulation. Xie et al. [19] performed a six-year simulation to examine the PTES long-term performance at different values of soil thermal conductivity and thermal capacity. After four years, it was found a thermal balance between PTES and surrounding had been achieved. Their study concluded that thermal conductivity had a greater impact than thermal capacity, with lower thermal conductivity resulting in higher storage efficiency. In an attempt to consider both temporal and spatial scales, Gao et al [20] applied relative Fourier number to depict the influence of soil thermal properties on PTES performance. The comparison results showed that as the relative Fourier number increased, the charging energy increased, while the discharging energy and storage cycle decreased. Although the models implemented on TRNSYS platform can quickly estimate the soil thermal properties on PTES system performance, the soil part can only be assumed isotropic. This means that real-world conditions with anisotropy soil properties cannot be considered. Additionally, the heat transfer coefficient between PTES and the surrounding soil depends not only on soil properties but also on natural convection near the sidewall caused by PTES temperature gradient. The empirical method for calculating heat transfer coefficients, however, is obtained in an isothermal environment in the studies that have already been done. As a result, as demonstrated by Xiang et al [17], this may result in significant deviations in heat loss calculations.

Furthermore, real-world conditions can include the existence of groundwater, which was frequently overlooked and assumed negligible in previous investigations. A one-dimensional or two-dimensional model cannot effectively represent the three-dimensional phenomena of groundwater. Thus, adding groundwater will increase the complexity of the TRNSYS models.

Recently, Dahash et al. [15] developed a model in COMSOL that enabled investigations of groundwater flow conditions. The outcomes of their investigations indicated that there was a noticeably higher heat loss from PTES when changing favorable geological conditions (i.e., no groundwater) to unfavorable geological conditions (i.e., groundwater flow). This study, however, lacked quantification of the degree of influence of different geological conditions on heat loss, regarding characteristic parameters such as soil thermal properties and PTES temperature gradients. Additionally, it is challenging to incorporate the model developed in COMSOL into system simulation.

Typically, the models used in previous simulation assumed that the soil was a homogeneous medium, meaning that its thermal conductivity and volumetric heat capacity were fixed constants across the soil region. However, the geological composition of different horizontal positions is essentially the same, while their considerable differences along varying vertical depth.

As mentioned above, there has been limited research on the influence of different soil conditions on PTES performance. To address this knowledge gap, this study develops a three-dimensional model to examine the interaction between PTES and surrounding soil thoroughly. A cross-comparison analysis is performed, considering variations in soil temperature distribution and PTES geometry, to evaluate their effect on PTES performance. The remainder of this paper is organized as follows: Section 2 provides a detailed description of the Dronninglund PTES system. Section 3 outlines the numerical approach. Section 4 presents and discusses the results, and Section 5 concludes this study and provides final remarks.

2. Experimental study

2.1 The Dronninglund PTES system

The PTES system studied is a 60000 m^3 located in Dronninglund, Denmark (57.16N, 10.29E) [21]. This system is considered one of the most successful PTES implementations in large-scale solar district heating plants [22]. Fig.1 depicts the Dronninglund PTES with its detailed dimensions. The Dronninglund PTES is a truncated pyramid stump, featuring a depth of 16 m and a sidewall inclination angle of 26.6º. The top surface measures 90 m × 90 m, while the bottom measures 26 m × 26 m [23,24]. To minimize heat loss, an insulated cover is installed on the top of the PTES. A 2.5 mm thick Geomembrane layer is incorporated on the side and bottom walls to prevent water infiltration into the surrounding soil [25].

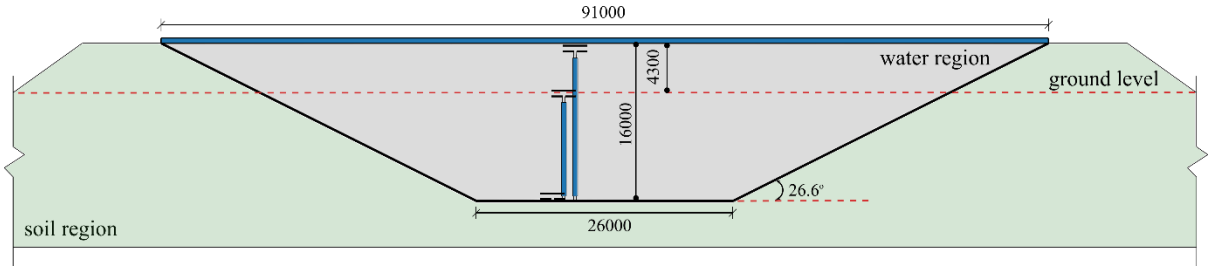

Fig.1 Illustration of Dronninglund PTES dimensions.

The primary measurements of the Dronninglund PTES system encompass PTES temperature distribution, soil temperature, ambient air temperature, inlet/outlet temperature, and inlet/outlet volume flowrate. These parameters are recorded with a time interval of 10 minutes [26].

Fig.2 provides a detailed illustration of the locations of temperature sensors within the water and soil regions. For the PTES performance assessment, 32 temperature sensors are evenly distributed throughout the PTES, spanning from the bottom to the top [27]. To monitor changes in soil temperature, four temperature sensors are inserted into the ground at depths of 10 m, 15 m, 20 m, and 25 m [27]. Additionally, temperature sensors and flow meters are installed in the inlet/outlet pipes in the technical room to measure the heat flow. The temperature sensors are Class A PT100, with an accuracy of ±0.15 K [28]. The flow meters are electromagnetic flow meters, offering an accuracy of ±0.4% [29].

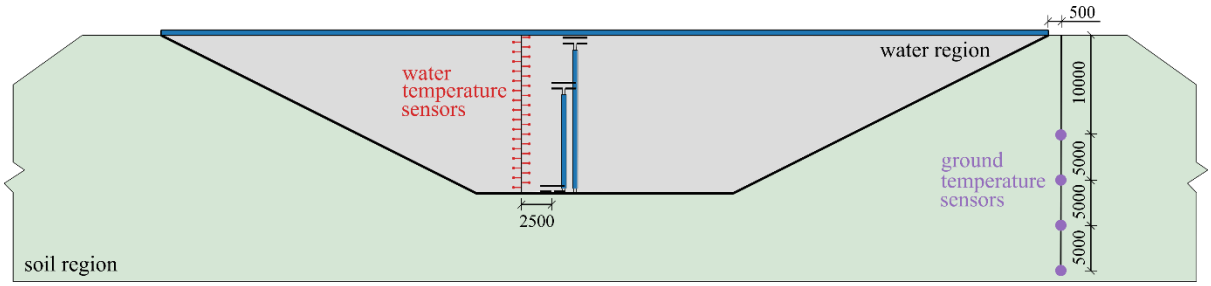

Fig.2 Placement of temperature monitoring sensors.

2.2 Geological exploration

A comprehensive study of the on-site soil properties is essential to accurately estimate the heat transfer between the PTES and surrounding soil. Fig.3 illustrates the vertical geological layers of heterogeneous soil based on the geological evaluation conducted at the Dronninglund project [30]. The upper layer consists mainly of medium-grained dry sand, extending to a depth of approximately 5 m. Below this, a mixture of fine sand, silt, and clay is present, ranging from 5 m to 10 m. From 10 m to 15 m, the soil becomes heavily silted. Beyond a depth of 15 m, the sand becomes medium-grained with less silt content. It is worth noting that from 5 m to 15 m depth, all the soil compositions exhibit a water content of around 25%. Moreover, it has been

reported that there is a small horizontal groundwater flow in part V, although with a relatively modest flow gradient.

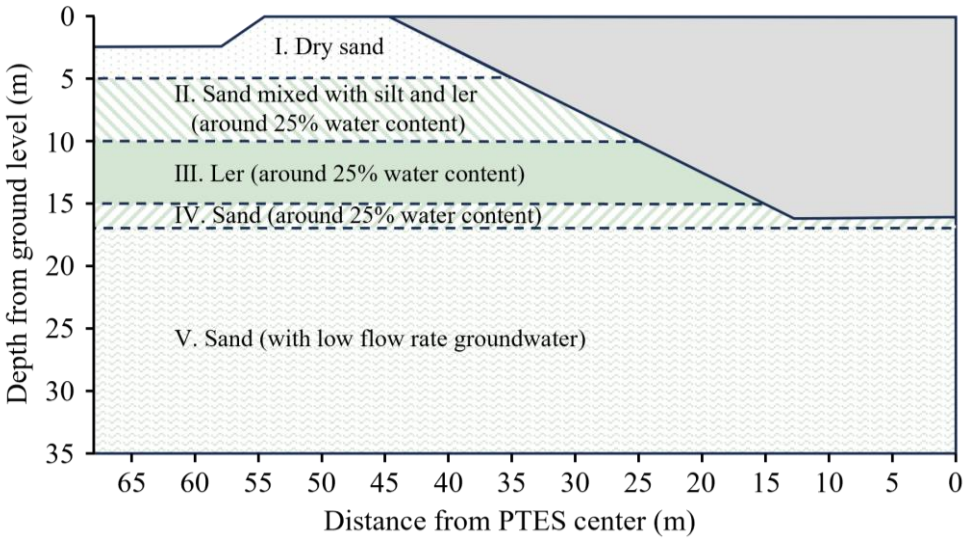

Fig. 3 Section schematic of vertical geological layers of heterogeneous soil [23]

Table 1 presents the soil properties at different depths in the Dronninglund site. Due to limited available information on the on-site soil properties, reference values from existing literature have been utilized to calibrate the PTES model for this study appropriately. The thermal conductivity was 0.4 W/(m · K), and the density was set at 2000 kg/m^3 for the dry sand based on the geological study [23]. Additional values for saturated sand and clay are obtained from Ref. [31]. It should be noted that the soil below 17 m was simplified without considering groundwater flow for computational efficiency. However, a higher heat transfer coefficient was assigned to account for the increased water content in that region.

Table1 The reference values of average soil thermal properties at different depth.

Depth [m]	Soil compositions	Density [kg/m^3]	Thermal conductivity [W/(m · K)]	Thermal capacity [J/(kg · K)]
0-5	Dry sand	2000	0.4	700
5-10	Sand (25% water content)	1840	1.8	1200
10-15	Clay (25% water content)	2200	1.7	900
15-17	Sand (25% water content)	1840	1.8	1200
Below 17	Sand (with groundwater)	1840	2.3	1200

2.3 Operation of PTES system

The Dronninglund PTES has been in operation since 2014. Fig.4 displays the variation in PTES and soil temperatures at different heights during the long-term operation from 2014 to

2017. The PTES temperature is depicted using a range of colors from red to purple, with each storage layer represented by a different. The solid curves, varying in color from black to light grey, represent the variation in soil temperature at each measuring point. It is important to note that due to hardware failures, only a portion of the measured soil temperature data was successfully recorded [27].

During the long-term operation, the PTES temperature experiences a maximum of 89°C and a minimum of 9°C. The soil temperature at depths of 10 m and 15 m initially shows an upward trend in the first year of operation. However, starting from the second year, the temperature of 10 m fluctuates around 25°C, and the temperature at 15 m fluctuates around 17°C. The soil temperature fluctuation is affected by the PTES temperature variation. In addition, slight differences are observed between years, indicating that the soil temperature variation trend will stabilize over an extended period of operation. Moreover, the soil temperature at depths of 20 m and 25 m does not exhibit significant changes over several years of operation, as the distance from the PTES is considerable.

Notably, there are instances when the temperature inside the PTES is lower than the temperature recorded by the soil temperature measurement at 10 m depth (highlighted with the grey background). During these time period, it is expected that heat may transfer back from the soil to the PTES.

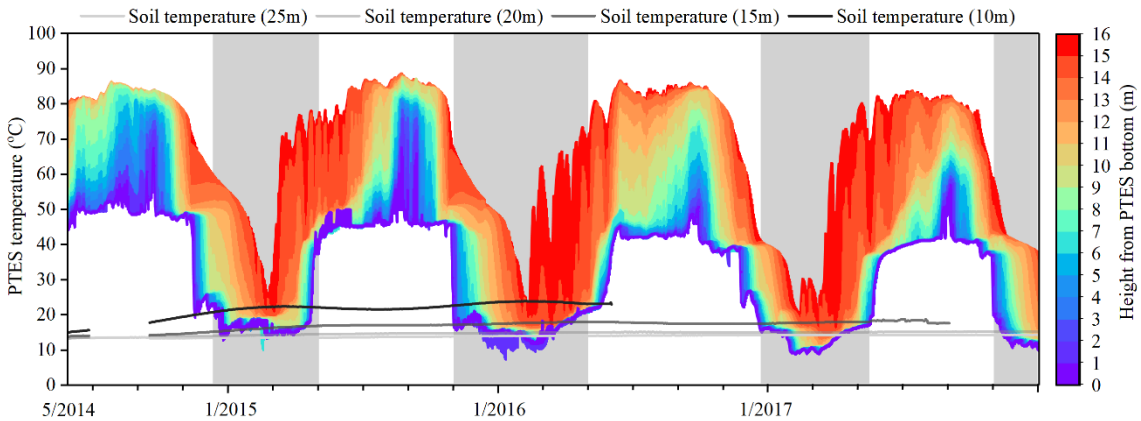

Fig. 4 PTES and soil temperature distribution variation from 2014 to 2017.

3. Numerical approach

3.1 CFD model

A full-scale three-dimensional model was developed in ANSYS R19.2 based on the dimensions of the Dronninglund PTES described in Section 2.1. The model aims to accurately simulate the heat transfer process by simultaneously considering the water and soil regions. To simplify the computational effort, the inlet/outlet diffusers inside PTES were relocated to the

PTES center. As a result, the model was further simplified to a one-quarter model, as shown in Fig.5. To minimize the impact of soil boundaries on changes in soil temperature near the water body, the soil region was created large enough. It is worth mentioning that the groundwater flow was neglected in this model.

In the investigation conducted in [32], a grid density independence study was performed for the complete full-scale model. The results demonstrated the optimal grid size distribution for the water and soil regions used for the Dronninglund PTES investigation, striking a balance between calculation accuracy and time. In this context, the grid size distribution employed in this study was aligned with the settings of the complete full-scale model. Besides, a boundary layer was incorporated at the interface between the water and soil regions to capture the heat transfer characteristics accurately. Fig.5 indicates the mesh used for the CFD simulation in this study, featuring a total cell number of 0.17 million.

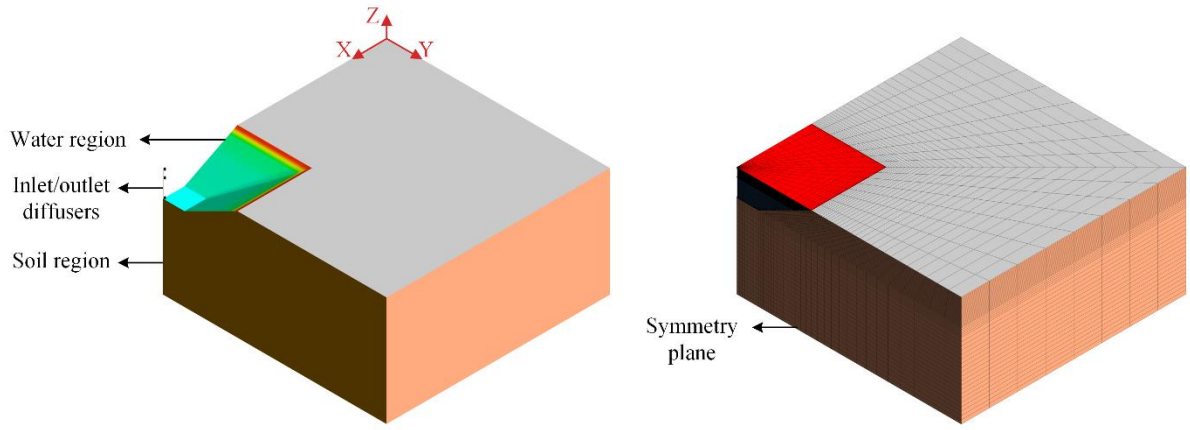

Fig. 5 Three-dimensional CFD model. Left: model diagram; Right: grid scheme.

The water region in the CFD model was treated as an incompressible fluid with temperature-dependent thermophysical properties. These properties can be described using Eq. (1) to (4), where T represents the temperature in Kelvin. The soil region was considered a solid region with different thermal properties depending on the depth based on Table 1.

Density, [kg/m^3] $$\rho = 863 + 1.21 * T - 2.57 * 10^{-3} * T^2 \quad (1)$$

Dynamic viscosity, [kg/m·s]

$$\mu = 9.67 * 10^{-2} - 8.207 * 10^{-4} * T + 2.344 * 10^{-6} * T^2 - 2.244 * 10^{-9} * T^3 \quad (2)$$

Thermal conductivity, [W/m·K] $$\lambda = 3.75 * 10^{-1} + 8.84 * 10^{-4} * T \quad (3)$$

Specific heat, [J/kg·K] $$C_p = 4432.6 - 1.819 * T + 3.3 * 10^{-3} * T^2 \quad (4)$$

The governing equations were solved numerically using the finite volume method. The simulations were performed in three-dimensional and double-precision. The transient nature of

the system was considered, and parallel computations were employed to enhance computational efficiency. A gravitational acceleration (g) of -9.81 m/s^2 in the Z direction was considered to incorporate the effects of gravity The PRESTO method was used for discretizing the pressure, while the second order upwind method was employed for discretizing the energy and momentum equations. The pressure-velocity coupling was treated using the SIMPLE algorithm. Considering that the flow inside PTES system is primarily in the laminar region, the laminar model was utilized to reduce computational time further. Convergence of the CFD calculation was considered achieved when the scaled residuals fell below certain thresholds, set to be less than 10^{-3} for the continuity equations, 10^{-3} for the momentum equations, and 10^{-6} for the energy equation. The calculations were performed using a time step of 2 seconds over an entire year.

3.2 Initial and boundary conditions

In this study, the measurements of the Dronninglund PTES in 2017 were utilized for model validation. According to Fig.6, the maximum PTES temperature recorded in early 2017 is 39.5ºC, while the minimum PTES temperature reaches 16.4ºC. The soil region adjacent to the PTES exhibits temperature changes over an area approximately 20 m away from the side of the PTES top surface and about 30 m below the PTES in the Z direction. Additionally, the soil temperature near the PTES sidewalls ranges between 30 and 40ºC. The soil temperature near the PTES bottom wall ranges from 10 to 20ºC.

In the validation scenario, the PTES temperature distribution starting in 2017 was used as the initial water temperature distribution for the calculation. Simultaneously, the soil temperature distribution starting 2017 was employed as the initial soil temperature. For the comparison analysis, the initial soil temperature was set to a constant value of 8.5ºC, as described in Section 4. It is worth mentioning that a zero-velocity field inside PTES was assumed at the start of all CFD calculations.

Regarding boundary conditions, the top surface of PTES was defined as a convection boundary condition with a heat transfer coefficient of 26.6 W/(m^2·K) [19]. The top surface of the soil region was also assigned a convection boundary condition with a heat transfer coefficient of 25 W/(m^2·K) [33]. The side surface of the soil region was considered an adiabatic boundary condition, and the bottom surface of the soil region was set to have a constant temperature of 8.5ºC. Additionally, the surfaces between the water and soil regions were defined as interfaces. These interfaces allowed calculating heat transfer flux between the water and soil regions in the CFD simulations.

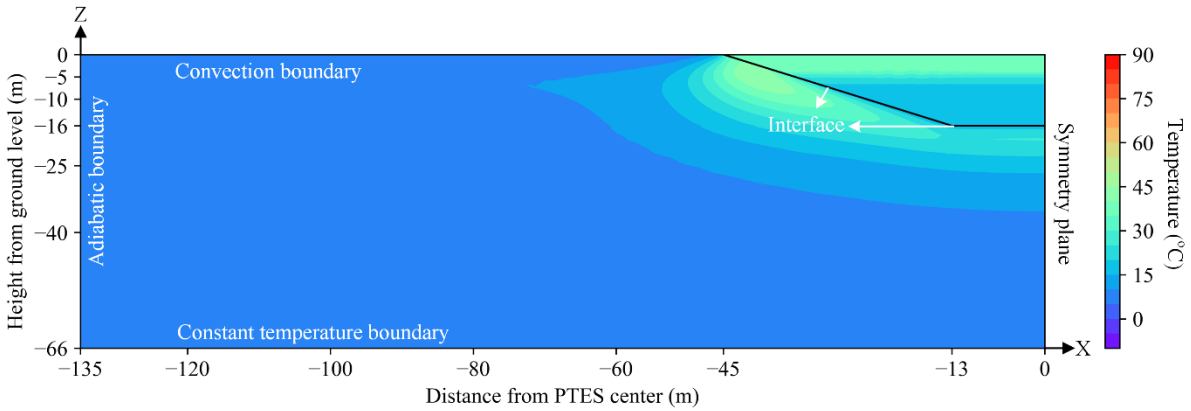

Fig. 6 Illustration of the initial and boundary conditions.

Furthermore, the measured inlet temperature and flow rate for the Dronninglund PTES in 2017 were given as input data for the inlet diffusers in the CFD simulations. The calculation results, including the PTES temperature, soil temperature, charging/discharging conditions, and heat flux between the water and soil regions, were recorded every 10 mins consistent with the measurements.

3.3 Performance assessment

3.3.1 Energy calculation

The calculated thermal performance of Dronninglund PTES was compared to the measured results to assess the calculation accuracy of the CFD model. The charged and discharged energy of the PTES can be derived using Eq. (5) [8], which takes into account factors such as the inlet/outlet temperatures, water density, and heat capacity. The water properties were obtained using the measured inlet/outlet temperature, as described in Eq. (1) and (4).

$$Q_{char/dischar} = \left(\rho_{in} C_{p,in} T_{in} - \rho_{out} C_{p,out} T_{out}\right) \times V_{in} \times \Delta t \tag{5}$$

It is challenging to measure the heat loss from the PTES side and bottom walls directly. Thus, the measured total heat loss of the PTES was calculated by utilizing the energy balance equation, as described in Eq. (6). The $Q_{st,start}$ and $Q_{st,end}$ represent the energy content of the PTES at the start and end of the calculation period. To calculate the energy content of the PTES during a one-year calculation, Eq. (7) was employed.

$$Q_{loss.meas} = \sum Q_{char/dischar.meas} + (Q_{st,start} - Q_{st,end}) \tag{6}$$

$$Q_{st} = C_p \times V_j \times \rho_j \times \sum_1^n (T_j - T_{ref}) \tag{7}$$

In the CFD simulation, the calculated total heat loss can be expressed using Eq. (8). The terms $Q_{loss,top}$, $Q_{loss,side}$, and $Q_{loss,bottom}$ represent the heat loss from the PTES top, side, and bottom walls, respectively. The results of these terms were obtained directly from the CFD simulation.

$$Q_{loss.simu} = Q_{loss,top} + Q_{loss,side} + Q_{loss,bottom} \tag{8}$$

3.3.2 Storage performance

To facilitate the comparison of different storage designs, it is valuable to analyze critical indicators that assess the performance of the PTES during long-term operation. Two commonly used parameters were selected for this purpose. The first indicator is storage efficiency, which is defined by Eq. (9). Storage efficiency provides insights into the effectiveness of the PTES in storing and retrieving thermal energy [34]. The second indicator is the storage cycle, defined as the ratio of the discharge energy to the maximum heat capacity of the PETS, as expressed in Eq. (10). The maximum heat capacity ($Q_{capa.max}$) is calculated using Eq. (11).

$$\eta_{st} = (Q_{dischar} + \Delta Q_{st})/Q_{char} \tag{9}$$

$$N_{cycle} = Q_{dischar}/Q_{capa,max} \tag{10}$$

$$Q_{capa,max} = C_p \times V_{st} \times \rho_{st} \times (T_{st,max} - T_{st,min}) \tag{11}$$

3.4 Investigation scenarios

To gain comprehensive insights into the PTES performance and heat transfer characteristics between the water and soil, three scenarios were proposed in this study. Table 2 provides an overview of the parameters related to these scenarios. In all three scenarios, the dimensions of the PTES, including storage volume, surface areas, and storage height remained unchanged.

In scenarios 2 and 3, the initial soil temperature was set to a uniform value of 8.5°C. Scenario 3 introduced a different geometry, where the PTES has rectangular top and bottom surfaces instead of square top and bottom surfaces. This new geometry is commonly observed in newly developed PTES projects. Apart from the differences specified in the table, the simulation process, boundary conditions, and other settings remain consistent over the three scenarios.

Table2 Parameters for different scenarios.

Parameter	Scenario 1	Scenario 2	Scenario 3
Top dimension [m × m]	90 × 90	90 × 90	127.28 × 63.64
Bottom dimension [m × m]	26 × 26	26 × 26	36.76 × 18.38
PTES height [m]	16	16	16
Slope angle [^{o}]	26.6	26.6	35.3/19.5
Top surface area [m^2]	8100	8100	8100
Bottom surface area [m^2]	676	676	676
Side surface area [m^2]	8300	8300	8484
PTES volume [m^3]	59285	59285	59281
Initial soil temperature [^{o}C]	Temperature distribution starting 2017	8.5	8.5

4. Results and discussion

4.1 Model validation

4.1.1 Overall performance

Table 3 summarizes the comparison between the measured and simulated results. The measured values are rounded, considering the uncertainties associated with the measurements. Table 3 demonstrates a good agreement between the measured and simulated results.

The maximum and minimum PTES temperatures obtained from the CFD simulation exhibit a difference within 1.5 K compared to the measured values. The charge and discharge energy show a deviation within 1% when comparing the measured and simulated values. However, the heat loss shows a deviation larger than 5% when comparing the measured and simulated values. The reasons for this more significant deviation in heat loss are addressed in Section 4.1.4 of the study, where potential factors contributing to this discrepancy are discussed.

Table 3 Thermal performance comparison of the Dronninglund PTES in 2017.

Parameters	Measured	Simulated	Deviation
Maximum PTES temperature (^{o}C)	84.4	85.8	1.4 K
Minimum PTES temperature (^{o}C)	8.7	8.2	0.5 K
Heat capacity (MWh)	5153	5281	2.5%
Charged energy (MWh)	11,565	11,625	0.5%
Discharged energy (MWh)	11,089	11,184	0.9%
Internal energy change (MWh)	-594	-569	4.2%
Heat loss (MWh)	1070	1009	5.7%

Storage efficiency (%)	90.5	91.3	0.7%
Storage cycle	2.1	2.1	0.0%

4.1.2 Temperature

Fig. 7 compares the simulated temperatures and the corresponding measured results at the same measurement positions in the Dronninglund PTES. The solid curve represents the measured results, while the dotted curve represents the calculated results.

The comparison shows that the simulated PTES temperatures agree well with the measured results for heights below 13 m. The temperature difference between the measured and simulated values is within 2 K over the year. However, a noticeable deviation is seen for heights above 13 m, particularly between February and May. This discrepancy can be attributed to two main reasons. Firstly, in the CFD calculation, the monitored temperature points inside the PTES are assumed to be fixed. Yet, there may be an uncertainty of ±0.3 m in the actual position of the temperature sensors [32]. Secondly, there is a considerable temperature difference within a smaller thickness above 14 m inside the PTES. In this situation, having only two measurement points may not accurately reflect the actual temperature distribution over such a small thickness.

For the soil temperature, the discontinuity in the measured soil temperature at 10 m is attributed to a hardware failure in the SCADA system [27]. Regarding the soil temperature at 15 m, 20 m, and 25 m, the maximum differences between the measured and calculated values are 1.8 K, 1.6 K, and 0.8 K, respectively. These differences can be explained by the variations in the soil thermal properties caused by changes in soil moisture content over time.

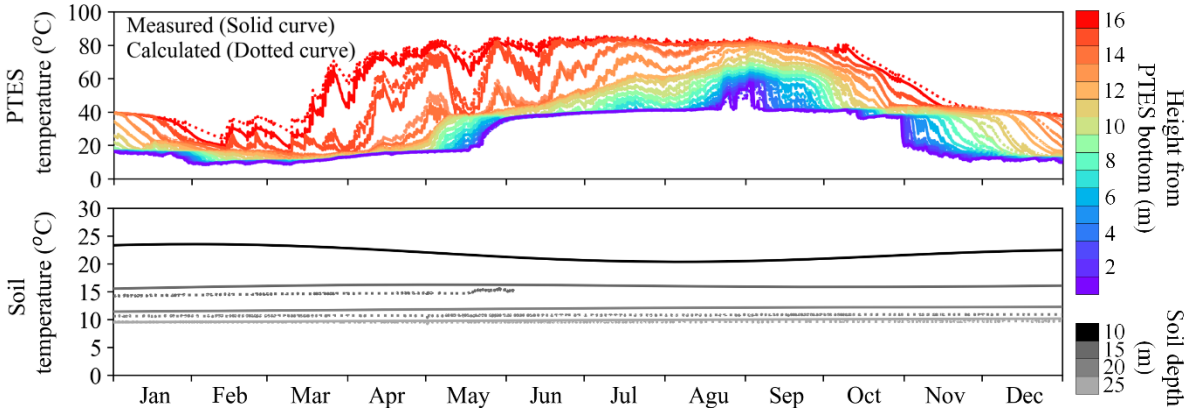

Fig. 7 Measured and calculated PTES temperature and soil temperature in 2017.

4.1.3 Charge and discharge energy

Fig. 8 provides an overview of the monthly variation in charge and discharge energy for Dronninglund PTES, along with the relative deviation ratio between measured and calculated results. The figure indicates that the PTES serves as both long-term and short-term storage, as evidenced by charging and discharging in summer and winter. Notably, the relative deviation between measured and calculated results for the charge/discharge energy remains within 5% for most months. The minor deviations demonstrate the model's capability to predict the energy dynamics within the PTES system accurately.

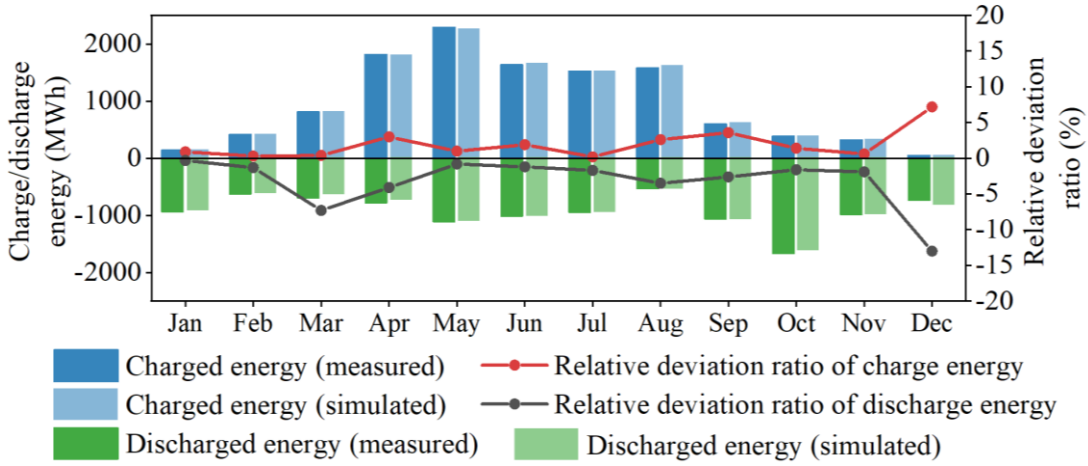

Fig. 8 Measured and calculated monthly charge/discharge energy in 2017.

4.1.4 Heat loss

Fig.9 presents a comparison between the measured and simulated heat loss of the Dronninglund PTES. The measured total heat loss was calculated using Eq. (6). The simulated total heat loss was obtained based on Eq. (8). In the figure, positive values indicate that the water region transfers heat to the surroundings, while negative values indicate that the surroundings transfer heat back to the water region.

It is evident that the top heat loss shows a slight variation over months due to the effective insulated cover. The side heat loss accounts for the largest proportion from April to September. During this period, the primary heat transfer process involves heat transfer from the water to the soil region. However, starting from October, the heat stored in the soil region begins to transmit back to the water region through the side and bottom walls. The heat transfer process is attributed to the differences between PTES and soil temperature over the year.

Notably, the simulated total heat loss variation trend aligns with the measured total heat loss variation trend. There are slight differences between simulated and measured results for certain months, such as February, March, Auguste, and September. However, from April to July, the simulated heat loss is higher than the measured results, while from October to January, the

simulated heat loss is lower than the measured results. This disparity can be attributed to the variations in soil moisture content caused by precipitation. From October to January, heavy precipitation may have increased the soil moisture content, increasing the heat transfer coefficient of the soil. Conversely, the lower simulated heat loss from April to July may be related to reduced rainfall and drier soil conditions. Nevertheless, the CFD model did not consider the time-dependent variation of the heat transfer coefficient over a year.

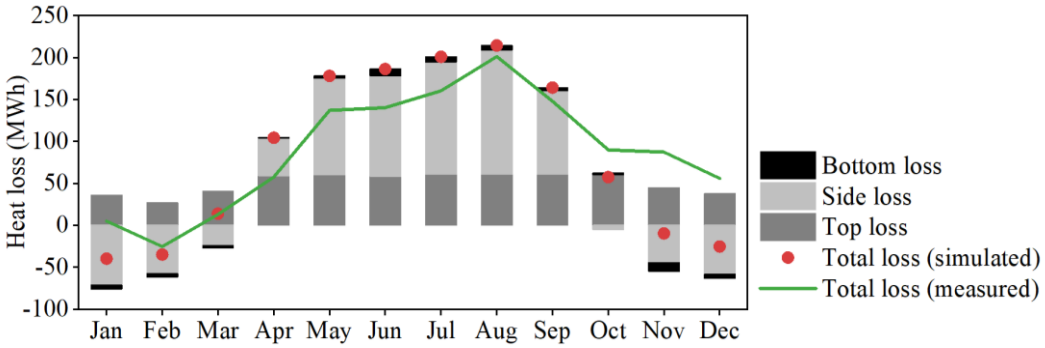

Fig. 9 Comparison of monthly calculated and measured heat loss.

Overall, the comparison between the measured and simulated results indicates a generally good agreement, with minor differences observed for certain parameters. Therefore, the CFD model can be used effectively to investigate the long-term performance of PTES with acceptable computational time and accuracy.

4.2 PTES performance

Fig.10 compares monthly heat loss in different scenarios. Notably, the most significant discrepancies are observed in the side heat loss. During the initial three months, scenarios 2 and 3 exhibit PTES temperature exceeding the soil temperature, as both scenarios start operating with a uniform initial soil temperature of 8.5°C. In this case, heat is lost from water to the surrounding soil. From April to May, there is a notable increase in heat losses in scenarios 2 and 3 compared to scenario 1. This discrepancy can be attributed to the fact that the temperature distribution within the soil has not yet been established in scenarios 2 and 3, whereas scenario 1 establishes a stable soil temperature distribution. Additionally, scenario 3 demonstrates slightly increased side heat loss to scenario 2 due to its larger side area. In November, both scenario 2 and scenario 3 accumulate more heat from the soil than scenario 1 since the heat near the water region has not had sufficient time to propagate deeper into the soil.

The results indicate that at the beginning of the operation, the proportion of side heat loss constitutes approximately 60% of the total heat loss. However, as the soil temperature distribution gradually stabilizes, the side heat loss decreases to approximately 40% of the total

heat loss. This finding suggests that the side heat loss plays a significant role in the initial stages, but its relative contribution diminishes as the soil temperature distribution reaches a stable state.

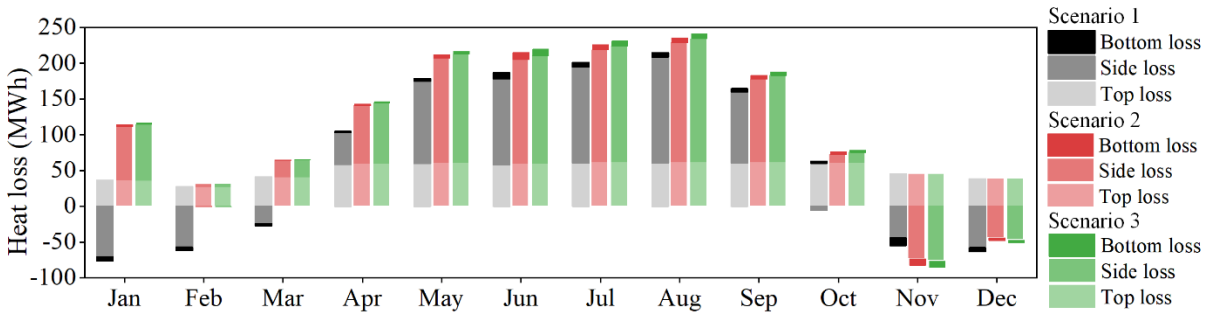

Fig. 10 Monthly heat loss comparison under different scenarios.

Table 4 provides an overview of PTES thermal performance under different scenarios. It reveals that these three scenarios achieve similar PTES temperature levels. However, scenarios 2 and 3 experience approximately 43% more heat loss compared to scenario 1, which leads to a reduction in storage efficiency by approximately 3.7%.

Table 4 Thermal performance comparison under different scenarios in 2017.

Parameters	Scenario1	Scenario2	Scenario3
Maximum PTES temperature (°C)	85.8	85.8	85.8
Minimum PTES temperature (°C)	8.2	8.6	8.6
Heat capacity (MWh)	5281	5253	5253
Charged energy (MWh)	11,625	11,770	11,768
Discharged energy (MWh)	11,184	10,873	10,873
Internal energy change (MWh)	-564	-550	-584
Thermal loss (MWh)	1005	1448	1479
Storage cycle	2.12	2.07	2.07
Storage efficiency (%)	91.4	87.7	87.4

4.3 Soil temperature distribution

The absence of insulation in the side and bottom walls of underground storage poses a risk of the underground temperature exceeding certain limits set by national or local environmental standards. This failure to maintain the desired underground environment standards can lead to various environmental challenges. Therefore, it is crucial to understand the soil temperature distribution under different scenarios.

Fig.11 depicts the soil temperature distribution for scenarios 1 and 2. The temperature within 1m below the ground is significantly influenced by the outdoor temperature. The soil temperature adjacent to the water region demonstrates variations throughout the year, contingent upon water temperature distribution within the PTES. However, in scenario 1, the

maximum area of soil temperature affected remains relatively consistent throughout the year, specifically at a depth of 20 m below the PTES. This area is approximately 1.5 times the size of the PTES top surface in the radial direction. Conversely, in scenario 2, where the soil temperature stratification is in the early stages of establishment, the range of influence gradually expands over the year.

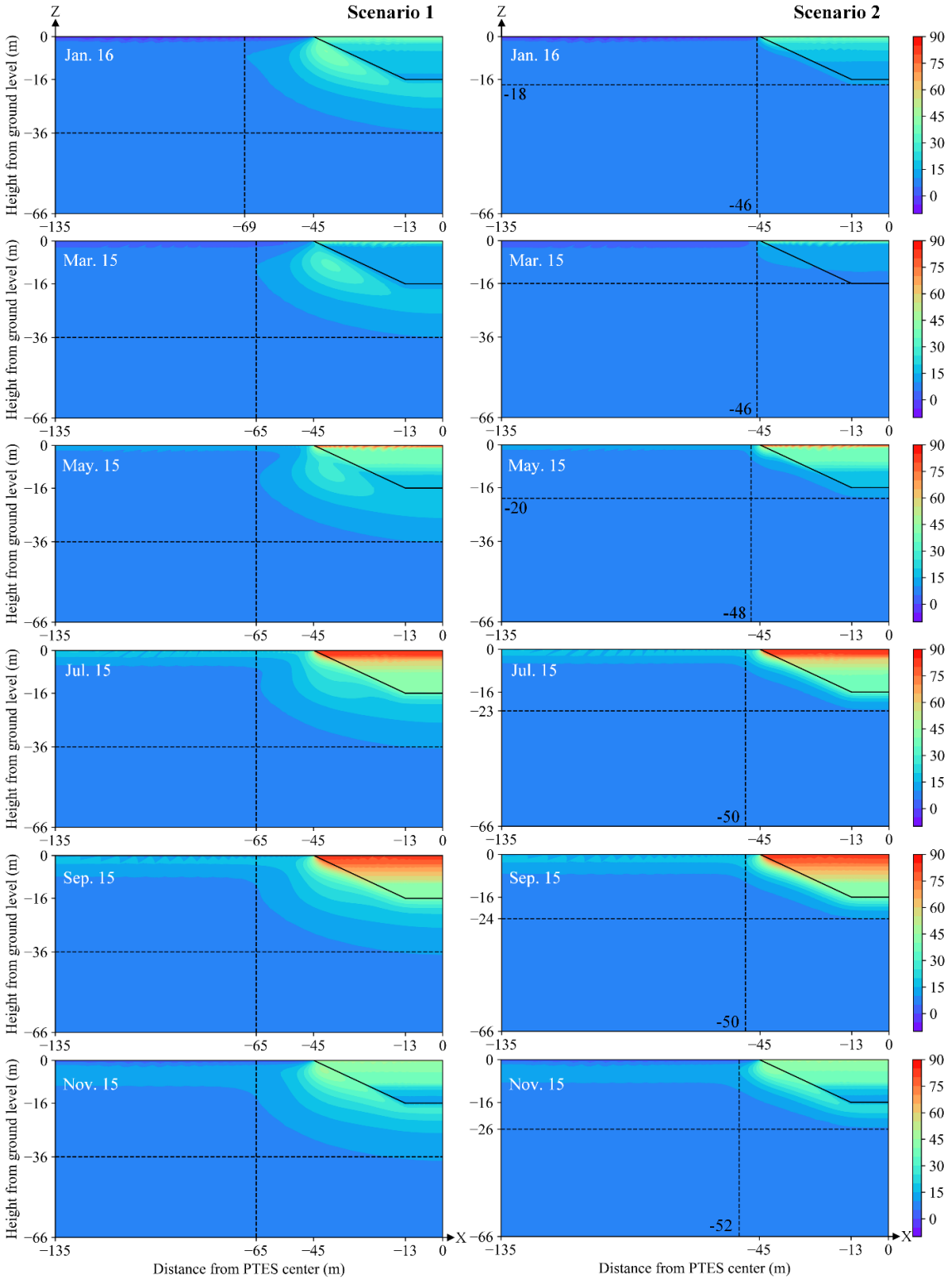

Fig. 11 Temperature distribution for different dates. Left: scenario 1; Right: scenario 2.

Scenario 3 features a non-rotationally symmetric geometry. In this context, Fig. 12 illustrates the temperature distribution of two symmetrical surfaces: the X-Z symmetrical plane on the left and the Y-Z symmetrical plane on the right. The observed soil temperature variation trend in scenario 3 is essentially similar to that of scenario 2. The depth affected ranges from 2 m to 10 m away blow the PTES bottom. In the radial direction, the influence extends from the PTES top surface boundary to approximately 1.2 times the size of the PTES top surface.

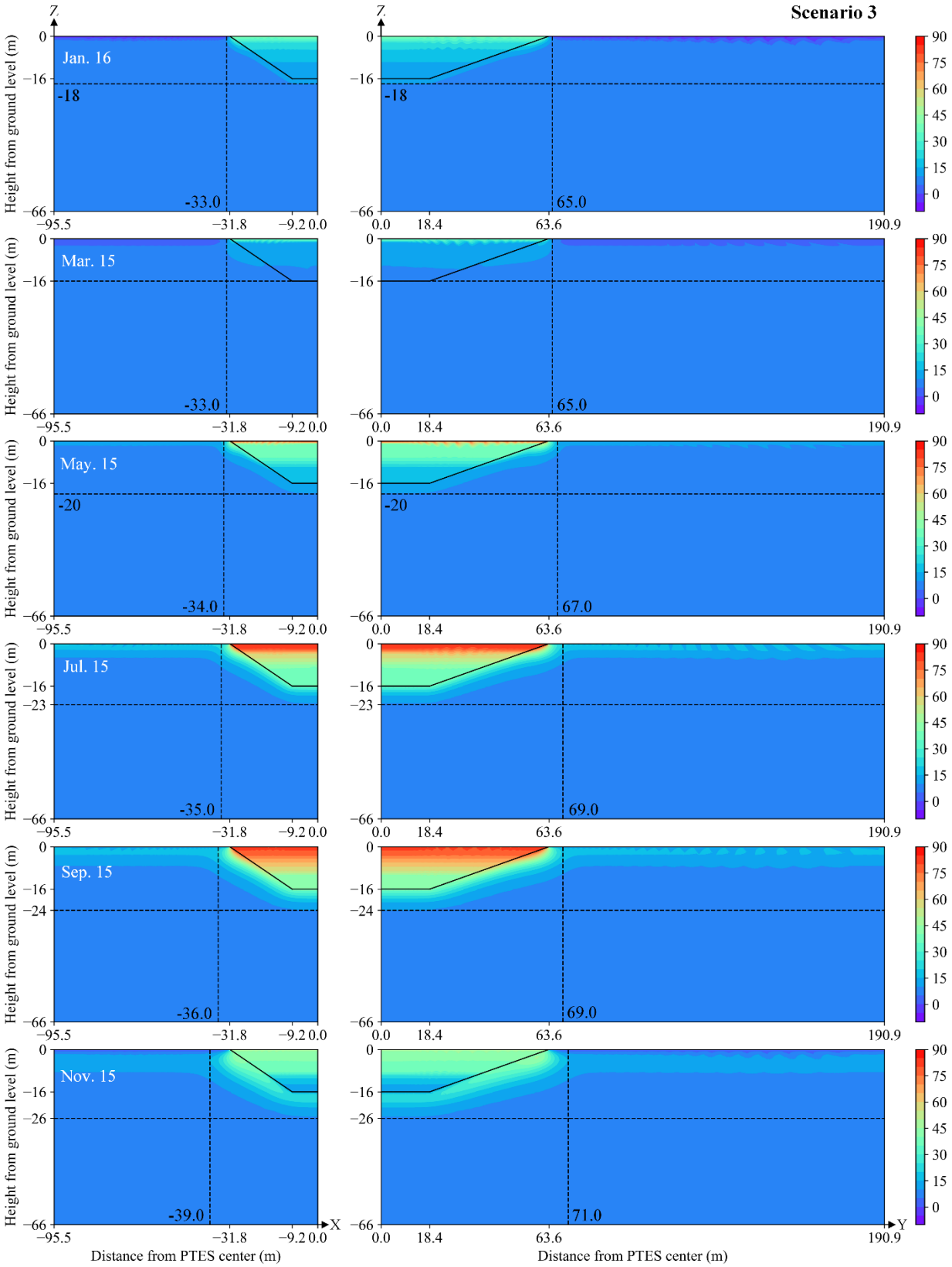

Fig. 12 Temperature distribution for different dates under scenario 3. Left: X-Z plane; Right: Y-Z plane.

4.3 Heat transfer coefficient

Accurately simulating the heat flux through the side walls under dynamic operation requires careful consideration of the overall heat transfer coefficient along these walls. Using a constant parameter along the side walls may lead to an overestimation of heat loss prediction. In this case, this study investigated heat transfer characteristics between the water and soil regions under different scenarios were investigated by analyzing the overall heat transfer coefficient along the side walls.

Fig.13 depicts the overall heat transfer coefficient along the side walls for various representative days throughout the year in scenario 1. In addition, the corresponding water and soil temperatures adjacent to the sidewalls are provided to illustrate the factors influencing sudden changes in the heat transfer coefficient. Negative values of the overall heat transfer coefficient indicate heat transfer from the water body to the soil, while positive values indicate heat gain by the water body from the soil.

Throughout the year, the overall heat transfer coefficient along the side walls typically varies between -20 and -30 $W/m^2 \cdot K$. However, notable fluctuations occur at specific heights. For example, at heights above 15 m, the overall heat transfer coefficient reaches a maximum of around -250 $W/m^2 \cdot$. This phenomenon can be attributed to the presence of an “inverse thermocline”, where the upper layer’s temperature is lower than that of the lower layer. The “inverse thermocline” results from heat losses through the PTES cover. The “inverse thermocline” creates a flow along the side wall, thereby increasing the heat transfer coefficient.

In addition, on June 15, an additional fluctuation in the overall heat transfer coefficient is observed at a height of approximately 12 m inside the PTES. The fluctuation can be attributed to a significant temperature difference between the soil and water. The soil temperature is notably lower than the water temperature, leading to water cooling near the side wall to a lower temperature than the water in the lower layer. As a result, a downward flow is induced along the side wall, thereby increasing the overall heat transfer coefficient.

Moreover, on March 15 and May 15, there is a notable increase in the overall heat transfer coefficient at 14.5 m, indicated by positive values. On these dates, specific locations within the PTES exhibit a significant temperature gradient, coinciding with the soil temperature being higher than the water temperature. This temperature disparity results in the water near the side wall being warmed to a higher temperature than the water in the upper layer. Therefore, disturbances are induced along the side wall, enhancing the overall heat transfer coefficient.

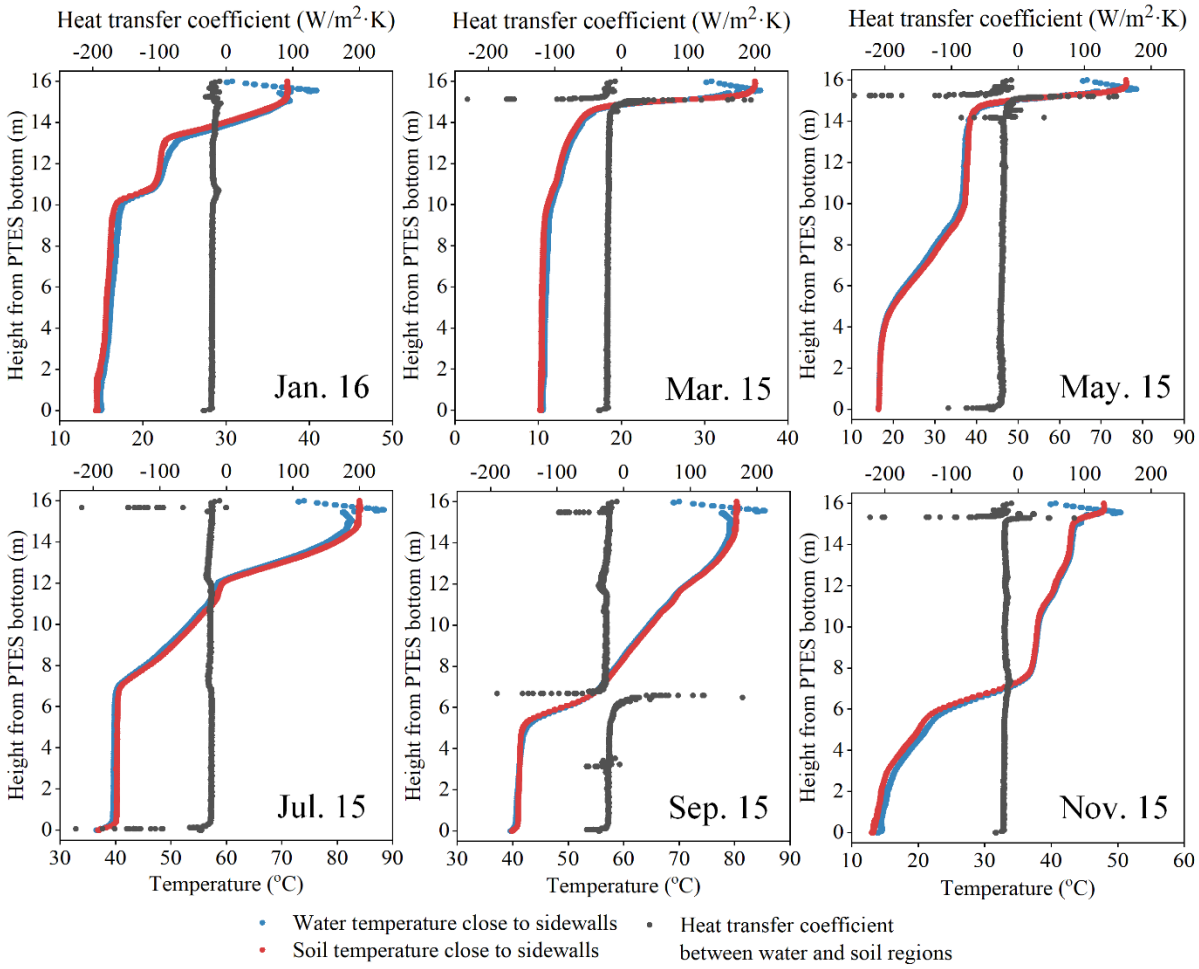

Fig. 13 Overall heat transfer coefficient, water temperature and soil temperatures adjacent to the sidewalls under scenario 1.

Fig.14 shows the overall heat transfer coefficient along the side walls for typical days throughout the year in scenario 2. It is observed that the water and soil temperatures adjacent to the PTES sidewalls follow a similar pattern to that observed in scenario 1. This indicates that the initial soil temperature distribution does not significantly affect the water and soil temperatures along the sidewalls.

Moreover, similar to scenario 1, the overall heat transfer coefficient along most of the height along the PTES sidewalls in scenario 2 also fluctuates within the range of -20 to -30 W/m²·K. However, notable fluctuations are observed on January 15, March 15, and December 15. These fluctuations can be attributed to the soil temperature being in the early establishment stage in scenario 2, leading to an unstable temperature distribution along the PTES sidewalls.

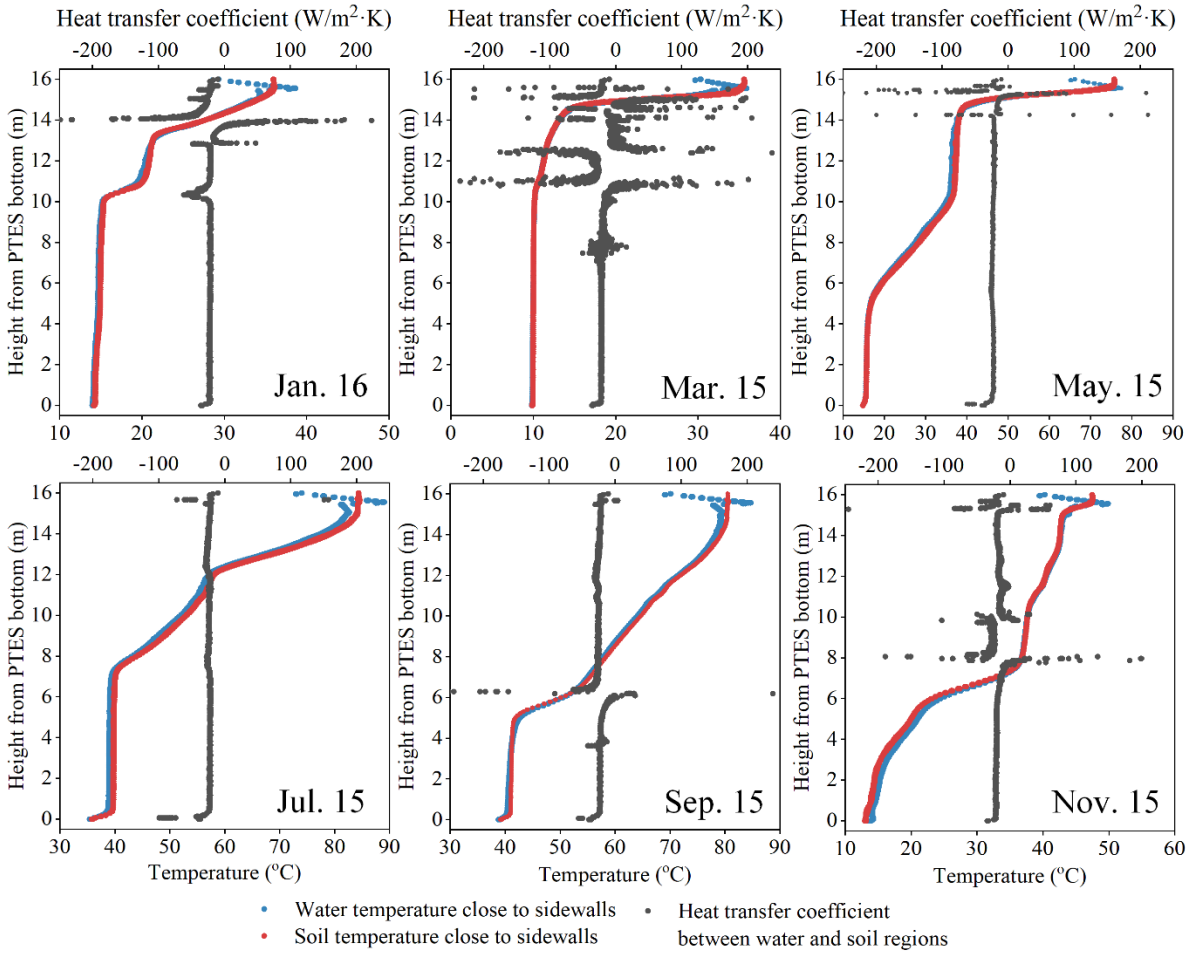

Fig. 14 Overall heat transfer coefficient, water temperature and soil temperatures adjacent to the sidewalls under scenario 2.

Fig.15 indicates the overall heat transfer coefficient along the side walls for typical days throughout the year in scenario 3. Scenario 3 exhibits similar water and soil temperature distribution, as well as overall heat transfer coefficient along the sidewalls, compared to scenario 2. This suggests that changing the PTES geometry has a minor impact on these parameters along the sidewalls.

However, it is worth noting the presence of scatters highlighted by the green curve. These scatters correspond to larger overall heat transfer coefficients compared to the other scatters at the same heights. These scatters were obtained from the X-Z symmetrical plane, while the other scatters were obtained from the Y-Z symmetrical plane. The larger slope angle of the X-Z symmetrical plane contributes to increased downward flow induced by the buoyant force, which is further enhanced by gravity. Consequently, the overall heat transfer coefficient slightly increases in these cases.

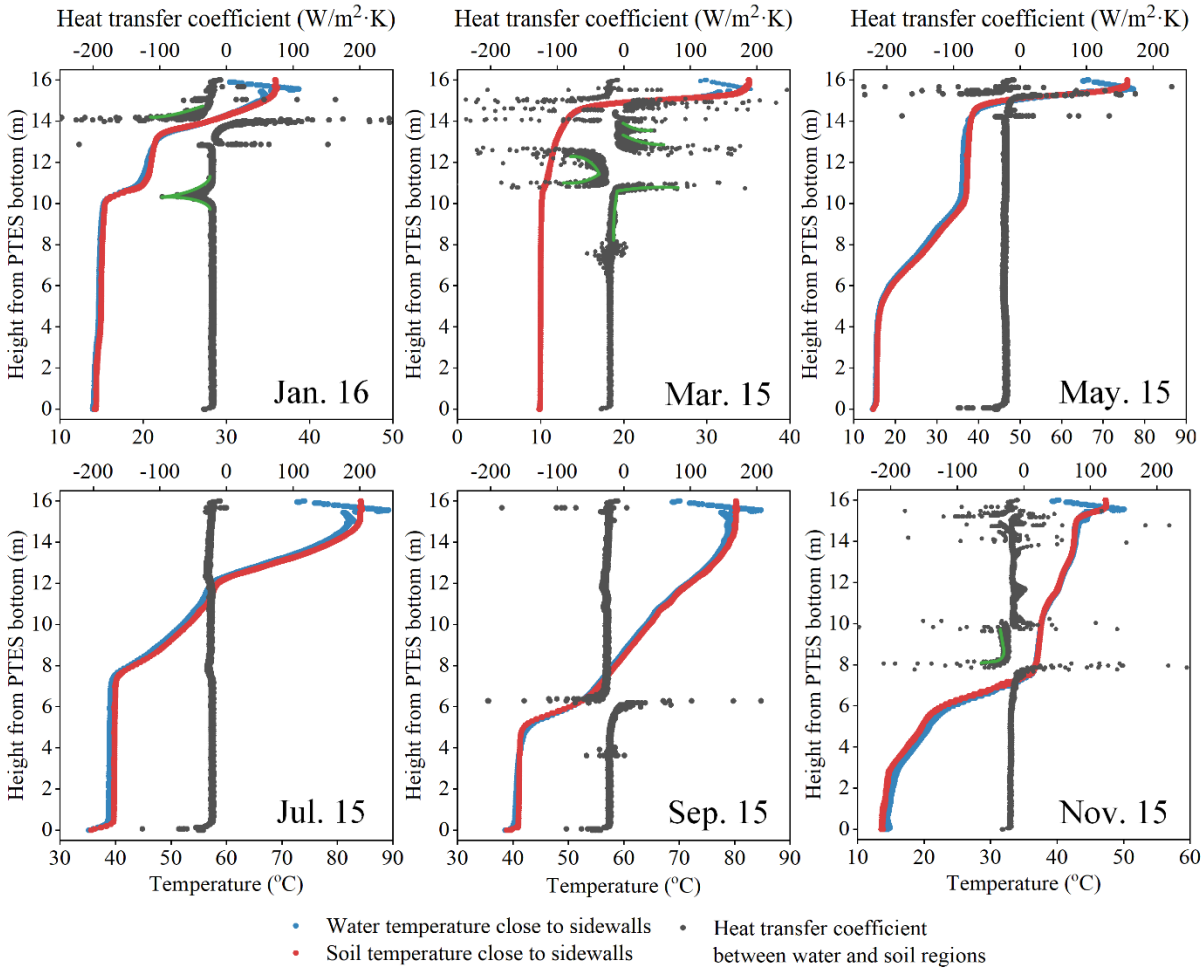

Fig. 14 Overall heat transfer coefficient, water temperature and soil temperatures adjacent to the sidewalls under scenario 3.

5. Conclusion and future directions

Based on the three-dimensional CFD model developed for the Dronninglund SDH plant, this study aimed to analyze the dynamic thermal performance of a large-scale PTES system. The model incorporated both water and soil regions, with particular emphasis on detailed geological conditions within the soil. By conducting a cross-comparison investigation, the study examined the effects of different initial soil temperature distributions and PTES geometries on heat transfer between the water and soil regions. The following conclusions were drawn from the study:

(1) The developed 3D CFD model has demonstrated its capability to accurately predict the long-term thermal performance of large-scale PTES. For 2017, the temperature difference between the measured and simulated values remains within 2 K for most of the heights inside PTES. The relative deviation between the monthly calculated and measured charge and discharge energy is within 5%. The relative deviation between the annual calculated and measured total heat loss is within 6%.

(2) At the beginning of the operation, when the soil has a uniform temperature of 8.5°C, the side heat loss accounts for approximately 60% of the total heat loss in the PTES system. This indicates that a significant portion of the heat loss occurs through the side walls during the initial stages. However, as the system operates and the soil temperature distribution gradually stabilizes over three years, the proportion of side heat loss decreases to approximately 40% of the total heat loss.

(3) Through the conducted comparison investigation across different scenarios, it was observed that an increase of approximately 43% in heat loss could result in a reduction in storage efficiency by around 3.7%. This finding suggests that heat loss has a significant impact on the overall performance and efficiency of the PTES system.

(4) The outdoor temperature greatly influences the soil temperature within 1m below the ground. In the case of the Dronninglund PTES, after three years of operation, the established soil temperature distribution shows that the maximum area of soil temperature influence remains relatively consistent throughout the year, specifically at a depth of 20 meters below the PTES. In addition, this area of influence is approximately 1.5 times the size of the PTES top surface in the radial direction. Conversely, during the early stages of soil temperature stratification, the range of influence gradually expands over the year. The depth affected ranges from 2 m to 10 m below the PTES bottom. In the radial direction, the influence extends from the PTES top surface boundary to approximately 1.2 times the size of the PTES top surface.

(5) The overall heat transfer coefficient along the PTES sidewalls generally ranges from -20 to -30 $W/m^2 \cdot K$ for most of the height. However, special attention should be given to situations where an "invert thermocline" occurs and there are significant temperature differences between the water and soil adjacent to the PTES sidewalls. During an "invert thermocline," the overall heat transfer coefficient along the sidewalls can reach a maximum value of -250 $W/m^2 \cdot K$.

In the past, three-dimensional modeling has been less commonly used due to the computational effort required. However, the model developed in this study successfully achieves a balance between computational efficiency and accuracy. By employing this model, the study provides valuable insights into the influence of various factors on the performance of PTES systems. One significant contribution of this study is the investigation of different soil temperature distributions and PTES geometries and their impact on PTES performance. This analysis helps understand the role of these factors in shaping the thermal behavior of PTES systems. Furthermore, the observed overall heat transfer coefficient along the PTES sidewalls

is a particularly important finding from this study. This information can be used as a valuable reference for developing and improving one-dimensional models.

Groundwater is indeed an important factor that can have a significant impact on the heat transfer processes within a PTES system. Although this study did not consider groundwater to reduce computational effort, investigating its influence on PTES performance using the developed three-dimensional model would be an interesting avenue for future research.

References

[1] Abokersh MH, Vallès M, Cabeza LF, Boer D. A framework for the optimal integration of solar assisted district heating in different urban sized communities: A robust machine learning approach incorporating global sensitivity analysis. Applied Energy 2020;267:114903. https://doi.org/10.1016/j.apenergy.2020.114903.

[2] Tschopp D, Tian Z, Berberich M, Fan J, Perers B, Furbo S. Large-scale solar thermal systems in leading countries: A review and comparative study of Denmark, China, Germany and Austria. Applied Energy 2020;270:1–31. https://doi.org/10.1016/j.apenergy.2020.114997.

[3] McKenna R, Fehrenbach D, Merkel E. The role of seasonal thermal energy storage in increasing renewable heating shares: A techno-economic analysis for a typical residential district. Energy and Buildings 2019;187:38–49. https://doi.org/10.1016/j.enbuild.2019.01.044.

[4] Luc KM, Li R, Xu L, Nielsen TR, Hensen JLM. Energy flexibility potential of a small district connected to a district heating system. Energy and Buildings 2020;225:110074. https://doi.org/10.1016/j.enbuild.2020.110074.

[5] Fridgen G, Keller R, Körner MF, Schöpf M. A holistic view on sector coupling. Energy Policy 2020;147. https://doi.org/10.1016/j.enpol.2020.111913.

[6] Bott C, Dressel I, Bayer P. State-of-technology review of water-based closed seasonal thermal energy storage systems. Renewable and Sustainable Energy Reviews 2019;113:109241. https://doi.org/10.1016/j.rser.2019.06.048.

[7] Ochs F, Dahash A, Tosatto A, Bianchi Janetti M. Techno-economic planning and construction of cost-effective large-scale hot water thermal energy storage for Renewable District heating systems. Renewable Energy 2020;150:1165–77. https://doi.org/10.1016/j.renene.2019.11.017.

[8] Guelpa E, Verda V. Thermal energy storage in district heating and cooling systems: A review. Applied Energy 2019;252:113474. https://doi.org/10.1016/j.apenergy.2019.113474.

[9] Pelay U, Luo L, Fan Y, Stitou D, Rood M. Thermal energy storage systems for concentrated solar power plants. Renewable and Sustainable Energy Reviews 2017;79:82–100. https://doi.org/10.1016/j.rser.2017.03.139.

[10] Sarbu I, Sebarchievici C. A comprehensive review of thermal energy storage. Sustainability 2018;10. https://doi.org/10.3390/su10010191.

[11] Schmidt T, Pauschinger T, Sørensen PA, Snijders A, Djebbar R, Boulter R, et al. Design Aspects for Large-scale Pit and Aquifer Thermal Energy Storage for District Heating and Cooling. Energy Procedia 2018;149:585–94. https://doi.org/10.1016/j.egypro.2018.08.223.

[12] Planenergi. Best practice for implementation and operation of large sale borehole and pit heat thermal storage 2019:1–22. https://www.solar-district-heating.eu/wp-content/uploads/2019/10/Best-practice-Br%C3%A6dstrup-Marstal-Dronninglund-and-Gram-003.pdf

[13] Pfeil M, Koch H. High Performance - Low cost gravel / water storage pit. Solar

Energy 2000;69:461–7.

[14] Matos CR, Carneiro JF, Silva PP. Overview of large-scale underground energy storage technologies for integration of renewable energies and criteria for reservoir identification. Journal of Energy Storage 2019;21:241–58. https://doi.org/10.1016/j.est.2018.11.023.

[15] Dahash A, Ochs F, Giuliani G, Tosatto A. Understanding the interaction between groundwater and large-scale underground hot-water tanks and pits. Sustainable Cities and Society 2021;71:102928. https://doi.org/10.1016/j.scs.2021.102928.

[16] Dahash A, Ochs F. Simulation based design optimization of large scale seasonal thermal energy storage in renewabe based district heating systems 2020. https://doi.org/10.3217/978-3-85125-786-1-12.

[17] Xiang Y, Xie Z, Furbo S, Wang D, Fan J. A comprehensive review on pit thermal energy storage: recent application, design and simulation approaches. Journal of Energy Storage 2022;55:105716. http://doi.org/1016/j.est.2022.105716.

[18] Renaldi R, Friedrich D. Techno-economic analysis of a solar district heating system with seasonal thermal storage in the UK. Applied Energy 2019;236:388–400. https://doi.org/10.1016/j.apenergy.2018.11.030.

[19] Xie Z, Xiang Y, Wang D, Kusyy O, Kong W, Furbo S, et al. Numerical investigations of long-term thermal performance of a large water pit heat storage. Solar Energy 2021;224:808–22. https://doi.org/10.1016/j.solener.2021.06.027.

[20] Gao M. Shao S, Xiang Y, Fan J, Furbo S. Numerical analysis of the long-term performane of a large-scale pit heat storage. (submitted to Engineering)

[21] PlanEnergi, Niras. Dronninglund solar thermal plant. 2014:1–12. https://www.dronninglundfjernvarme.dk/media/2984/brochure_dronninglund_2015_booklet_eng_web_.pdf

[22] Djebbar R, Boulter R, Thomas Schmidt C, , Per Alex Sørensen G, Jeff Thornton D, et al. Large-scale thermal storage for district heating and cooling. 2020.

[23] PlanEnergi. Sunstore 3. Fase 1: Projektering og udbud 2011.

[24] Kallesøe AJ, Vangkilde-Pedersen T. HEATSTORE. Underground Thermal Energy Storage (UTES) – state-of-the-art, example cases and lessons learned. 2019.

[25] Mangold D., Deschaintre L., Seasonal thermal energy storage - report on state of the art and necessary further R + D. IEA-SHC Task 45 Large Systems 2015:1–48. http://task45.iea-shc.org/data/sites/1/publications/IEA_SHC_Task45_B_Report.pdf

[26] Gauthier G. Benchmarking and improving models of subsurface heat storage dynamics. Comparison of Danish Ptes and BTES installation measurements with their corresponding TRNSYS models. 2020.

[27] Winterscheid C. Dronninglund District Heating Monitaring Data Evaluation for the Years 2015-2017 2017.

[28] Sifnaios I, Gauthier G, Trier D, Fan J, Jensen AR. Dronninglund water pit thermal energy storage dataset. Solar Energy 2023;251:68–76. https://doi.org/10.1016/j.solener.2022.12.046.

[29] Sifnaios I, Jensen AR, Furbo S, Fan J. Performance comparison of two water pit thermal energy storage (PTES) systems using energy, exergy, and stratification indicators. Journal of Energy Storage 2022;52:104947. https://doi.org/10.1016/j.est.2022.104947.

[30] Geo. 37304 Dronninglund Måling af grundvandstemperatur 2015.

[31] Dannemand Andersen J, Bødker L, Jensen M V. Large thermal energy storage at Marstal district heating. 18th International Conference on Soil Mechanics and Geotechnical Engineering: Challenges and Innovations in Geotechnics, ICSMGE 2013 2013;4:3351–4.

[32] Xiang Y, Gao M, Furbo S, Wang D, Tian Z, Fan J. Heat transfer of a large-scale water pit heat storage under transient operations. Journal of Energy Storage 2022;55:105455. https://doi.org/10.1016/j.est.2022.105455.

[33] Ochs F. Modelling large-scale thermal energy stores. University of Stuttgart 2009.

[34] Pan X, Xiang Y, Gao M, Fan J, Furbo S, Wang D, et al. Long-term thermal performance analysis of a large-scale water pit thermal energy storage. Journal of Energy Storage 2022;52:105001. https://doi.org/10.1016/j.est.2022.105001.

DTU Construct

Section of Energy and Services
Brovej Building 118
2800 Kongens Lyngby

www.construct.dtu.dk

978-87-7475-764-1 DCAMM: S337